A2A-98-U-0-021 (APL)
EERL-98-12A (EERL)
December 1998

Handbook of Propagation Effects for Vehicular and Personal Mobile Satellite Systems

Overview of Experimental and Modeling Results

Julius Goldhirsh*
and
Wolfhard J. Vogel#

* THE JOHNS HOPKINS UNIVERSITY, APPLIED PHYSICS LABORATORY
11100 JOHNS HOPKINS ROAD, LAUREL, MARYLAND 20723-6099

THE UNIVERSITY OF TEXAS AT AUSTIN
ELECTRICAL ENGINEERING RESEARCH LABORATORY
10100 BURNET ROAD, AUSTIN, TEXAS 78758

Acknowledgements

This work was performed under JPL Contract No. 960204 for The Johns Hopkins University, Applied Physics Laboratory and JPL Contract No. 956520 for The University of Texas at Austin, Electrical Engineering Research Laboratory.

Table of Contents

Chapter 1
Introduction

Table of Contents

Chapter 1
Introduction

1.1 Background

This handbook is a revision of NASA Reference Publication 1274 entitled, "Propagation Effects for Land Mobile Satellite Systems: Overview of Experimental and Modeling Results," by Goldhirsh and Vogel. The revised text contains pertinent features of the original document plus updates of experiments and models available since 1992 dealing with propagation effects for earth-satellite scenarios. Additional topics that have reached an appropriate level of maturity are also described. These include optical means to establish propagation statistics, propagation effects on satellite paths reaching inside buildings and marine-satellite propagation. To streamline the reading and the acquisition of information, each chapter contains its own table of contents, table of figures, listing of tables, recommendations, and references. The chapters are written such that they are self-contained requiring little or no searching for information in other chapters. The following paragraphs give a brief overview of the contents of each of the chapters with new information denoted by *(NEW)*. Also presented is a step-by-step procedure for accessing this text on the World Wide Web and interacting with the authors.

1.2 Overview of Chapters in Revised Text

1.2.1 Chapter 2: Attenuation Due to Trees: Static Case

This chapter deals with propagation effects caused by trees derived from stationary measurements. It presents values of attenuation coefficients and path attenuations associated with single trees of different "types." Largest and average values measured are given for frequencies at UHF (870 MHz) and L-Band (1.6 GHz). Plots of attenuation coefficient versus frequency are presented covering the frequency range of 30 MHz through 3 GHz corresponding to ground-to-ground measurements through woodland, forest or jungle over paths of 100 m or more *(NEW)*. Cumulative distributions of attenuation at L-Band and K-Band (19.6 GHz) are presented for Pecan trees "with" and

"without" leaves *(NEW)*. Formulations are presented giving the attenuation versus elevation angle at UHF (870 MHz) and L-Band with and without leaves. Frequency scaling formulations are given for intervals between UHF (870 MHz) and L-Band, L-Band (1 GHz) and S-Band (4 GHz), and L-Band (1.6 GHz) and K-Band (19.6 GHz) *(NEW)*.

1.2.2 Chapter 3: Attenuation Due to Roadside Trees: Mobile Case

Measurements and empirical models are examined in this chapter for earth-satellite scenarios in which a vehicle is driven along tree-lined roads and where the signal degradation is primarily due to attenuation from tree canopies. Examples of time-series of attenuation and phase at L-Band (1.5 GHz) and K-Band (20 GHz) are presented *(NEW)*. An Extended Empirical Roadside Shadowing model is characterized with a step-by-step procedure for implementation *(NEW)*. This model was adopted by the International Telecommunication Union Radio Communication Sector (ITU-R). It extends the previous empirical roadside shadowing model as follows: (1) It provides frequency scaling from UHF (870 MHz) to K-Band (20 GHz), (2) it enables elevation angle scaling from 7° to 80°, and (3) it may be applied to percentage ranges from 1% to 80%. Probability distributions of attenuations for measurements in Central Maryland, Australia, Texas, Washington State, and Alaska are compared with the distributions derived from the EERS model *(NEW)*. Comparisons are also made with measurements made by the European Space Agency (ESA) *(NEW)*. An equal probability formulation for attenuation by trees with and without foliage at K-Band (20 GHz) is presented and validated using an independent set of measurements *(NEW)*. Other empirical models are presented and compared with the EERS model *(NEW)*. These include the Modified Empirical Roadside Shadowing (MERS), Empirical Fading Model (EFM), and the Combined Empirical Fading Model (CEFM). An examination of the ITU-R Fade Model at elevations above 60° is also examined *(NEW)*.

1.2.3 Chapter 4: Signal Degradation for Line-of-Sight Communications

Mobile satellite signal degradation is examined for a geometry in which line-of-sight communications are maintained with minimal shadowing and where signal variability is due to multipath from the ground, roadside trees, utility poles, hills, mountains, or a nearby body of water. Cumulative distribution models are given for canyon measurements at UHF (870 MHz) and L-Band (1.5 GHz) at elevations of 30° and 45°, hilly environments at L-Band at elevations of 7° to 14° *(NEW)*, and roadside trees at UHF and L-Band at 30°, 45°, and 60°. Cumulative fade distributions at K-Band (20 GHz) associated with multipath due to reflections from a nearby body of water and from dry land at 8° elevation for various vehicle orientations are described *(NEW)*. Cumulative fade distributions at K-Band (20 GHz and 18.7 GHz) due to multipath for various pointing aspects relative to the satellite location and tree-line geometries are given *(NEW)*. An empirical multipath model of the cumulative fade distribution was developed representing the median of 12 multipath distributions at frequencies from 870 MHz to 20 GHz and elevation angles from 8° to 60° *(NEW)*. The model covers a percentage range of 1% to 50%.

1.2.4 Chapter 5: Fade and Non-Fade Durations and Phase Spreads

Fade duration distributions for tree-lined roads at L-Band (1.5 GHz) are presented. Dependence of fade duration distributions at L-Band on elevation angle for measurements in the United States and Europe are described ***(NEW)***. The ITU-R model describing the cumulative distribution of fade duration is given and compared with measurements ***(NEW)***. Non-fade durations for tree-lined road scenarios are characterized for L-Band. Dependence of non-fade duration distributions as a function of elevation angle is examined ***(NEW)***. Phase fluctuation distributions for "moderate" and "extreme" shadowing" conditions are presented and a corresponding model is given.

1.2.5 Chapter 6: Polarization, Antenna Gain, and Diversity Considerations

Fade effects at L-Band (1.5 GHz) and UHF (870 MHz) are related to depolarization, antenna gain, lane changing, antenna space diversity, and satellite path diversity ***(NEW)***. A curve and corresponding formulation describing the cross-polarization isolation at L-Band (1.5 GHz) versus the co-polarization fade level is presented for a roadside tree environment. An example describing the effects on fade distributions is reviewed when high and low gain antennas are used for a tree-lined environment. The effects of fade reduction (or enhancement) achieved by "changing lanes" are described and a "fade-reduction" formulation is given for elevation angles of 30°, 45°, and 60° for UHF (870 MHz) and L-Band (1.5 GHz). A model for diversity improvement factor is presented at L-Band (1.5 GHz). (This quantity is the ratio of the single terminal probability to the joint probability for a given spacing at a given fade margin.) Diversity gain (tree-lined roads) versus antenna spacing from 1 to 10 m is presented. Diversity gains at L-Band for expressway driving in Japan for antenna separations of 5 m and 10 m are reviewed ***(NEW)***. Single and joint fade distributions are presented associated with switching communications to different satellites in a given constellation such that smaller fading is experienced ***(NEW)***. These satellite diversity distributions were based on simulations employing optical measurements of the skyline. Direct satellite diversity measurements of single and joint fading distributions at S-Band (2 GHz) employing NASA's Tracking and Data Relay Satellite System (TDRSS) are described ***(NEW)***.

1.2.6 Chapter 7: Investigations from Different Countries

A compendium of measured cumulative fade distributions for Land-Mobile-Satellite System (LMSS) is presented. The different measurement campaigns' frequency, elevation angle, 1% and 10% fades, environment, and associated reference is tabulated ***(NEW)***. A brief background description associated with each of these measurements is given and the corresponding cumulative fade distributions are presented for frequencies of UHF (870 MHz) through K-Band (20 GHz) and elevation angles from 8° to 80° ***(NEW)***.

1.2.7 Chapter 8: Earth-Satellite Propagation Effects Inside Buildings ***(NEW)***

This new chapter describes propagation effects for the case in which transmissions originate from a satellite and receiver measurements are made inside various building types. Relative signal losses associated with spatial, temporal, and frequency intervals are described. Signal level variation with frequency is characterized over a frequency

interval of 700 MHz to 1.8 GHz, 1.6 GHz, and 2.5 GHz. Cumulative fade distributions at these frequencies are characterized. The efficacy of space and frequency diversity interior to buildings is examined. Bandwidth distortion is considered.

1.2.8 Chapter 9: Maritime-Mobile Satellite Propagation Effects *(NEW)*

Multipath fading from the ocean is characterized when low gain antennas are used for low-elevation angle marine-satellite scenarios. An overview of early multipath ship-to-satellite fade measurements at various frequencies ranging from 240 MHz to 30 GHz is reviewed. Characteristics of specular and diffuse multipath fading due to sea surface reflections are examined. Models are presented giving the fading depth versus the elevation angle at various probability levels. Fade duration models are also presented. Dependence of the model values on significant wave height and frequencies ranging from 1 GHz to 10 GHz is examined.

1.2.9 Chapter 10: Optical Methods for Assessing Fade Margins for Shadowing, Blockage and Clear Line-of-Sight Conditions *(NEW)*

This new chapter deals with single and joint earth-satellite fade distributions derived from the photographing of roadside images of the skyline and analyzing the ambient scene in terms of (1) clear line-of-sight with multipath reflections, (2) shadowed state, and (3) blocked state. The general methodology of making such measurements is described and examples of skyline statistics are presented. The formulations for "clear," shadowed," and "blocked" propagation states are presented. Parameter values for earth-satellite measurements at L-Band (1.5 GHz) for urban Japan are given. Cumulative fade distributions are derived from these formulations and compared with a measured distribution. Probability distributions for a series of elevation angles are presented for elevation angles ranging from 7° to 82°. Single and joint cumulative fade distributions are derived from a simulated constellation of satellites for urban areas of London, Tokyo, and Singapore. Statistics of potentially visible satellites in various states given a constellation are derived. Diversity gains are derived for "combining" and "handoff" diversity modes.

1.2.10 Chapter 11: Theoretical Modeling Considerations

In this chapter are reviewed the elements of diffuse and specular scattering. Density functions used in propagation modeling are examined. These include Nakagami-Rice, Rayleigh, and lognormal density functions. The theoretical models examined are (1) Loo Distribution, (2) Lutz Total Shadowing Model, (3) Lognormal Shadowing, and (4) Simplified Lognormal Shadowing. Models are also considered associated with "fade state transitions." In particular, 2-state and 4-state Markov models are characterized. Geometric analytic models associated with signal and multiple point scatterers are presented. Recommendations regarding the efficacy of each of the models are made throughout the chapter.

1.2.11 Chapter 12: Recommendations for Further Investigations

In this chapter are reviewed the gaps in our understanding of propagation effects vis-à-vis present and projected scenarios for mobile-satellite scenarios. These scenarios include land (mobile and personal), marine, and aeronautical to satellite scenarios for geostationary and orbiting constellations. Recommendations are made for further investigations to fill the indicated gaps.

1.3 Mobile Satellite Handbook on the Web

It is the author's intention to make this handbook fully accessible via the World Wide Web, both as a service to the users, but also to facilitate feedback for improvements and revisions.

A step-by-step procedure is provided for accessing the individual handbook chapters already on the world-wide-web, downloading these chapters onto your personal computer, printing them in a paper format and saving them to a file. As mentioned, this handbook is a revision of NASA Reference Publication 1274 that may be also accessed and downloaded from the "home" page whose address is given in the following paragraph.

1.3.1 Contents of the Home Page

The "home page" may be attained after dialing the web address http://www.utexas.edu/research/mopro/index.html titled "Propagation Effects/MSS." The home page contains linkages to a number of locations. From top to bottom, these include

- Home pages of NASA, APL, EERL, and JPL by clicking appropriate icon
- Submission of e-mail messages to the authors by clicking e-mail addresses under the individual author's name
- Previous publication (NASA Reference Publication 1274) obtained by clicking the blue report at center-left
- Table of contents of revised document by clicking "Table of Contents,"
- Glossary of terms and abbreviations (under construction) by clicking "Glossary of Terms and Abbreviations,"
- Paper copy of individual chapters obtained by clicking "How to Get a Paper Copy,"
- Submittal of your comments to authors by clicking "Your Feedback," and
- A short biography of the authors by clicking "The Authors."

1.3.2 From Table of Contents to Viewing a Chapter Text

Clicking "Table of Contents" links the user to a listing of chapters. The chapter titles displayed as links are those available on the web and ready for downloading. Clicking on the title link may access the Table of Contents for any particular chapter. As an example, by clicking on Chapter 10 (Optical Methods for Assessing Fade Margins), we link to the corresponding Table of Contents for Chapter 10. Any of the chapter sections listed in the table of contents may be viewed by clicking on the desired section title. For example, clicking the title for Section 10.2 (General Methodology) links only to this section, which may be saved or printed. One may also link to a particular figure or reference by clicking on a particular figure number or reference (shown as link). For example, clicking on "Figure 10.1" results in the display of Figure 10.1, and clicking on the reference "Vogel and Hong, 1988" links to the corresponding entry in the list of references. Both the figure and the listing of references are capable of being printed out in this mode.

1.3.3 Downloading a Chapter into a PDF File for Printout or Saving into a File

One may download an Adobe PDF version of each chapter for off-line browsing or printing by clicking "How to Get a Paper Copy" in the home page. This will link to another page enabling you to download the Adobe Acrobat software. Assuming Acrobat is already loaded onto the personal computer, one may download Chapter 10 (for example) by clicking on its chapter title. After the chapter is downloaded, it may be printed or saved to a file in your personal computer.

1.3.4 Communicating with the Authors

The reader may send a message to the authors by clicking "Your Feedback" or by clicking the authors email addresses given as links at the top of the home page. The authors encourage comments regarding errors in the text or suggested subjects to be included in a follow-up edition of this handbook.

Chapter 2

Attenuation Due to Trees: Static Case

Table of Contents

Table of Figures

Table of Tables

Chapter 2
Attenuation Due to Trees: Static Case

2.1 Background

A typical scenario in which fading occurs is depicted in Figure 2-1, which shows a vehicle receiving satellite transmissions. The vehicle, which has an antenna mounted on its roof, is presumed to be at a distance of 10 to 20 m from the roadside trees, and the path to the satellite is generally above 20° in elevation. The antenna is to some extent directive in elevation such that multipath from lower elevation (i.e., near zero degrees and below) is filtered out by the antenna gain pattern characteristics. Although there may exist multipath contributions at various azimuths, shadowing from the canopies of one or two trees give rise to the major attenuation contributions. That is, the signal fade for this case is due primarily to scattering and absorption from both branches and foliage where the attenuation path length is the interval within the first few Fresnel zones intersected by the canopies.

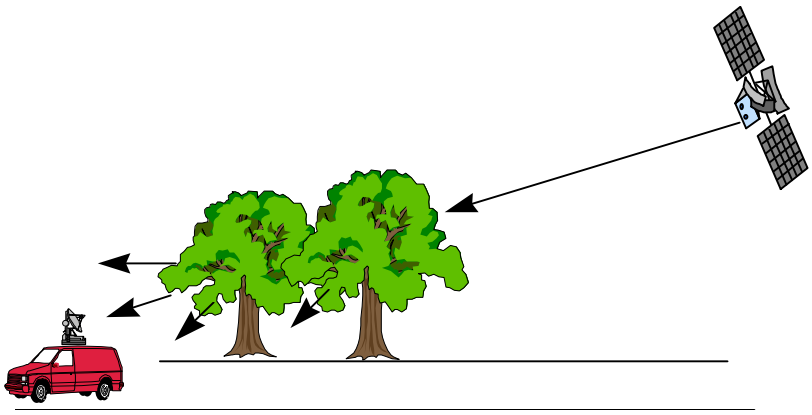

Figure 2-1: LMSS propagation path shadowed by the canopies of one or two trees in which the attenuation path length is relatively well defined.

This geometry is in contrast to the configuration in which the transmitter and receiver are located near the ground and propagation takes place through a grove of trees as shown in

Figure 2-2. The attenuation contribution for this configuration is a manifestation of the combined absorption and multiple scattering from the conglomeration of tree canopies and trunks. For this case, an estimation of the attenuation coefficient from attenuation measurements requires knowledge of the path length usually estimated to be the "grove thickness." This thickness may encompass a proportionately large interval of non-attenuating space between the trees. Hence attenuation coefficients as derived for groves of trees may underestimate the attenuation coefficient vis-à-vis those derived for path lengths intersecting one or two contiguous canopies for LMSS scenarios as shown in Figure 2-1. This chapter deals primarily with characterizing the path attenuation through tree canopies pertaining to the scenario of Figure 2-1, although attenuation coefficients associated with that of Figure 2-2 are briefly characterized in Section 2.4.

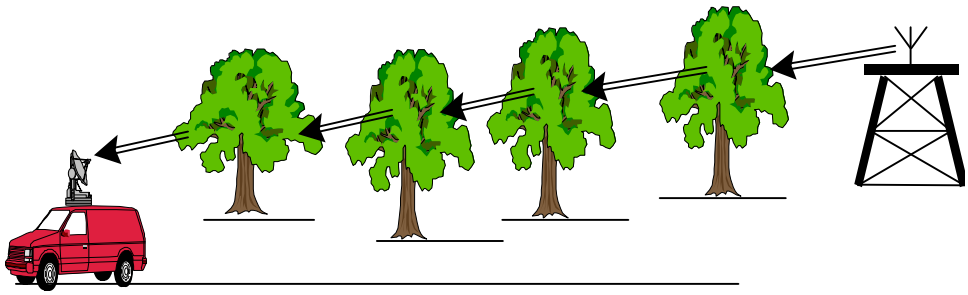

Figure 2-2: Low elevation propagation through a grove of trees giving rise to ambiguity in attenuation path length.

Static measurements of attenuation due to isolated trees for LMSS configurations have been systematically performed at UHF, L-Band, S-Band and or K-Band by Benzair et al. [1991], Butterworth [1984a; 1984b], Cavdar et al. [1994], Vogel and Goldhirsh [1994; 1993; 1986], Vogel et al. [1995], Ulaby et al. [1990], and Yoshikawa and Kagohara [1989].

2.2 Attenuation and Attenuation Coefficient at UHF

For those cases in which shadowing dominates, the attenuation primarily depends on the path length through the canopy, and the density of foliage and branches in the first Fresnel region along the line-of-sight path. The receiver antenna pattern may also influence the extent of fading or signal enhancements via the mechanism of multipath scattering from surrounding trees or nearby illuminated terrain. An azimuthally omni-directional antenna is more susceptible to such multipath scattering than a directive antenna. Nevertheless, the authors found through measurements and modeling considerations for LMSS scenarios, the major fading effects are a result of the extent of shadowing along the line-of-sight direction.

In Table 2-1 is given a summary of the single tree attenuation results at 870 MHz based on the measurements by the authors [Vogel and Goldhirsh, 1986; Goldhirsh and Vogel, 1987] who employed remotely piloted aircraft and helicopter transmitter platforms. The attenuations were calculated by comparing the power changes for a configuration in which the receiving antenna (on the roof of a van) was "in front of" and

"behind" a particular tree. The former and latter cases offered non-shadowed and maximum shadowing conditions, respectively, relative to the line of sight propagation path from the transmitter on the aircraft to the stationary receiver. During each flyby, the signal levels as a function of time were expressed in terms of a series of median fades derived from the 1024 samples measured over one second periods. The attenuation assigned to the particular flyby was the highest median fade level observed at the measured elevation angle. It may be deduced that the motion of the transmitter aperture and the receiver's sampling rate of 1024 samples per second resulted in more than 200 independent samples averaged each second. This sample size is normally adequate to provide a well-defined average of a noisy signal. The individual samples from which the median was derived over the one-second period were observed to fluctuate on the average ±2 dB about the median due to the influence of variable shadowing and multipath.

Table 2-1: Summary of Single Tree Attenuations at f = 870 MHz.

Tree Type	Attenuation (dB)		Attenuation Coefficient (dB/m)	
	Largest	Average	Largest	Average
Burr Oak*	13.9	11.1	1.0	0.8
Callery Pear	18.4	10.6	1.7	1.0
Holly*	19.9	12.1	2.3	1.2
Norway Maple	10.8	10.0	3.5	3.2
Pin Oak	8.4	6.3	0.85	0.6
Pin Oak*	18.4	13.1	1.85	1.3
Pine Grove	17.2	15.4	1.3	1.1
Sassafras	16.1	9.8	3.2	1.9
Scotch Pine	7.7	6.6	0.9	0.7
White Pine*	12.1	10.6	1.5	1.2
Average	14.3	10.6	1.8	1.3
RMS	4.15	2.6	0.9	0.7

The first column in Table 2-1 lists the trees examined where the presence of an asterisk corresponds to results of measurements at Wallops Island, VA in June 1985 (remotely piloted aircraft), and the absence of the asterisk represents measurements in central MD in October 1985 (helicopter). During both measurement periods, the trees examined were approximately in full foliage conditions. The second and third columns labeled "Largest" and "Average" represent the largest and average values, respectively, of attenuation (in dB) derived for the sum total of flybys for that particular tree. The fourth and fifth columns denote the corresponding attenuation coefficients derived from the path length through the canopy. The path length was estimated from measurements of the elevation angle, the tree dimensions, and the relative geometry between the tree and the receiving antenna height. The dependence of the attenuation on elevation angle is described in Section 2.6. We note that the attenuations from Pin Oak as measured at Wallops Island (with asterisk) is significantly larger than that measured in central Maryland (without

asterisk) because the former tree had a significantly greater density of foliage over approximately the same path length interval. This result demonstrates that a description of the attenuation from trees for LMSS scenarios may only be handled employing statistical processes.

Butterworth [1984b] performed single tree fade measurements at 800 MHz (circularly polarized transmissions) at seven sites in Ottawa, Canada over the path elevation interval 15^o to 20^o. The transmitter was located on a tower and receiver measurements were taken at a height of 0.6 m above the ground. Measurements were performed from April 28 to November 4, 1981 covering the period when leaf buds started to open until after the leaves had fallen from the trees. A cumulative distribution of foliage attenuation readings covering a 19 day period in June 1981 was noted to be lognormal, where the fades exceeded 3 and 17 dB for 80% and 1% of the measured samples, respectively. The median attenuation was approximately 7 dB with an approximate median attenuation coefficient of 0.3 dB/m (24 m mean foliage depth). The average attenuation coefficient of Butterworth is smaller than those measured by the authors in central Maryland and Virginia. The disparity between these results may be due to differences in the methods of averaging, the heights of the receiver and the interpretation of the shadowing path length as previously described.

2.3 Single Tree Attenuation at L-Band

Single tree attenuation measurements at 1.6 GHz were conducted in Turkey between April and September of 1993 by Cavdar et al. [1994]. The transmitter was placed atop a building and the receiver antenna was located on top of a mobile unit which positioned itself at different locations in the shadowed region of a number of trees.

Table 2-2 gives the total path attenuation and attenuation coefficients for a series of trees. The average attenuation and attenuation coefficient are similar at UHF (Table 2-1) to their respective values at L-Band (Table 2-2), although their respective RMS values are significantly different.

Table 2-2: Attenuation coefficient and average attenuations at 1.6 GHz of the different tree types.

Tree Type	Average Attenuation (dB)	Attenuation Coefficient (dB/m)
Willow	10.45	1.1
Pine	18.0	1.8
Linden	9.1	1.4
European Alder	7.0	1.0
Acacia	6.75	0.9
Poplar	3.5	0.7
Elm	9.0	1.2
Hazelnut	2.75	1.1
Maple	16.25	1.25
White Spruce	20.1	1.75
Laurel Cherry	12.0	2.0
Plane	16.9	1.35
Fir	12.75	1.5
Fruit	9.6	1.2
Average	11.0	1.3
RMS	5.1	0.35

2.4 Attenuation through Vegetation: ITU-R Results

The ITU-R [1994] designates attenuation through vegetation in terms of ground-to-ground measurements over paths of approximately 100 m or more, in woodland, forest or jungle with antenna heights of 2-3 m above the ground with only part of the ray passing through the foliage as designated in Figure 2-2. Attenuation corresponding to this scenario is referred to as “long path.” A “short-path attenuation” scenario is also designated corresponding to short ground-to-ground or slant-path measurements through the foliage of individual trees with foliage depths of no more than 10-15 m as shown in Figure 2-1. Figure 2-3 gives the attenuation coefficient in dB/m versus frequency for both the short-path (squares) and long-path (solid and dashed curves and diamond at approximately 10 GHz). As mentioned, the long-path results show attenuation coefficients significantly smaller than the short path results. Short-path attenuation coefficients between 1 and 2 dB/m are generally indicated at frequencies between approximately 1 and 4 GHz consistent with the results of Table 2-1 and Table 2-2.

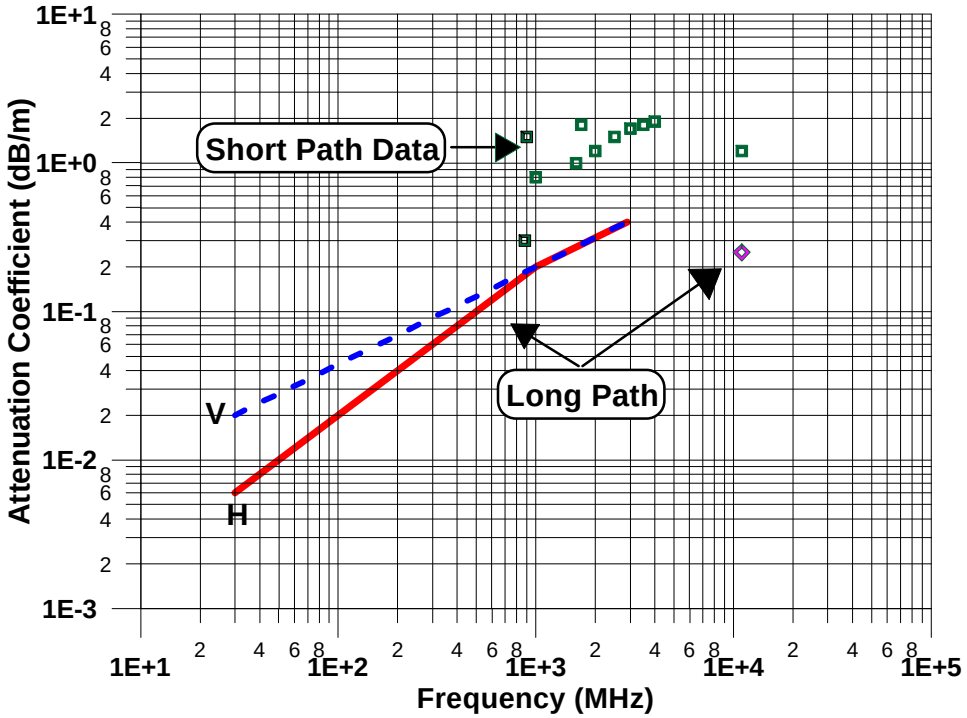

Figure 2-3: Attenuation coefficients as described by the ITU-R for both "short paths" (square points) and "long path" (solid and dashed lines and diamond point at 10 GHz) scenarios.

2.5 Distributions of Tree Attenuation at L-Band and K-Band

Static tree attenuation measurements at L- (1.6 GHz) and K-Band (19.6 GHz) were executed in Austin, Texas [Vogel and Goldhirsh, 1993; 1994]. The trees sampled were Pecan (deciduous) and Magnolia (evergreen). The L-Band measurements were performed in December 1990 and July 1991 during which times the sampled Pecan tree was "without foliage" and in "full foliage," respectively. The transmitter was placed atop a 20 m tall tower and the receiving antenna was mounted on a motorized positioner placed within the geometric shadow zone of each tree. The antenna was moved slowly over a horizontal distance of several meters, and the received power was sampled every 0.1 s for about 100 s. The K-Band measurements were performed in March and May, 1993 employing the same approximate geometry. These months also correspond to periods in which the Pecan tree was without leaves and in full foliage, respectively. The receiving antenna was hand-held and moved horizontally over a distance of several meters, first in the shadow of the same Pecan tree, and then in the shadow of the nearby Magnolia tree. Quadrature detector receiver voltages were sampled at a 1000 Hz rate for several minutes. The path lengths within the Pecan and Magnolia crowns were on average 9 m and 4.5 m, respectively. The clear line-of-sight reference signal levels were determined for all cases by moving the receiver to an equi-distant position where the signal path was unobstructed.

Resulting cumulative fade distributions are given in Figure 2-4 for cases in which the canopy optically shadowed the line-of-sight path between the transmitter and the receiver (curves A through E). Also given, as a reference, is the distribution for the unobstructed K-Band line-of-sight case (curve F). In Table 2-3 is given a summary of the total attenuation and attenuation coefficient for the median (50%) and 1% cases for the different frequencies and tree scenarios characterized in Figure 2-4. The elevation angles for the K and L-Band measurements relative to the Pecan tree were approximately 26° and 30°, respectively.

Table 2-3: Median and 1% attenuation and attenuation coefficients at K- and L-Band.

Tree Condition	Percentage	Total Fade (dB)		Attenuation Coefficient (dB/m)	
		L-Band	K-Band	L-Band	K-Band
Clear LOS	Median		0.5		
	1%		2.6		
Bare Pecan	Median	10.3	6.9	1.1	0.75
	1%	18.4	25.0	2.0	2.8
Pecan in leaf	Median	11.6	22.7	1.3	2.5
	1%	18.6	43.0	2.1	4.8
Magnolia	Median		19.6		4.4
(evergreen)	1%		39.6		8.8

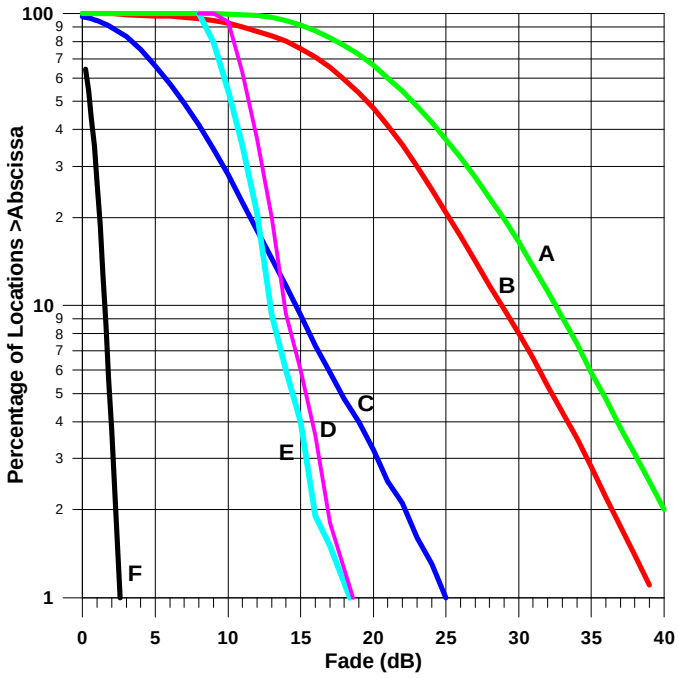

Figure 2-4: Cumulative distributions at L-Band (1.6 GHz) and K-Band (19.6 GHz). The cases considered are: (A) K-Band Pecan in leaf, (B) K-Band Magnolia (evergreen), (C) K-Band Pecan without leaves, (D) L-Band Pecan in leaf, (E) L-Band Pecan without leaves, (F) K-Band unobstructed line-of-sight

2.6 Seasonal Effects on Path Attenuation

2.6.1 Effects of Foliage at UHF

It is observed from the configuration of Figure 2-1, that at smaller elevation angles, the path length through the canopy will increase. Likewise, it is expected that the attenuation will also increase assuming the path cuts through the canopy. Single tree attenuation measurements for 870 MHz at different elevation angles were performed in central-Maryland in October 1985 and in March 1986 for a Callery Pear tree employing a helicopter as the transmitter platform [Goldhirsh and Vogel, 1987]. The approximate geometry of the tree and relative location of the receiving antenna is given in Figure 2-5. Figure 2-6 shows the corresponding results for the two seasons during which the tree was in full foliage (October) and without leaves (March). Also shown are the linear fits for each of the sets of data points.

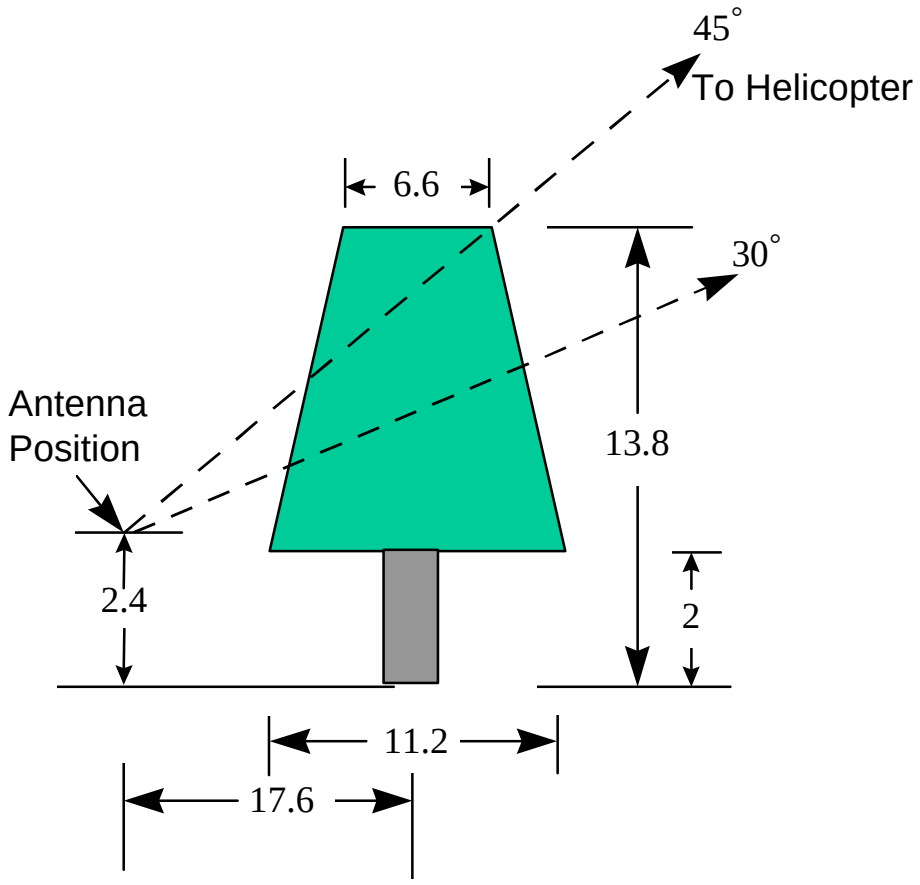

Figure 2-5: Configuration showing the approximate dimensions of the Callery Pear tree and the relative location of the receiver. All dimensions are expressed in meters.

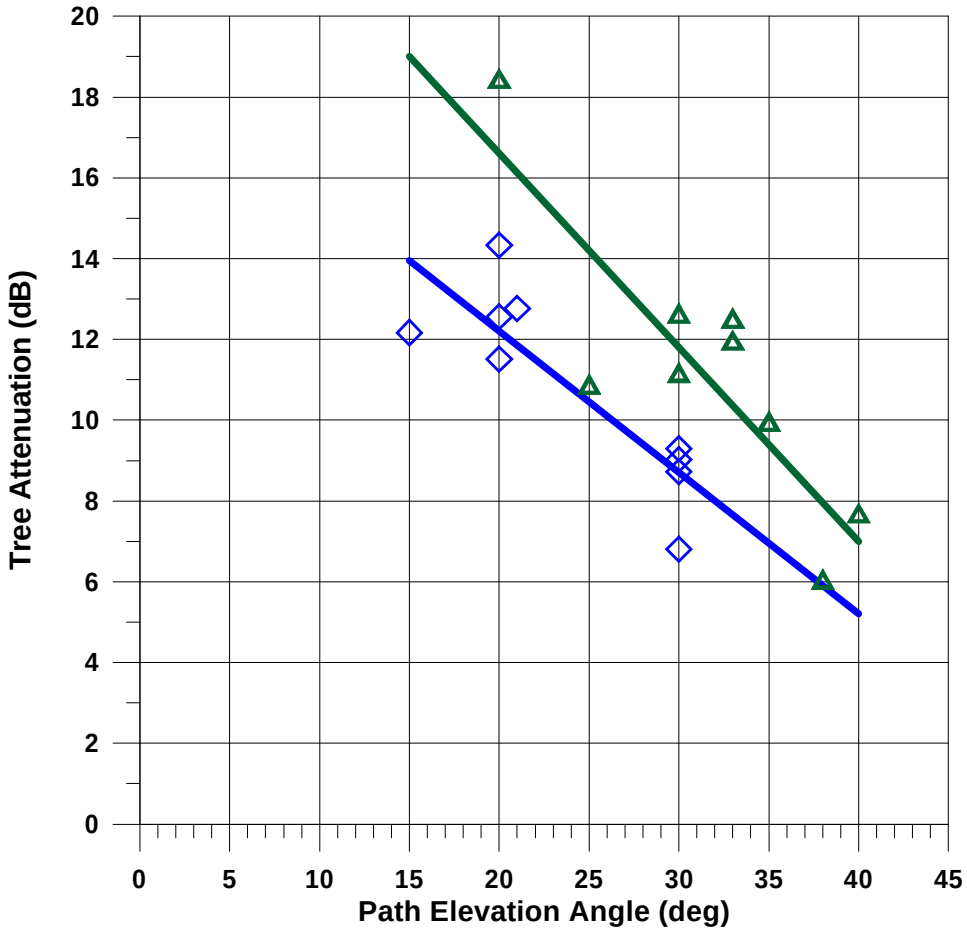

Figure 2-6: Static tree attenuation versus elevation angle at 870 MHz for the Callery Pear tree configuration in Figure 2-5. Triangles represent the full-foliage case, diamonds the no-foliage case.

The linear best fits in Figure 2-6 may be described as follows:

for $15^o < q < 40^o$ (*full foliage*)

$$A(q) = -0.48q + 26.2 \tag{2-1}$$

for $15^o < q < 40^o$ (*bare tree*)

$$A(q) = -0.35q + 19.2 \tag{2-2}$$

where q is in degrees and $A(q)$ is in dB. We derive from (2-1) and (2-2) over the given angular range at 870 MHz:

for 5 dB < *A(no foliage)* < 14 dB,

$$A(\textit{full foliage}) = 1.35A(\textit{no foliage}) \tag{2-3}$$

which states that for the static case, the maximum attenuation contribution (in dB) for the full-foliage case is 35% larger than the corresponding attenuation for the bare tree case.

This results suggests that the predominant attenuation at 870 MHz arises from the tree branches via the mechanism of absorption and the scattering of energy away from the receiver. The conclusion that the wood part of the tree is the major contributor to attenuation has also been substantiated at UHF for the mobile case (Chapter 3). The above results are limited to elevation angles above approximately 15°. At smaller angles, the path may pass through the bottom part of the canopy. More complicated scenarios may result in which there may be multiple tree effects as depicted in Figure 2-2 or terrain blockage may arise. The lower angle limit for mobile scenarios is broached in Chapter 3.

2.6.2 Effects of Foliage at L-Band

Upon analyzing the data points at equal probability levels for the L-Band distributions with and without foliage (curves D and E of Figure 2-4), we observed that the percent difference in fades between the foliage relative to the no-foliage cases for the Pecan tree ranged from approximately 15% at 70% probability to 1% at 1% probability with an average percent difference of approximately 7% (average fade difference = 0.8 dB). The linear least square relation with a standard error of 0.1 dB relating the attenuation with foliage to that with no foliage is given by,

for 9 dB < $A($no *foliage)* < 18 dB

$$A(\,full\ foliage) = 2.33 + 0.9A(no\ foliage) \tag{2-4}$$

Here again, we observe that the major contribution due to attenuation is the wood part of the tree. Since the tree configurations, tree types, and foliage path lengths were different for the Callery Pear sampled at UHF and the Pecan tree sampled at L-Band, no inference should be made as to the frequency relationships pertaining to foliage versus no-foliage fading.

2.6.3 Effects of Foliage at K-Band

Curves B and C in Figure 2-4 give the distributions for the attenuation with and without foliage, respectively. The following formulation relates the attenuation for the foliage case versus the no-foliage case:

for 5 dB < *A(no foliage)* < 25 dB (*static case*)

$$A(\,foliage) = a + bA(no\ \ foliage)^{c} \tag{2-5}$$

where the coefficients *a*, *b*, and *c* are given by

$$\begin{aligned} a &= 0.351 \\ b &= 6.8253 \\ c &= 0.5776 \end{aligned} \tag{2-6}$$

Although the above formulation was derived from a mobile run of a street lined with a high density of Pecan trees in Austin, Texas, it appears to give predictions (dashed curves) which agree quite well with the static runs (solid curves) as shown in Figure 2-7.

The range of no-foliage attenuations shown in the line preceding (2-5) corresponds to the static attenuation measurement range depicted in Figure 2-7.

2.7 Frequency Scaling Considerations

2.7.1 Scaling between 870 MHz and L-Band

Ulaby et al. [1990] measured the attenuation properties at 50° elevation associated with transmission at 1.6 GHz through a canopy of red pine foliage in Michigan at both horizontal and vertical polarizations. The path length through the canopy was approximately 5.2 m and the average attenuations measured at horizontal and vertical polarizations were 9.3 and 9.2 dB. Their measurements gave rise to an average attenuation coefficient of approximately 1.8 dB/m. Combining this result at L-Band with the average value of 1.3 dB/m at UHF given in Table 2-1, the frequency scaling formulation found applicable between UHF (870 MHz) and L-Band (1.6 GHz) assuming a full foliage scenario is given by

$$A(f_2) = A(f_1)\sqrt{\frac{f_2}{f_1}} \tag{2-7}$$

where $A(f_1)$ and $A(f_2)$ are the equal probability attenuations expressed in dB at the indicated frequencies between 870 MHz and 1.6 GHz. This expression was found also to be applicable for frequencies between UHF and S-Band for mobile scenarios as discussed in Chapter 3.

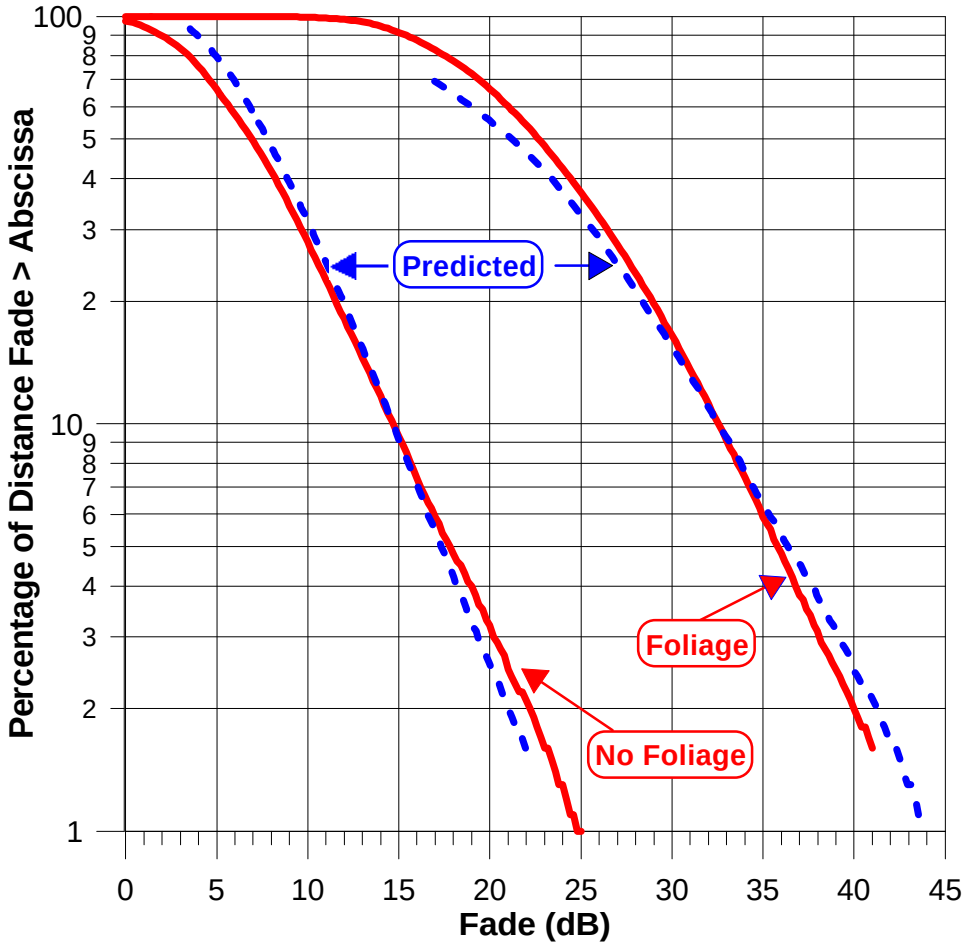

Figure 2-7: Comparison of measured (solid curves) and predicted (dashed) attenuation distributions at 19.6 GHz corresponding to foliage and non-foliage cases.

2.7.2 Scaling between 1 GHz and 4 GHz

Benzair et al. [1991] performed static attenuation measurements on a mature deciduous tree in full foliage at a series of frequencies between 1 and 4 GHz at an elevation angle of approximately 45°. They found the attenuation coefficient to obey the following expression.

For 1 GHz $\leq f \leq$ 4 GHz

$$MEL = 0.79\, f^{0.61} \tag{2-8}$$

where f is the frequency in GHz and MEL (mean excess loss) represents the mean attenuation coefficient in dB/m. This expression (normalized to 1 GHz) is plotted in Figure 2-8 (dashed curve) with other frequency scaling curves. In Figure 2-9, the various frequency-scaling criteria are also applied to the measured L-Band distribution and compared with the measured S-Band distribution as measured by Vogel et al. [1995]. The three frequency scaling techniques are shown to give similar results over the indicated frequency ranges.

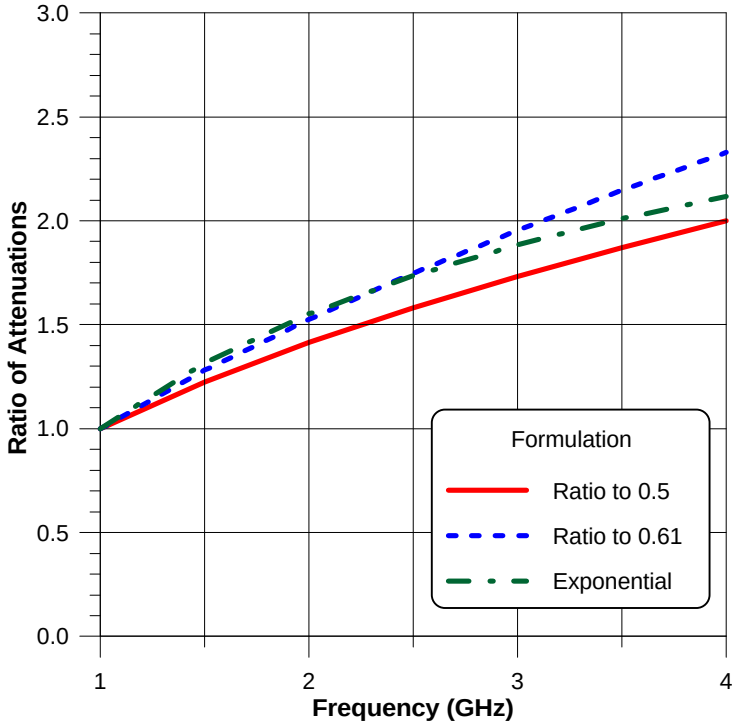

Figure 2-8: Ratio of Attenuations versus frequency using different frequency scaling criteria normalized to 1 GHz. The solid curve corresponds to (2-7), the dashed curve to (2-8) and the dot-dashed curve to (2-9).

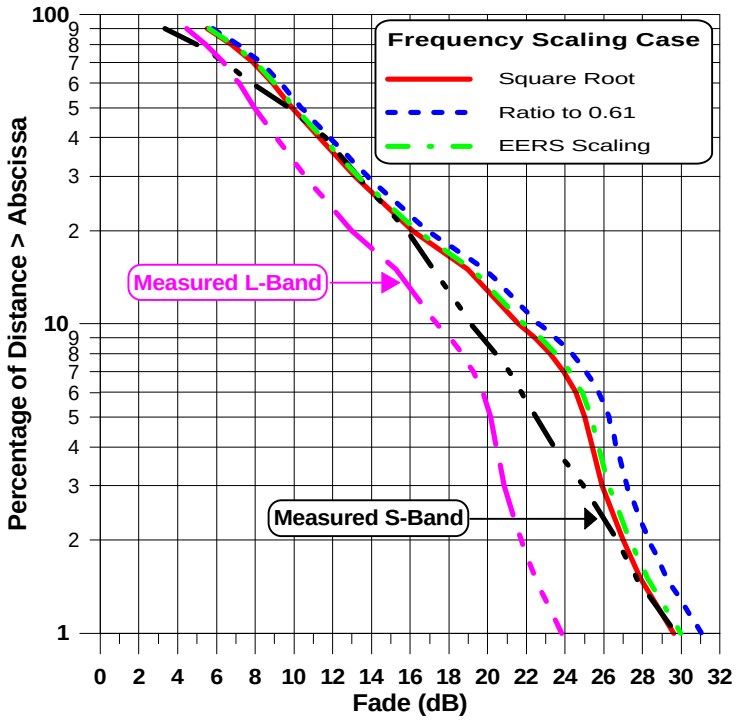

Figure 2-9: Frequency scaling of attenuation distribution of measured L-Band (1.6 GHz) to S-Band frequencies using different criteria. Also shown is measured S-Band distribution.

2.7.3 Scaling between L-Band and K-Band

A frequency scaling formulation which extends between L- and K-Band for the static case and also applicable for the mobile case has been derived by the authors [Vogel and Goldhirsh, 1993] and is given by

$$A(f_2) = A(f_1)\exp\left\{b\cdot\left[\left(\frac{1}{f_1}\right)^{0.5} - \left(\frac{1}{f_2}\right)^{0.5}\right]\right\} \tag{2-9}$$

where

$$b = 1.5 \tag{2-10}$$

and where $A(f_1)$ and $A(f_2)$ are the attenuations in dB at frequencies f_1 and f_2 (in GHz).

Figure 2-10 shows a comparison of L- (1.6 GHz; curve A) and K-Band (19.6 GHz; curve B) cumulative fade distributions calculated from static measurements of a Pecan tree in full leaf. Curves C, D, and E are the frequency scaled distributions (L to K) derived employing (2-9), (2-7), and (2-8), respectively.

The transmitters at L- and K-Bands were placed atop a 20 m tower and the receiver systems were located within the geometric shadow zone of the tree where the elevation angle was approximately 30^o [Vogel and Goldhirsh, 1993]. The vertical scale represents the percentage of optically shadowed locations over which the abscissa fade was exceeded. Curve C represents the application of (2-9), D makes use of (2-7) and E was derived applying (2-8) on the L-Band curve at equal probability values. The frequency scaling formulation shows agreement to within a few dB for percentages between 2% and 20% for the static case. The formulations (2-7) and (2-8) are shown to give excessive fades and are not applicable at K-Band. In the paper by Vogel and Goldhirsh [1993], a multiplying constant of b = 1.173 was given as being applicable at the median fade level (i.e., P = 50%). The constant as given by (2-10) is the suggested value for the static case as it gives good agreement over the dominant part of the fade distribution curve B in Figure 2-10. Hence, (2-9) is also the same frequency scaling formulation for the mobile scenario case.

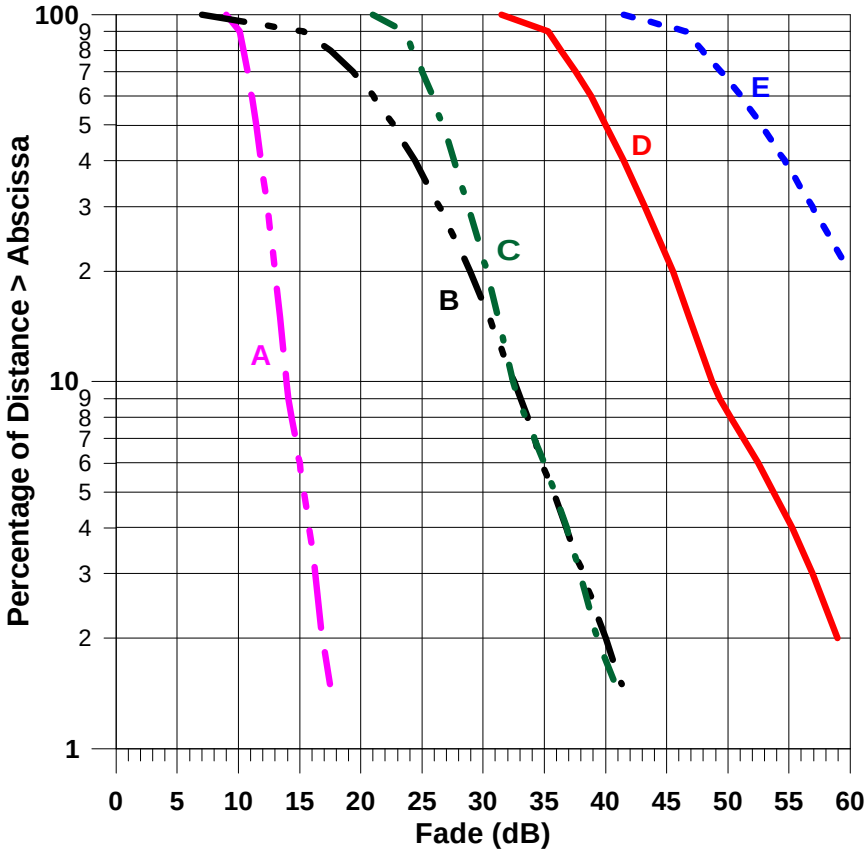

Figure 2-10: Cumulative distributions at L (1.6 GHz; curve A) and K (19.6 GHz curve B) derived from measurements. Curves C, D, and E are the frequency scaled distributions (L to K) derived employing (2-9), (2-7), and (2-8), respectively.

2.8 Conclusions and Recommendations

1. The average single tree attenuation at UHF (870 MHz) is 10.6 dB (2.6 dB RMS) (Table 2-1).
2. The average single tree attenuation at L-Band (1.6 GHz) is 11 dB (5.1 dB RMS) (Table 2-2).
3. The median single tree attenuation at K-Band (20 GHz) is 23 dB (Table 2-3).
4. The recommended frequency scaling formulation pertaining to single trees in full foliage at frequencies between UHF (870 MHz) and K-Band (20 GHz) is given by

$$A(f_2) = A(f_1)\exp\left\{b\left[\left(\frac{1}{f_1}\right)^{0.5} - \left(\frac{1}{f_2}\right)^{0.5}\right]\right\} \qquad (2\text{-}11)$$

where $A(f_1)$, $A(f_2)$ are the respective equal probability attenuations (dB) at frequencies f_1, f_2 (in GHz).

5. The dominant contributor to attenuation is the wood part of the tree at frequencies between UHF (870 MHz) and S-Band (4 GHz). For example, foliage has been found to introduce approximately 35% additional attenuation at UHF (Equation (2-3) and 15% at L-Band (Figure 2-4).

6. At K-Band (20 GHz), the wood and leaf parts of the tree are both important showing increases due to foliage ranging from 2 to 3 times the attenuation (Figure 2-7).

2.9 References

Benzair, B., H. Smith, and J. R. Norbury, [1991], "Tree Attenuation Measurements at 1-4 GHz for Mobile Radio Systems, Sixth International Conference on Mobile Radio and Personal Communications, 9-11 December, London, England, pp. 16-20. (IEE Conference Publication No. 351).

Butterworth, J. S. [1984a], "Propagation Measurements for Land-Mobile Satellite Systems at 1542 MHz," Communication Research Centre Technical Note 723, August. (Communication Research Centre, Ottawa, Canada.)

Butterworth, J. S. [1984b], "Propagation Measurements for Land-Mobile Satellite Services in the 800 MHz," Communication Research Centre Technical Note 724, August. (Communication Research Centre, Ottawa, Canada.)

Cavdar, I. H., H. Dincer, and K. Erdogdu [1994], "Propagation Measurements at L-Band for Land Mobile Satellite Link Design," Proceedings of the 7th Mediterranean Electrotechnical Conference, April 12-14, Antalya, Turkey, pp. 1162-1165.

Goldhirsh, J. and W. J. Vogel [1987], "Roadside Tree Attenuation Measurements at UHF for Land-Mobile Satellite Systems," IEEE Transactions on Antennas and Propagation, Vol. AP-35, pp. 589-596, May.

ITU-R [1994] (International Telecommunication Union, Radio Communications Study Groups), "Propagation Data Required for the Design of Earth-Space Land Mobile Telecommunication Systems," Recommendation ITU-R PN.681-1, International Telecommunication Union, ITU-R Recommendations, 1994 PN Series Volume, Propagation in Non-Ionized Media, pp. 203-204.

Ulaby, F. T., M. W. Whitt, and M. C. Dobson [1990], "Measuring the Propagation Properties of A Forest Canopy Using A Polarimetric Scatterometer," IEEE Transactions on Antennas and Propagation, Vol. AP-38, No. 2, pp. 251-258, Feb.

Vogel, W. J. and J. Goldhirsh [1994], "Tree Attenuation at 20 GHz: Foliage Effects," Presentations of the Sixth ACTS Propagation Studies Workshop (APSW VI), Clearwater Beach, Florida, November 28-30, pp. 219-223. (Jet Propulsion Laboratory Technical Report, JPL D-12350, California Institute of Technology, Pasadena, California.)

Vogel, W. J., G. W. Torrence, and H. P. Lin [1995], "Simultaneous Measurements of L- and S-Band Tree Shadowing for Space-Earth Communications," IEEE Transactions on Antennas and Propagation, Vol. AP-43, pp. 713-719, July

Vogel, W. J. and J. Goldhirsh [1993], "Earth-Satellite Tree Attenuation at 20 GHz: Foliage Effects," Electronics Letters, Vol. 29, No. 18, 2nd September, 19, pp. 1640-1641.

Vogel, W. J., and J. Goldhirsh [1986], "Tree Attenuation at 869 MHz Derived from Remotely Piloted Aircraft Measurements, IEEE Transactions on Antennas and Propagation, Vol. AP-34, No. 12, pp. 1460-1464, Dec.

Yoshikawa, M. and M. Kagohara [1989], "Propagation Characteristics in Land Mobile Satellite Systems," 39th IEEE Vehicular Technology Conference, pp. 550-556, 1-3 May.

Chapter 3

Attenuation Due to Roadside Trees: Mobile Case

Table of Contents

Table of Figures

Table of Tables

Chapter 3

Attenuation Due to Roadside Trees: Mobile Case

3.1 Background

In this chapter we examine measurements and empirical models associated with land-mobile satellite signal attenuation for scenarios in which a vehicle is driven along tree-lined roads, where signal degradation is predominantly due to absorption and scatter from tree canopies. Various models are compared with one another and with distributions derived directly from measurements. In particular, we examine the Empirical Roadside Shadowing Model (ERS) [ITU-R, 1994, Goldhirsh and Vogel, 1992; Vogel et al., 1992], Extended Empirical Roadside Shadowing Model (EERS) [Goldhirsh and Vogel; 1995a, 1995b], Empirical Fading Model (EFM) [Parks et al., 1993a], the Combined Empirical Fading Model (CEFM) [Parks et al., 1993a], and the Merged Empirical Roadside Shadowing Model (MERS) [Sforza et al.; 1993a; 1993b].

3.2 Time-Series Fade Measurements

In the analysis of times-series roadside fades for Land-Mobile-Satellite Service (LMSS) scenarios, the attenuation levels are represented by the dB ratio of the non-shadowed power received under conditions of negligible multipath relative to the shadowed levels. Figure 3-1 and Figure 3-2 are examples of relative power measurements depicting nominal characteristics of fading and phase variations for non-shadowed and shadowed line-of-sight cases, respectively. These measurements were performed by Vogel and Goldhirsh [1995] in Bismarck, North Dakota and in central-Maryland where L-Band transmissions (1.5 GHz) emanating from the MARECS B-2 satellite were received at elevation angles of 22° (Figure 3-1) and 40° (Figure 3-2). The fluctuations due to receiver noise were within 1 dB (RMS). The non-shadowed environment (Figure 3-1) may be characterized as an open rural road and the shadowed case (Figure 3-2) a tree-lined highway where the line-of-site path was obstructed by the roadside trees.

In Figure 3-1, fluctuations in the relative power (±1 dB) and in phase (±15°) are due to both system noise and to a small extent multipath. Nominally, peak-to-peak variations of less than 5 dB of power and 25° of phase may arise from multipath for non-shadowed cases. The shadowed case (Figure 3-2) has fades that are highly variable with fluctuations exceeding 15 dB. Some of these deep fades are also accompanied by rapid phase shifts. Time-series of fade and phase of the above types were obtained for various LMSS scenarios and environments and corresponding cumulative distributions were derived as described in the following paragraphs.

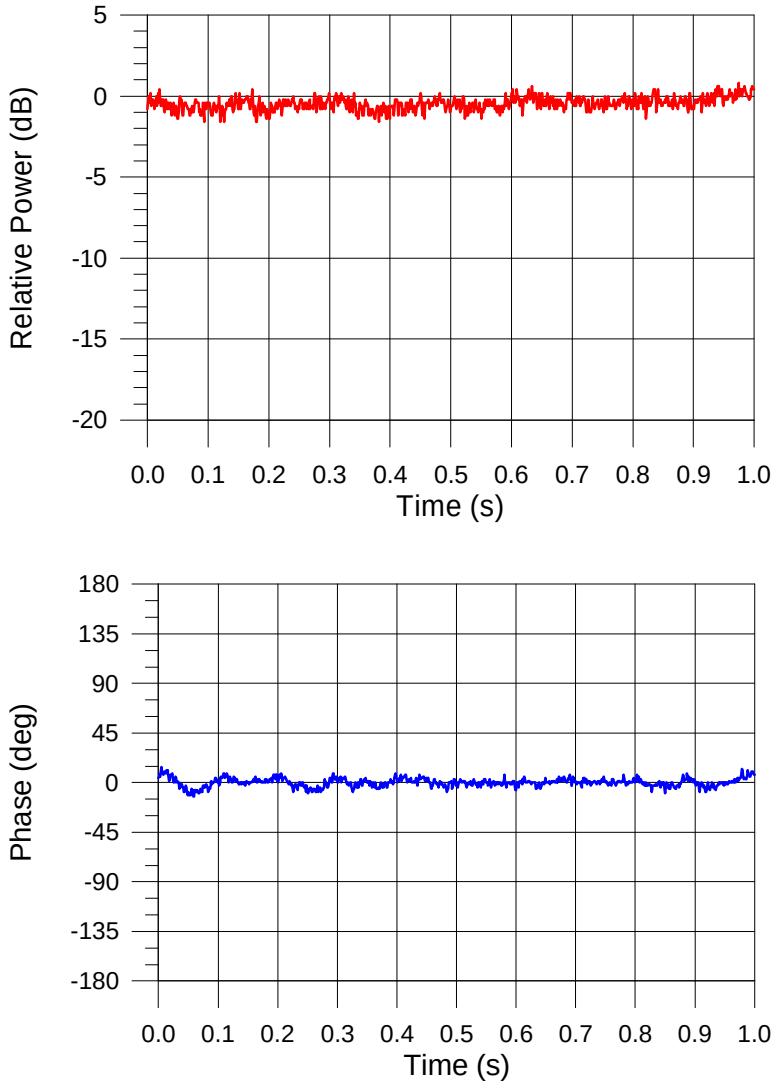

Figure 3-1: Time-series of 1.5 GHz fade (top) and phase (bottom) over a one second period at a sampling rate of 1 KHz. Measurements were taken of transmissions from MARECS-B2 at 22° elevation along an open road near Bismarck, North Dakota.

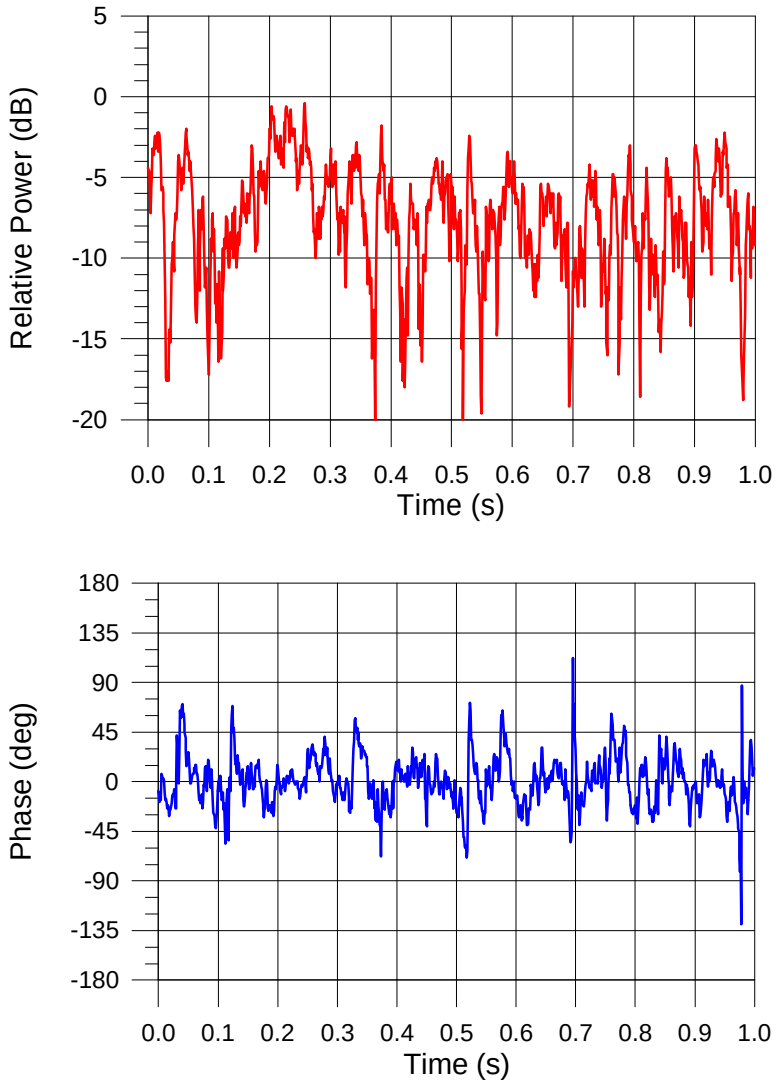

Figure 3-2: Time-series of 1.5 GHz fades (top) and phases (bottom) over a one second period at a sampling rate of 1 KHz. Measurements were taken of transmissions from MARECS-B2 at 40° elevation along a highway with roadside trees in central Maryland where the satellite line-of-sight was shadowed.

We show in Figure 3-3 an example of the variability of the minimum, maximum, and average fades over an approximate 10 minute period (approximately 10 km) pertaining to 20 GHz measurements of transmissions from the Advanced Communications Technology Satellite (ACTS) in Bastrop, Texas. The tree genus was predominantly Loblolly Pine (evergreen tree) and the elevation angle was approximately 55°. The central, red curve corresponds to the average signal level of 1000 samples taken over a one-second period (1 KHz sampling rate). The upper and lower curves correspond to the maximum and minimum signal level values obtained from the 1000 samples measured each second, respectively. Maximum values of three to four dB relative to the non-shadowed line-of-sight case arise because of constructive interference caused by multipath scatter by the foliage and branches. Large signal-level-drops to –20 dB and lower are due predominantly to canopy attenuation. The cumulative distribution for this run is described in Section 3.4.3 (Figure 3-12).

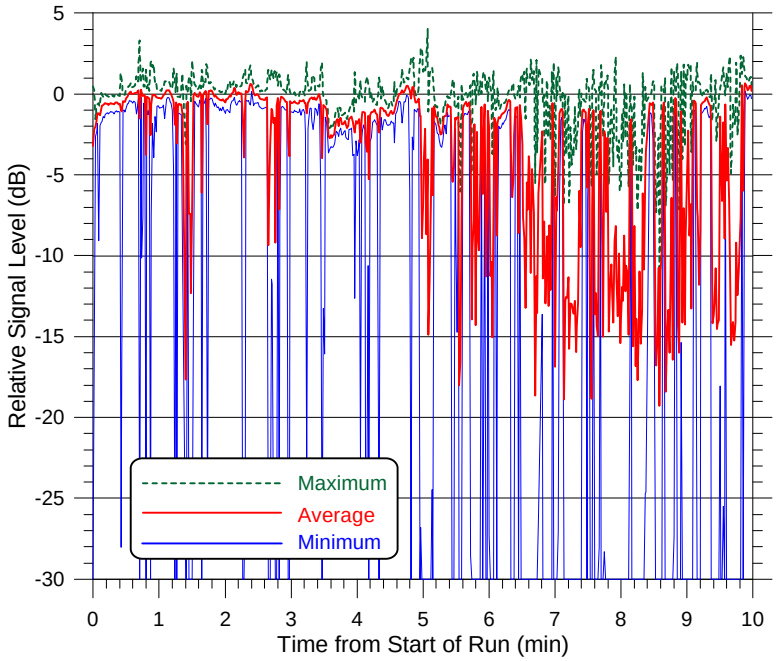

Figure 3-3: Relative K-Band signal time-series of maximum, minimum, and average levels for a 10 minute run (approximately 10 km) along a road lined with evergreen trees in Bastrop, Texas in February 1994.

3.3 Extended Empirical Roadside Model

3.3.1 Background

The empirical roadside shadowing (ERS) model gives estimates of cumulative fade distributions due to roadside trees:

- over the frequency range UHF (870 MHz) through S-Band (3 GHz),
- elevation angles to the satellite from 20° to 60°, and
- percentages from 1% to 20% [Goldhirsh and Vogel, 1992; Vogel et al., 1992; Vogel and Goldhirsh, 1990].

This model has been adopted as a recommendation of the ITU-R [1994]. The *extended* empirical roadside shadowing model (EERS) enhances the ERS model in the following ways:

- It may be used for elevation angles as low as 7°,
- it includes the frequency of 20 GHz, and
- it may be applied at a percentage range of 1% to 80% [Goldhirsh and Vogel, 1995a].

This model has been validated at UHF (870 MHz), L-Band (1.5 GHz), S-Band (3 GHz), and K-Band (20 GHz). It is offered as a candidate formulation at frequencies in-between

3 GHz and 20 GHz and at higher frequencies (e.g., 30 GHz) until data becomes available for validation. This revised model was adopted by the ITU-R in 1997 [ITU-R, 1997].

The ERS model was derived from the median of cumulative UHF and L-Band fade distributions systematically obtained from helicopter-mobile and satellite-mobile measurements in central Maryland. The measurements were made over approximately 600 km of driving distance comprising path elevation angles of 21°, 30°, 45° and 60°. The 21° case was executed employing the geostationary satellite MARECS-B2 [Vogel and Goldhirsh, 1990], whereas the measurements for the other angles were obtained employing a helicopter as the transmitter platform [Goldhirsh and Vogel, 1987; 1989]. The configuration corresponds to a shadowing condition in which the helicopter flew parallel to the moving vehicle and the propagation path was approximately normal to the line of roadside trees (e.g., azimuth of the satellite relative to the vehicle direction was 90°). Tree heights ranged from approximately 5 to 30 m. The satellite path directions were such that these were also predominantly along 90° shadowing orientation, although some of the roads sampled had a number of bends in them and deviations from this aspect did arise. The measurements were performed on two-lane highways (one lane in each direction), and a four-lane highway (two lanes in each direction), where the roadside trees were primarily of the deciduous variety. In order to assess the extent by which trees populate the side of the road, a quantity called percentage of optical shadowing (POS) was defined. This represents the percentage of optical shadowing caused by roadside trees at a path angle of 45° for right side of the road driving, where the path is to the right of the driver and the vehicle is in the right lane. The POS values for the roads driven were predominantly between 55% and 75% implying tree populations of at least these amounts.

In deriving the EERS model, use was made of the original previously developed body of data at UHF and L-Band in central Maryland as well as more recent developed databases. These correspond to mobile L-Band measurements of transmissions from MARECS B-2 in the western United States [Vogel and Goldhirsh, 1995], static K-Band (20 GHz) measurements in Austin, Texas [Vogel and Goldhirsh, 1993a; 1993b], and mobile K-Band measurements employing transmissions from ACTS [Goldhirsh and Vogel, 1995a; 1995b]. These latter measurements were performed during the first six months of 1994 during which a series of four 20 GHz mobile-ACTS campaigns were executed. The campaigns were performed in central Maryland (March, elevation = 39°), Austin, Texas (February and May, elevation = 55°) and Fairbanks, Alaska and environs (June, elevation = 8°). The mobile measurements in Austin, Texas during February and May enabled a determination of 20 GHz fading probability distributions for no-foliage and foliage conditions, respectively.

3.3.2 EERS Formulation

In the following paragraphs is given an overview of the EERS formulation followed by examples of its validation.

For $20\% \geq P \geq 1\%$ and $20° \leq \theta \leq 60°$

$$A(P,q,f) = A(P,q,f_L)\exp\left\{1.5\cdot\left[\left(\frac{1}{f_L}\right)^{0.5} - \left(\frac{1}{f}\right)^{0.5}\right]\right\} \tag{3-1}$$

and for $80\% \geq P > 20\%$ and $20° \leq \theta \leq 60°$

$$A(P,q,f) = A(20\%,q,f)\frac{\ln\left(\frac{80}{P}\right)}{\ln(4)} \tag{3-2}$$

where $A(P,\theta,f)$ is the attenuation (in dB) at the frequency f (in GHz) exceeded at P (in %) which represents the percentage of the driving distance for an Earth-satellite path angle θ (in degrees), and $A(P,\theta,f_L)$ is the corresponding attenuation (in dB) at f_L = 1.5 GHz. The attenuation is defined relative to non-shadowed and negligible multipath conditions.

The L-Band attenuation at f_L = 1.5 GHz (i.e., $A(P,\theta,f_L)$) for $20\% \geq P \geq 1\%$ and $20° \leq \theta \leq 60°$ is given by

$$A(P,q,f_L) = -M(q)\ln(P) + N(q) \tag{3-3}$$

where

$$M(q) = a + bq + cq^2 \tag{3-4}$$

$$N(q) = dq + e \tag{3-5}$$

and where

$$\begin{aligned} a &= 3.44 \\ b &= 0.0975 \\ c &= -0.002 \\ d &= -0.443 \\ e &= 34.76 \end{aligned} \tag{3-6}$$

In Equation (3-3), P is in %, θ is in degrees, f is in GHz, and $A(P,\theta,f_L)$ is in dB. Substituting (3-4) through (3-6) into (3-3), $A(P,\theta,f_L)$ may alternately be expressed by

$$A(P,q,f_L) = a(P) + b(P)q + g(P)q^2 \tag{3-7}$$

where $\alpha(P),\beta(P),\gamma(P)$ are tabulated in Table 3-1 for a series of fixed percentages in the interval between 1% and 80%.

Table 3-1: Listing of parameter values of $\alpha(P), \beta(P), \gamma(P)$ in Equation (3-7).

Percentage, *P*	$\alpha(P)$	$\beta(P)$	$\gamma(P)$
1	34.7600	-0.4430	0.0
2	32.3756	-0.5106	$1.3863X10^{-3}$
5	29.2235	-0.5999	$3.2189X10^{-3}$
10	26.8391	-0.6675	$4.6052X10^{-3}$
20	24.4547	-0.7351	$5.9915X10^{-3}$
30	17.3022	-0.5201	$4.2391X10^{-3}$
40	12.2273	-0.36754	$2.9957X10^{-3}$
50	8.2910	-0.2492	$2.0313X10^{-3}$
60	5.0748	-0.1525	$1.2433X10^{-3}$
70	2.3556	$-7.0805X10^{-2}$	$5.7711X10^{-4}$
80	0.0	0.0	0.0

For the case in which $20° > \theta \geq 7°$, the distribution derived using the formulations () or (3-7) is first calculated at $\theta = 20°$. This distribution for $\theta = 20°$ is subsequently assumed to be invariant at the smaller elevation angles. That is,

for $80\% \geq P \geq 1\%$ and $20° > \theta \geq 7°$

$$A(P, q, f) = A(P, 20°, f). \tag{3-8}$$

Equation (3-8) implies that the probability distributions at elevation angles smaller than 20° are the same as those at 20°. Extending the model to elevation angles smaller than 20° is a complex task for the following reasons: (1) The EERS model tacitly assumes that the canopies of single trees shadow the Earth-satellite path. At lower angles, there may be a greater likelihood that the path cuts the canopies of multiple trees or multiple tree trunks. (2) At smaller angles, there may also be a greater likelihood that the terrain itself blocks the Earth-satellite path creating high attenuation. (3) Ground multipath may also influence the distribution considerably. Based upon empirical experience for cases where the above caveats did not arise, it has been found that with good approximation the EERS model at 20° elevation is representative of results at 7° or 8°. The rationale for this assumption is characterized in Figure 3-4. At 20° elevation, the Earth-satellite path is already passing through the lower part of the tree canopies. Reducing the path elevation angle is likely to result in attenuation caused by tree trunks that may tend to mitigate the signal degradation. On the other hand, attenuation effects may increase because of fading from those tree canopies that are further offset from the road (as was the case in Alaska). The combination of these two effects generally results in the median fade statistics to be relatively invariant to angles below 20°, although larger deviations about the median are expected because of the breakdown of the aforementioned underlying assumptions.

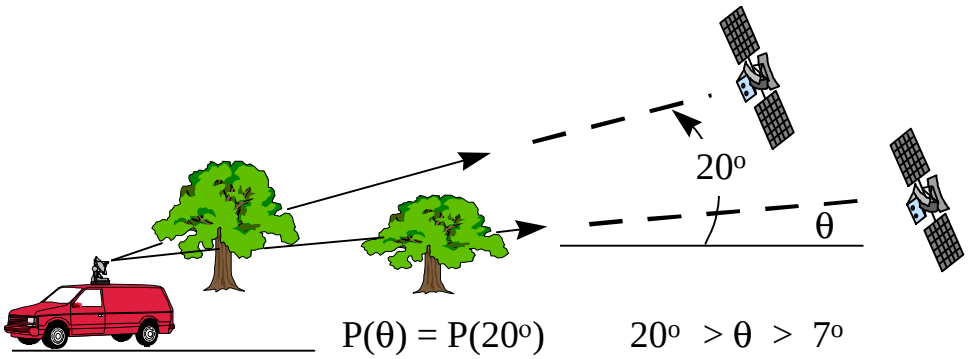

Figure 3-4: Cartoon depicting the mechanism by which the fades are statistically invariant at angles smaller than 20° (down to 7°). At angles smaller than 20°, Earth-satellite paths tend to fall below the canopy of nearby trees but intersect more distant tree canopies.

3.3.3 Step by Step Implementation of the EERS Model

We presume that it is desired to determine the percentage P of distance traveled over which a fade is exceeded for a LMSS tree-shadowing scenario at frequency f (in GHz) and elevation angle to the satellite θ (in degrees). We present here the step-by-step approach of determining this distribution using the EERS model given by () through (3-8). Initially, consider the angular interval $60° \geq \theta \geq 20°$. We will return to the extension of the formulation outside these angle bounds shortly.

Step 1: Calculate the fade distribution at $f_L = 1.5\ GHz$, valid for percentages of distance traveled of $20\% \geq P \geq 1\%$, at the desired path elevation angle, $60° \geq \theta \geq 20°$:

$$A(P, q, f_L) = -M(q)\ln(P) + N(q) \tag{3-9}$$

where

$$M(q) = 3.44 + 0.0975q - 0.002q^2 \tag{3-10}$$

$$N(q) = -0.443q + 34.76 \tag{3-11}$$

Step 2: Convert the fade distribution at $f_L = 1.5\ GHz$, valid for $20\% \geq P \geq 1\%$, to the desired frequency, f (GHz), where $0.8\ GHz \leq f \leq 20\ GHz$.

$$A(P, q, f) = A(P, q, f_L)\exp\left\{1.5 \cdot \left[\left(\frac{1}{f_L}\right)^{0.5} - \left(\frac{1}{f}\right)^{0.5}\right]\right\} \tag{3-12}$$

Step 3: Scale the fade distribution to percentages of distance traveled $80\% \geq P > 20\%$:

$$A(P,q,f) = A(20\%,q,f)\frac{\ln\left(\frac{80}{P}\right)}{\ln(4)} \tag{3-13}$$

Step 4: For path elevation angles in the range $20° > \theta \geq 7°$, the fade distribution is assumed to have the same value as at $q = 20°$:

$$A(P,q,f) = A(P,20°,f) \tag{3-14}$$

In Section 3.7.4, a methodology is outlined for extending the EERS model at L- and S-Bands to elevation angles greater than 60°.

3.3.4 Example Plots

Applying the above steps, we show plotted in Figure 3-5 to Figure 3-8 a family of curves describing the cumulative fade distributions at UHF (870 MHz), L-Band (1.5 GHz), S-Band (3.0 GHz), and K-Band (20 GHz). In Figure 3-9 is given the fade exceeded versus elevation angle for a family of constant percentages at L Band using (3-7) and the constants in Table 3-1. These curves may be used for establishing fade-margin design criteria for LMSS scenarios.

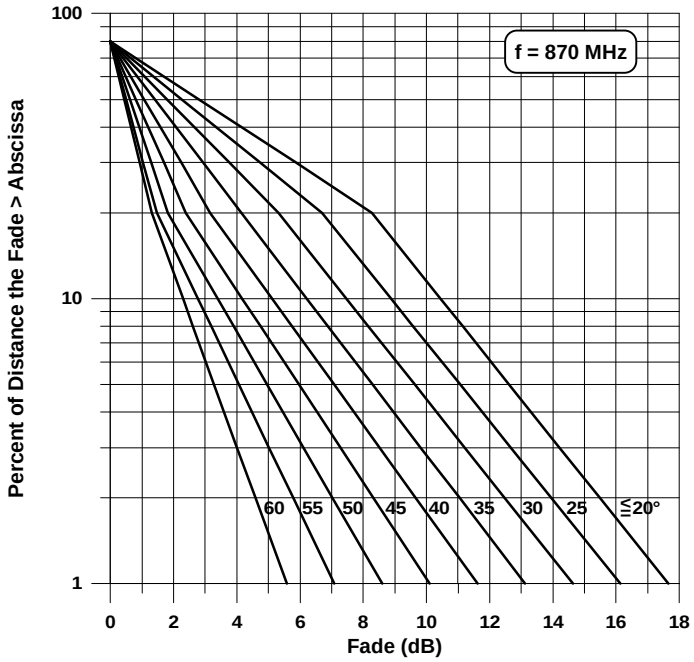

Figure 3-5: Family of cumulative fade distribution curves derived from the extended empirical roadside shadowing model (EERS) at UHF (870 MHz). The curve labeled "$\leq 20\,\mathrm{deg}$" is applicable at angles smaller than 20 degrees as described in the text.

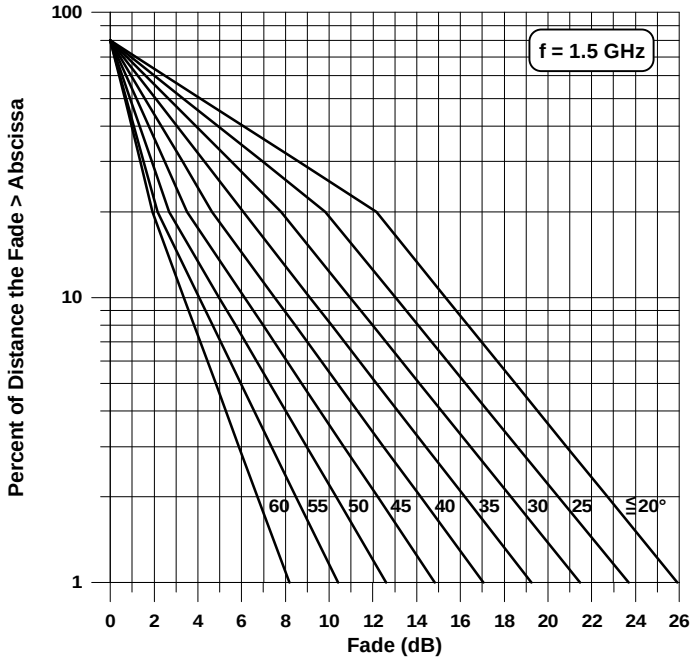

Figure 3-6: Family of cumulative fade distribution curves derived from the extended empirical roadside shadowing model (EERS) at L-Band (f = 1.5 GHz).

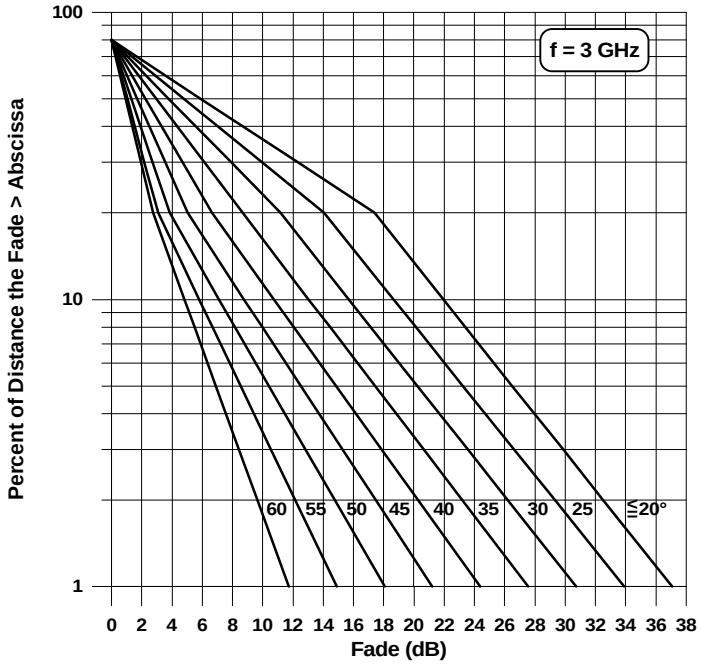

Figure 3-7: Family of cumulative fade distribution curves derived from the extended empirical roadside shadowing model (EERS) at S-Band (3 GHz).

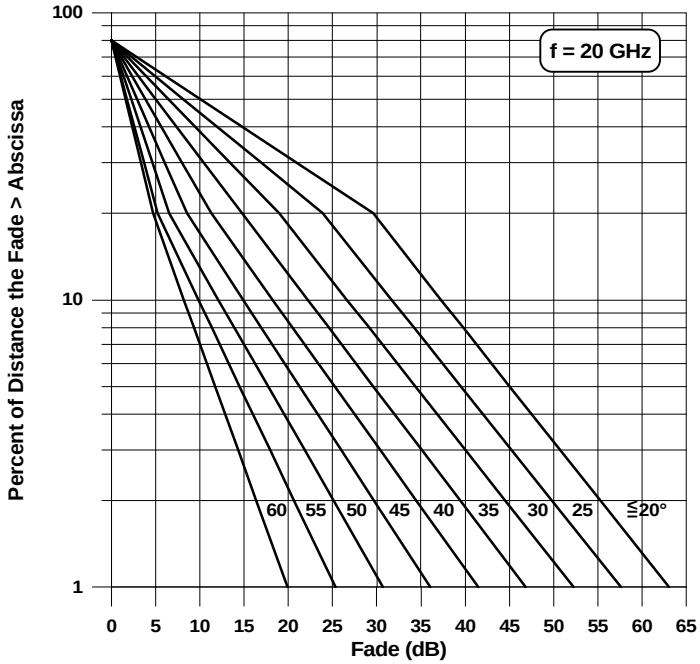

Figure 3-8: Family of cumulative fade distribution curves derived from the extended empirical roadside shadowing model (EERS) at K-Band (f = 20 GHz).

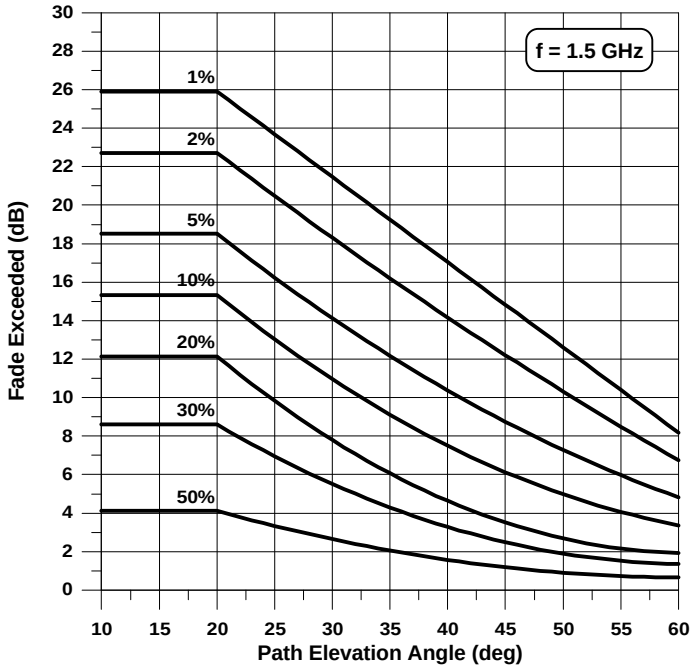

Figure 3-9: L-Band (1.5 GHz) fade values exceeded versus elevation angle for a family of fixed percentages using the EERS model.

3.4 Validation of the Extended Empirical Roadside Shadowing Model

3.4.1 Central Maryland at L-Band

In Figure 3-10 is shown a comparison of the above EERS model at 1.5 GHz for distributions derived from measurements in Central Maryland using a helicopter as the transmitter platform for an elevation angle of 45° [Goldhirsh and Vogel, 1989]. Shown are eight cumulative distributions corresponding to eight runs with different scenarios pertaining to three roads in central Maryland. The first legend item refers to the EERS model curve (solid black line) which is shown to approximate the median of the distributions whose fade values at any given probability are within ±5 dB of the measured distributions. The next item in the legend refers to Route 295 driving south (295 S), right lane driving (RL), with the helicopter on the right (HR). The other items in the legend have analogous definitions. Sets of other distributions were derived for elevation angles of 20°, 45°, and 60° with similar results associated with the EERS model [Goldhirsh and Vogel, 1995b].

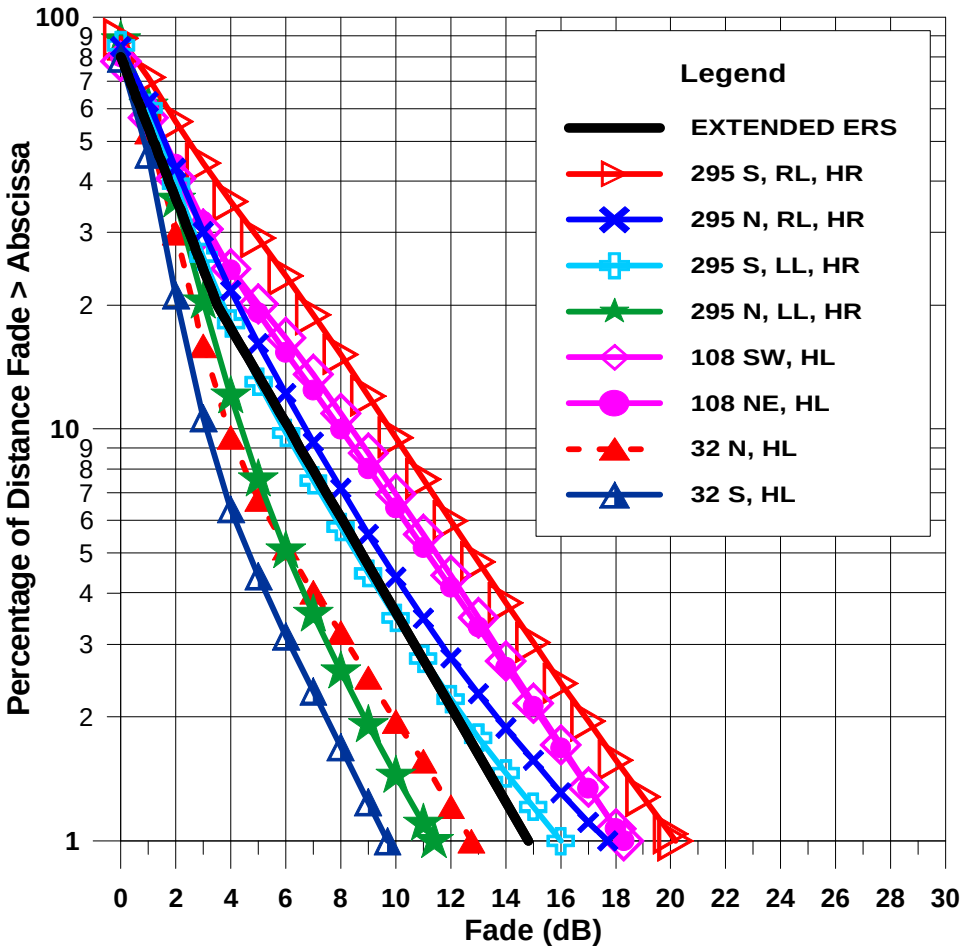

Figure 3-10: Comparison of EERS (solid black curve) model distribution with cumulative distributions for eight runs in central Maryland at 1.5 GHz and elevation angle of 45°.

3.4.2 Australian Fade Distributions at L-Band

In Figure 3-11 is shown a comparison of the EERS model with measurements made in Australia by the authors at 1.55 GHz [Vogel et al., 1992]. The Australian cumulative distribution reflects measurements made over a distance of 403 km comprising 15 individual runs in the Sydney region using the Japanese ETS-V geostationary satellite. The elevation angle to the satellite was 51°. Two major vegetation zones were traversed; forests along the coastal roads and woodlands further inland. Forests ranged from dry sclerophyll, in which the crowns of contiguous trees did not touch each other to tropical rain-forests, in which the leafy crowns of the trees intermingled. The dominating tree genus in the forests was Eucalyptus. Other than tree types, general similarities existed between the roads traveled in Australia and those in central Maryland (e.g., tree heights, POS, setbacks). Shown also is the EERS model at 51°. We note that the maximum difference between the two distributions is less than 2 dB, which occurs at 14%. The differences reduce monotonically above and below this percentage.

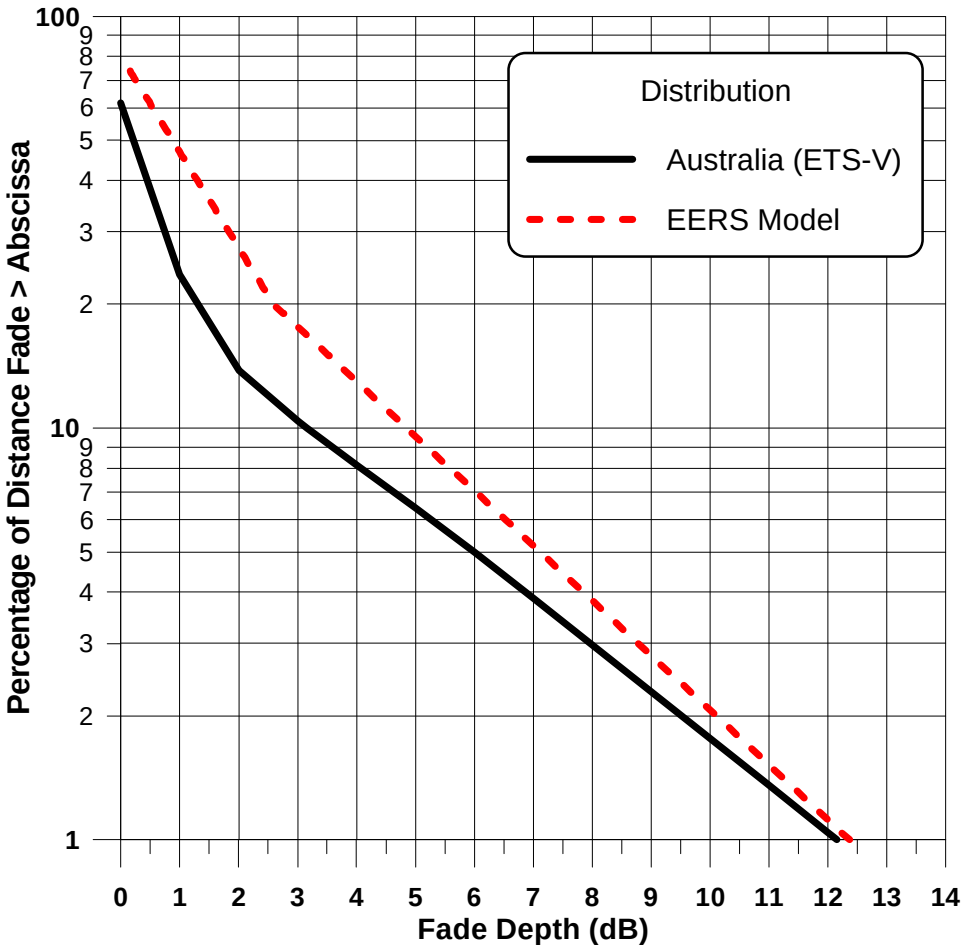

Figure 3-11: Comparison of Australian fade distribution with EERS model at elevation angle of 51° at a frequency of 1.55 GHz.

3.4.3 Austin, Texas at K-Band

In Figure 3-12 is shown a K-Band (20 GHz) distribution (elevation angle = 55°) for an approximate 10 km run along an evergreen (Loblolly Pine) tree-lined road in Bastrop, Texas derived from the ACTS campaign. This distribution corresponds to the fade time-series plot in Figure 3-3 and was alluded to in Section 3.2. The Earth-satellite paths cut the line of roadside trees on average at an angle of 57°. The population of trees was in excess of 55%, and there were considerable segments of road where the trees formed a tunnel with branches and foliage overhead. Also shown plotted is the EERS model (dashed curve). We note that the EERS model underestimates the fade by at most 5 dB for probabilities between 1% and 20%. This deviation is within the variability expected in comparing the EERS model with measured distributions as exemplified for L-Band in Figure 3-10. The underestimation of the EERS model at the smaller probabilities is most likely caused by the prevalence of foliage tunnels giving a greater likelihood of fading at the higher elevation angles.

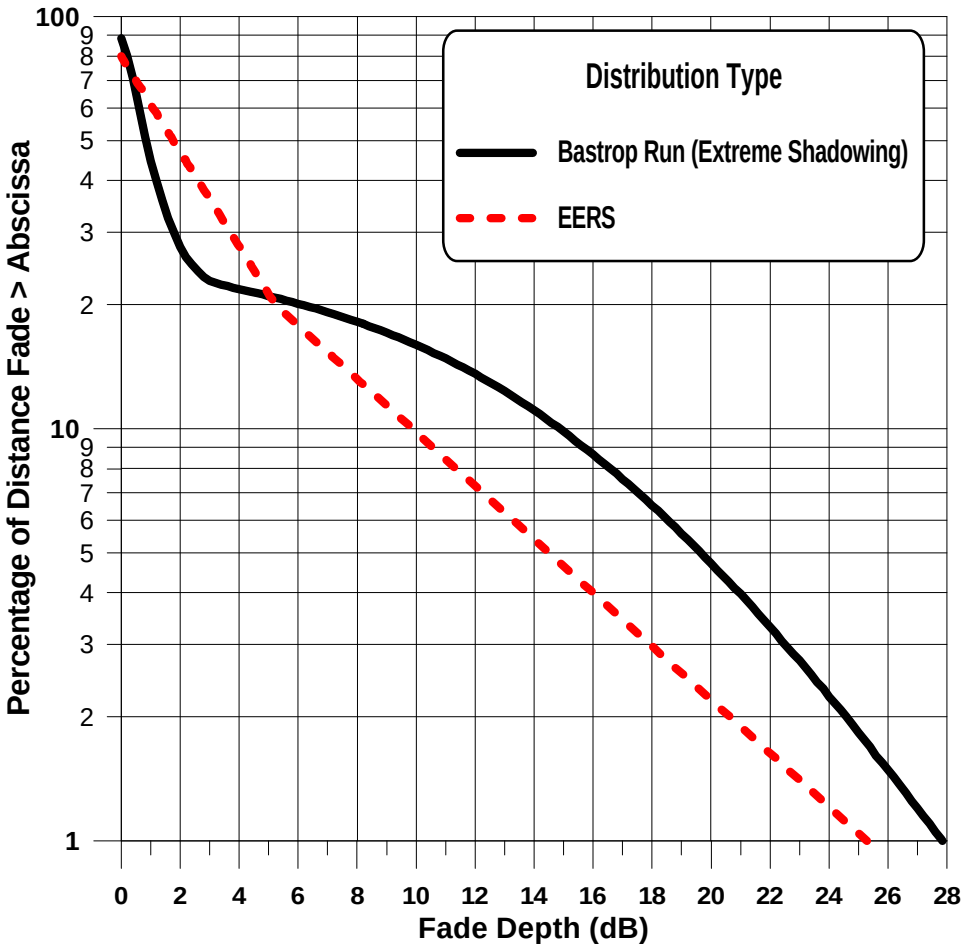

Figure 3-12: Distribution (solid) from ACTS 20 GHz measurements made in Bastrop, Texas at an elevation angle of 54.5°. The dashed curve represents the corresponding EERS model.

3.4.4 Low Angle Measurements in Washington State at L-Band

In Figure 3-13 is shown an L-Band (1.5 GHz) cumulative fade distribution corresponding to a tree-lined road along an approximate 16 km stretch of road in Washington State (elevation angle = 7°), where the satellite path was orthogonal to the line of trees [Vogel and Goldhirsh, 1995]. Also plotted (dashed curve) is the EERS model employing the assumption that the 20° fade is the same as that at 7° as described by (3-8). The EERS distribution agrees with the measured distribution to within 2 dB for percentages smaller than 10% and larger than 50%, and is within 5 dB for the other percentage levels. The above deviations are comparable to those obtained when comparing the ERS model with L-Band distributions from multiple runs in central Maryland (Figure 3-10).

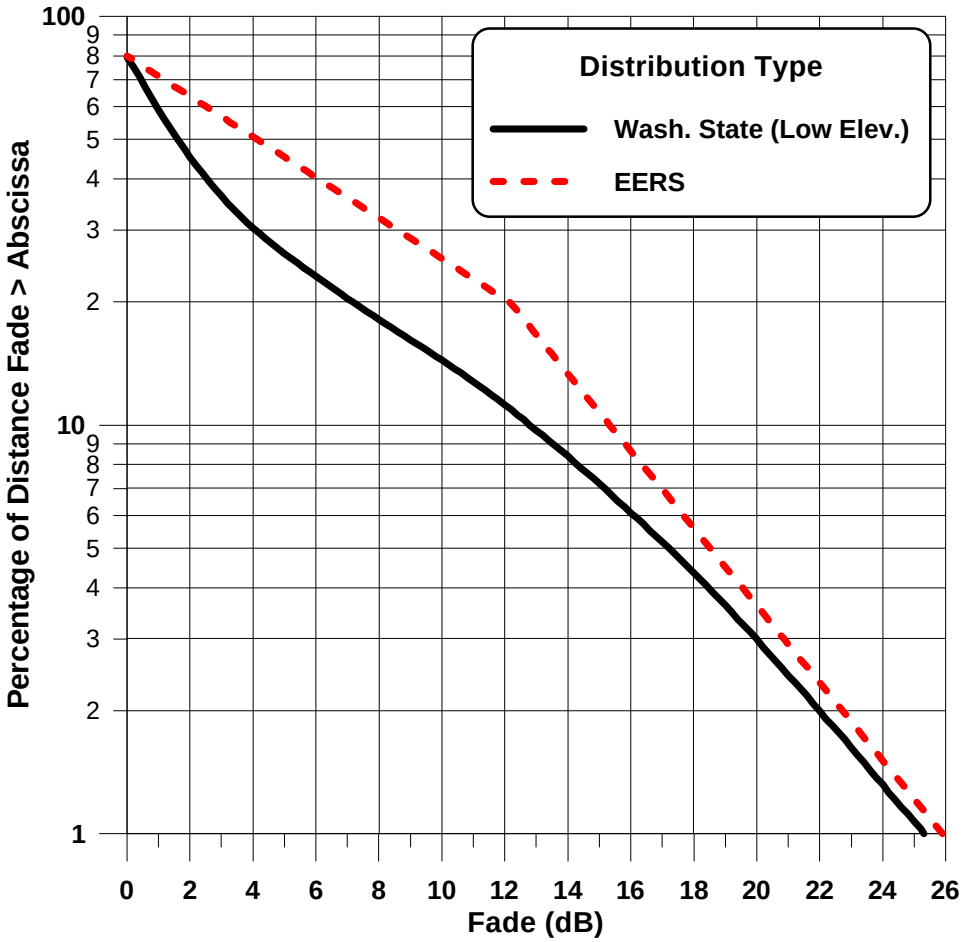

Figure 3-13: Cumulative fade distribution (solid curve) derived from L Band (1.5 GHz) measurements in Washington State over an approximate 16 km stretch of road (elevation = 7°). The dashed curve corresponds to the EERS model distribution.

3.4.5 Low Elevation Angle Measurements at K-Band in Alaska

In Figure 3-14 are shown a set of K-Band distributions (elevation = 8°) derived from ACTS measurements in Alaska corresponding to different roads in which the Earth-satellite path was orthogonal to the line of roadside trees. Also shown is the EERS

model. We note that the EERS model maintains its median characteristic, although the variability about the median is large. The low angle distributions are shown to vary considerably because of the reasons enumerated in Section 3.3.2, with the high probability fades caused by terrain blockage and multiple trees along the Earth-satellite path.

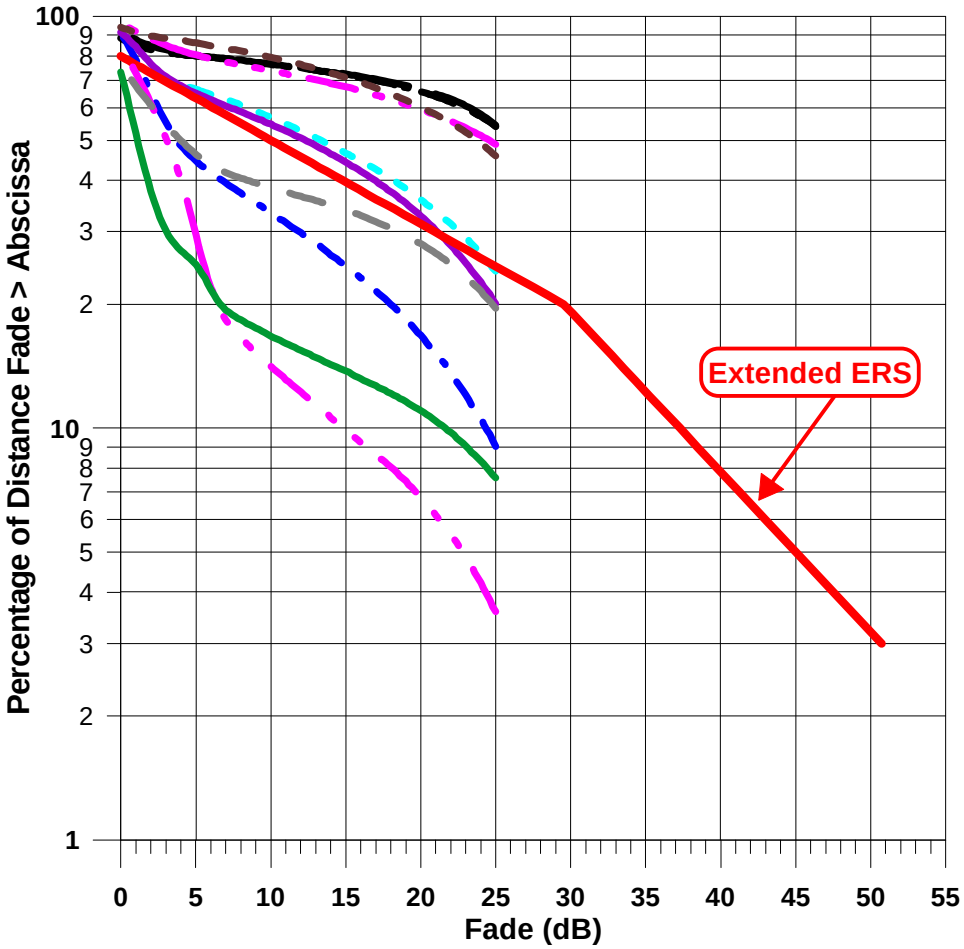

Figure 3-14: K-band (20 GHz) distributions (elevation = 8°) derived from ACTS measurements in Alaska. The solid red curve is the EERS model distribution.

3.4.6 K-Band Measurements in Central Maryland

In Figure 3-15 are shown several plots which validate elements of the EERS model. The solid curve to the left (with circled points) represents the measured distribution derived from ACTS 20 GHz measurements in March 1994 for Route 108 (traveling south-west) for the case in which the deciduous trees were without leaves. For this case, the satellite was on the left and the Earth-satellite path frequently cut the line of roadside trees at or near orthogonal angles. Shown also (green solid line) is the distribution derived by applying the foliage adjustment formulation described in the next section. This adjusted distribution thus represents a predictor of the full foliage case. Also shown is the EERS

distribution at K-Band (dashed curve). We observe that the EERS distribution deviates from the adjusted measured distribution by less than 5 dB.

The red dot-dashed curve in Figure 3-15 was derived from previous L-Band helicopter measurements in June 1987 [Goldhirsh and Vogel, 1989] employing the following procedures: (1) Distributions were examined which corresponded to the same scenario as for the K-Band measurements; namely, the vehicle was traveling in the southwest direction and the helicopter was on the left, (2) a resultant 39° distribution was derived by interpolating the 45° and the 30° distributions at L-Band, and (3) the L-Band distribution was extended to K-Band employing the frequency scaling factor given by the exponential term in (3-1). We note that relatively close agreement exists between the adjusted distribution (based on helicopter measurements; dot-dashed curve), the foliage adjusted ACTS distribution (right solid curve), and the EERS model (dashed curve) [Goldhirsh and Vogel, 1995a; 1995b].

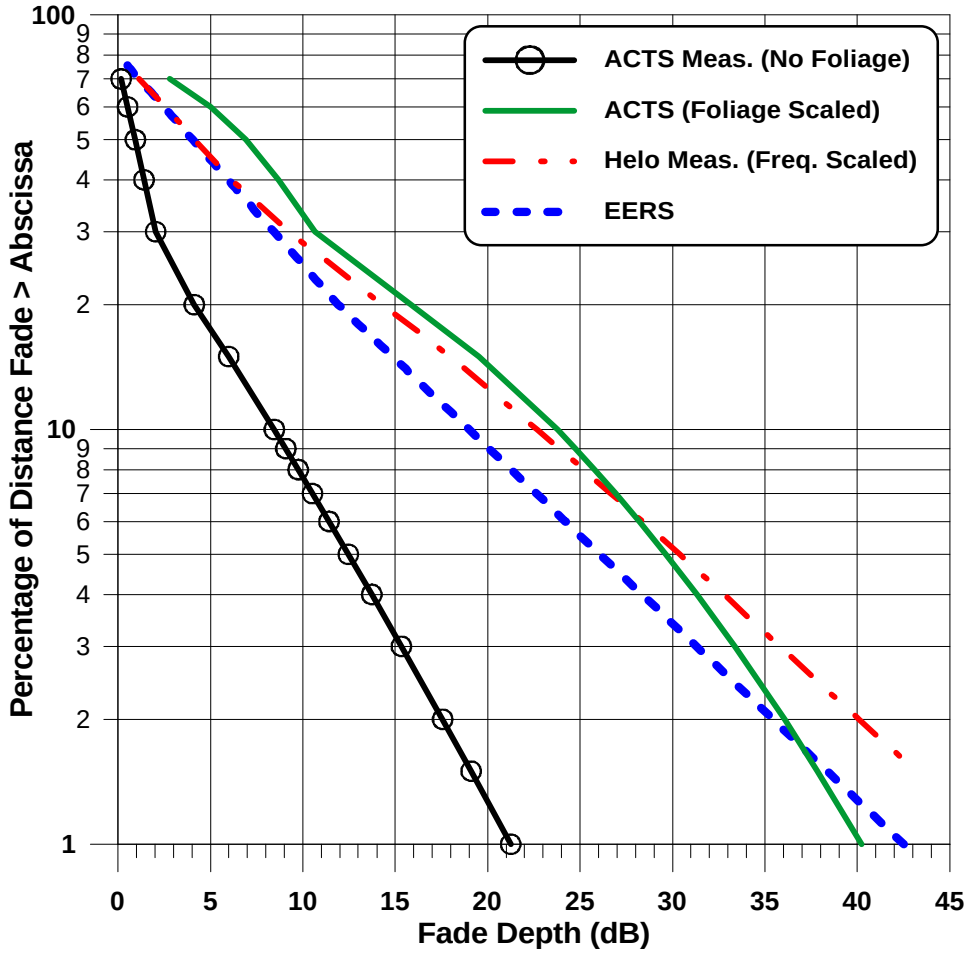

Figure 3-15: Plots of K-Band (20 GHz) cumulative fade distributions from measurements in central Maryland at elevation angle of 39°.

3.4.7 Comparison with ESA K-Band Measurements

We compare here EERS model distributions at 18.7 GHz with measured distributions by Murr et al. [1995] obtained in a series of campaigns supported by the European Space Agency (ESA). The campaigns used a radiating source on board the geostationary satellite Italsat F1 [Paraboni and Giannone, 1991] and a mobile van with a tracking antenna [Joanneum Research, 1995]. The elevation angles were between 30° and 35° and a number of runs in four European countries were executed for different driving directions relative to the satellite position. In Figure 3-16 are shown two measured distributions (solid curves) made along tree shadowed roads in Munich, Germany [Murr et al., 1995]. Also shown is the corresponding EERS model distribution (dashed curve). We note that the two measured distributions generally flank the EERS model between percentage values of 5% to 30% with fade deviations in excess of 10 dB occurring at percentages smaller than 5%. Murr et al. [1995], in these measurements, found that a 90° relative satellite azimuth scenario did not always represent a worst case fading situation. Some distributions showed larger fades at the 45° relative satellite azimuths. This was explained as follows: For some 90° cases, the Earth-satellite path encountered clear spaces between adjacent trees giving rise to minimal fade conditions during the corresponding time intervals. On the other hand, at 45°, the tree canopies overlapped and the incidence of optically non-shadowed Earth-satellite path scenarios was not as prevalent as for the 90° case. Hence the 45° case sometimes gave rise to longer periods with extended shadowing.

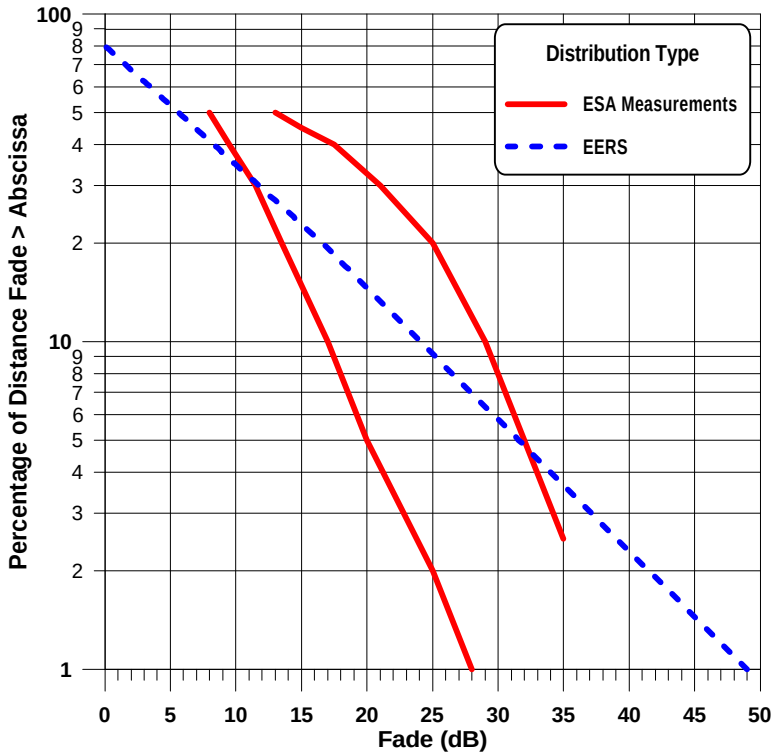

Figure 3-16: Measured cumulative distributions for tree shadowed environments at 18.7 GHz and elevation angle of 32.5°, where the satellite azimuth was 90° relative to the driving direction [Murr et al., 1995]. The dashed curved represents the EERS model.

3.5 Attenuation Effects of Foliage

3.5.1 K-Band Effects

Measurements made in Austin, Texas during February and May when the trees were without and with leaves, respectively, enabled a "foliage'' adjustment model to be developed. The formulation relates equal probability attenuation (dB) corresponding to "foliage" and "no-foliage" cases at K-Band and is given by

$$A(Foliage) = a + bA(No\ Foliage)^C \tag{3-15}$$

$$\begin{aligned} a &= 0.351 \\ b &= 6.8253\,, \\ c &= 0.5776 \end{aligned} \tag{3-16}$$

and where

$$1 \le A(No\ Foliage) \le 15\ dB \text{ and} \tag{3-17}$$

$$8 \le A(Foliage) \le 32\ dB\,. \tag{3-18}$$

This formulation was derived from "no-foliage" and "foliage" mobile measurements made during February and May of 1994, respectively, in Austin, Texas during the ACTS campaigns. The time-series signal level characteristics for these two cases are shown in Figure 3-17 and Figure 3-18, where the measurements were made along a one kilometer segment of a street heavily populated with Pecan trees. Shown are the minimum, maximum, and average signal levels over one second periods for a sampling rate of 1 KHz. The corresponding cumulative fade distributions are shown in Figure 3-19 where the dashed and solid curves correspond to the "no-foliage" and "foliage" cases. The direction of travel for these runs was approximately orthogonal to the satellite pointing direction. The optical blockage to the satellite during the full foliage period was estimated to be well in excess of 55%. Performing a least square fit associated with equal probability levels of the attenuation for the two curves in Figure 3-19, the formulation (3-15) was derived. A comparison of the measured and predicted levels describing the foliage versus no foliage fades is given in Figure 3-20. The predicted curve (dashed) is shown to agree to within a fraction of a dB up to fades (with foliage) of approximately 38 dB.

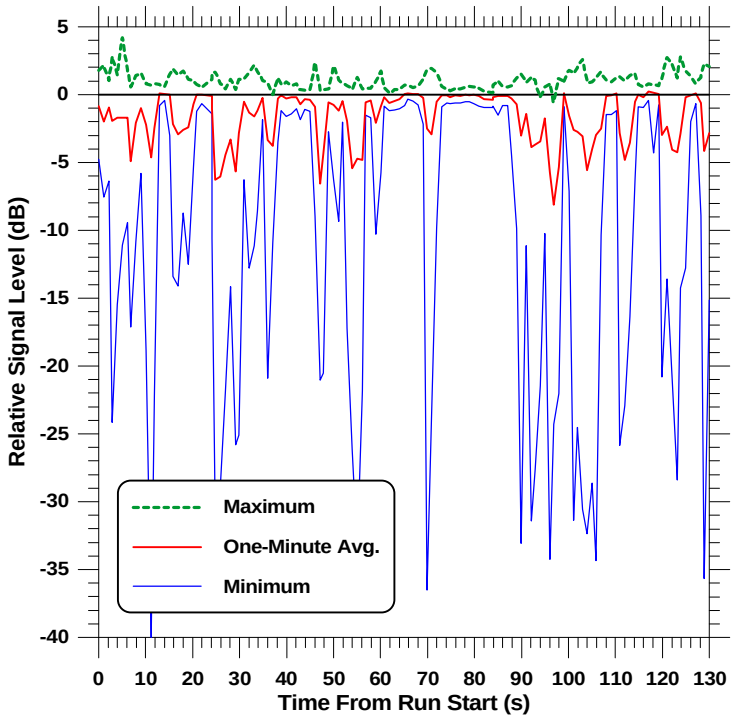

Figure 3-17: Minimum, maximum, and average fades over 1 second interval at 20 GHz for a tree-lined run in Austin, Texas during February 6, 1994. Deciduous trees (Pecan) were devoid of leaves.

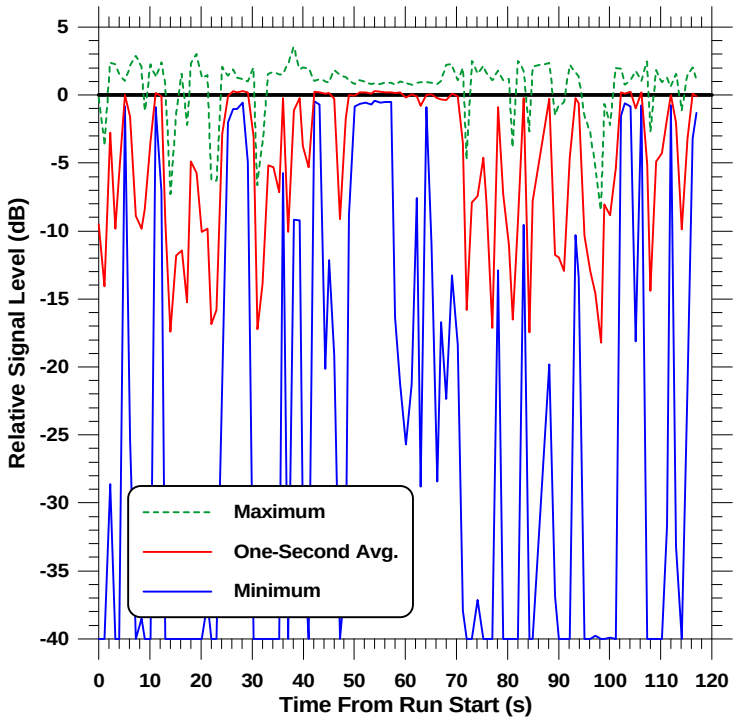

Figure 3-18: Minimum, maximum, and average fades over 1 second intervals at 20 GHz for a tree-lined run in Austin, Texas during May 2, 1994. Trees (Pecan) were in full foliage.

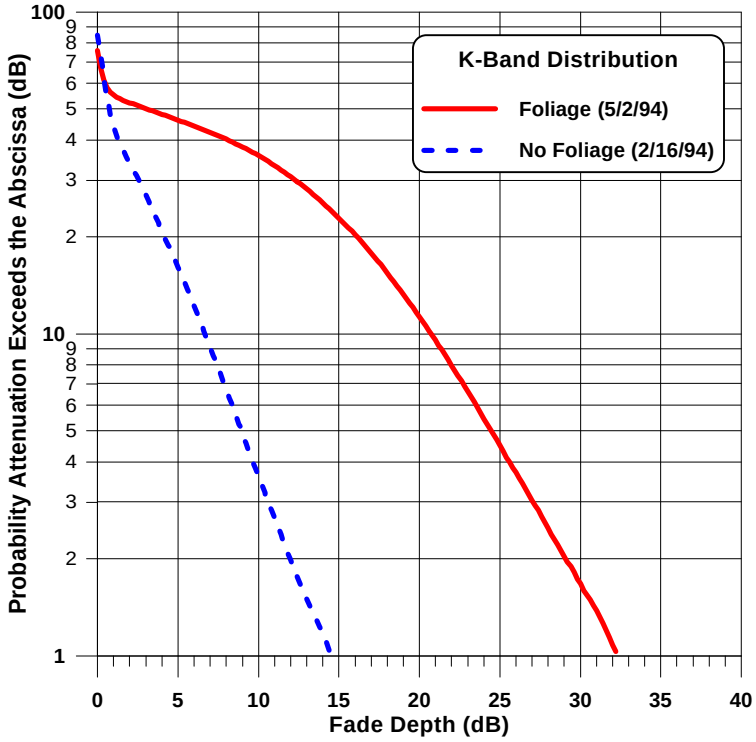

Figure 3-19: Cumulative distributions at K-Band (20 GHz) for foliage and no-foliage runs in Austin, Texas.

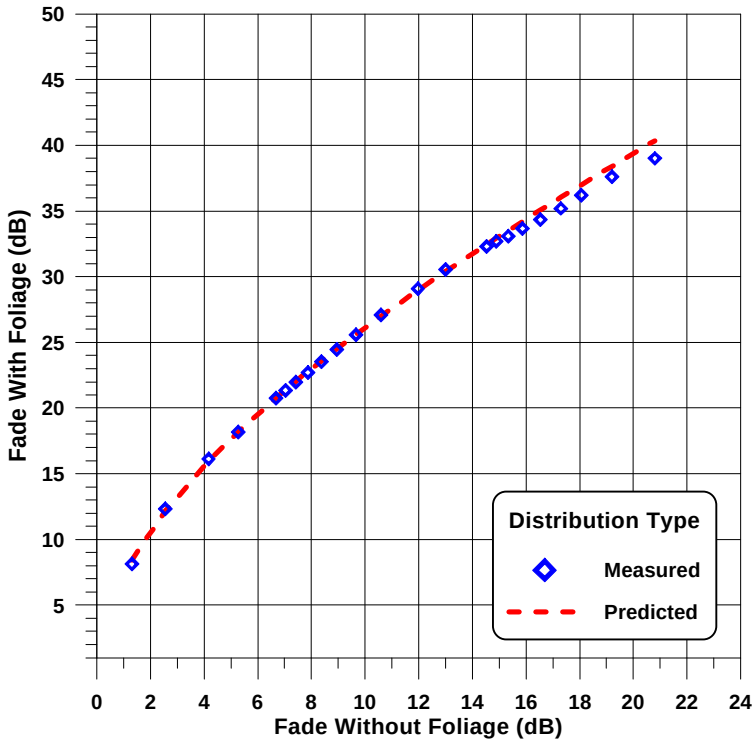

Figure 3-20: Measured and predicted levels of "foliage" versus "no-foliage" fades at 20 GHz.

Figure 3-21 represents an independent validation of the above foliage formulation for a set of static measurements at f = 19.6 GHz in Austin, Texas pertaining to a Pecan tree in full foliage and the same tree devoid of leaves [Vogel and Goldhirsh, 1993a]. The resulting distributions calculated from measurements correspond to the left and right solid curves, respectively. The dashed curves represent the predicted levels using the formulation given by (3-15). That is, the dashed curve on the right is the predicted level of A(Foliage) where equal probabilities of the measured A(No Foliage) as given by the left solid curve was injected into (3-15). The left dashed curve represents the predicted levels of the A(No Foliage), where the measured levels of A(Foliage) as given by the right solid curve values were injected into (3-15). The formulation (3-15) generally produces agreement to within 1 dB or smaller over most of the indicated static probability range.

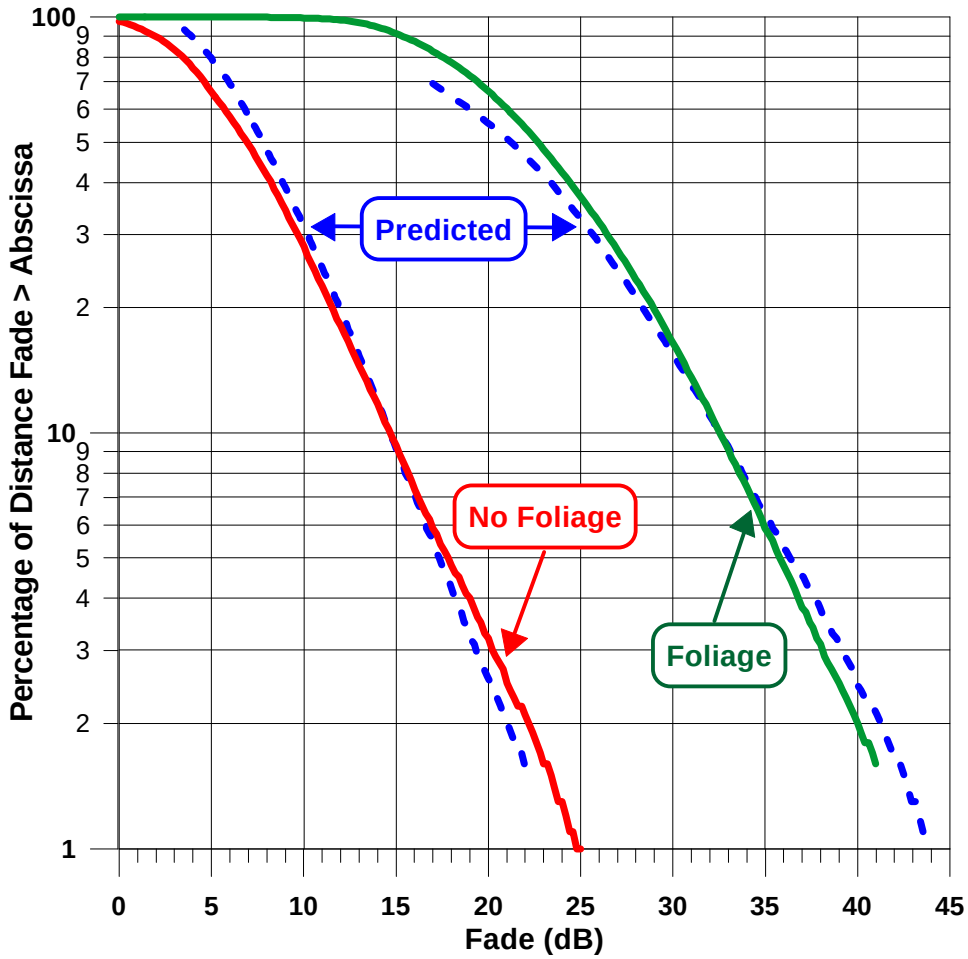

Figure 3-21: Independent validation of "no-foliage" versus "foliage" prediction formulation (3-15) employing static measurements in Austin, Texas at 20 GHz. Solid curves represent measurements made during different seasons and dashed curves are the predicted levels.

3.5.2 UHF (870 MHz)

In Chapter 2 it was shown that a 35% increase in the dB attenuation was experienced at 870 MHz when comparing attenuation from trees having no foliage and those having foliage (winter versus summer) for the static measurement case. This case corresponded to a configuration in which the vehicle was stationary and the propagation path intersected the canopy. Seasonal measurements employing a helicopter as the transmitter platform were also performed by the authors for the dynamic case in which the vehicle traveled along a tree-lined highway in Central Maryland (Route 295) along which the propagation path was shadowed over approximately 75% of the road distance [Goldhirsh and Vogel, 1987; 1989]. Cumulative fade distributions obtained from measurements in October 1985 (trees with leaves) and in March 1986 (trees without leaves) are shown in Figure 3-22. The results demonstrate the following:

At f = 870 MHz, $1\% \le P \le 80\%$:

$$A(\textit{full foliage}) = 1.24A(\textit{no foliage}) \tag{3-19}$$

Equation (3-19) states that over the percentage range from 1% to 80% of the seasonal cumulative distributions, there is an average increase of 24% (at equal probability values) in the dB fade of trees with leaves relative to trees with no leaves. The dB error associated with the above formulation over this percentage range for the curves in Figure 3-22 is less than 0.2 dB. The percentage fade increase (seasonal) for the dynamic case (24%) is less than that for the static case (35%) because the former case represents a condition in which the optical path is always shadowed, whereas the dynamic case has associated with it measurements between trees.

The question arises "Why is there a small difference between the "foliage" and "no-foliage" distributions at UHF (e.g. 24% change), whereas at K-Band, there is a large change between the distributions for these two scenarios (e.g., two to three times)?" This question may be answered as follows: The major contributor due to tree attenuation at the UHF frequency (wavelength of approximately 35 cm) for trees without leaves are the branches, since the separation between contiguous branches along the path are generally smaller than 35 cm. That is, since the branch separation is generally smaller than a wavelength at UHF, no substantial difference exists between the "leaf" and "no-leaf" cases as both scenarios result in attenuating environments. On the other hand, because the K-Band measurements have an associated wavelength of 1.5 cm, the separation between branches for the "no leaf" case is generally larger than this dimension resulting in a smaller relative fading condition. On the other hand, the "full blossom" case is highly attenuating at K-Band because of the continuous blockage caused by the high density of leaves.

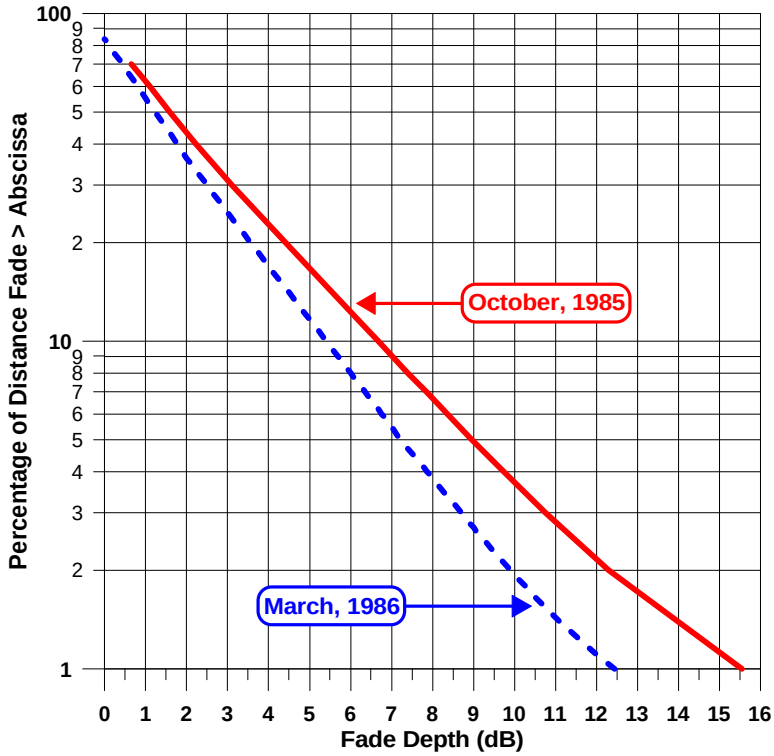

Figure 3-22: Cumulative fade distributions at L-Band (1.5 GHz) in central-Maryland during various seasons.

3.6 Frequency Scaling Considerations

The frequency scaling formulation applied to the ERS model is applicable between UHF (870 MHz) and S-Band (3 GHz) and is given by

for $1\% \le P \le 30\%$ and $870\ MHz \le f \le 3\ GHz$:

$$A(f) = A(f_L)\sqrt{\frac{f}{f_L}}\ dB, \tag{3-20}$$

where $f_L = 1.5\ GHz$ and where $A(f)$ is the attenuation expressed in dB at the frequency f (expressed in GHz). The frequency scaling in the EERS model is given by exponent factor in (3-1).

Figure 3-23 depicts a comparison using both frequency scaling formulations and the measurements of Bundrock and Harvey [1988]. The open circled points correspond to the formulation (3-20) and the solid points represent the formulation (3-1) with $A(f_L)$ corresponding to the L-Band frequency (1.55 GHz) and attenuation values of Bundrock and Harvey. That is, the estimated points shown were derived from the middle curve corresponding to the L-Band measured distribution. Since both scaling methods give approximately similar results, it is suggested that (3-1) be used for simplicity over the

entire frequency range (up to 20 GHz), although both are applicable between UHF and S-Band.

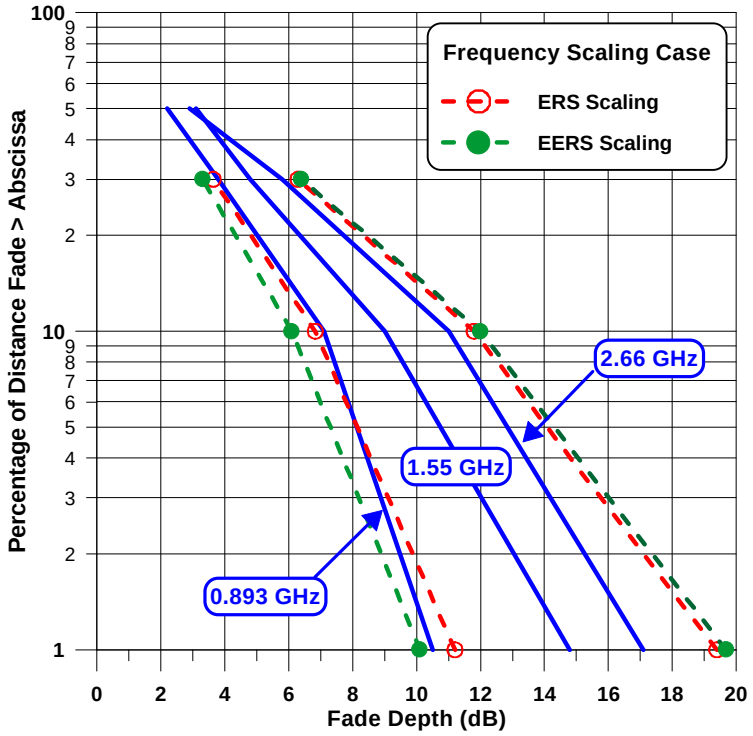

Figure 3-23: Fade distributions at L-Band, S-Band and UHF measured by Bundrock and Harvey [1988] (solid curves). The open circular and solid circular points represent the ERS and the EERS frequency scaling estimates, respectively.

3.7 Comparison of EERS Model with Other Empirical Models

3.7.1 Modified Empirical Roadside Shadowing Model (MERS)

This model is an outgrowth of campaigns carried out by the European Space Agency (ESA) [Jongejans et al., 1986] and is described by Sforza et al. [1993a; 1993b] and Butt et al. [1995]. It is called the Modified Empirical Roadside Shadowing (MERS) and is representative of mobile-satellite attenuation from deciduous trees corresponding to POS values from 35% to 85%. The formulation has the same form as the ERS model (3-3) and is given by

$$A(P,q) = -M(q)\ln(P) + N(q), \tag{3-21}$$

where

$$\begin{aligned} M(q) &= a_1 q^2 + a_2 q + a_3 \\ N(q) &= b_1 q^2 + b_2 q + b_3 \end{aligned}, \tag{3-22}$$

and where

$$\begin{aligned} a_1 &= 1.117\text{X}10^{-4} \\ a_2 &= -0.0701 \\ a_3 &= 6.1304 \\ b_1 &= 0.0032 \\ b_2 &= -0.6612 \\ b_3 &= 37.8581 \end{aligned} \tag{3-23}$$

In the above, $A(\theta, P)$ is the L-Band (1.5 GHz) fade in dB, P is the percentage of fade exceeded applicable in the range 1% to 30%, and θ is the elevation angle (in degrees) valid from 20° to 80°. In Figure 3-24, the above MERS formulation is compared with the EERS model at 30°, 45°, and 60°. The two models at the different angles generally agree with one another to approximately 1 dB at the equal percentage levels. The 60° MERS distribution appears shifted to the right relative to the EERS model by approximately 1 dB. Although the above formulation is described for L-Band, it may be used for S-Band frequencies applying the frequency scaling relation (3-20) [Butt et al., 1995].

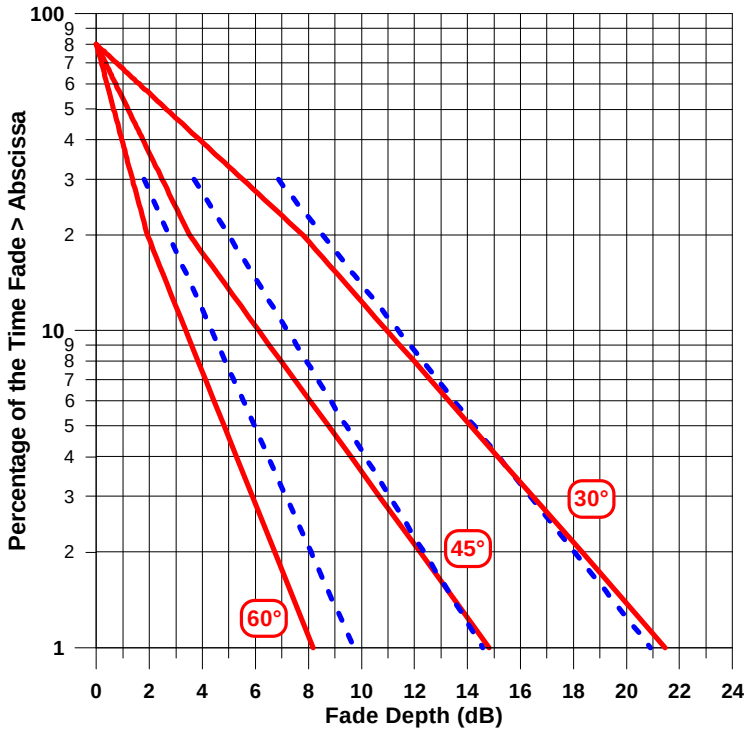

Figure 3-24: Comparison of EERS model (solid) with MERS (dashed) results at L-Band (1.5 GHz).

3.7.2 Empirical Fading Model (EFM)

This model was derived from measurements made by the Centre for Satellite Engineering at the University of Surrey, UK. It is based on simultaneous measurements at L, S, and K_u bands at the higher elevation angles from 60° to 80° [Butt et al., 1993; 1995]. This model also has a form similar to the ERS model (3-3) and is given by

$$A(P,q,f) = -M \ln(P) + N \tag{3-24}$$

with

$$\begin{aligned} M &= -0.029q + 0.182f + 6.315 \\ N &= -0.129q + 1.483f + 21.374 \end{aligned} \tag{3-25}$$

and where $A(P,\theta,f)$ is the attenuation (in dB) at the percentage P (in %) valid from 1% to 20%, q is the elevation angle (in degrees) applicable from 60° to 80°, and the frequency f (in GHz) may be applied in the range 1.3 GHz to 10.4 GHz. The multiplying constants on the right hand side of M in (3-25) are the negative of those presented by Butt et al. [1993, 1995] because M in (3-24) is preceded by a negative sign to maintain consistency with the EERS model. (Their multiplying coefficient was positive). Figure 3-25 shows a comparison of the above model distribution at 60° elevation with those corresponding to the EERS, MERS, and CEFM (to be described shortly). It is interesting to note that the other three models cluster about one another, whereas the EFM model deviates considerably from the grouping; especially at percentages smaller than 5%.

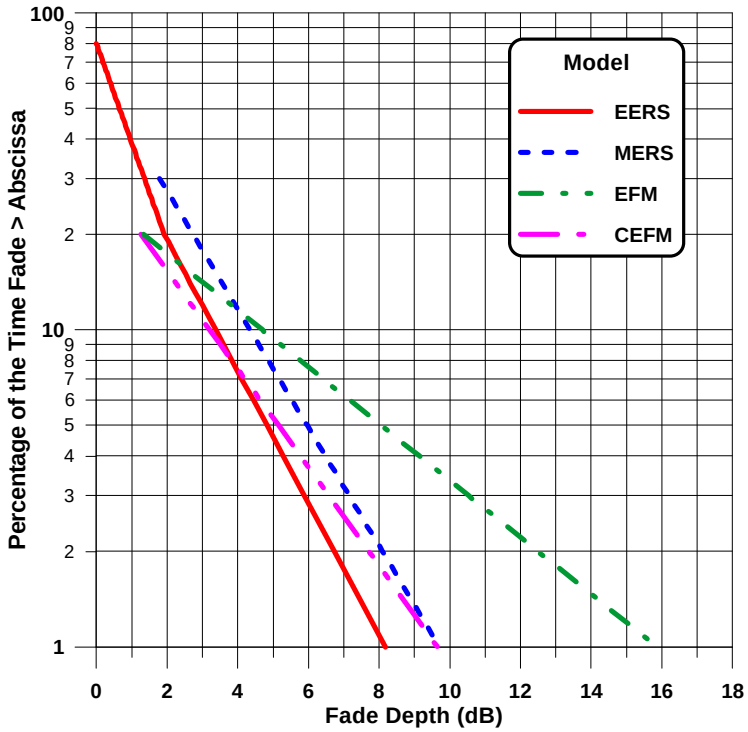

Figure 3-25: Comparison of various models at 60° elevation with EERS (solid) at 1.5 GHz.

3.7.3 Combined Empirical Fading Model (CEFM)

The Combined EFM (CEFM) model extends the above high elevation angle results with those contained in the ERS model. It is described by Parks et al. [1993a] and Butt et al. [1995] and is given as follows:

$$A(P,q,f) = -M\ln(P) + N\,, \tag{3-26}$$

with

$$\begin{aligned} M &= -0.002q^2 + 0.15q + 0.2f + 0.7 \\ N &= -0.33q + 1.5f + 27.2 \end{aligned}\,, \tag{3-27}$$

and where the units are the same as described previously. This formulation may be applied in the angular range 20° to 80°, over the frequency interval from 1.3 GHz to 3 GHz, and percentage range from 1% to 20%. Here again, the constants in M are the negative of those presented by Parks et al. [1993a; 1993b] because a negative sign precedes M in (3-26). The CEFM distributions are shown plotted at L-Band (1.5 GHz) in Figure 3-26 (dashed curves) and are compared with the EERS model (solid curves) at 30°, 45°, and 60°. Agreement at the three angles is generally within 1 dB.

In order to obtain a handle on the behavior of the distributions at the higher elevation angles (above 60°), we show plotted the distributions for the MERS and CEFM models in Figure 3-27 at 70° and 80°. The MERS model at the higher elevation angles is

shown to exhibit more self-consistency, whereas the CEFM model distributions are noted to cross over at approximately 10%.

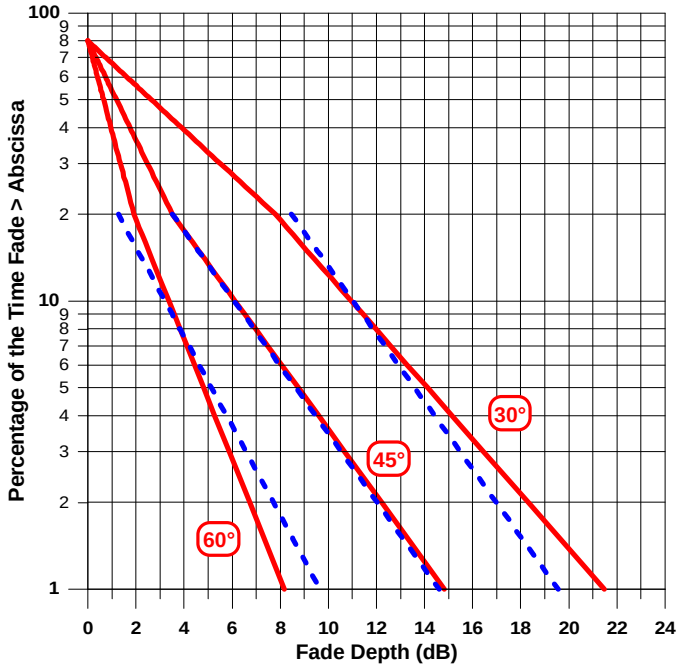

Figure 3-26: Comparison of EERS model (solid) with CEFM model (dashed) results at L-Band (1.5 GHz).

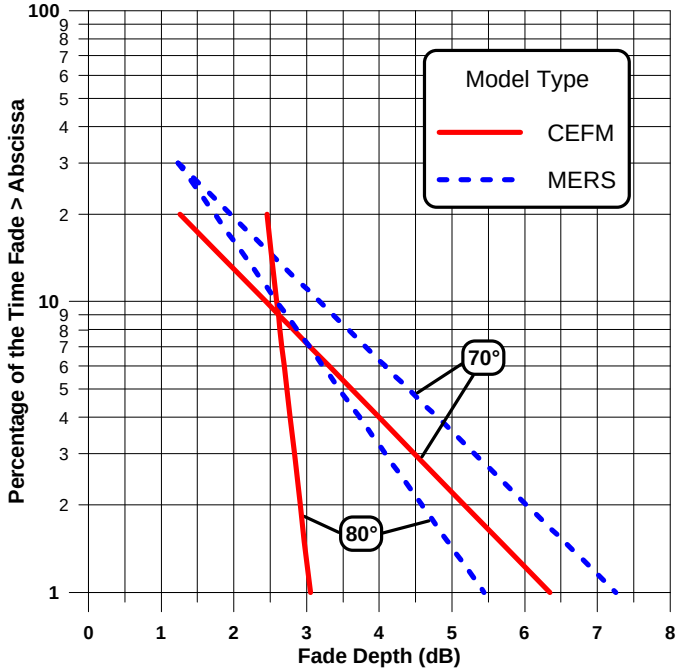

Figure 3-27: EFM and MERS model values at 70° and 80° elevations at L-Band (1.5 GHz).

3.7.4 ITU-R Fade Model at Elevation Angles above 60°

The ITU-R has recommended that for elevation angles greater than 60°, the ERS model be linearly interpolated with the fade values listed in Table 3-2 (at 80°) and plotted in Figure 3-28 for the frequencies of 1.6 GHz or 2.6 GHz at the indicated percentages [ITU-R, 1994]. The tabulated values in the right two columns of Table 3-2 were derived from measurements described by Smith et al. [1993]. We have extended this methodology below to apply to the formulation (3-1) employing the following steps:

1. Apply equation (3-1) at the frequency of 1.6 GHz and 2.6 GHz at an elevation angle of 60° (values in the second and third columns).
2. Linearly interpolate between the fade calculated for an angle of 60° and the fade for an elevation angle of 80° provided in Table 3-2 (second and fourth columns) at 1.6 GHz.
3. Linearly interpolate between the value calculated for an angle of 60° and the fade values for an elevation angle of 80° provided in Table 3-2 at 2.6 GHz (third and fifth columns) only for percentages of 15% and smaller.
4. Linearly interpolate between the values in the fourth and fifth columns in Table 3-2 and a value of zero at 90° to arrive at fade levels at elevation angles between 80° and 90°.

The above methodology is self-consistent at 1.5 GHz for percentages between 1% and 30% in that the 60° elevation fade values derived from the EERS model are larger than the respective tabulated 80° fade values at the same percentages. On the other hand, this is not the case at 2.6 GHz for percentages of 20% and larger (see columns three and five of Table 3-2 showing values with *). It is therefore suggested that at 2.6 GHz the above methodology be used at percentages of 15% and smaller as stated in Step 3 above. In Figure 3-29 is shown plotted the L-Band (1.5 GHz) fade exceeded versus elevation angle showing linear interpolation of fades between angles 60° and 90°.

Table 3-2: Fades exceeded at elevations of 60° and 80°.

Percentage, P	EERS Fade (dB) at Elevation = 60°		Fade (dB) at Elevation = 80°	
	f = 1.6 GHz	f = 2.6 GHz	f = 1.6 GHz	f = 2.6 GHz
1	8.2	11.0	4.1	9.0
5	4.8	6.5	2.0	5.2
10	3.4	4.5	1.5	3.8
15	2.6	3.4	1.4	3.2
20	1.9	2.6*	1.3	2.8*
30	1.4	1.8*	1.2	2.5*

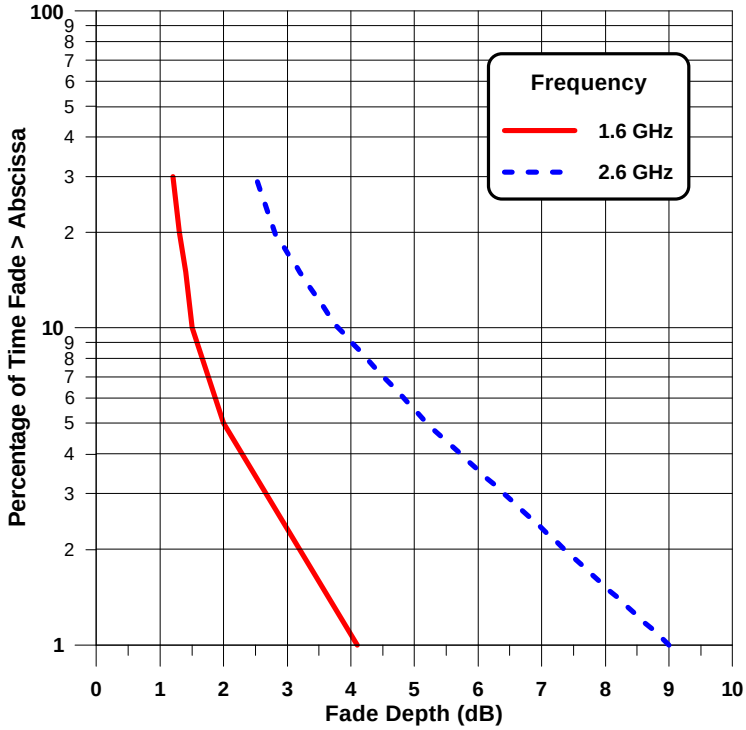

Figure 3-28: Cumulative distributions at 80° for frequencies of 1.6 and 2.6 GHz.

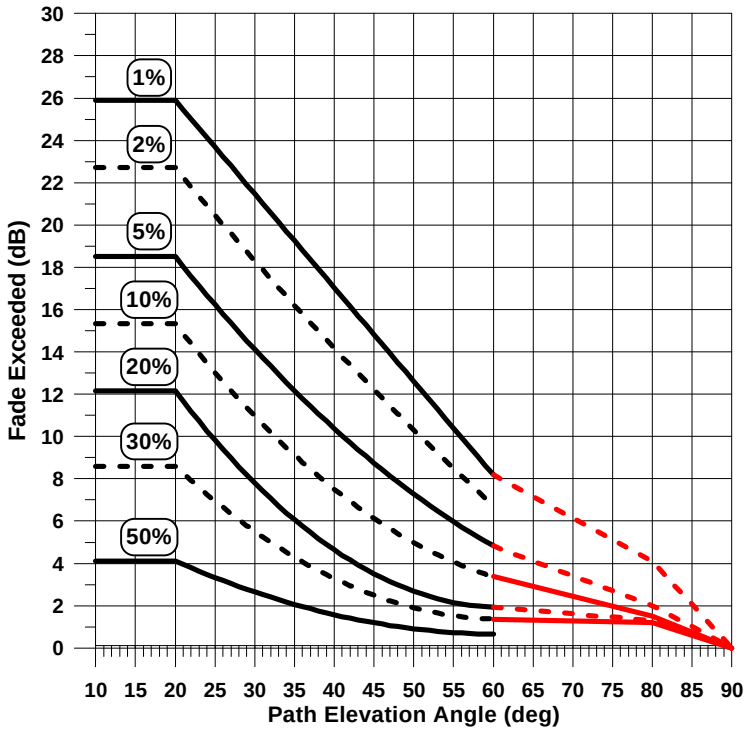

Figure 3-29: Fade versus elevation angle at L-Band (1.5 GHz) with ITU-R extension to 90°.

3.7.5 Comparative Summary of Model Limits

In Table 3-3 is given a comparative summary of the above competing models and their domains of validity. The EERS model covers a wider range of percentages than the other models (1% to 80%) and includes angles as low as 7°. The other models are limited to 20° elevation. It also covers the greatest range of frequencies (e.g., 0.87 to 20 GHz). The EERS model limitation vis-à-vis the other models is that it does not include elevation angles greater than 60°. The ITU-R model extends the EERS model from 60° to 90° at 1.6 GHz and 2.6 GHz. The EFM, CEFM, and MERS models include elevation angles up to 80°.

Table 3-3: Summary of empirical models and their domains of validity.

Model Name	Percentage Range (%)	Elevation Angle Range (deg)	Frequency Range (GHz)	Reference
EERS	1-80	7-60	0.87-20	Goldhirsh and Vogel [1995a], ITU-R [1997]
ERS	1-20	20-60	0.87-3	Goldhirsh and Vogel [1992], ITU-R [1994]
ITU-R	1-30	60-90	1.6-2.6	ITU-R [1997]
EFM	1-20	60-80	1.3-10.4	Parks et al. [1993a]
MERS	1-30	20-80	1.5-2.6	Sforza et al. [1993a]
CEFM	1-20	20-80	1.5-2.6	Butt et al. [1995]

3.8 Conclusions and Model Recommendations

The following is recommended:

1. In the elevation angle interval between 20° to 60°, the EERS model should be executed as outlined in Section 3.3.2 using the step by step approach in Section 3.3.3. The ITU-R angle extension procedure from 60° to 90° may be used at 1.6 GHz and 2.6 GHz as outlined in Section 3.7.4. The MERS model (Equation (3-21) and Figure 3-24) and the CEFM model (Equation (3-26) and Figure 3-26) show relatively small differences with the EERS model in the angular range 20° to 60°.
2. For elevation angles between 7° and 20° the EERS model should continue to be employed in the absence of any direct measurements. The model provides a median of measured distributions at the smaller angles, but the deviation from the measured levels may be significantly larger than 5 dB at equal probability levels because of terrain blockage and multiple canopy tree-shadowing. Where direct measurements exist, these should be substituted for the model.

3.9 References

Bundrock, A. and Harvey, R. [1988], "Propagation Measurements for an Australian Land Mobile Satellite System," *Proceedings of International Mobile Satellite Conference*, Pasadena, CA, pp. 119-124.

Butt, G., B. G. Evans, M. Parks [1995], "Modeling the Mobile Satellite Channel for Communication System Design," *Ninth International Conference on Antennas and Propagation*," 4-7 April, 1995, pp. 387-393.

Butt, G., B. G. Evans, M. Richharia [1993], "Results of Multiband (L, S, Ku Band Propagation Measurements for High Elevation Angle Land Mobile Satellite Channel," *Eighth International Conference on Antennas and Propagation*, 30 March-2 April, 1993, Herriot-Watt University, U.K., pp. 796-799 (Institution of Electrical Engineers, London, Conference Publication 370.)

Goldhirsh, J. and W. J. Vogel [1995a], "An Extended Empirical Roadside Shadowing Model for Estimating Fade Distributions from UHF to K Band for Mobile Satellite Communications," *Space Communications (Special Issue on Satellite Mobile and Personal Communications)*, Vol. 13, No. 3 (IOS Press).

Goldhirsh, J. and W. J. Vogel [1995b], "Extended Empirical Roadside Shadowing Model from ACTS Mobile Measurements," *Proceedings of the Nineteenth NASA Propagation Experimenters Meeting (NAPEX XIX) and the Seventh Advanced Communications Technology Satellite (ACTS) Propagation Studies Workshop (APSW VII)*, Fort Collins, Colorado, June 14-16, pp. 91-101. (JPL Publication 95-15, Jet Propulsion Laboratory, California Institute of Technology, Pasadena, California.)

Goldhirsh, J., W. J. Vogel, and G. W. Torrence [1995], "Mobile Propagation Measurements in the U.S. at 20 GHz Using ACTS," *International Conference on Antennas and Propagation (ICAP '95)*, Vol. 2, Conference Publication No. 407, Eindhoven, The Netherlands, pp. 381-386.

Goldhirsh, J., W. J. Vogel, and G. W. Torrence [1994], "ACTS Mobile Propagation Campaign," *Proceedings of the Eighteenth NASA Propagation Experimenters Meeting (NAPEX XVIII) and the Advanced Communications Technology Satellite (ACTS) Propagation Studies Miniworkshop*, Vancouver, British Columbia, June 16-17, 1994, pp. 135-150. (JPL Publication 94-19, Jet Propulsion Laboratory, California Institute of Technology, Pasadena, California.)

Goldhirsh, J. and W. J. Vogel [1992], "Propagation Effects for Land Mobile Satellite Systems: Overview of Experimental and Modeling Results," *NASA Reference Publication 1274*, (Office of Management, Scientific and Technical Information Program), February.

Goldhirsh, J. and W. J. Vogel [1989], "Mobile Satellite System Fade Statistics for Shadowing and Multipath from Roadside Trees at UHF and L Band," *IEEE Transactions on Antennas and Propagation*, Vol. AP-37, No. 4, April, pp. 489-498.

Goldhirsh, J. and W. J. Vogel [1987], "Roadside Tree Attenuation Measurements at UHF for Land-Mobile Satellite Systems," *IEEE Transactions on Antennas and Propagation*, Vol. AP-35, pp. 589-596, May.

ITU-R [1994] (International Telecommunication Union, Radio Communication Study Groups), "Propagation Data Required for the Design of Earth-Space Land Mobile Telecommunication Systems," *Recommendation ITU-R PN.681-1, International Telecommunication Union, ITU-R Recommendations,* 1994 PN Series Volume, Propagation in Non-Ionized Media, pp. 358-365.

ITU-R [1997] (International Telecommunications Union, Radio Communication Study Groups, "Revision of Recommendation ITU-R P.681," *Document 3M/3* - February.

Joanneum Research [1995], "Land Mobile Satellite Narrowband Propagation Campaign at Ka Band," Final Report W.O. #4, ESTEC Contract 9949/92/NL, January.

Jongejans, A., A. Dissanayake, N. Hart, H. Haugli, C. Loisy, and R. Rogard [1986], "PROSAT-Phase 1 Report," European Space Agency Tech. Rep. ESA STR-216, May. (European Space Agency, 8-10 Rue Mario-Nikis, 75738 Paris Cedex 15, France.)

Murr, F., B. Arbesser-Rastburg, S. Buonomo, Joanneum Research [1995], "Land Mobile Satellite Narrowband Propagation Campaign at Ka Band," International Mobile Satellite Conference (IMSC '95), Ottawa, Canada, pp. 134-138.

Paraboni, A. and B. Giannone, [1991], "Information for the participation to the ITALSAT Propagation Experiment," Politecnico di Milano Report 91.032.

Parks, M. A. N., G. Butt, and B. G. Evans [1993a], "Empirical Models Applicable to Land Mobile Satellite System Propagation Channel Modeling," Colloquium on Communications Simulation and Modeling Techniques, London, England, pp. 12/1-12/6. (The Institution of Electrical Engineers, Savoy Place, London, WC2R OBL, UK.)

Parks, M. A. N., G. Butt, B. G. Evans, M. Richharia [1993b], "Results of Multiband (L, S, Ku Band) Propagation Measurements and Model for High Elevation Angle Land Mobile Satellite Channel," *Proceedings of XVII NAPEX Conference*, June 14th -15th, Pasadena, California, pp. 193-202. (JPL Publication 93-21; Jet Propulsion Laboratory, California Institute of Technology, Pasadena, California.)

Sforza, M., S. Buonomo, J. P. V. Poiares Baptista [1993a], "Global Coverage Mobile Satellite Systems: System Availability versus Channel Propagation Impairments," IMCS '93, June, pp. 361-372.

Sforza, M. and S. Buonomo [1993b], "Characterization of the LMS Propagation Channel at L- and S- Bands: Narrowband Experimental Data and Channel Modeling," *Proceedings of XVII NAPEX Conference*, June 14th-15th, Pasadena, California, pp. 183-192. (JPL Publication 93-21; Jet Propulsion Laboratory, California Institute of Technology, Pasadena, California.)

Smith, H., J. G. Gardiner, and S. K. Barton [1993], "Measurements on the Satellite-Mobile Channel at L & S Bands," *Proceedings of the Third International Mobile Satellite Conference (IMSC '93)*, June 16-18, Pasadena, California, pp. 319-324.

Vogel, W. J., G. W. Torrence, and J. Goldhirsh [1994], "ACTS 20 GHz Mobile Propagation Campaign in Alaska," *Presentations of the Sixth ACTS Propagation Studies Workshop*," Clearwater Beach, Florida, November 28-30, pp. 283-294. (JPL Technical Report JPL D-12350, December 1994, Jet Propulsion Laboratory, California Institute of Technology, Pasadena, California.)

Vogel, W. J. and J. Goldhirsh [1993a], "Earth-Satellite Tree Attenuation at 20 GHz: Foliage Effects," *Electronics Letters*, Vol. 29, No. 18, 2nd September, 19, pp. 1640-1641.

Vogel, W. J. and J. Goldhirsh [1995], "Multipath Fading at L Band for Low Elevation Angle, Land Mobile Satellite Scenarios," *IEEE Journal on Selected Areas in Communications*, Vol. 13, No. 2, February, pp. 197-204.

Vogel, W. J. and J. Goldhirsh [1993b], "Tree Attenuation at 20 GHz: Foliage Effects," *Proceedings of the Seventeenth NASA Propagation Experimenters Meeting (NAPEX XVII) and the Advanced Communications Technology Satellite (ACTS) Propagation Studies Miniworkshop*," Pasadena, California, June 14-15, pp. 219-223. (JPL Publication 93-21, Jet Propulsion Laboratory, California Institute of Technology, Pasadena, California.)

Vogel, W. J., J. Goldhirsh, and Y. Hase [1992], "Land-Mobile-Satellite Fade Measurements in Australia," *AIAA Journal of Spacecraft and Rockets*, Vol. 29, No. 1, Jan-Feb, pp. 123-128.

Vogel, W. J. and J. Goldhirsh [1990], "Mobile Satellite System Propagation Measurements at L Band Using MARECS-B2," *IEEE Transactions on Antennas and Propagation*, Vol. AP-38, No. 2, February, pp. 259-264.

Chapter 4

Signal Degradation for Line-of-Sight Communications

Table of Contents

Table of Figures

Table of Tables

Chapter 4

Signal Degradation for Line-of-Sight Communications

4.1 Background

This chapter broaches the question, "What is the LMSS signal degradation for a configuration in which line-of-sight communications are maintained with negligible shadowing in an environment where multipath is prevalent?" The multipath environment may consist of roadside trees, utility poles, hills and mountains, the ground, or a body of water. This question was, in part, addressed through the implementation of a series of experiments by the authors in central Maryland [Goldhirsh and Vogel, 1989], north-central Colorado [Vogel and Goldhirsh, 1988], western United States [Vogel and Goldhirsh, 1995], and Alaska [Vogel et al., 1994] at UHF (870 MHz), L-Band (1.5 GHz), and K-Band (20 GHz).

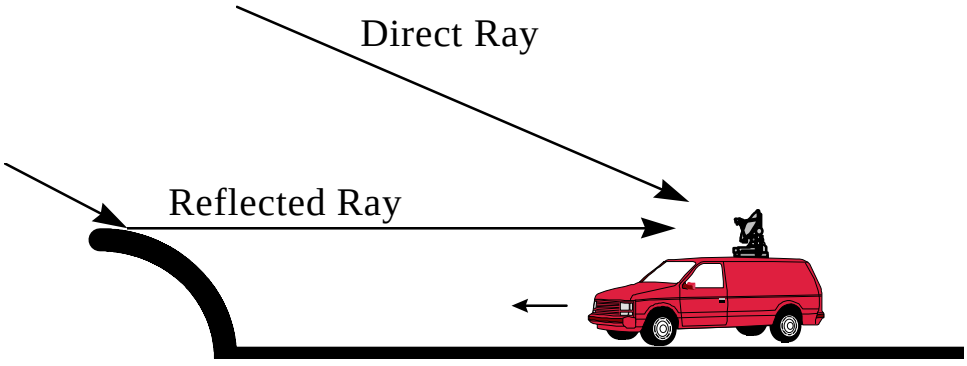

Figure 4-1: Illustration of multipath scenario showing direct ray and reflected ray from nearby mountainside arriving at receiving antenna.

A typical multipath scenario is one in which direct signals are received at the same time as indirect ones which arrive at the antenna via scattering from nearby trees, utility poles, other structures, the side of a mountain, or a nearby body of water. The sum total of

received signals may add constructively or destructively resulting in signal enhancement or fade. An example scenario is illustrated in Figure 4-1. The received power is a manifestation of the phasor sum of the direct transmission and the combined indirect voltage levels. These depend upon the scattering cross sections of the multipath reflectors, their number, and their relative distances to the antenna, the received field polarizations, and the receiving antenna gain pattern, which may be influenced by a vehicle roof.

4.2 Multipath for a Canyon and Hilly Environments

4.2.1 Canyon Environment

The results described here were obtained by the authors from LMSS line-of-sight measurements in canyon passes in north central Colorado [Vogel and Goldhirsh, 1988]. The transmitter was on a helicopter which, for each run, flew behind a receiving mobile van and maintained a relatively fixed distance and path depression angle relative to the receiving antenna. The radiating antennas on the helicopter transmitted simultaneous L-Band (1.5 GHz) and UHF (870 MHz) CW signals. Simultaneous LMSS measurements were made at L-Band and UHF. The experimental parameters are summarized in Table 4-1. The receiving antennas were located on the roof of a van (2.4 m above the ground) where the pattern functions were nominally omni-directional in azimuth with a 3 dB beamwidth in elevation between 15° and 75°. Below 15°, the antenna gain function dropped off rapidly and any multipath arriving via scattering from surfaces near or below the horizontal were diminished by the pattern by at least 10 dB.

For each of the canyon roads driven, the wall facets were highly variable in height, orientation, foliage overlay, and distance from the roads. The mountain walls consisted of randomly oriented facets of rocks with protruding patches of trees. The roads through the canyons made many twists and turns, offering highly variable aspects to the multipath illumination scene. Such a scenario was considered as a worst case for multipath.

Table 4-1: Summary of experimental parameters for canyon measurements [Vogel and Goldhirsh, 1988]**.**

Characteristic	L-Band	UHF
Source Platform		
Antenna Type	Spiral/Conical	Microstrip
Polarization	Right-hand Circular	
Antenna Beamwidths	60°	
Platform Type	Bell Jet Ranger Helicopter	
Receiver Platform		
Antenna Type	Crossed Drooping Dipoles	
Polarization	Right-hand Circular	
Height of Antenna (m)	2.4	
Beamwidth	60° (15° to 75°)	
Detection Bandwidth (Hz)	400	
Sampling Rate (KHz)	1	
Frequencies (GHz)	1.502	0.870
Signal Data Recorded	Quadrature Detected Outputs	Power
Other Data Recorded	Elapsed Time, Vehicle Speed	

Figure 4-2 shows four cumulative fade distributions depicting "least square power curve fits" for the above described multipath scenarios at frequencies of 870 MHz and 1.5 GHz and path elevation angle 30° and 45°. Each curve was derived from a subset of four runs taken in two canyon passes (Boulder and Big Thompson Canyons); a run representing measurements where the vehicle traveled up or down a canyon pass at a particular path elevation angle to the transmitter. The resultant curves correspond to a combined driving distance of 87 km through canyon passes. Each of the best fit power curves agree with the measured cumulative distribution data points to within 0.1 dB rms. As mentioned, simultaneous measurements at L-Band and UHF were made for each run.

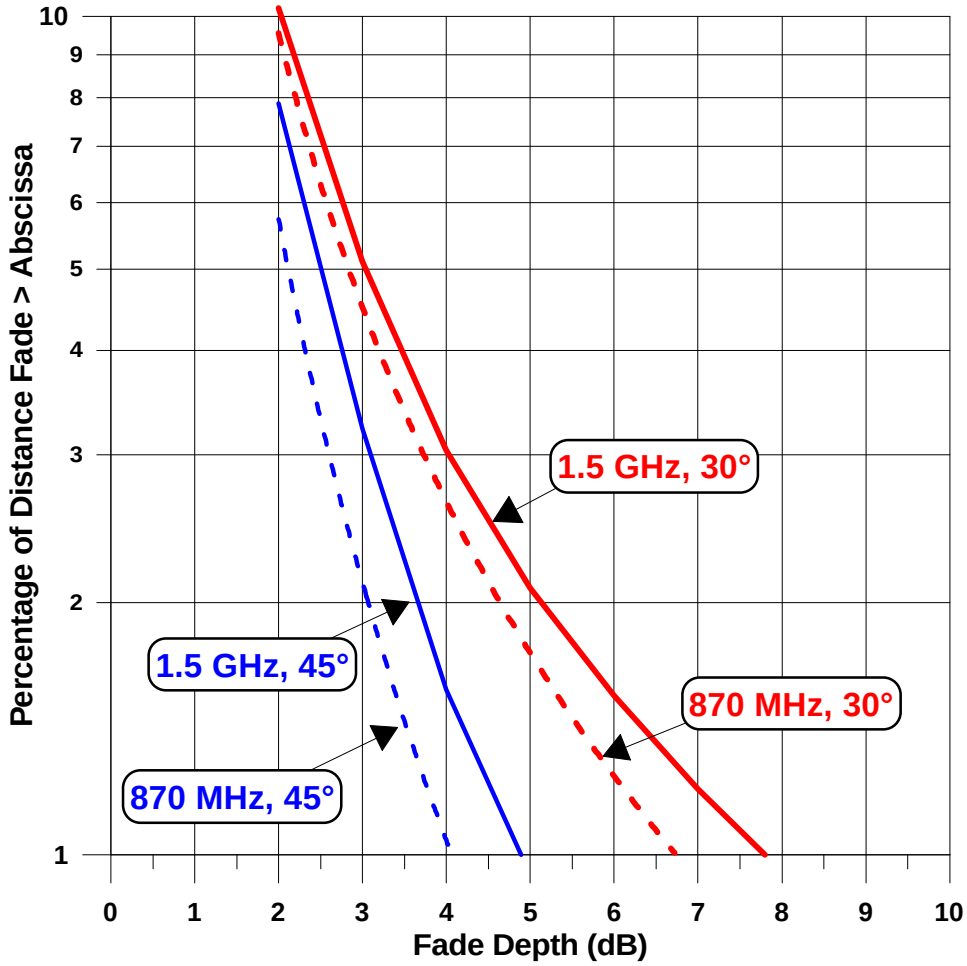

Figure 4-2: Best-fit power curves (Table 4-2) of formulation (4-1) for line-of-sight distributions in which non-shadowed multipath fading dominates for mountainous terrain.

The distributions may be expressed by

for P = 1 to 10 %

$$P = aA^{-b}, \tag{4-1}$$

where P is the percentage of distance the fade A (in dB) is exceeded, and where the values of a, b are tabulated in Table 4-2 at the two frequencies and elevation angles of 30° and 45°. Equation (4-1) and the values in Table 4-2 have been adopted as a multipath model for mountainous terrain by the ITU-R [1994, 1997].

Table 4-2: Coefficients *a, b* in formulation (4-1) describing best fit cumulative fade distributions for multipath in mountainous terrain.

Frequency	Elevation = 30°			Elevation = 45°		
(GHz)	a	b	dB Range	a	b	dB Range
0.870	34.52	1.855	2-7	31.65	2.464	2-4
1.5	33.19	1.710	2-8	39.95	2.321	2-5

Figure 4-2 shows that over the percentage range of 1% to 10%, the fades due to multipath vary between 2 and 5 dB at 45° and 2 and 8 dB at 30° elevation. The higher frequency (L-Band) exhibits slightly larger fades that are generally within 1 dB or less relative to UHF. The slightly larger fades at L-Band might be attributed to the small amount of tree fading that may have been present. There may also have been a presence of more reflecting facets on the canyon walls with sizes comparable to 20 cm (L-Band) or larger than does exist for the UHF case (34 cm). Such facets (L-Band case) would offer larger cross sections (Mie scattering) than facets whose dimensions were small relative to a wavelength (UHF case) where Rayleigh scattering is applicable. Larger fades at the 30° elevation relative to 45° may be attributed to some tree shadowing. It also may be attributed to the fact that multipath is dominated by illuminated surfaces closer to the vehicle; this implies lower reflecting heights and more shallow elevation angles.

4.2.2 Hilly Terrain

Multipath fading at 1.5 GHz for low elevation angles and unshadowed line-of-sight propagation in hilly terrain was characterized by the authors [Vogel and Goldhirsh, 1995]. The receiving van employed a tracking helix antenna with beamwidths in the principal planes of approximately 36° (i.e., ± 18° about the geometric axis). CW signals from INMARSAT's geostationary satellite MARECS B-2 were received at elevation angles ranging from 7° to 14° for measurements made in Utah, Nevada, Washington and Oregon.

Distributions corresponding to measurements for several well-defined scenarios were executed and the results are given in Figure 4-3. Curve 1 (elevation = 14°) represents a nine-minute distribution for the case in which the vehicle was standing in an open area with minimal nearby terrain features. It therefore may be considered to represent a "benchmark" where minimal propagation effects are combined with the stability of the system dependent upon the receiver noise, and the transmitter and receiver gain changes. It is observed that the fade level is less than 1 dB at 1% probability. Curve 2 (elevation = 14°) represents a reference for the vehicle in motion (12 minute run) in a flat open terrain. In additions to effects described for the static case, signal fluctuations caused by antenna tracking errors may also have been introduced here. For the open field measurements, fades of less than 2 dB are experienced at the 1% probability. Curve 3 (labeled best aspect) corresponds to the scenario in which the line-of-sight was orthogonal to the driving direction. This distribution (17 minute run at 14° elevation) corresponds to the case in which the satellite and reflecting surfaces are on the same side of the vehicle (labeled "Best Aspect"). On the other hand, Curve 4 (10 minute run at elevation = 10°) corresponds to the case in which the satellite was (on average) ahead of

the vehicle and the straight four-lane divided highway approached chains of hills through a flat, wide valley. Because the road itself was rolling (e.g., sinusoidal), it may be reasoned that a greater likelihood exists for specular scattering from reflecting surfaces on the mountainous terrain in front of the vehicle than does exist for the case in which the satellite and scatterers are to the side of the vehicle. For the former case (labeled "worst aspect"), multipath levels approaching 7 dB were experienced for 1% of the driving distance.

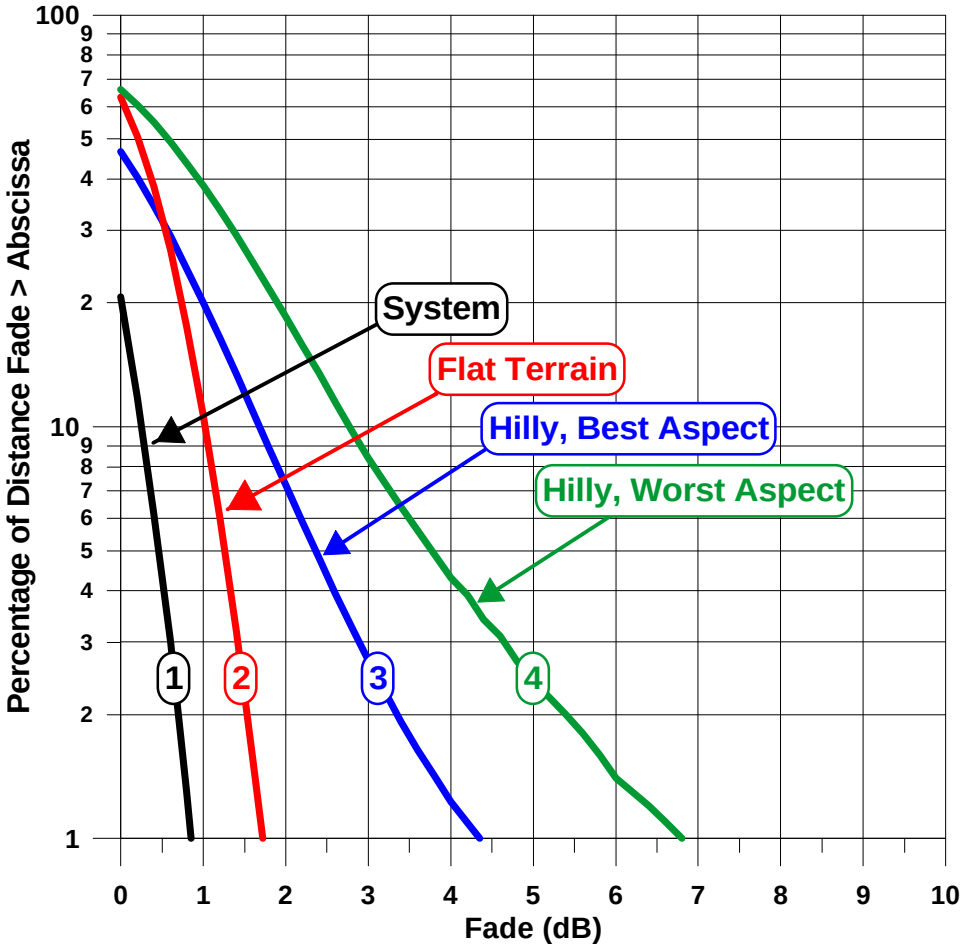

Figure 4-3: Comparison of multipath fading for several well defined low-elevation angle scenarios in western United States [Vogel and Goldhirsh, 1995].

4.3 Multipath Due to Roadside Trees

Similar types of line-of-sight measurements were performed by the authors in central Maryland along tree lined roads [Goldhirsh and Vogel, 1989] as were described for the mountainous terrain case in Section 4.2. That is, repeated measurement runs at 30°, 45°, and 60° were implemented with the helicopter following the vehicle and cumulative distributions were derived at both UHF and L-Band. The distributions were observed to be relatively insensitive to path elevation. The three runs were combined into one

distribution at each frequency comprising 75 km of driving. The resultant distributions were found to follow an exponential form given by,

for P = 1 to 50%

$$P = u \exp(-vA), \tag{4-2}$$

where P is the percentage distance traveled in which the fade A is exceeded, and u, v are tabulated in Table 4-3. The corresponding distributions are plotted in Figure 4-4. Equation (4-2) and the corresponding values in Table 4-3 have been adopted by the ITU-R [1994, 1997] as a model for multipath caused by canopies from roadside trees.

Table 4-3: Coefficients u, v in formulation (4-2) describing best fit exponential cumulative fade distributions for multipath associated with tree-lined roads.

Frequency (GHz)	u	v	Fade Range (dB)
0.870	125.6	1.116	1-4.5
1.5	127.7	0.8573	1-6

The fades at the two frequencies fit an exponential function from 1 dB (at an exceedance of 40% to 50%) to approximately 4.5 to 6.0 dB (at an exceedance of 1%). A slight dependence is exhibited due to frequency with L-Band giving approximately 1.5 dB greater fades at 1%. The indicated best-fit exponential curves were found to agree with each of the original measured cumulative distributions to within 0.2 dB. Fading due to multipath is presumed to emanate from scattering off tree canopies that reradiate, more or less, isotropically in elevation angle. Such an explanation is consistent with the fact that the distributions were relatively insensitive to path elevation angle in the angular interval between 30° and 60°.

Enhanced fading due to multipath effects are expected for antennas pointed at lower elevation angles (e.g., 5° to 20°) where scattering from tree canopies and trunks, other vehicles, and the road itself may be received with smaller antenna gain filtering.

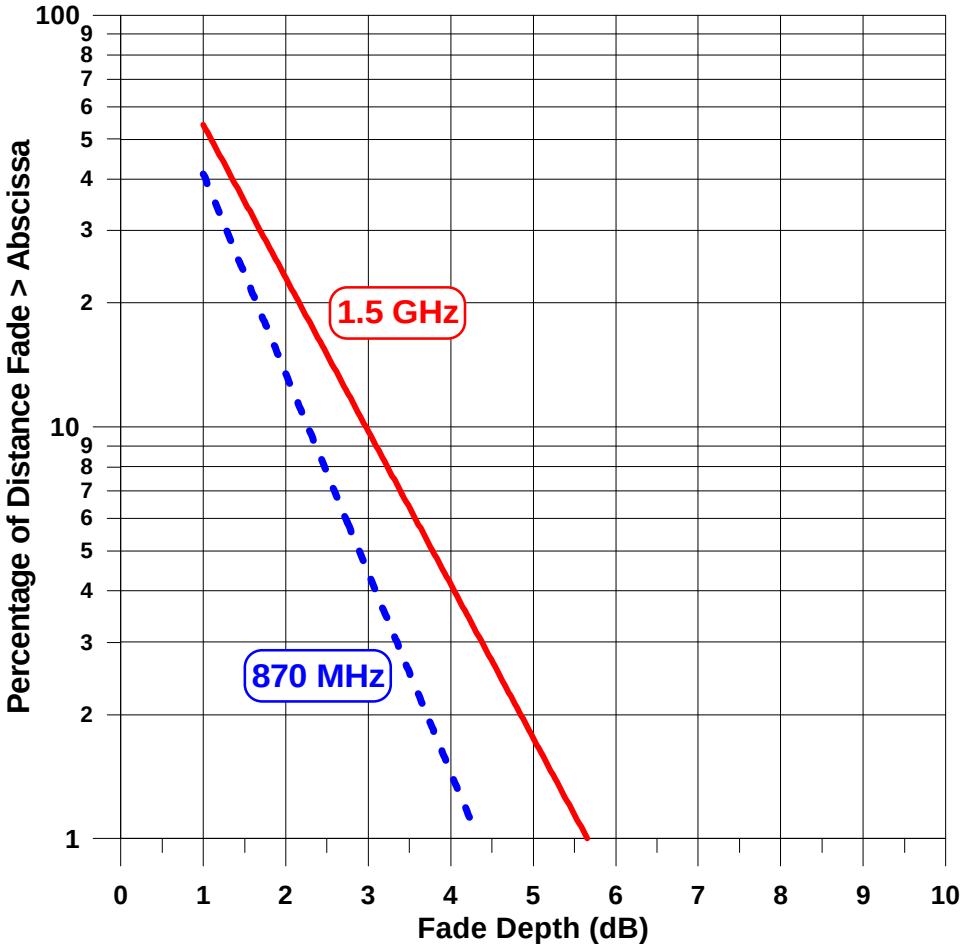

Figure 4-4: Best fit exponential cumulative fade distributions of the formulation (4-2) for line-of-sight propagation in which multipath fading dominates for tree-lined roads.

4.4 Multipath at 20 GHz Near Body of Water - Low Elevation Angle Effects

As mention in Section 4-3, it is expected that the multi-path fading effects should be more pronounced at lower elevation angles where forward scattering from the ground is more likely. Low elevation angle (e.g., 8°) mobile satellite measurements were executed by the authors at 20 GHz in Alaska employing transmissions from the Advanced Communications Technology Satellite (ACTS) [Goldhirsh et al., 1994]. The extent to which ground reflections are important at low elevation angles depends on the location of the antenna on the vehicle's roof relative to the satellite azimuth location, as well as the type of ground (e.g., dry versus wet ground). Cumulative fade distributions corresponding to various multipath (not shadowed) line-of-sight scenarios are given in Figure 4-5. These distributions were derived from measurements employing a tracking antenna located on the rear of the roof of a van, where the antenna beamwidth was 27°.

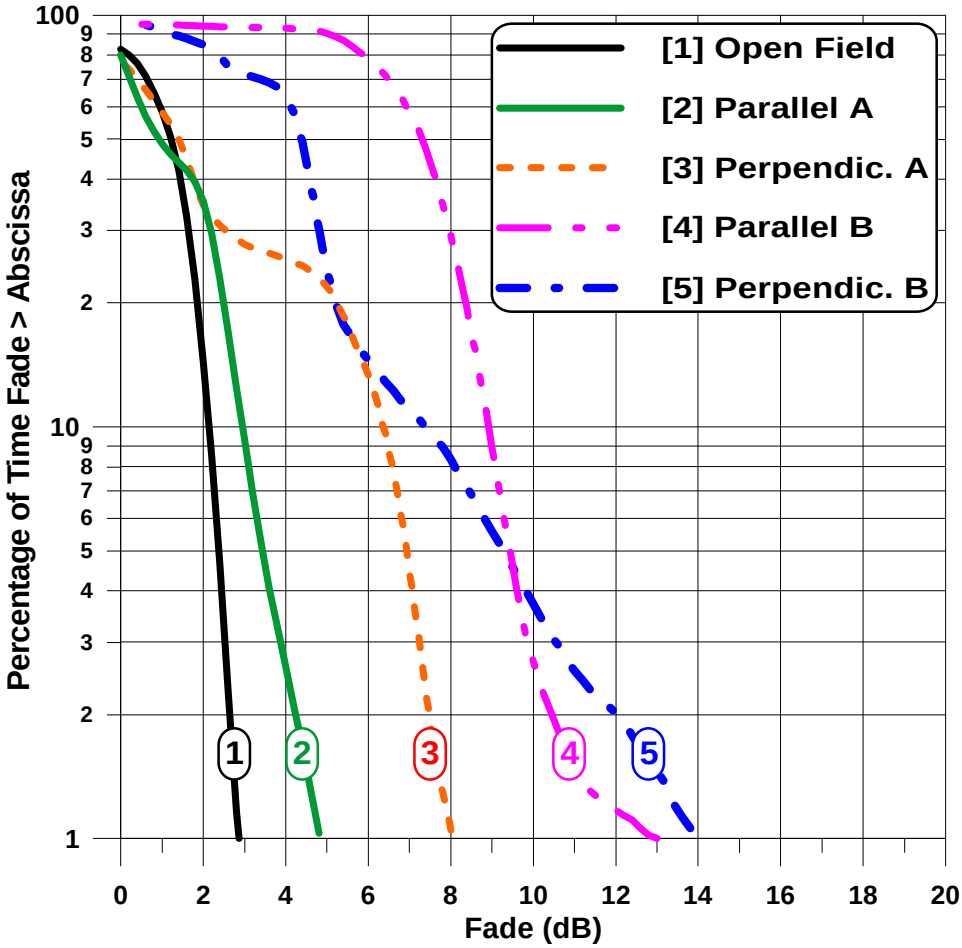

Figure 4-5: Multipath distributions for over-water and dry land scenarios at 20 GHz in vicinity of Fairbanks, Alaska. Elevation angle to satellite was 8°.

Curve 1 was obtained from measurements obtained in an open dry field in Fairbanks, Alaska where the vehicle was moving slowly. This distribution shows a maximum fade level due to multipath of approximately 3 dB at 1% probability. For this situation, the small contribution due to multipath is from diffuse scattering from a ground having a low reflection coefficient. On the other hand, the other four curves were obtained when the vehicle was parked near a body of water (Tanana River), and the earth-satellite path was directed over the water in front of the vehicle. Each curve corresponds to a different vehicle orientation vis-à-vis the earth satellite path. Curve 2 labeled as "Parallel A" represents the scenario in which the front of the vehicle was facing the satellite. On other hand, Curve 4 labeled as "Parallel B" corresponds to the configuration in which the rear of the vehicle was facing the satellite. Curve 3 labeled as "Perpendicular A" represents the case in which one side of the vehicle was facing the satellite, and Curve 5 denoted as "Perpendicular B" corresponds to the scenario in which the other side of the vehicle was facing the satellite. Although the vehicle was stationary for each orientation, the tracking antenna was in slight motion as it was continuously tracking the satellite position. Hence, the multipath scene was in a constant state of change simulating vehicle motion. These measurement runs individually ranged from 2 to 5 minutes, and the antenna pointing varied within ± 5° of true line of sight (well within the antenna beamwidth of ± 13.5°)

during this time. The most benign of the near-water multipath distributions is given by Curve 2, which shows a maximum fade of 5 dB at 1%. As mentioned, this orientation (Parallel A) was such that vehicle was facing the satellite and the antenna was located at the rear of the vehicle. Hence, the vehicle shielded reflections from the body of water mitigating multipath effects. On the other hand, when the vehicle's rear was facing the satellite (Curve 4 and Parallel B), relatively large multipath fading is observed. For this case, minimal shielding by the vehicle occurred. For this case, fading as high a 13 dB existed at 1% probability. Perpendicular orientation also offers an aspect with minimal roof shielding. Perpendicular B case shows the largest multipath fading of 14 dB at 1%. It is conjectured that the distributions for the two perpendicular cases are not similar because the vehicle was located at different relative positions relative to the surrounding scene for these cases.

4.5 Multipath Versus Driving Directions

Figure 4-6 shows eight distributions derived from measurements corresponding to different driving scenarios for three roads in central-Maryland during the 20 GHz ACTS mobile-propagation campaign [Goldhirsh et al., 1994]. The measurements associated with these distributions were performed in March (1994) during which time the deciduous trees were devoid of leaves. For the Route 295 driving measurements, the earth-satellite path was slightly to the right of the driver traveling south and to the left of the driver traveling north as shown in the sketch of Figure 4-7. Hence, for the condition in which the vehicle is driven south, less shadowing should be expected in the left lane (as shown) vis-à-vis the right lane. The low fades associated with the distributions of Curves 1 and 2 correspond to the above cases (left lane traveling south and right lane traveling north). Signal degradation for these cases is caused by multipath as is evident from the relative low fade values associated with the distributions. Curves 3 and 4 in Figure 4-6 correspond to the geometry in which the vehicle is closer to the line of roadside trees where the likelihood for shadowing and tree attenuation is more pronounced. Curves 5 to 8 represent distributions for other directions and other roads in which the shadowing aspect is more pronounced. It is apparent from the highly variable fade levels in Figure 4-6, for the same geographic location, the driving direction relative to the vehicle-satellite bearing plays a significant role in establishing the level of fading.

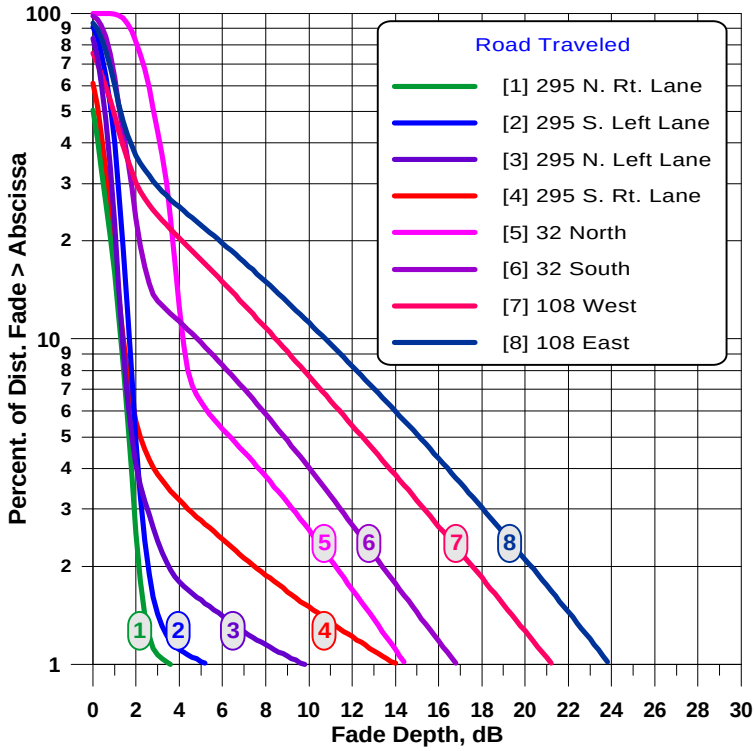

Figure 4-6: Fade distributions due to multipath and shadowing in central Maryland at 20 GHz. Curves 1 and 2 represent primarily multipath, other curves correspond to varying degrees of tree shadowing from canopies devoid of foliage.

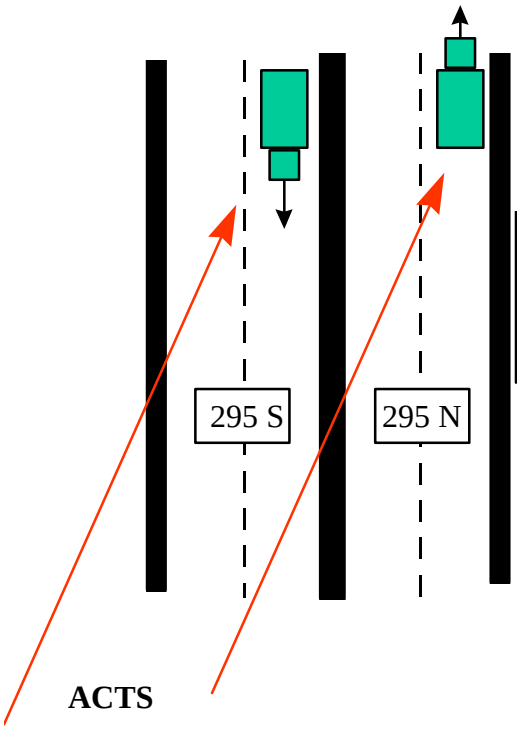

Figure 4-7: Relative azimuths of mobile-satellite path and driving direction for Route 295 (four-lane highway with two lanes in each direction).

Another example showing multipath fade levels at K-Band (18.7 GHz) in a roadside tree environment, when the satellite was directly in front of or behind the moving vehicle, is shown in Figure 4-8 as the curve labeled 0° orientation. The other curves in this figure show distributions for tree lined scenarios in which the orientation of the earth-satellite path relative to the vehicle direction was 45° and 90°. These curves, also alluded to in Chapter 7, were derived from measurements in Germany employing a tracking antenna on a mobile van. This effort was commissioned by the European Space Agency employing Italsat F1 as the radiating source platform [Joanneum Research, 1995; Paraboni and Giannone, 1991]. It is clear that the fading for the 0°-orientation case was primarily due to multipath although some tree shadowing effects may have existed near the 1% fade level.

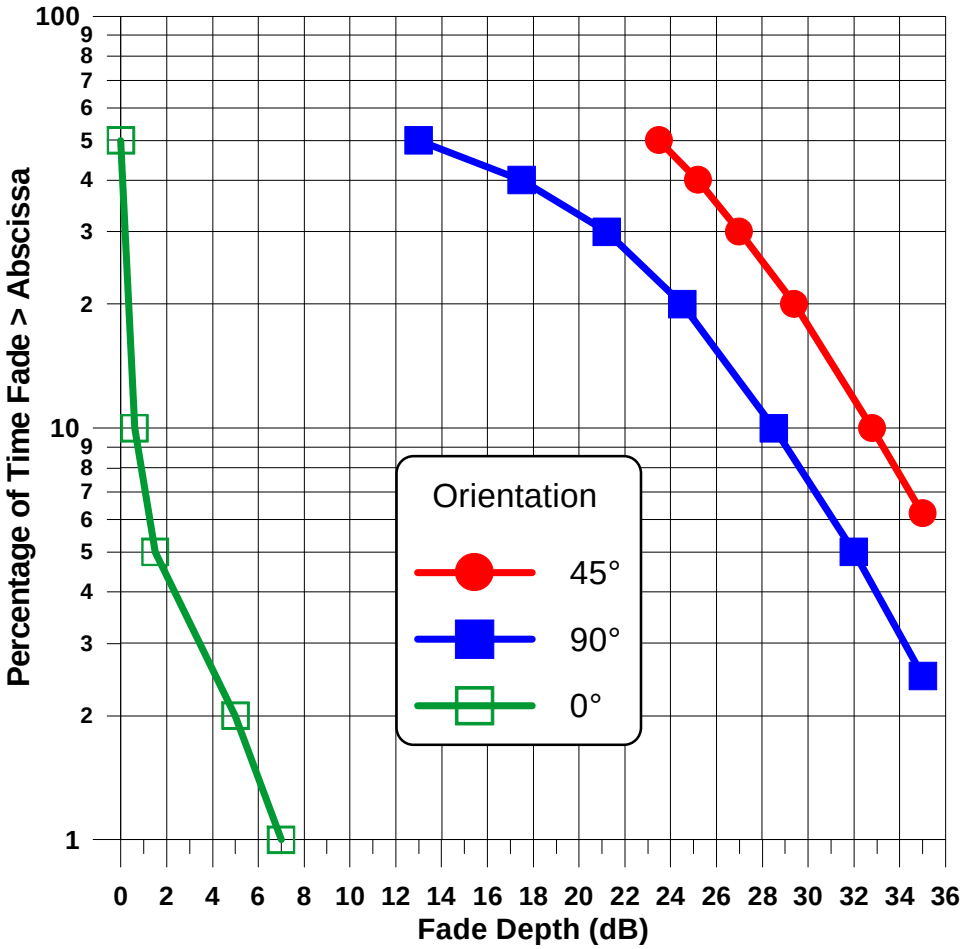

Figure 4-8: Cumulative fade distributions from measurements made in Germany at 18.7 GHz in a tree-shadowed environment at elevation angles 30°-35°. The curve labeled 0° orientation is representative primarily of line-of-sight multipath. The other indicated orientation angles are the driving azimuths relative to the satellite [Murr et al., 1995].

4.6 Empirical Multipath Model

We have observed that a large variability of multipath fading occurred for different road scenarios, frequencies, and elevation angles. Nevertheless, the range of attenuation values at the different percentages is sufficiently small to enable development of a single empirical model. The model proposed here, called *Empirical Multipath Model* (EMM), represents the median of 12 multipath distributions previously considered here at frequencies from 870 MHz to 20 GHz and elevation angles from 8° to 60°. This model encompasses the following measurement scenarios: (1) Canyons at 870 MHz and 1.5 GHz for 30° and 45° elevations, (2) rolling hills and mountains at 1.5 GHz for 10° and 14° elevations, (3) roadside tree measurements at 870 MHz and 1.5 GHz for 30° to 60° elevations, (4) roadside tree measurements at 20 GHz for 38° elevation, (5) open fields and near-water (with vehicle shielding) at 20 GHz for elevation of 8°. The resultant model is given by, for A between 1 and 4.6 dB

$$P = u \exp(-vA), \tag{4-3}$$

where

$$u = 94.37,\ v = 0.9863, \tag{4-4}$$

and where P is the percentage of distance driven over which the attenuation A (dB) is exceeded assuming only multipath conditions. The range of P covered by the above interval of A is between 1% to 50%. A comparison of the EMM model distribution with the above mentioned 12 distributions is given in Figure 4-9 (solid line with no data points). For probabilities of 2% and greater, the model distribution is approximately within ±1.5 dB of the measured distributions and at 1%, it is within ±3 dB. The distributions having high fade values at the lower percentages (e.g., 1%) might also include some shadowing effects. In employing (4-3) at the lower elevation angles (e.g., 8°), the model does not include multipath for over-water scenarios unless the vehicle roof shields the multipath ray. At the higher elevation angles (e.g., above 20°), it is assumed the antenna pattern rejects reflections from the ground.

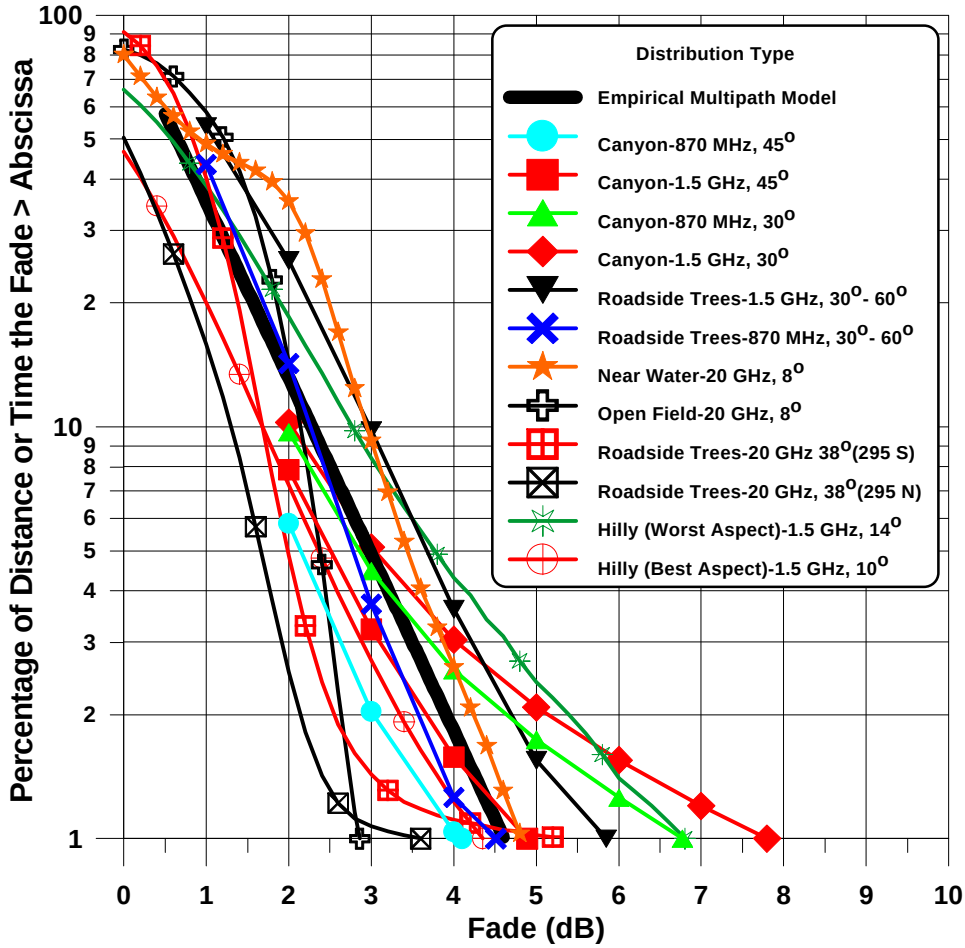

Figure 4-9: Comparison of line-of-sight multipath distributions for different scenarios and frequencies with single empirical multipath model (EMM) distribution (thick curve without data points).

4.7 Summary and Recommendations

Several models have been described giving the relationship between percentage of distance traveled and attenuation. The different models pertain to various multipath scenarios where the mechanism of fading is caused by the direct signal and an interfering multipath signal being received at the antenna as shown in Figure 4-1. The models considered here are: (1) Mountainous terrain at 870 MHz and 1.5 GHz for 30° and 45° elevation angles (see Equation (4-1)) and Table 4-2) [ITU-R, 1994; 1997]. (2) Roadside tree measurements at 870 MHz and 1.5 GHz for elevation angles between 30° and 60° (see Equation (4-2)) and Table 4-3). Models pertaining to (1) and (2) are ITU-R recommendations [ITU-R, 1994: 1997]. (3) The Empirical Multipath Model (EMM) is given by (4-3) and (4-4) and shown in Figure 4-9. Unlike the previous models described, the new empirical relationship covers elevation angles between 8° and 60° and frequencies between 870 MHz and 20 GHz and is representative of all terrain. The one exception corresponds to the scenario where the vehicle is in proximity to a body of

water and the elevation angle and antenna beamwidths are such that rays within the main beam may reflect from the water and are not obstructed by the vehicle. This scenario at the 1% probability level gave fades at 20 GHz which ranged from 8 dB to 14 dB (Figure 4-5).

The EMM is representative of the median of 12 measured distributions encompassing the above described scenarios and falls within ±1.5 dB of the measured distributions at 2% probability and greater. At 10% and greater, the model values fall within ±1 dB. The engineer may conveniently employ this single exponential expression with the caveat that it is in agreement with the measured distributions to within the stated dB variations.

4.8 References

Goldhirsh, J., W. J. Vogel, and G. W. Torrence [1994], "ACTS Mobile Propagation Campaign," Proceedings of the Eighteenth NASA Propagation Experimenters Meeting (NAPEX XVIII) and the Advanced Communications Technology Satellite (ACTS) Propagation Studies Miniworkshop, Vancouver, British Columbia, June 16-17, pp. 135-150. (Jet Propulsion Laboratory Publication JPL 94-19, August 1, 1994, California, Institute of Technology, Pasadena, California.)

Goldhirsh, J. and W. J. Vogel [1989], "Mobile Satellite System Fade Statistics for Shadowing and Multipath from Roadside Trees at UHF and L-band," *IEEE Transactions on Antennas and Propagation*, Vol. AP-37, No. 4, pp. 489-498, April.

ITU-R [1994] (International Telecommunication Union, Radio Communication Study Groups), "Propagation Data Required for the Design of Earth-Space Land Mobile Telecommunication Systems," Recommendation ITU-R PN.681-1, International Telecommunication Union, ITU-R Recommendations, 1994 PN Series Volume, Propagation in Non-Ionized Media, pp. 358-365.

ITU-R [1997] (International Telecommunications Union, Radio Communication Study Groups, "Revision of Recommendation ITU-R P.681," Document 3M/3 - February.

Joanneum Research [1995], "Land Mobile Satellite Narrowband Propagation Campaign at K_a-Band," Final Report W.O. #4, ESTEC Contract 9949/92/NL, January.

Murr, F., B. Arbesser-Rastburg, S. Buonomo, Joanneum Research [1995], "Land Mobile Satellite Narrowband Propagation Campaign at K_a-Band," International Mobile Satellite Conference (IMSC '95), Ottawa, Canada, pp. 134-138.

Paraboni, A. and B. Giannone, [1991], "Information for the participation to the ITALSAT Propagation Experiment," Politecnico di Milano Report 91.032.

Vogel, W. J. and J. Goldhirsh [1995], "Multipath Fading at L-Band for Low Elevation Angle, Land Mobile Satellite Scenarios," *IEEE Journal on Selected Areas in Communications*, Vol. 13, No. 2, February, pp. 197-204.

Vogel, W. J, G. W. Torrence and J. Goldhirsh [1994], "ACTS 20 GHz Mobile Propagation Campaign in Alaska," Presentations of the Sixth ACTS Propagation Studies Workshop (APSW VI), Sheraton Sand Key Resort, Clearwater Beach, Florida, November 28-30, pp. 283-294. (Jet Propulsion Laboratory Publication JPL-

D-12350, December 1994, California, Institute of Technology, Pasadena, California.)

Vogel, W. J. and J. Goldhirsh [1988], "Fade Measurements at L-band and UHF in Mountainous Terrain for Land Mobile Satellite Systems," *IEEE Transactions on Antennas and Propagation*, Vol. AP-36, No. 1, pp. 104-113, June.

Chapter 5

Fade and Non-Fade Durations and Phase Spreads

Table of Contents

Table of Figures

Table of Tables

Chapter 5

Fade and Non-Fade Durations and Phase Spreads

5.1 Background

It is important to know the length of time an LMSS channel is available and unavailable without interruption for optimally designing communication systems that handle coded messages over defined bandwidths. Receivers designed by communication engineers may, for example, be equipped with a digital soft-decision modem and a powerful forward error correcting code implemented with a convolution coder and Viterbi decoder. To optimally design such receivers, which have only two states, good or bad, knowledge of the statistics associated with durations of fades that fall below and above defined attenuation thresholds is required. In order to implement proper designs of demodulators for coded data, it is also important to have knowledge of the phase fluctuations during conditions of fading arising due to multipath and shadowing.

Fade duration results for tree-lined roads at L-Band were derived by the authors from measurements in Central Maryland [Goldhirsh and Vogel; 1989] and southeastern Australia [Hase et al.; 1991]. The former measurement campaign was implemented employing a helicopter as the transmitter platform, and the latter, the Japanese ETS-V geostationary satellite [Vogel et al., 1992]. During the latter campaign, phase fluctuations were also measured and associated statistics described [Hase et al., 1991]. Sforza and Buonomo [1993] have reported other fade duration results for tree-lined roads.

5.2 Concept of Fade and Non-Fade Durations

A simplified scenario describing the mechanism of fade and non-fade durations is given in Figure 5-1. It shows (a) a series of trees aligned along the side of a road (top), and (b) idealized relative signal levels received from a satellite versus the distance the vehicle travels parallel to the line of roadside trees (bottom). We assume in this figure that the

line of sight between the mobile and the satellite intersects the canopy of the respective tree over the spatial intervals dd_1, dd_2 … dd_N, and that the non-intersecting intervals are nfd_1, nfd_2, … nfd_N. It is also assumed (as an example) that the signal level falls and remains below the indicated relative threshold of -5 dB during each intersection of the line-of-sight ray and the canopy. Given a knowledge of the vehicle speed at any instant of time, the *distance durations* over which the 5 dB attenuation is exceeded (i.e., dd_1, dd_2, … dd_N) may be calculated, and density and cumulative distributions determined subject to the condition that the fade exceeds 5 dB. Distributions for the non-fade durations (i.e., nfd_1, nfd_2, … nfd_N) may also be calculated for the condition that the fade is smaller than 5 dB. In this manner, conditional fade and non-fade distance duration distributions may be determined. This normalized representation may then be converted to *time duration* distributions by division of the vehicle speed. It is apparent that the fade duration distributions will be dependent upon the canopy dimensions of the individual trees, the density of foliage, the vehicle offset from the trees, the elevation angle of the line-of-sight ray to the satellite and the tree heights.

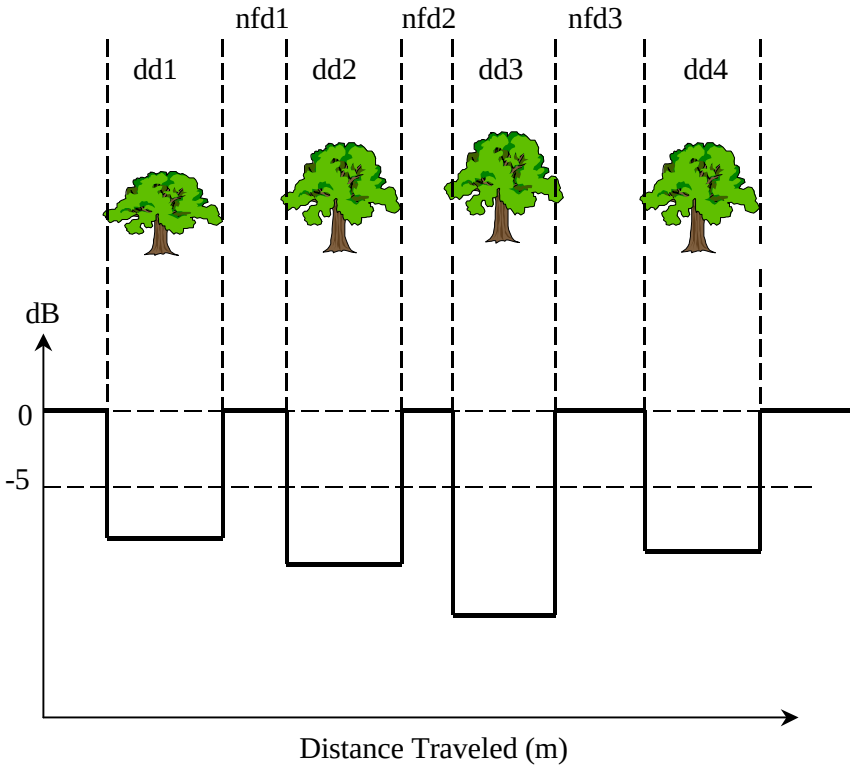

Figure 5-1: Idealized scenario showing line of roadside trees (top) and relative signal levels (bottom) for the case in which a vehicle receiving satellite signals drives parallel to the roadside trees and the line-of-sight ray to the satellite intersects the tree canopies.

5.3 Fade Durations Derived from Measurements in Australia

5.3.1 Experimental Aspects

Measurements performed in south-eastern Australia received left-hand circularly polarized CW transmissions radiated from the Japanese ETS-V satellite at a frequency of 1.5 GHz (elevation to satellite = 51°). The in- and quadrature-phase detector voltages (noise bandwidth = 1 kHz) as well as the output from a power detector with pre-detection bandwidth of 200 Hz were recorded at a 1 kHz rate. The receiver antenna was comprised of a crossed drooping dipole antenna having 4 dB gain, an azimuthally omni-directional radiation pattern, and a relatively flat elevation pattern over the beamwidth from 15° to 75°.

Fade duration results were derived by analyzing the average of two consecutive 1 millisecond samples. All fade and non-fade durations were expressed in units of traveled distance (m) for which the fades were continuously exceeded or were less than thresholds ranging from 1 to 8 dB. As mentioned, the *distance durations* may be converted to *time durations* by dividing the former by the speed (which was usually in the range from 5 to 25 m/s).

The phase data were extracted from the quadrature detected signals with the low frequency components, due primarily to oscillator drift and Doppler shift changes, rejected by digital filtering. Roadside obstacles and scatterers therefore caused the phase shifts measured.

5.3.2 Fade Duration Model

Hase et al. [1991] described the following results, which represent recommendations by the ITU-R [1994]. Fade durations derived from the Australian measurements were with good accuracy observed to follow the lognormal distribution.

For $dd \geq 0.02\ m$

$$P(FD > dd | A > A_q) = \frac{1}{2}\left\{1 - erf\left[\frac{(\ln dd - \ln a}{\sqrt{2}s}\right]\right\}, \qquad (5\text{-}1)$$

where $P(\ FD > dd |\ A > A_q)$ represents the probability that the fade duration *FD* exceeds the duration distance *dd* under the condition that the attenuation *A* exceeds A_q. Also, *erf* is the error function, s is the standard deviation of ln(*dd*), and ln(a) represents the mean value of ln(*dd*). The left-hand expression (5-1) was estimated by computing the percentage number of "duration events" which exceed *dd* relative to the total number of events for which $A > A_q$. An event of duration distance *dd* occurs whenever the fade crosses a threshold level A_q and persists "above that level" for the driving distance *dd*. A desired expression is the joint probability that FD exceeds *dd* and *A* exceeds A_q. This is given by

$$P(FD > dd, A > A_q) = P(FD > dd \mid A > A_q) P(A > A_q), \tag{5-2}$$

where $P(A > A_q)$ is the is the absolute probability that the fade exceeds the threshold A_q. Cumulative fade distributions $P(A > A_q)$ are described in Figure 5-2 for road-types whose degrees of shadowing are classified as "extreme" and "moderate." These distributions are described by the "best fit" exponential

$$P(A > A_q) = u \exp(-vA_q), \tag{5-3}$$

where P is the percentage of the distance driven over which the fade A_q (in dB) is exceeded. The parameters u and v are tabulated in Table 5-1 along with the RMS deviations of the measured distributions relative to the best fit curves. Also plotted in Figure 5-2 is the EERS model that shows general agreement with the "moderate" distribution to within approximately 2 dB over the indicated percentage range.

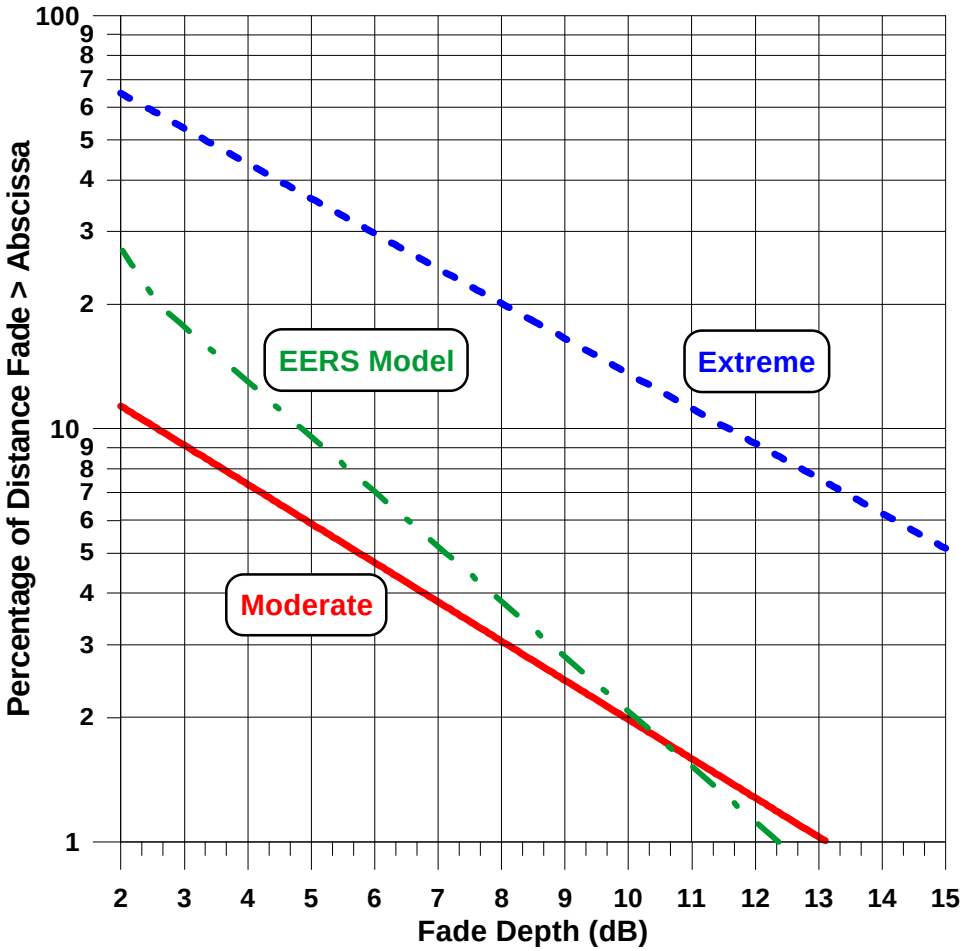

Figure 5-2: Best fit exponential fade distributions of the form (5-3) derived from measurements in south-eastern Australia along road types classified as "moderate" and "extreme." Measurements were made at L-Band (1.5 GHz) at an elevation of 51°. Also shown is the EERS model distribution.

Table 5-1: Best fit exponential cumulative fade distribution parameters *u*, *v* from (5-3) derived from measurements on roads exhibiting "extreme" and "moderate" shadowing for a path elevation angle of 51°.

Road Type	u	v	RMS (dB)	Fade Range (dB)
Moderate	17.57	0.2184	0.1	2 … 13
Extreme	95.78	0.1951	0.3	2 … 15

For the case in which there was a 5 dB fade threshold, fade duration measurements executed on three roads (two moderate and one extreme) exhibited values of a and s in (5-1) which were nearly identical for the individual runs. The resultant "best fit" regression values are given by

$$a = 0.22 \tag{5-4}$$

$$s = 1.215 \tag{5-5}$$

In Table 5-2 are shown RMS deviations relative to the log normal fit of (5-1) with values of a, s given by (5-4) and (5-5) for a fade duration threshold of 5 dB for various runs exhibiting moderate and extreme shadowing. The RMS deviations relative to the lognormal fit (5-1) for both the "moderate" and "extreme" shadowing levels are noted to be smaller than 20%. In Figure 5-3 is plotted (5-1) with parameters (5-4) and (5-5) versus logarithmic scales (for convenience in reading).

The fact that a single set of values of a, s may be applied to the "moderate" and "extreme" road-types suggests that whenever a fade is encountered which exceeds 5 dB, the physical characteristics of the trees which create the fades are the same. In other words, the different roads are distinguished by the frequency with which tree shadowing is encountered. Once encountered, the shadowing duration characteristics are similar.

Table 5-2: RMS deviations relative to the log normal fit of the fade duration distribution given by (5-1) with a, s given by (5-4) and (5-5) for various runs exhibiting moderate and extreme shadowing as shown in Figure 5-1.

Shadowing Level	RMS Deviation (%)	Distance (km)
Moderate (Run 1)	16.4	33.0
Moderate (Run 2)	18.0	8.1
Extreme	13.6	2.4

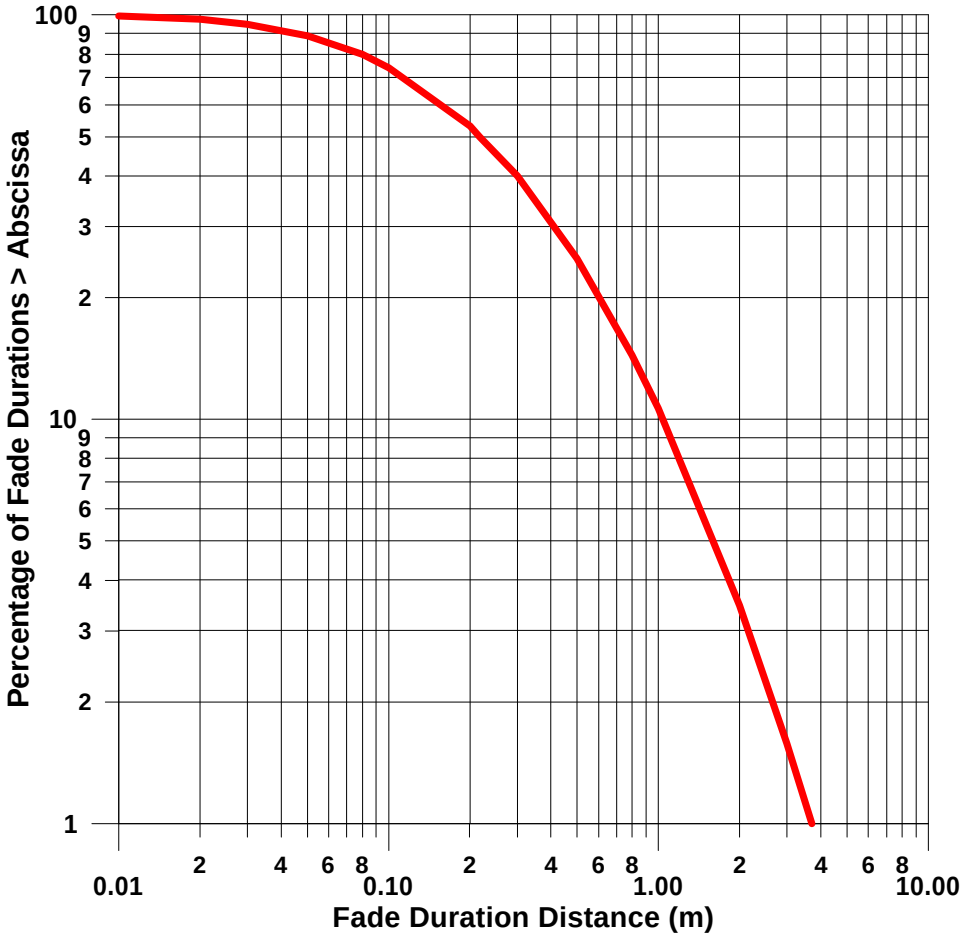

Figure 5-3: Best fit lognormal distribution (5-1) of fade duration distances for a 5-dB threshold. The distribution (1.5 GHz, elevation = 51°) encompasses road types which exhibit "moderate" and "extreme" shadowing and is plotted against logarithmic scales.

5.4 Fade Duration Measurements in Central Maryland

Goldhirsh and Vogel [1989] have also compiled fade duration statistics from 1.5 GHz measurements in central Maryland for angles of 30°, 45° and 60° for 5 dB and 10 dB thresholds. The duration distributions (5 dB threshold) shown in Figure 5-4 exhibit a slight elevation angle dependence. For example, the 30° fade duration is approximately twice that for the 60° case. The increased duration distance at the smaller elevation angles is consistent with the fact that at the lower elevation angles the line-of-sight path is likely to be shadowed over longer distances for each tree canopy than at the higher elevation angles.

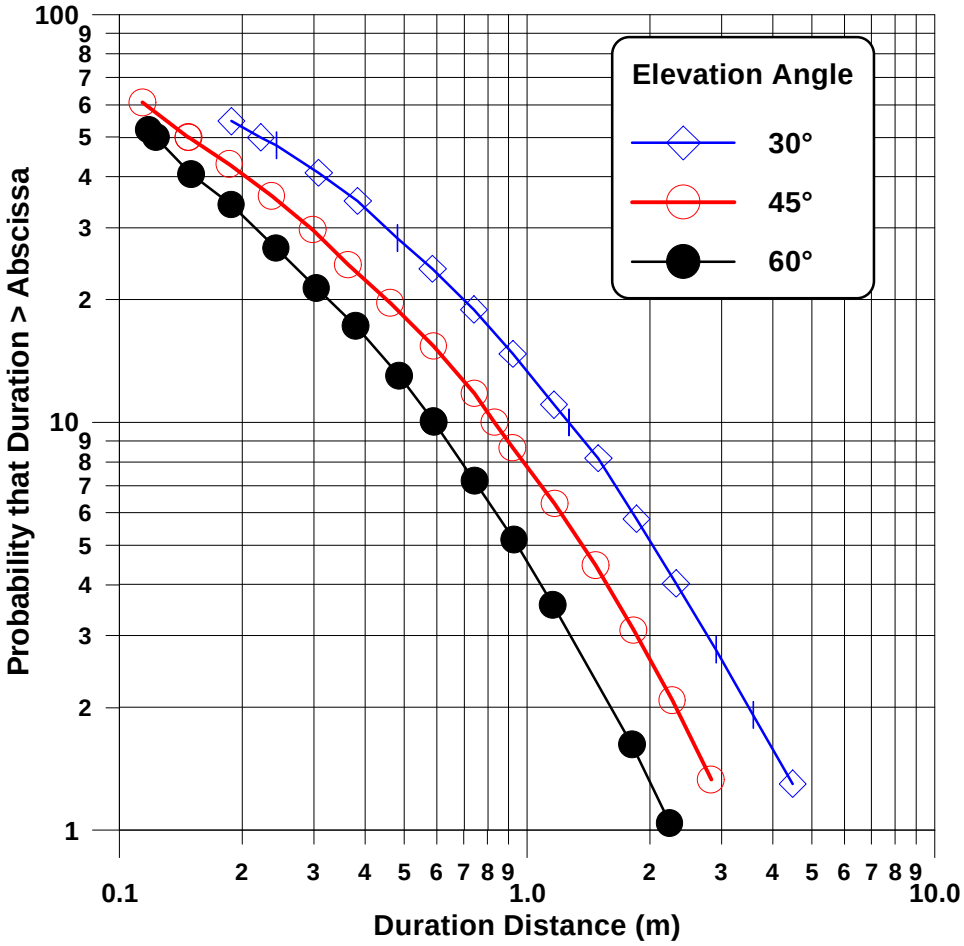

Figure 5-4: Fade durations (1.5 GHz) at elevation angles of 30°, 45°, and 60° for tree-lined road in central-Maryland [Goldhirsh and Vogel, 1989]. The probability is conditioned to a 5 dB fade threshold.

5.5 Fade Duration Distributions at Higher Elevation Angles

Sforza and Buonomo [1993] derived fade duration distributions at 1.3 GHz from aircraft measurements executed in North Yorkshire, UK at elevation angles of 40°, 60° and 80° for a "wooded" environment with percentage of optical shadowing (POS) varying between 35% and 85%. In Figure 5-5 are shown fade duration distributions for these elevation angles and a fade threshold of 6 dB. These distributions were converted from a time duration abscissa to the shown distance duration distribution employing their stated average vehicle speed of 8.6 m/s. As in Figure 5-4, an elevation angle dependence is exhibited for each of the distributions.

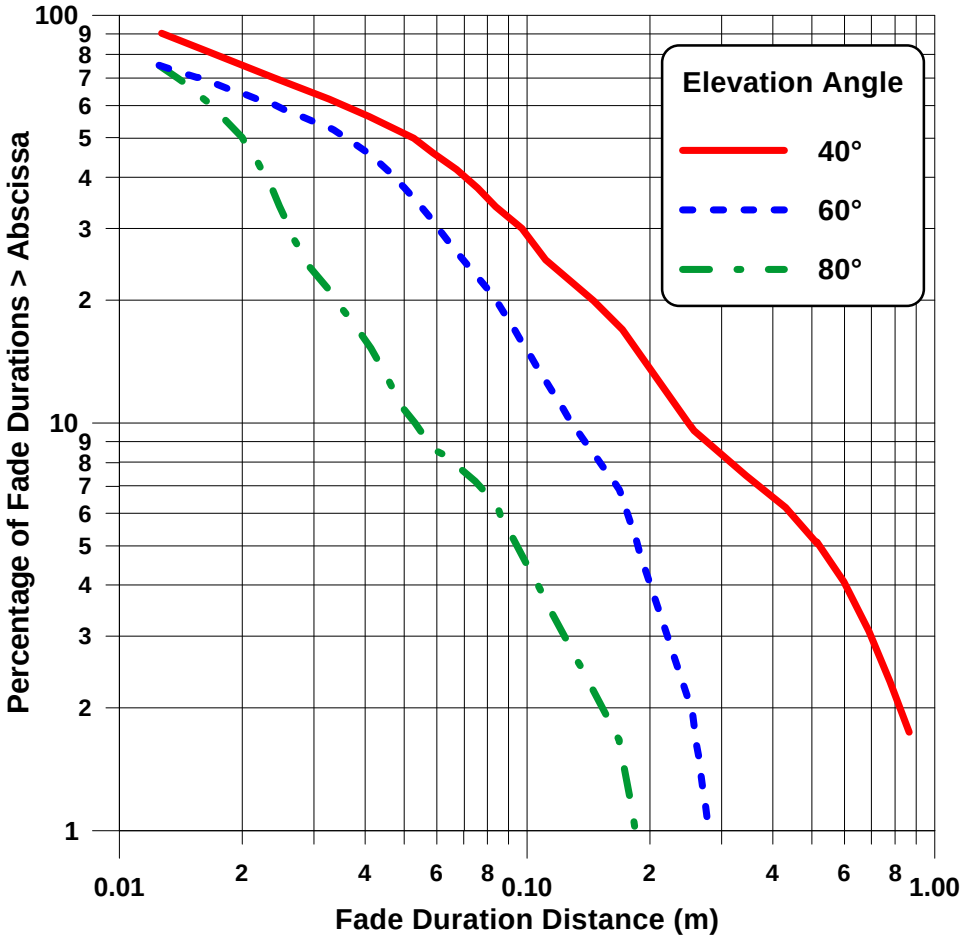

Figure 5-5: Fade duration distributions at 1.3 GHz derived from measurements of Sforza and Buonomo [1993] in North Yorkshire, U.K. for a "wooded" environment.

5.6 Summary of Fade Duration Results

In Figure 5-6 are shown the above described duration distributions given in Figure 5-3 through Figure 5-5. In Table 5-3 are summarized the 50% and 10% probability values of the durations for the various curves. It is noted in Figure 5-6 that the Central Maryland fade durations at 30°, 45° and 60° are in close proximity to the ITU-R model results derived from the Australian database at 51°. The roadside tree conditions for these databases were, in general, similar. On the other hand, the duration results from England give significantly smaller fade durations. These results suggest that the canopy dimensions, tree heights and foliage densities were also significantly different. The median and 10% time durations may be determined by dividing the values in Table 5-3 by the appropriate vehicle speed. For example, the ITU-R model gives median and ten percentile time durations of 8.8 ms and 41.6 ms, respectively, assuming a vehicle speed of 25 m/s (approximately 55 miles/h).

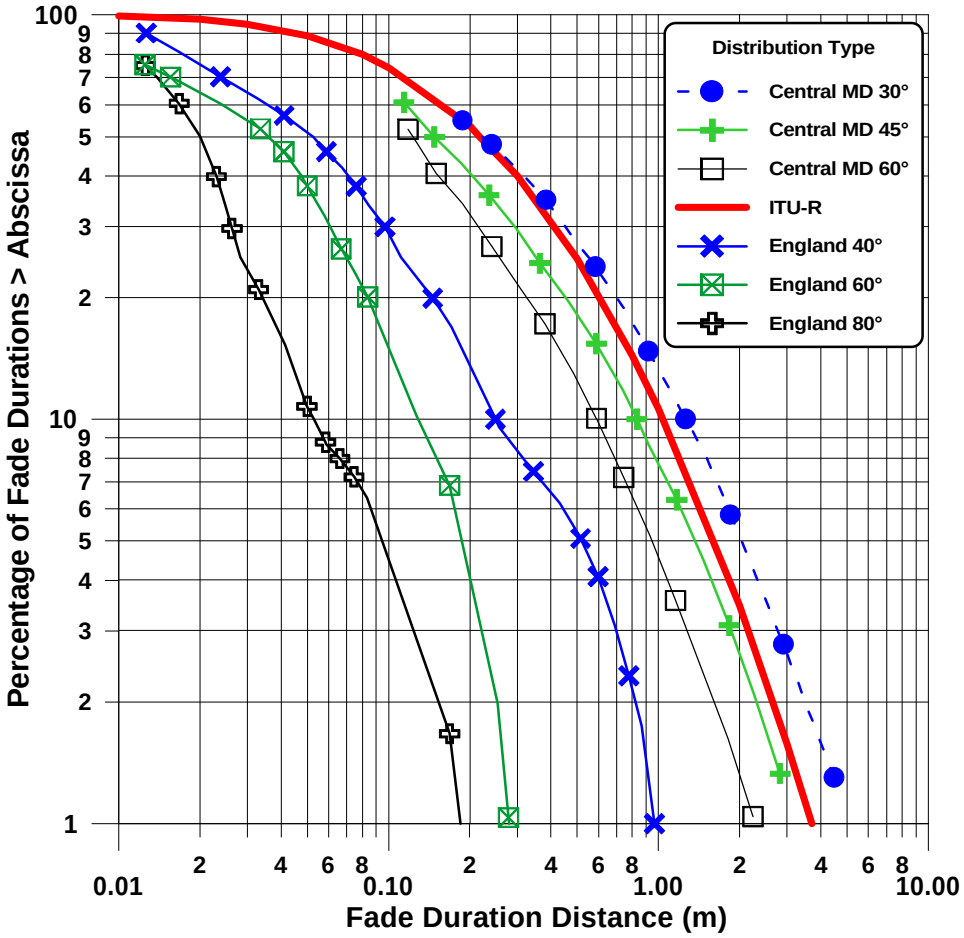

Figure 5-6: Fade durations from different investigations (Figure 5-3 through Figure 5-5) shown together.

Table 5-3: Summary of distance durations at probabilities of 50% and 10% for a fade threshold of 5-6 dB at L-Band for various investigations.

Distribution	Duration Distance *dd* (m)		Elevation (°)	Tree Shadowing
	P = 50%	P = 10%		
ITU-R	0.22	1.04	51	Moderate to Extreme
Central MD	0.22	1.26	30	POS=75%
	0.15	0.83	45	
	0.12	0.59	60	
England	0.05	0.25	40	POS=35% to 85%
	0.04	0.13	60	
	0.02	0.05	80	

5.7 Cumulative Distributions of Non-Fade Durations: Australian Measurements

As mentioned in Section 5.2, a "non-fade duration" event of distance duration *dd* is defined as the distance over which the fade levels are persistently smaller than a prescribed fade threshold. In the example previously portrayed in Figure 5-1, the non-fade durations distributions are derived through analysis of *nfd1, nfd2, nfd3, …* for the condition that the fade is smaller than the 5 dB threshold. The authors employing the Australian database in an analogous fashion as described above for the "fade duration" case performed a non-fade duration analysis. The measured data were noted to fit the power expression

$$P(NFD > dd \mid A < A_q) = b\,(dd)^{-g}\,, \tag{5-6}$$

where *P(NFD > dd| A < Aq)* is the percentage probability that a continuous non-fade distance *NFD* exceeds the duration distance *dd* (in m) given the condition that the fade is smaller than the threshold A_q. The values of the parameters b , g in the formulation (5-6) are listed in Table 5-4 for road types exhibiting "moderate" and "extreme" shadowing assuming a 5 dB fade threshold. A single best-fit power curve has been derived for the two "moderate" runs. In Figure 5-7 are plotted the best fit curves (5-6) for the moderate and extreme road type values of b , g given in Table 5-4. We note non-fade durations of 3.5 m and 0.22 m at the 10% and 90% levels, respectively, for the "moderate" case, and 1.2 m and 0.18 m, respectively for the "extreme" case. The model (5-6) and values b , g in Table 5-4 were adopted by the ITU-R as the recommended formulations describing the non-fade duration distributions for the "moderate" and "extreme" fade cases [ITU-R, 1994].

Employing an analogous expression to (5-2), the joint absolute probability of exceeding a non-fade duration distance *dd* for which the fade is smaller than A_q is given by

$$P(NFD > dd, A < A_q) = P(NFD > dd | A < A_q)\,P(A < A_q)\,, \tag{5-7}$$

where the first right hand factor is given by (5-6) and the second factor is obtained from *1 - P(A>Aq)* using (5-3).

Table 5-4: Non-fade duration regression values of b , g satisfying the power expression (5-6) at a 5 dB threshold for road types exhibiting "moderate" and "extreme" shadowing at a path elevation angle of 51° (f = 1.5 GHz).

Shadowing Level	b	g	% RMS Deviation	Distance (km)
Moderate (Run 1)	20.54	0.58	33.3	33.0
Moderate (Run 2)	20.54	0.58	20.5	8.1
Extreme	11.71	0.8371	9.3	2.4

5.8 Cumulative Distributions of Non-Fade Duration: Central Maryland

Also shown plotted in Figure 5-7 are 1.5 GHz non-fade duration distributions derived from helicopter measurements in central Maryland for elevation angles of 30°, 45° and 60° [Goldhirsh and Vogel, 1989]. It is noted that these distributions generally flank the interval of durations derived employing the Australian measurements (51° elevation) between the "extreme" and "moderate" cases. At the 10% probability, the 60° central Maryland distribution coincides with the "moderate" case and the 30° distribution is close to the "extreme" distribution. Close agreement between the above curves also exists at the median level.

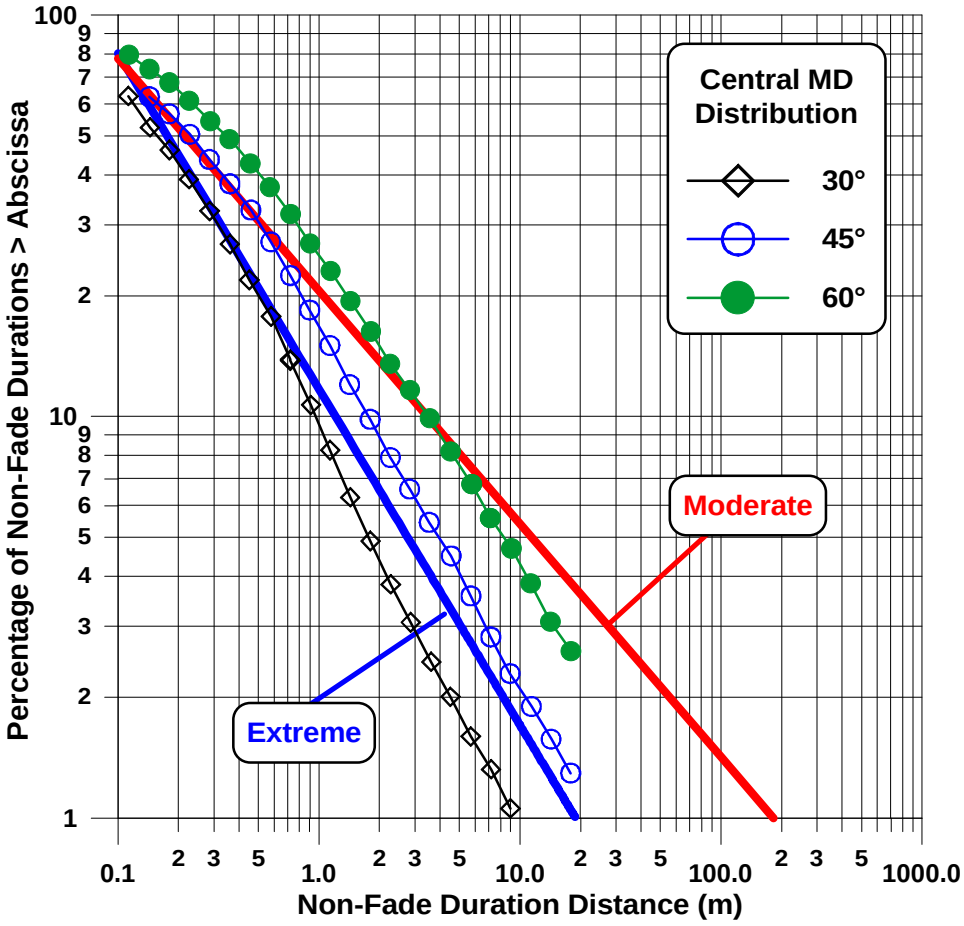

Figure 5-7: Best fit power curves (5-6) showing non-fade duration distributions for a 5 dB threshold for road types which exhibit "moderate" and "extreme" shadowing.

5.9 Cumulative Distributions of Phase Fluctuations: Australian Measurements

Through further analysis of the Australian data base, phase time-series were obtained from measured I and Q components after variations due to Doppler and oscillator drifts were eliminated using a high pass filter [Hase et al., 1991]. Conditional cumulative

phase distributions were derived for each of the road-types described above. The condition for these distributions was that the fade exceed attenuation thresholds levels ranging between 2-8 dB.

The "best fit" phase fluctuation distributions were found with good accuracy to follow a fifth order polynomial over a percentage exceedance range of 1% to 90% having the form

$$P(f > f_u \mid A > A_q) = \sum_{i=1}^{6} a_{i-1} f^{\,i-1}, \tag{5-8}$$

where (5-8) may be read as the probability that the phase f (degrees) exceeds the threshold level f_u given a fade A (dB) exceeds the threshold level A_q. In Table 5-5 is given a listing of the values of the polynomial coefficients a_i at the threshold fade level of 5 dB for the "extreme" and "moderate" road types (Figure 5-2). The corresponding phase fluctuation distributions are given in Figure 5-8.

Table 5-5: Listing of polynomial coefficients characterizing phase fluctuation distributions of the form (5-8) for road types exhibiting "moderate" and "extreme" shadowing and a 5 dB fade threshold.

Road Type	Polynomial Coefficients					
	a_o	a_1	a_2	a_3	a_4	a_5
Moderate	56.51	-6.516	$7.325\text{x}10^{-2}$	$2.380\text{x}10^{-2}$	$2.059\text{x}10^{-4}$	$-3.985\text{x}10^{-5}$
Extreme	54.23	-4.242	$-1.0897\text{x}10^{-2}$	$6.425\text{x}10^{-3}$	$2.082\text{x}10^{-5}$	$-4.258\text{x}10^{-6}$

Over the range 5% to 95% in Figure 5-8, the phases are within $\pm 15°$ relative to the median for both the "moderate" and "extreme" cases. The indicated "best fit" polynomials agreed with the individual measured distributions to within 15% RMS.

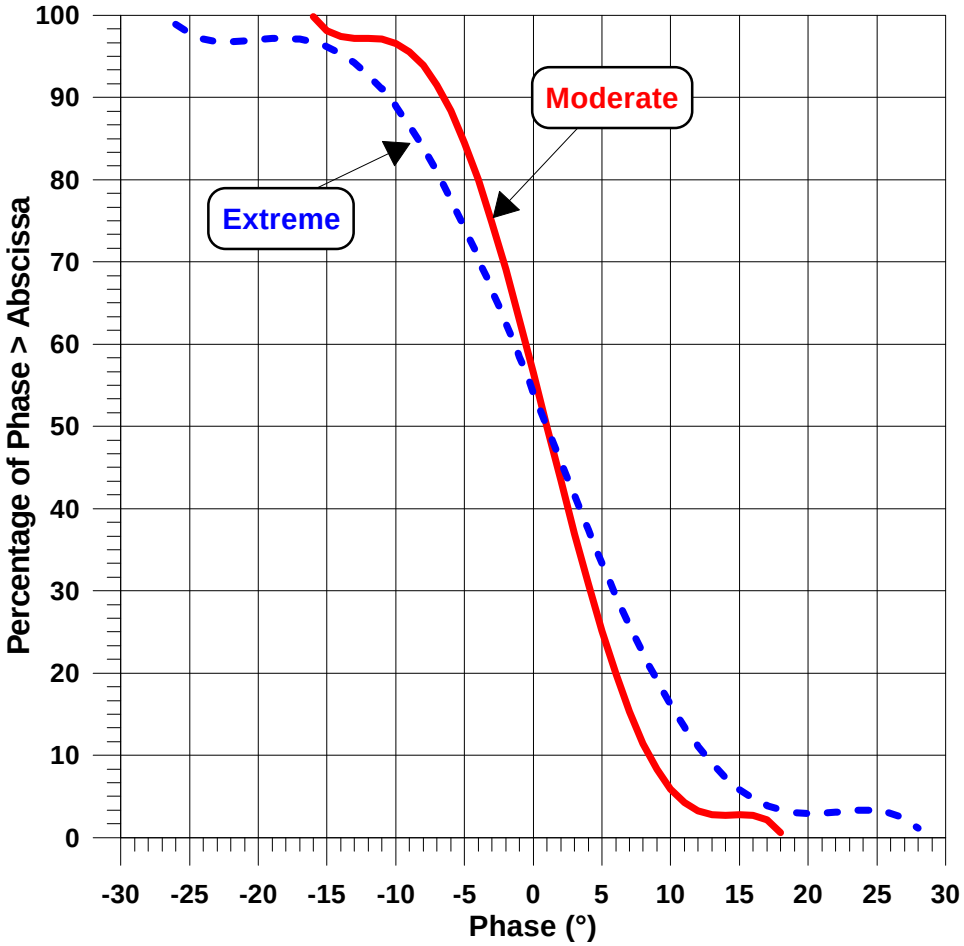

Figure 5-8: Best polynomial fit (5-8) cumulative phase distribution for "extreme" and "moderate" road types and 5 dB fade threshold (f = 1.5 GHz and elevation = 51°).

For the "moderate" runs, cumulative distributions of phases over the probability range 1% to 90% were found to be minimally dependent on fade thresholds from 2 to 8 dB. We define the "phase spread" as the maximum phase difference (at equal probability) between the individual distributions for the different fade thresholds. A phase spread of less than 5° was noted for the "moderate" case over the range of distributions having fade thresholds 2 to 8 dB. For the "extreme" case, an approximate 20° phase spread (or less) was noted within the 1% and 99% levels over the fade threshold level from 2 to 8 dB.

Based on the above results, it would appear the influence of phase fluctuations on demodulation techniques at the elevation angle considered (e.g., 51°) is minimal and that LMSS channel characteristics can be estimated without considering phase. At lower elevation angles (e.g., between 5° and 20°), greater multipath may be prevalent, increasing the phase fluctuation spread and potentially enhancing the impact on digital communications.

5.10 Summary and Recommendations

The recommended fade duration distribution is given by (5-1) and plotted in Figure 5-3 for L-Band frequencies and a 5 dB threshold fade [ITU-R, 1994]. This relation may be used for moderate elevation angles ranging from 30° to 60° and roadside tree conditions corresponding from moderate to severe tree shadowing having percentage of optical shadowing levels (POS) of 55% to 75%. The corresponding median and 10% distance durations are 0.22 m and 1.04 m, respectively.

The recommended non-fade duration distribution is given by (5-6) and plotted in Figure 5-7 for "moderate" and "extreme" shadowing conditions. These are applicable for the same conditions described above for the fade duration distributions. The parameters of (5-6) are tabulated in Table 5-4. Non-fade duration distances are 3.5 m and 0.22 m for the 10% and 50% levels, respectively, associated with the "moderate" tree shadowing case, and 1.2 m and 0.18 m for the "extreme" shadowing case. The "extreme" and "moderate" non-fade duration distributions were similar to the "non-fade" duration distributions measured in central Maryland at 30° and 60°, respectively.

Equation (5-8) and Figure 5-8 for the "moderate" and "extreme" road shadowing conditions, respectively, give the phase fluctuation distribution. Over the range 5% to 95%, the phases are within $\pm 15°$ relative to the median. Hence, the influence of phase fluctuations on demodulation techniques at the elevation angle considered (e.g., 51°) is minimal and LMSS channel characteristics can be estimated without considering phase. At lower elevation angles (e.g., smaller than 20°), this may not be the case.

5.11 References

Butt, G., M., A. N. Parks, and B. G. Evans [1995], "Narrowband and Wideband Characterisation of Satellite Mobile/PCN Channel," *International Mobile Satellite Conference, IMSC '95*, Ottawa, Ontario, Canada, pp. 128-133.

Goldhirsh, J. and W. J. Vogel [1989], "Mobile Satellite System Fade Statistics for Shadowing and Multipath from Roadside Trees at UHF and L-Band," *IEEE Transactions on Antennas and Propagation*, Vol. 37, No. 4, April, pp. 489-498.

Hase, Y., W. J. Vogel, and J. Goldhirsh [1991], "Fade-Durations Derived from Land-Mobile-Satellite Measurements in Australia," *IEEE Transactions on Communications*, Vol. 39, No. 5, May, pp. 664-668.

ITU-R [1994], "Propagation Data Required for the Design of Earth-Space Land Mobile Telecommunication Systems," Recommendation ITU-R PN.681-1, pp. 358-365.

Sforza, M. and S. Buonomo [1993], "Characterisation of the LMS Propagation Channel at L- and S-bands: Narrowband Experimental Data and Channel Modelling," *Proceedings of the Seventeenth NASA Propagation Experimenters Meeting (NAPEX XVII) and the Advanced Communications Technology Satellite (ACTS) Propagation Studies Miniworkshop*, Pasadena, California, June 14-15, 1993 (JPL Publication 93-21, August 1, 1993, F. Davarian; Editor).

Vogel, W. J., J. Goldhirsh, and Y. Hase [1992], "Land-Mobile Satellite Fade Measurements in Australia," *AIAA Journal of Spacecraft and Rockets*, Vol. 29, No. 1, Jan-Feb, pp. 123-128.

Chapter 6

Polarization, Antenna Gain and Diversity Considerations

Table of Contents

Table of Figures

Table of Tables

Chapter 6

Polarization, Antenna Gain and Diversity Considerations

6.1 Background

This chapter reviews a number of L-Band and UHF propagation effects associated with land-mobile propagation scenarios. These include fading effects related to: (1) depolarization, (2) antenna gain, (3) lane changing, (4) antenna space diversity, and (5) satellite diversity. A number of the effects examined were derived from measurements by Vogel et al. [1992], Akturan and Vogel [1997], Vogel [1997], Goldhirsh and Vogel [1987; 1989], and Ryuko and Saruwatari [1991].

6.2 Depolarization Effects

By making repeated measurements with co- and cross-polarization at 1.5 GHz for selected runs (elevation = 51°) during an Australian campaign, equi-probability "cross-polar isolation levels, *CPI*" were determined by Vogel et al. [1992]. The cross polarization isolation is defined as

$$CPI(P) = \frac{COPS(P)}{CRPS(P)}, \tag{6-1}$$

where *COPS(P)* and *CRPS(P)* represent the co-polarization and cross-polarization signal levels at the equi-probability value *P*. The *CPI* (in dB) is plotted in Figure 6-1 and was found to follow the linear relation

$$CPI = -1.605A + 18.94, \tag{6-2}$$

where *A* is the co-polarized fade (in dB) with a range between 0 and 11.8 dB.

The RMS deviation between the "best-fit linear" relation (6-2) and the data points for the corresponding runs was 0.4 dB. We note from the plot in Figure 6-1 that the isolation severely degrades as a function of fade level. For example, an approximate 11 dB isolation is observed at a 5 dB fade. This result suggests that the simultaneous employment of co- and cross-polarized transmissions in a "frequency re-use" system is implausible because of the poor isolation due to multipath scattering into the cross-polarized channel. Although the instantaneous isolation is poor, polarization diversity may nevertheless be helpful in reducing the statistical interference between two satellite systems that manage to share the same frequency band by employing code-division multiple access (CDMA). In that case, one system's signals contribute to the other's noise. Cross-polarizing the alternate system would tend to reduce the noise at the victim satellite reverse-link receiver while the alternate system's mobile earth terminals are in a clear line-of-sight condition. Estimating the net benefits of such a scheme is not straightforward, however, because the impact of power control has to be factored in.

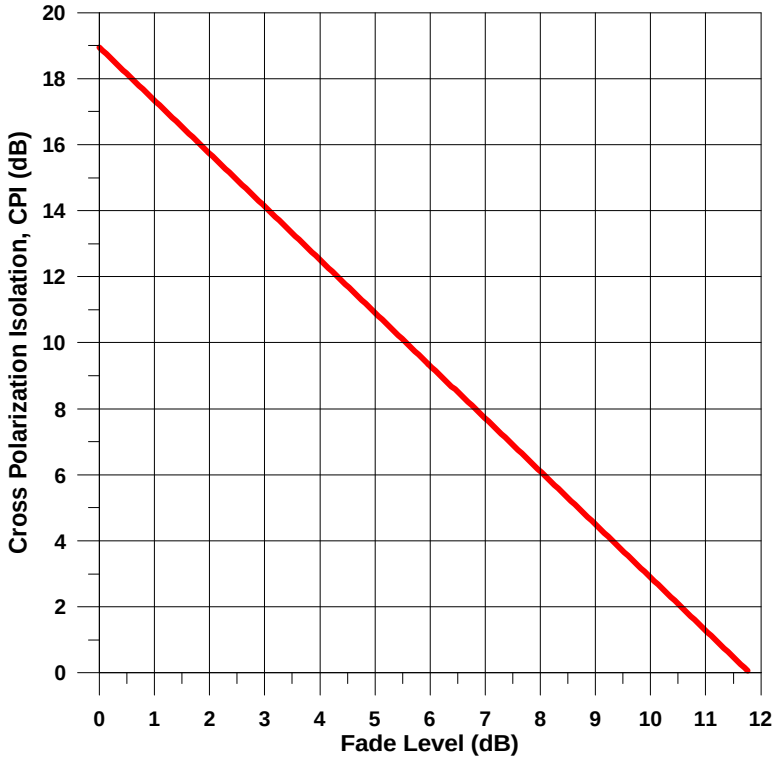

Figure 6-1: Cross polarization isolation (*CPI*) as a function of co-polarization fade at equi-probability levels.

6.3 Distributions from Low- and High-Gain Receiving Antennas

During the Australian campaign by Vogel et al. [1992], a number of repeated runs were executed in which high- and low-gain antennas were employed. The characteristics of these antennas are given in Table 6-1. Figure 6-2 shows a plot of the high gain receiver

fade versus the low gain fade over the low gain fade interval of 0 to 15 dB. The data points were found to follow the linear relation

$$A(HG) = 1.133 \cdot A(LG) + 0.51, \tag{6-3}$$

where *A(HG)* and *A(LG)* represent the high and low gain fades (in dB), respectively. Agreement between relation (6-3) and the data points for *A(HG)* is within 0.2 dB RMS.

Table 6-1: Summary of pertinent antenna characteristics [Vogel et al., 1992].

Characteristic	Low Gain	High Gain
Type	Crossed Drooping Dipoles	Helix
Gain (dB)	4	14
Nominal Pattern (El.)	15°-70°	45° (Principal Planes)
Nominal Pattern (Az.)	omni-directional	45°
Polarization	LHCP or RHCP	RHCP or LHCP

The high-gain antenna system consistently experienced slightly more fading than the low-gain system. For example, at 3 and 14.5 dB (of low-gain fades), the high gain fades were 4 and 17 dB, respectively, which represents 33% and 17% increases. This slight increase in attenuation for the high-gain case occurs because less average power is received via multipath from surrounding obstacles as the associated antenna beam is narrower. In contrast, the azimuthally omni-directional low gain antenna receives more scattered multipath contributions resulting in an enhanced average received power. It should be emphasized that negligible ground specular backscatter was received by either antenna because of the gain filtering characteristics at low elevation angles. The slight increase of signal for the lower gain azimuthally omni-directional antenna came from diffuse scatter from surrounding tree canopies. It is important to note that because the high-gain antenna has 10 dB more gain associated with it, the net power received by it is still significantly higher than that received for the low-gain case. Even at the 15 dB fade level (low-gain receiver system), the net received power for the high gain mode is larger by 7.5 dB.

Mayer [1996] examined the effects of antenna gains for low elevation angle measurements (8°) at 20 GHz in Alaska through measurement and analysis of transmissions from the Advanced Communications Technology Satellite (ACTS). He compared clear line-of-sight multipath effects for aperture antennas with gains of approximately 16 dB, 22 dB, and 28 dB. Because of the low elevation angle, ground multipath is more likely for the lower gain antennas. The 28 dB gain antenna clearly showed the smallest clear line-of-sight multipath fading, giving magnitudes between 1 to 2 dB. The smaller fading is due to reduced specular scattering from the road. This compares to multipath fading of approximately 10 dB for the lowest gain antenna. However, tracking of the satellite with the higher gain antenna was found to be more difficult. Tracking errors for the higher gain antenna was found to result in substantial fading of the satellite signals vis-à-vis the lower gain antenna.

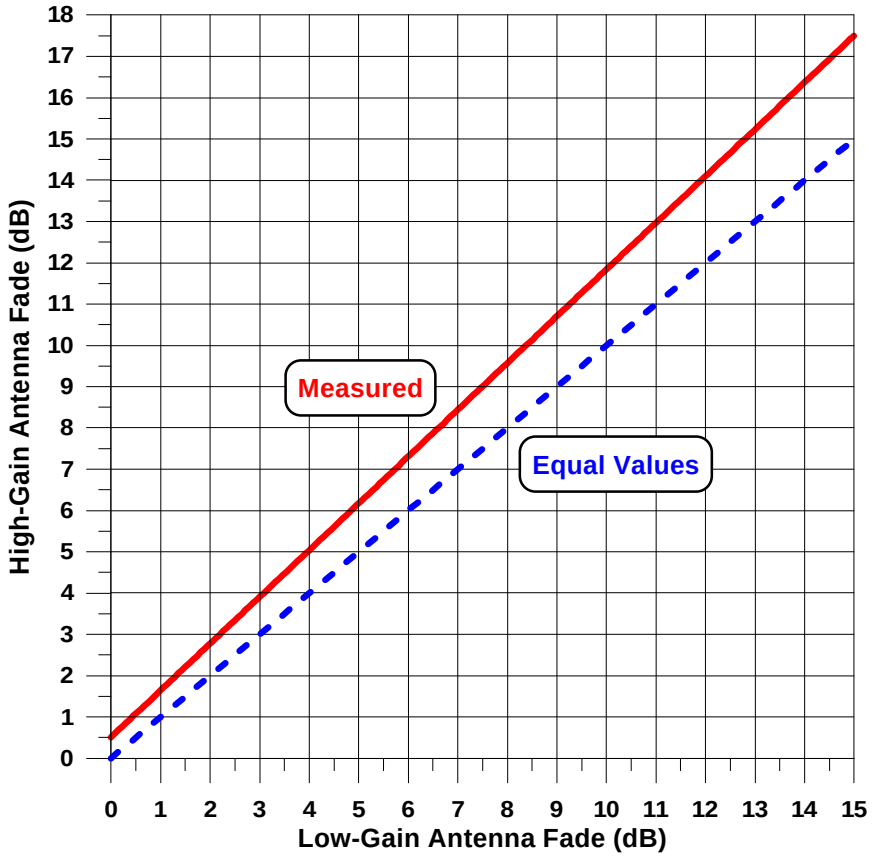

Figure 6-2: Fades measured by high- and low-gain systems at equi-probability levels.

6.4 Fade Reduction Due to Lane Diversity

We examine the extent by which fades are reduced (or increased) when switching lanes for LMSS configurations. Figure 6-3 shows vehicles on the inner and outer lanes, respectively, where the satellite is to the side and the propagation path passes through the tree canopy on the side of the road. We note that the path length through the canopy is greater when the vehicle is closest to the tree line (inner lane). Switching lanes from the inner to the outer lanes should therefore produce a fade reduction. The authors measured this effect at UHF (870 MHz) [Goldhirsh and Vogel, 1987], and L-Band (1.5 GHz) [Goldhirsh and Vogel, 1989]. Repeated measurements were executed employing a helicopter as the transmitter platform, and corresponding cumulative fade distributions were derived for inner and outer lane scenarios at fixed path elevation angles of 30°, 45°, and 60°. To characterize the increase in signal power by switching from the inner to the outer lanes, a quantity known as the "fade reduction, *FR*" was defined. This quantity is obtained is obtained by taking the difference between equi-probability fade values from distributions pertaining to inner and outer lane driving.

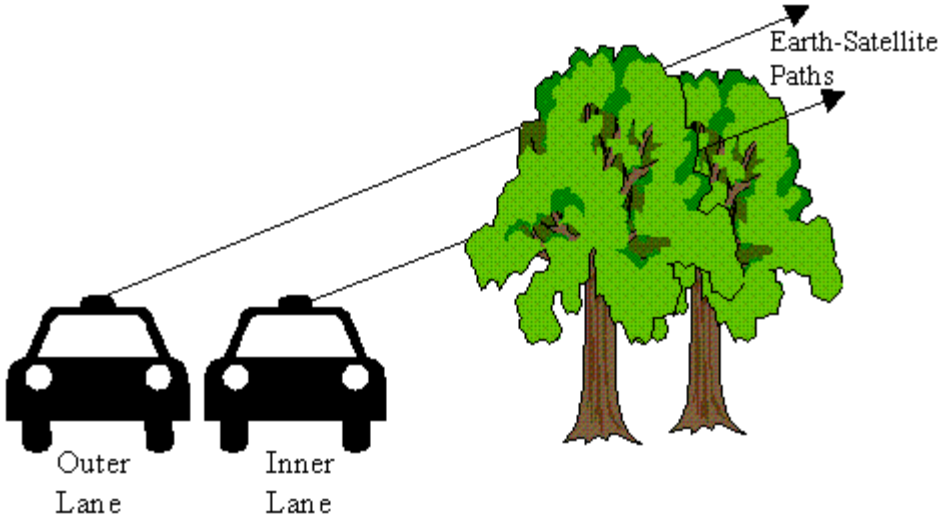

Figure 6-3: Mobile satellite scenario showing larger intersecting path length through tree canopy for inner lane driving relative to the outer lane case.

The fade reductions at UHF and L-Band are plotted in Figure 6-4 and Figure 6-5 respectively, for the indicated elevation angles as a function of the maximum fade as derived for inner lane driving. These curves fit the third order polynomial expressed as

$$FR = a_o + a_1 A + a_2 A^2 + a_3 A^3, \tag{6-4}$$

where *FR* (in dB) represents the fade reduction obtained by switching from the inner to the outer lanes (Figure 6-3) and *A* represents the maximum fade (in dB) derived for the inner lane driving scenario. The coefficients in (6-4) are tabulated in Table 6-2 and Table 6-3 for the UHF and L-Band frequencies, respectively. The "best fit polynomials" agree with the *FR* values derived from the measured distributions to within 0.1 dB RMS.

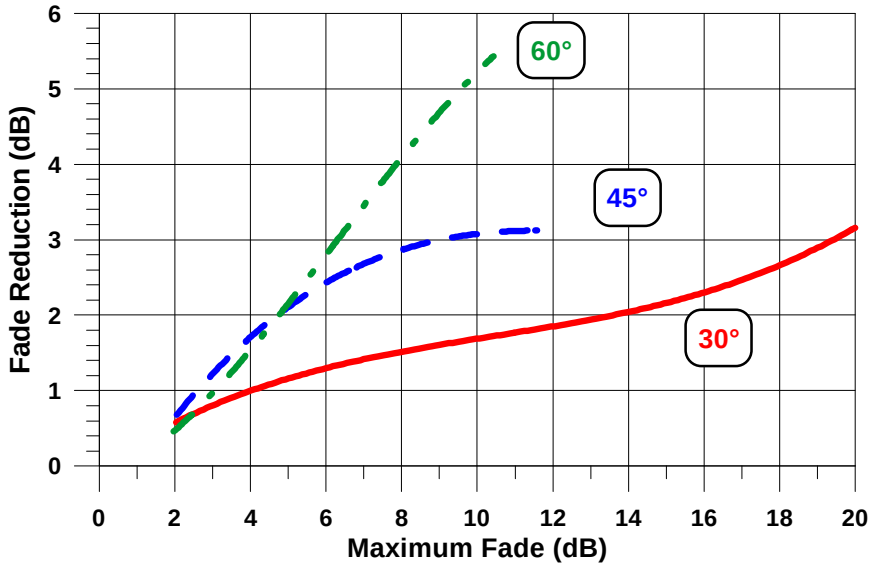

Figure 6-4: Fade reduction due to switching lanes at 870 MHz versus equi-probability attenuation at the indicated path elevation angles.

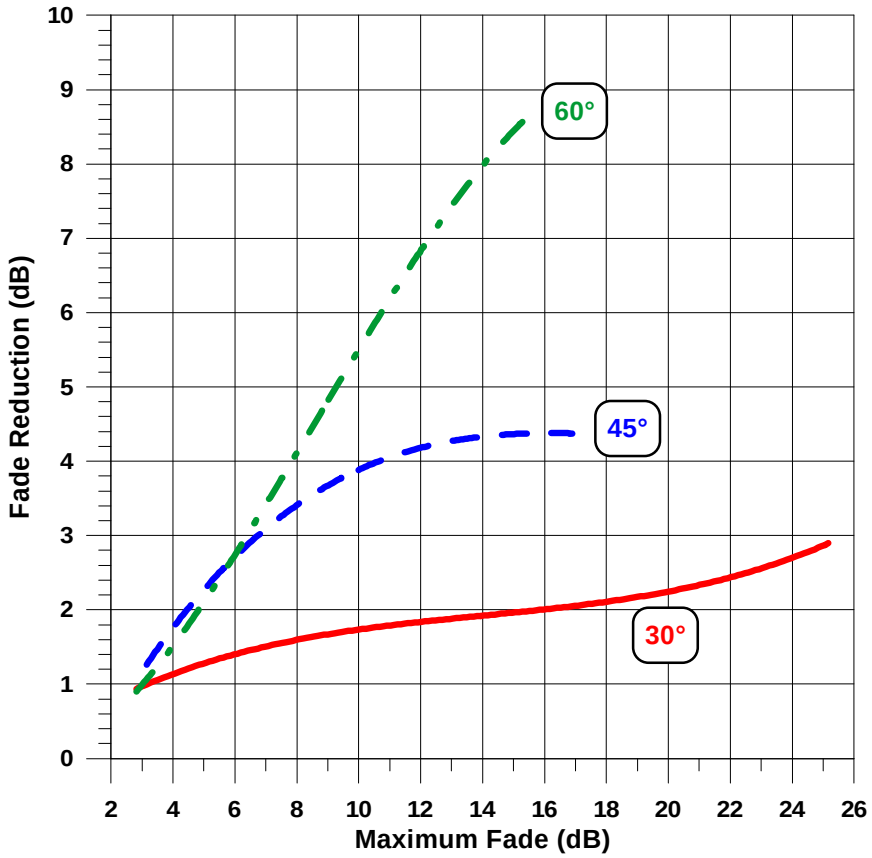

Figure 6-5: Fade reduction due to switching lanes at 1.5 GHz versus equi-probability attenuation (inner lane) at the indicated path elevation angles.

Table 6-2: Coefficients of the fade reduction formulation at f = 870 MHz.

El. Angle (°)	a_0	a_1	a_2	a_3	dB Range
30	-5.020×10^{-3}	0.3354	-2.439×10^{-2}	7.764×10^{-4}	2-20
45	-0.8193	0.8430	-5.758×10^{-2}	1.222×10^{-3}	2-12
60	-0.2305	0.2288	6.773×10^{-2}	-3.608×10^{-3}	2-11

Table 6-3: Coefficients of the fade reduction formulation at f = 1.5 GHz.

El. Angle (°)	a_0	a_1	a_2	a_3	dB Range
30	0.3181	0.26153	-1.573×10^{-2}	3.734×10^{-4}	3-25
45	-1.073	0.8816	-4.651×10^{-2}	7.942×10^{-4}	3-17
60	-8.127×10^{-2}	0.2044	5.781×10^{-2}	-2.235×10^{-3}	3-15

It is interesting to note that larger fade reductions occur at the greater elevation angles. This arises because at the larger angles, a change of lanes may radically alter the earth-satellite path from a shadowed to a non-shadowed state. At the lower elevation angles, this change of state becomes less likely. It is noted from Figure 6-5 that the L-Band fade is reduced from 10 dB to approximately 8 dB, 6 dB, and 4.5 dB at 30°, 45°, and 60°, respectively. At UHF (Figure 6-4), the 10 dB fade is reduced to 8 dB, 7 dB, and 5 dB at 30°, 45°, and 60°, respectively.

6.5 Antenna Separation Diversity Gain

A space diversity simulation has been carried out employing the database corresponding to 400 km of roadside tree shadowing measurements taken during the Australian campaign [Vogel et al., 1992]. Space diversity operation for LMSS configurations may be envisaged by the scenario of two spaced antennas mounted atop a vehicle where each antenna is fed to a separate receiver system. Because the signal levels at the two antennas are expected to be different at any instant of time, rapid switching between the two receiver outputs followed by subsequent processing should enable the larger signal to be accessed. Such a system should therefore require smaller fade margins for the same "signal access distance" than single terminal systems. The "signal access distance" represents that distance over which the received signal level operates within the designed fade margin.

Questions addressed here are: (1) what is the increase in "signal access distance" as a function of antenna spacing along the driving direction, and (2) what is the improvement in terms of reduced fading (enhanced signal) for a given "signal access distance" as a function of antenna spacing? The first question is addressed employing the concept of "diversity improvement factor, *DIF*" and the second "diversity gain, *DG*", both of which are characterized in the following paragraphs.

6.5.1 Joint Probabilities

In Figure 6-6 are shown a family of cumulative fade distribution functions derived from the above mentioned simulation. The curve labeled d = 0 represents the single terminal cumulative fade distribution corresponding to data acquired from over 400 km of driving in Australia. The curves labeled d = 1 to 10 m represent the individual joint probability cumulative fade distribution for the indicated antenna separations (in the direction of vehicle motion). Such a distribution represents the joint probability that two antennas spaced a distance d mutually exceed the abscissa value of fade. Finally, the curve labeled "independent fading" corresponds to the joint distribution of two links with single terminal fading, assuming that the two are independent. We note that the joint probabilities tend to coalesce with increasing antenna separation at about 2/3 the dB-distance to the independent fading case. That is, the fade distributions for 8 m and 10 m separations have insignificant differences.

6.5.2 Diversity Improvement Factor, DIF

The *DIF* is defined as

$$DIF(A,d) = \frac{P_o(A)}{P_d(A)}, \tag{6-5}$$

where $P_0(A)$ represents the single terminal probability distribution at the fade depth A, and $P_d(A)$ represents the joint probability distribution for an antenna spacing d assuming the same attenuation A is exceeded. These probabilities may be obtained from Figure 6-6.

Employing the above results, a least square estimate of *DIF* was derived given by,

$$DIF(A,d) = 1 + A[0.2\ln(d) + 0.23], \tag{6-6}$$

where d is the antenna separation expressed in m and A is the fade depth in dB. In Figure 6-7 are plotted a family of curves of *DIF* as a function of fade depth for antenna separations between 1 and 10 m. We note, for example, that $DIF(8,1) \approx 3$. This implies that when the antennas are separated 1 m, the distance over which the signal is received above noise is three times greater for diversity operation relative to the single terminal case assuming an 8 dB fade margin. At the larger separations for any given fade depth, the rate at which *DIF* increases is shown to diminish rapidly.

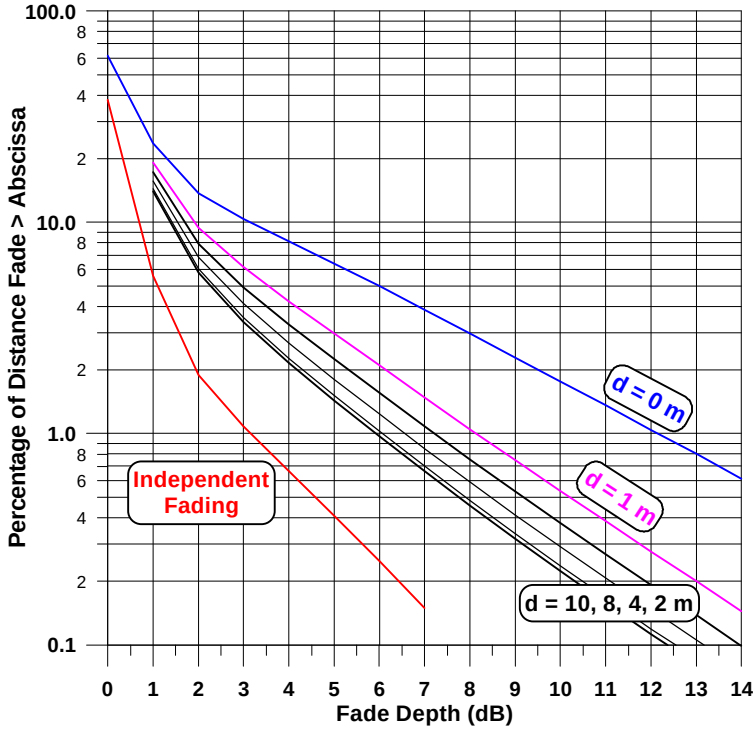

Figure 6-6: Single and joint probability fade distributions for mobile communications operating in a space diversity mode with antennas separated by the distance, *d*.

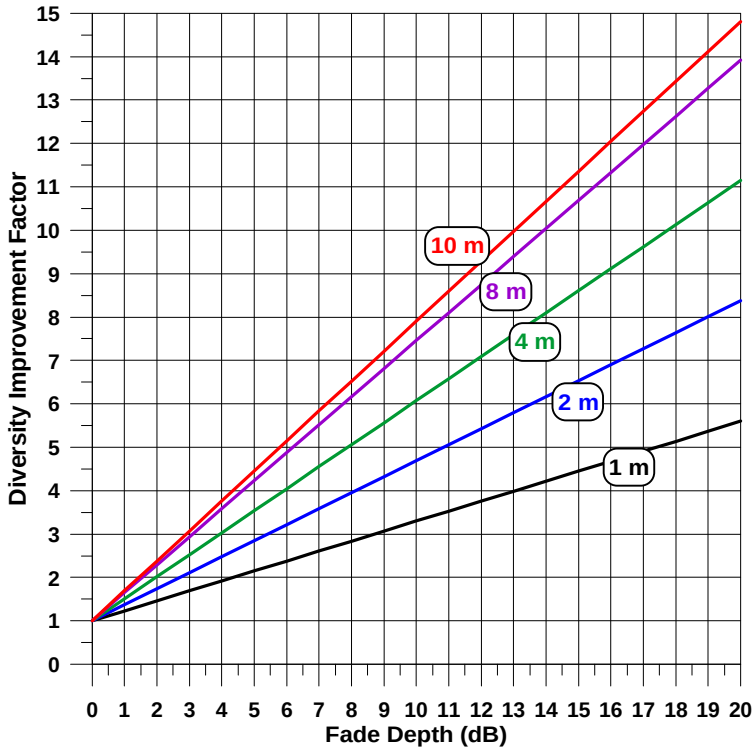

Figure 6-7: Diversity Improvement Factor (*DIF*) as a function of fade depth for a family of antenna separation distances.

6.5.3 Diversity Gain

Diversity gain is a concept defined by Hodge [1978] for an earth-satellite communications system involving two spaced antennas operating in a diversity mode in the presence of precipitation. This concept may also be applied to antennas separated atop a vehicle for LMSS scenarios. The diversity gain is defined as the fade reduction experienced while operating in the diversity mode at a given fade margin. It is equal to the difference in fades between the single terminal and joint probability distributions at a fixed probability level. For example, from Figure 6-6 we note that the diversity gain at a probability of 1% for a 1 m antenna separation is 4 dB. Hence, while the single terminal operation at 1% probability will experience a 12 dB fade, the diversity pair for a 1 m separation will experience only an 8 dB fade.

In Figure 6-8 are plotted the diversity gains versus antenna separations for a family of single terminal fade levels. Each single terminal fade uniquely defines a probability level. For example, an 8 dB fade occurs at a probability level of 3% as is noted from Figure 6-6 (for $d = 0$). Figure 6-8 shows that for any given fade margin, the effect of the antenna separation is dramatic the first 2 meters, whereas at larger spacing, relatively little additional fade reduction ensues.

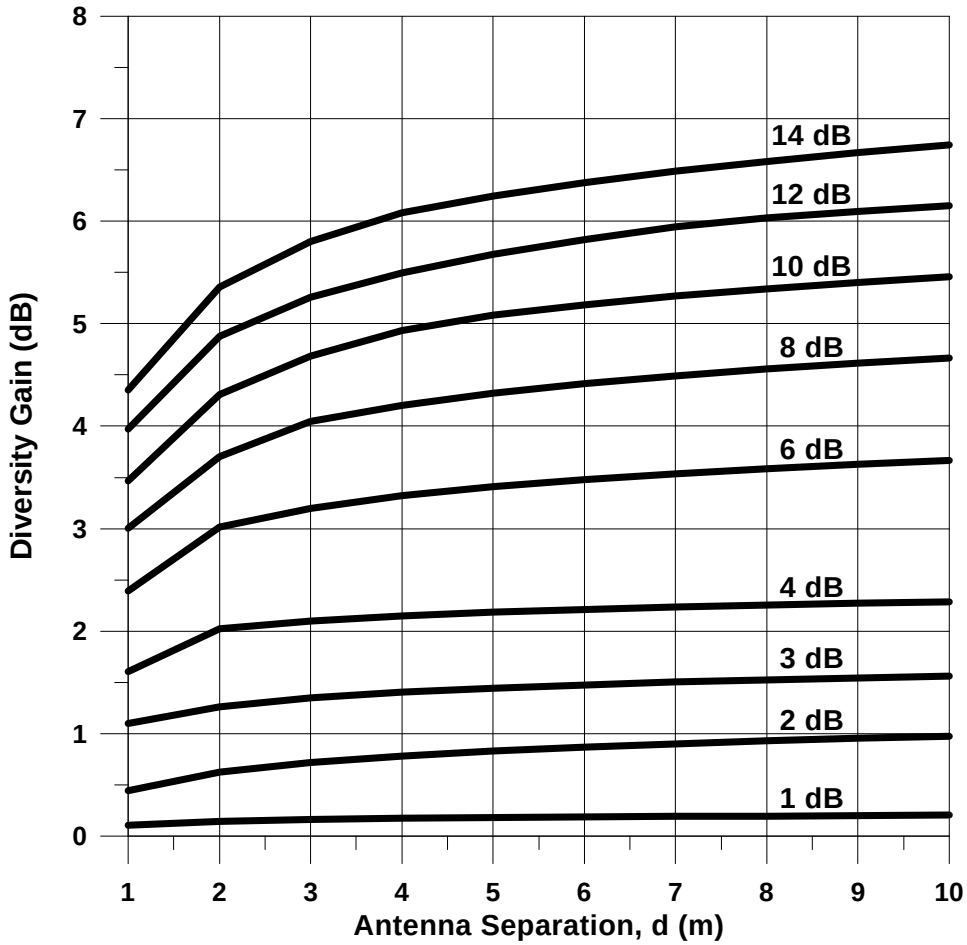

Figure 6-8: Diversity gain versus antenna separation distance for a family of single terminal fade levels.

6.5.4 Space Diversity for Expressway and Trunk Road Driving in Japan

Ryuko and Saruwatari [1991] describe 1.5 GHz cumulative fade distributions derived from road measurements in Japan using the Japanese Engineering Test Satellite V (ETS-V) as the transmitter platform. Using these measurements, joint probability distributions were calculated as a function of antenna spacing on the roof of a mobile vehicle. Measurements were made on roads labeled "expressways" and "trunk roads." The "expressways" in Japan run through mountainous areas and have many overpasses with local roads. The "trunk roads" are not as wide and run through urban areas. The major fading for "expressway" measurements was observed to depend primarily on the density of overpasses. On the other hand, tall buildings primarily cause "trunk road" fades. Table 6-4 summarizes the fading and diversity gain results for the Kan-etsu Expressway and the trunk road which correspond to measurements at an elevation angle of 46° to 47°. The Kan-etsu Expressway has a total length of 150 km between Tokyo and Yuzawa. The trunk road runs alongside the Kan-etsu Expressway, passes through local urban areas, suburbs, farming areas and has many bridge crossings for pedestrians. Pedestrian-bridge crossings, tall buildings, trees, utility poles and road signs caused fading for this road. Since this route runs approximately in the same direction as the satellite path, fading along other trunk roads not so favored by direction is expected to be more severe. The expressway case shows that a diversity gain of 4 dB exists at the 1% probability level. Negligible diversity gain differences exist when the antenna spacing is increased from 5 m to 10 m over the percentage interval shown. The trunk road exhibits similar results at the higher percentages. At the 0.5% fade (13 dB), diversity gains of 5 dB and 8 dB occur at an antenna spacing of 5 m and 10 m, respectively.

Table 6-4: Single terminal fade distribution and diversity gain values for Japan roads, Ryuko and Saruwatari [1991].

Road Type	Single Terminal Diversity		Gain for Given Antenna Separation (dB)	
	Prob (%)	Fade (dB)	d = 5 m	d = 10 m
Expressway	2.0	3	1	1
	1.0	6	4	4
	0.5	14	11	11.5
Trunk Road	2.0	3	1	1
	1.0	6	3	4
	0.5	13	5	8

6.6 Satellite Diversity

6.6.1 Background

Akturan and Vogel [1997] and Vogel [1997] describe a method by which they derive single and joint probability distributions and diversity gains associated with communications employing multiple satellites. The method consists of: (1) video recording hemispherical images of the surrounding environment through a fisheye lens mounted atop a mobile vehicle or photographing still images of the surrounding environment through a fisheye lens held head-high, (2) performing image analysis of sequences of the hemispherical scenes, (3) simulating a constellation of "potentially visible satellite" locations for the particular region of the world and different times of the day, (4) extracting "path-state" information associated with the line-of-sight for each "potentially visible satellite" (e.g., clear, shadowed, or blocked) for different times of the day for each scene, (5) injecting the "path-state" information into an appropriate density distribution model, and (6) computing single and joint cumulative distributions associated with different satellite-look scenarios. Details concerning the density function models for the different path states are described in Chapter 10.

6.6.2 Cumulative Distributions

Figure 6-9 depicts a series of L-Band distributions ($f \approx 1.6$ GHz) for different diversity scenarios to the satellite for urban Japan, assuming a simulated "Globalstar" constellation of 48 satellites [Schindall, 1995]. In deriving the distributions given in Figure 6-9, 236 images were combined with approximately 1000 independent constellation snapshots encompassing a 24 hour period (for each image). Hence, an equivalence of 236,000 sets of path states went into the database, where approximately 50% of the time three satellites were potentially visible. The distribution labeled "Highest Satellite" represents the distribution associated with the satellite having the greatest elevation angle. This distribution was derived under the condition that the mobile antenna transmits to or receives radiation from a different satellite position every time a new satellite achieves the highest elevation angle, independent of azimuth. The highest elevation path may not necessarily have a "clear" path state. That is, depending upon the scene at the time, it may be representative of a "blocked" path state. The distribution labeled "Best Satellite" is also derived from multiple satellites where the antenna is pointed to the satellite giving the smallest fade.

In calculating this distribution, a decision for "best satellite" was made approximately every 20 seconds before "hand-over" was potentially executed. The distribution labeled "2 Best Satellites" represents the joint distribution associated with the two satellites giving jointly the "smallest fades". At any instant of time, different pairs of satellites may fall under the "2 Best Satellite" category. The distributions labeled "3 Best Satellites" and "4 Best Satellites" are analogously defined. The above joint distributions were derived assuming "combining diversity" where the signals received are "added," as opposed to "hand-off" where the satellite with the "highest" signal is processed. It is apparent that each of the above distributions is calculated from many different satellites at variable elevation and azimuth angles. Using the "Highest Satellite" distribution as the

reference, the fade is considerably reduced by switching to the other diversity modes. For example, at the 20% probability, a 17 dB fade for the highest satellite may be compared to 6 dB for the "Best" satellite scenario, giving rise to an 11 dB diversity gain at that probability. We note that the higher diversity combinations (e.g., 2, 3, and 4 Best Satellites) do not significantly contribute to an increased diversity gain at percentages greater than 20%. Figure 6-9 shows that using the "3 Best Satellite" diversity mode, 1% probability gives rise to a 20 dB fade margin for an urban environment. This substantially high fade may preclude voice communications for urban environments at small probabilities even with satellite diversity.

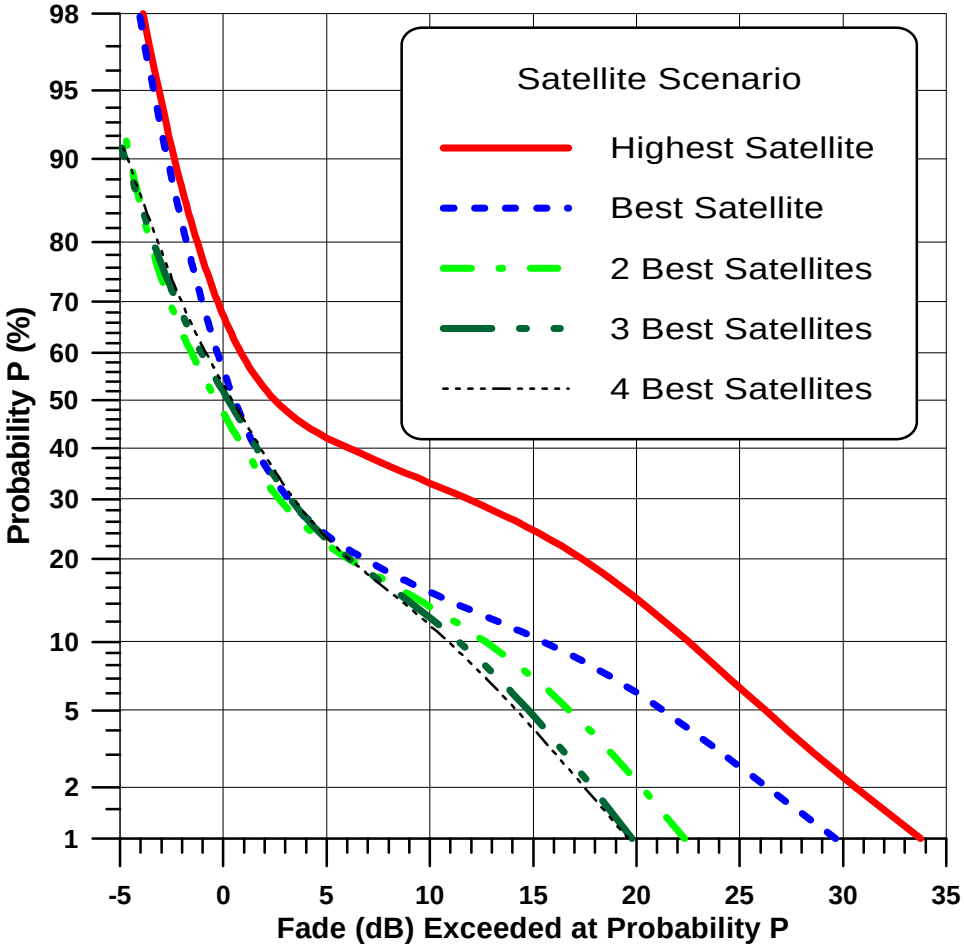

Figure 6-9: Cumulative fade distributions at L Band ($f \approx 1.6$ GHz) for the simulated Globalstar constellation with combining diversity for Tokyo, Japan [Vogel, 1997, Akturan and Vogel, 1997].

6.6.3 Satellite Diversity Gain

Figure 6-10 depicts the diversity gains for the distributions given in Figure 6-9 associated with the "combining diversity" mode. Also shown are the diversity gain results associated with the "hand-off" mode as defined above. For any fixed probability, these two processing modes differ by approximately 1 dB (at most), but also note that any

implementation losses have been neglected. All diversity gains are shown to have a peak at approximately 20% probability.

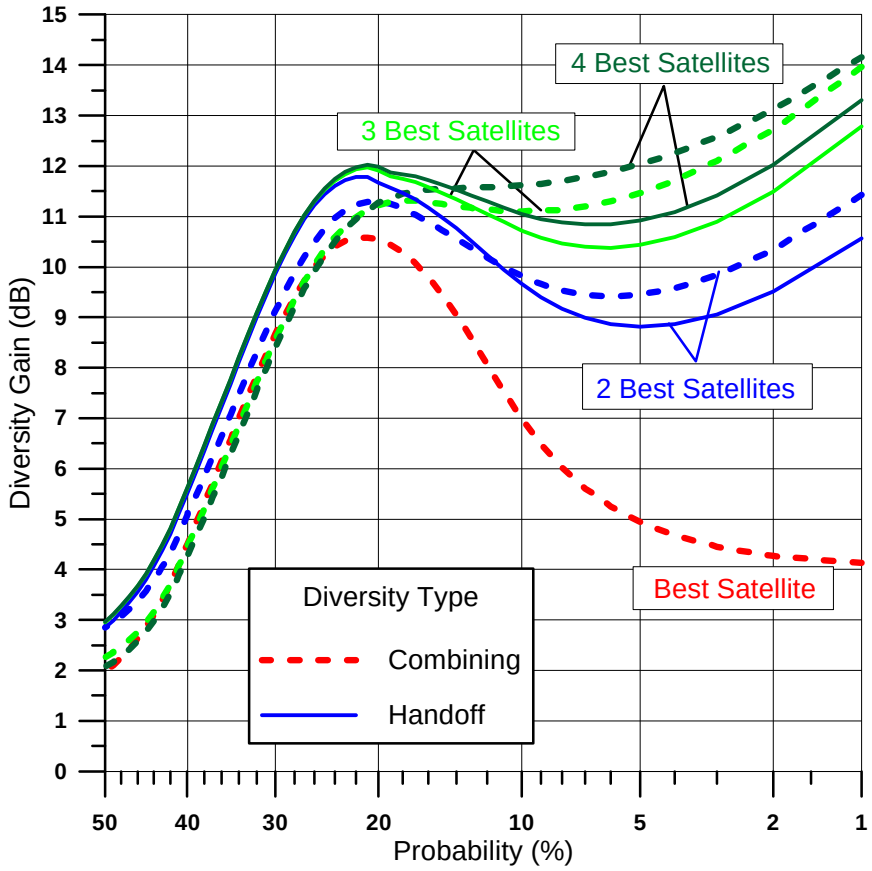

Figure 6-10: Path diversity gains at $f \approx 1.6$ GHz derived from distributions for the simulated Globalstar constellation with combining diversity and handoff for Tokyo, Japan [Vogel, 1997; Akturan and Vogel, 1997].

6.6.4 Satellite Diversity Measurements at S-Band Employing TDRSS

Direct orbital satellite mobile measurements were conducted by Vogel [1997] employing a portable satellite receiver with a prototype personal antenna system using NASA's Tracking and Data Relay Satellite System (TDRSS). During three occasions, NASA made available two TDRSS satellites for diversity measurements at ~2 GHz. The receiver recorded simultaneously the signals from the two satellites located at different azimuth and elevation angles. The mobile earth station (MES) was hand-carried to several typical environments in Austin, Texas during the spring-summer period when the deciduous trees were in full bloom. Figure 6-11 shows single and joint distributions for three path states which are characterized as follows for the specific environments considered: (1) "clear" denotes an open field with unobstructed line-of-sight paths to both satellites, (2) "shadowed" denotes walking in the vicinity of a grove of tall and thin deciduous trees, and (3) "blocked" denotes walking on the grounds of an apartment complex with multiple three-story buildings set at various angles. The azimuths and elevation pairs to the satellites denoted as T7 and T1 were respectively, 248°, 24° and

146°, 49°. Hence, these satellites were separated in azimuth and elevation by 102° and 25°, respectively.

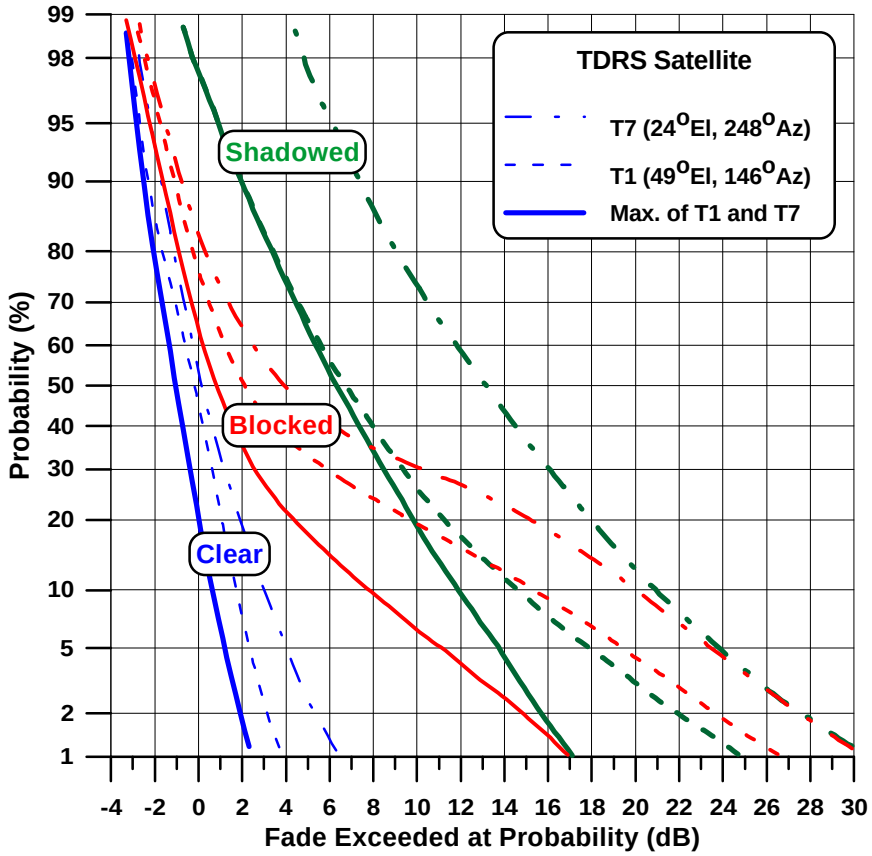

Figure 6-11: Single and joint probabilities for "clear", "shadowed" and "blocked" scenarios derived employing S-Band (f = 2 GHz) TDRSS measurements [Vogel, 1997].

The joint distributions in Figure 6-11 correspond to the "hand-off" mode (maximum of two satellite signals). Fading for the "clear" case at the smaller percentages is a result of ground specular reflections and shadowing by the head. At the 1% level, the joint distribution is shown to reduce the fade margin from a maximum of approximately 6 dB to 2 dB. The "blocked" distributions show smaller fading than the "shadowed" case for the following reasons. The "blocked" environment distribution is in part representative of an "on" or "off" switch where the line of sight is either "not blocked" or "blocked," respectively. In addition, this distribution also includes diffraction and multipath from the buildings, and some shadowing from a few trees. The distribution is therefore strongly dependent upon the density and height of the structures. On the other hand, the shadowed distribution represents an almost continuum of tree fading measured inside a grove; especially relative to the T7 satellite. The diversity gains at 1% from the "shadowed" and "blocked" environments are noted to range from 8 to 13 dB and 8 to 10 dB, respectively. These diversity gains have similar magnitudes to those calculated employing the optical measurements described in the previous section.

6.7 Conclusions and Recommendations

The following salient conclusions and recommendations are based on the results of this chapter.

1. Simultaneous employment of co- and cross-polarized transmissions in a "frequency re-use" system should not be used except to potentially help isolate different CDMA systems because of the potential for poor isolation caused by multipath scattering into the cross-polarized channel (Figure 6-1).
2. Where ground multipath effects do not arise, small equi-probability fade differences of 1 to 2 dB may occur (at L-Band) for mobile antennas having different antenna gains (Figure 6-2). At low elevation angles where ground multipath effects may arise, higher gain antenna has been found to substantially reduce fading by as much as 10 dB at 20 GHz.
3. Changing lanes may substantially reduce the equi-probability fading because of the shortening of the path length through roadside tree canopies (Figure 6-3). At a 10 dB fade at UHF and L-Band, lane changing has been found to reduce the equi-probability fade for 60° elevation by approximately 5 dB (Figure 6-4 and Figure 6-5). Equation (6-4) gives a model describing the reduced fading at equi-probability levels, where the coefficients are summarized in Table 6-2 and Table 6-3.
4. For a 5 m separation between antennas and single antenna fades of 3 dB and 6 dB, diversity gains at L-Band (based on simulations using measurements made in Australia) are approximately 1.5 dB and 3.5 dB (Figure 6-8). These results are within 0.5 dB of those derived from measurements made in Japan (Table 6-4).
5. Satellite diversity measurements at L-Band for urban areas gave rise to diversity gains as high as 14 dB for percentages as low as 1% (Figure 6-10). Nevertheless, even applying diversity gain methods, fade margin levels have been found to exceed 17 to 20 dB at the 1% probability (Figure 6-9 and Figure 6-11). Such high fade margins for urban areas may preclude direct earth-satellite voice communications that require near instantaneous two-way responses.

6.8 References

Akturan, R. and W. J. Vogel [1997], "Path Diversity for LEO Satellite-PCS in the Urban Environment," *IEEE Transactions on Antennas and Propagation*," Vol. 45, No. 7, July, pp. 1107-1116.

Goldhirsh, J. and W. J. Vogel [1987], "Roadside Tree Attenuation Measurements at UHF for Land-Mobile Satellite Systems," *IEEE Transactions on Antennas and Propagation*, Vol. 35, No. 5, May, pp. 589-596.

Goldhirsh, J. and W. J. Vogel [1989], "Mobile Satellite System Fade Statistics for Shadowing and Multipath from Roadside Trees at UHF and L-Band," *IEEE Trans. Antennas Propagation*, Vol. AP-37, No. 4, April, pp. 489-498.

Hodge, D. B. [1978], "Path Diversity for Earth-Space Communication Links," *Radio Science*, Vol. 13, No. 3, pp. 481-487.

Mayer, C. E. [1996], "Multipathing Effects on a Low Elevation Angle Mobile Experiment at K_A-Band," USNC/URSI Radio Science Meeting, July 21-26, p. 232.

Ryuko, H. and T. Saruwatari [1991], "Propagation Characteristics for Land Mobile Satellite Systems in 1.5 GHz Band," *Journal of the Communications Research Laboratory*, Vol. 38, No. 2, July, pp. 295-302.

Schindall, J. [1995], "Concept and Implementation of the Globalstar Mobile Satellite System," *Proceedings of the Fourth International Mobile Satellite Conference*, Ottawa, Canada, June 6-8, pp. A-11 to A-22.

Vogel, W. J. [1997], "Satellite Diversity for Personal Satellite Communications - Modeling and Measurements," *Proceedings of the Tenth International Conference on Antennas and Propagation*," Publication #436, Edinburgh, UK, 14-17 April, pp. 269-272.

Vogel, W.J., J. Goldhirsh, and Y. Hase [1992], "Land-Mobile-Satellite Fade Measurements in Australia," *AIAA Journal of Spacecraft and Rockets*, Vol. 29, No. 1, Jan-Feb, pp. 123-128.

Chapter 7

Investigations from Different Countries

Table of Contents

Table of Figures

Table of Tables

Chapter 7
Investigations from Different Countries

7.1 Background

The results described here provide a compendium of measured cumulative fade distributions for LMSS geometries pertaining to significant experiments in various countries. We emphasize distributions associated with rural and suburban regions as opposed to measurements in urban environments. In comparing the results of the different investigations, the reader should be cognizant of the fact that the various experiments were conducted at a variety of elevation angles and bearings to the source. The diverse geographic regions (e.g., wooded, forest, rural, mountainous, highways) also have associated with them dissimilar conditions of foliage density along the propagation path, and variable distances between vehicle and foliage line. Many of the distributions presented here have been extracted from their publication plots and have been re-plotted consistent with the scales considered in this text; namely; the fade (in dB) along the abscissa and the percentage of distance exceeded (or percentage probability) along the ordinate. In the re-plotting of curves, accuracy to within ± 0.5 dB has been maintained. Table 7-1 summarizes the pertinent mobile satellite measurement investigations. Also given in these tables are the nominal fade values at the 1% and 10% levels (to the nearest 0.5 dB), the referenced figure numbers in this chapter, the type of environment, and the corresponding publication reference. It is apparent from the wide variance of fades in these tables (at any given frequency), that elevation angle and environment play important roles in the determination of LMSS attenuation. Table 7-2 (at the end of this chapter) summarizes the results of Table 7-1 by combining environments for given elevation angle and frequency intervals.

7.2 Measurements in Australia

Bundrock and Harvey [1989] reported on cumulative fade distributions obtained on typical double-lane roads in Melbourne, Australia. Messmate (stringy-bark) Eucalyptus trees approximately 15 m high lined the road and measurements were made over sections

of the road corresponding to tree densities of 35% and 85%. Systematic measurements were made at varying elevation angles at simultaneous frequencies of 897 MHz, 1550 MHz, and 2660 MHz employing a helicopter as the transmitter platform and a receiver system in a mobile van. Figure 7-1 represents a set of cumulative fade distributions for the 85% tree density case at a frequency of 1550 MHz for elevation angles of 30°, 45°, and 60°. Figure 7-2 shows the distributions for the 85% tree density case at the three frequencies considered for the 45° elevation.

Vogel et al. [1992] also measured cumulative fade distributions in Australia employing the ETS-V and INMARSAT-Pacific geostationary satellites as transmitter platforms, where the nominal elevation angles were 51° and 40°, respectively (Figure 7-3). The road types examined were tree-lined with tree populations exceeding 55%.

Table 7-1: Listing of measurement campaigns from different countries.

Country	f (GHz)	El (°)	Fade (dB)		Fig.	Environment	Reference
			P = 1%	P = 10%			
Australia	1.55	30	17.5	11.5	7-1	Tree-lined road. (Tree Density = 85%)	Bundrock, 1989
		45	14	9.5			
		60	12	7.5			
Australia	0.893	45	11	7.5	7-2	Tree-lined road. (Tree Density = 85%)	Bundrock, 1989
	1.55		14	9.5			
	2.66		17.5	11.5			
Australia	1.55	40	15	6	7-3	Tree-lined road. (Tree Density >55%)	Vogel et al., 1992
		51	12	3			
Belgium	1.5	26	20	7.5	7-4	Tree-lined road (bare trees)	Jongejans et al., 1986
Canada	0.87	5	> 30	21.5	7-5	Woodlands, (Tree Density = 35%)	Butterworth, 1984b
		15	18	7.5			
		20	13	5.5			
Canada	1.5	19	21	10.5	7-6	Suburban	Butterworth, 1984a
			20	8		Rural/Forested	
			11	3.5		Rural/Farmland	
England	1.6	40	9	5.5	7-7	Tree-lined road	Renduchintala et al. 1990, Smith et al., 1990
		60	7	4			
England	1.6	40	13	7	7-8	Tree-lined roads	Smith et al., 1993
		60	9	4			
		80	6	2			
England	2.6	40	14	5.5	7-9	Tree-lined roads	Smith et al., 1993
		60	12	5			
		80	10.5	4.5			

Country	f (GHz)	El (°)	Fade (dB)		Fig.	Environment	Reference
			P = 1%	P = 10%			
England	1.3	60	18.5	7.5	7-10	Wooded	Butt et al., 1992
	2.5		22.5	9.0			
	10.4		28	18.5			
England	1.3	80	8	3	7-11	Wooded	Butt et al., 1992
	10.4		24	10.5			
England	1.3	60	16.5	5	7-12	Suburban	Butt et al., 1992
	2.5		18.5	6			
	10.4		27.5	13			
England	1.3	80	12	2.5	7-13	Suburban	Butt et al., 1992
	2.5		16	6			
	10.4		26	13			
France	18.7	30-35	28	17	7-14	Tree-lined (45° and 90° azimuth orientations)	Murr et al., 1995
Germany	18.7	30-35	>35	28.5-33	7-15	Tree-lined (45° and 90° azimuth orientations)	Murr et al, 1995
Japan	1.5	40-50	26-32	1.5-20	7-16	Expressway driving (mixed environment)	Obara et al., 1993
Japan	1.5	46	2.5-7	1-2	7-17	Expressway driving	Ryuko and Saruwatari, 1991
United States	0.87	30	14-20	6-10	7-18	Tree-lined roads (tree density > 55%)	Goldhirsh and Vogel, 1989
			15	7.5		EERS Model	
United States	0.87	45	7-15	2-5	7-19	Tree-lined roads (tree density > 55%)	Goldhirsh and Vogel, 1989
			10	4		EERS Model	
United States	0.87	60	3-12	2-5	7-20	Tree-lined roads (tree density > 55%)	Goldhirsh and Vogel, 1989
			5.5	2		EERS Model	
United States	1.5	21	>16	12 to >16	7-21	Tree-lined roads (tree density > 55%)	Goldhirsh and Vogel, 1995
			25.5	15		EERS Model	
United States	1.5	30	18-25	8-13	7-22	Tree-lined road (tree density >55%)	Goldhirsh and Vogel, 1995
			21.5	11		EERS Model	
United States	1.5	45	10-20	3-10	7-23	Tree-lined roads (tree density > 55%)	Goldhirsh and Vogel, 1995
			15	6		EERS Model	

Country	f (GHz)	El (°)	Fade (dB)		Fig.	Environment	Reference
			P = 1%	P = 10%			
United States	1.5	60	5-15	2-7	7-24	Tree-lined roads (tree density > 55%)	Goldhirsh and Vogel, 1995
			8	3		EERS-Model	
United States	2.05	21	>30	14	7-26	Mixed environment	Vaisnys and Vogel, 1995
United States	2.09	18	>15	>15	7-27	Tree-lined	Jenkins et al., 1995
		41	12	7			
United States	20	46	25	2	7-28	Suburban	Rice et al., 1996 Gargione et al., 1995
			8-27	1-8		Tree-Shadowed	
			>30	29 to >30		Mixed	
United States	20	38	40	24	7-29	Tree-lined (trees with foliage)	Goldhirsh and Vogel, 1995
			21	9		Tree-lined (trees without foliage)	
United States	20	54.5	28	15	7-30	Tree-lined (evergreen)	Goldhirsh and Vogel, 1995
United States	20	8	>25	>25	7-31	Tree-lined (Alaska)	Goldhirsh and Vogel, 1995

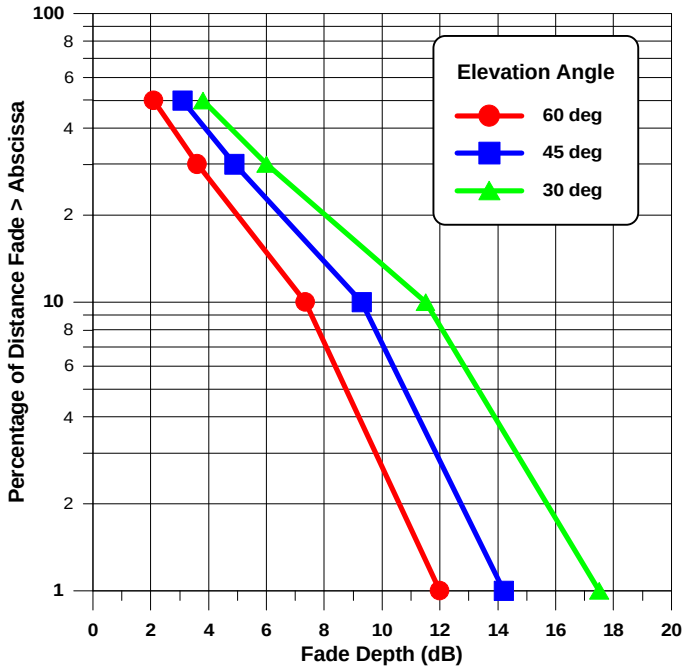

Figure 7-1: Cumulative fade distributions at various elevation angles obtained by Bundrock and Harvey [1989] for Melbourne, Australia at 1.55 GHz for a tree lined road having an 85% tree density.

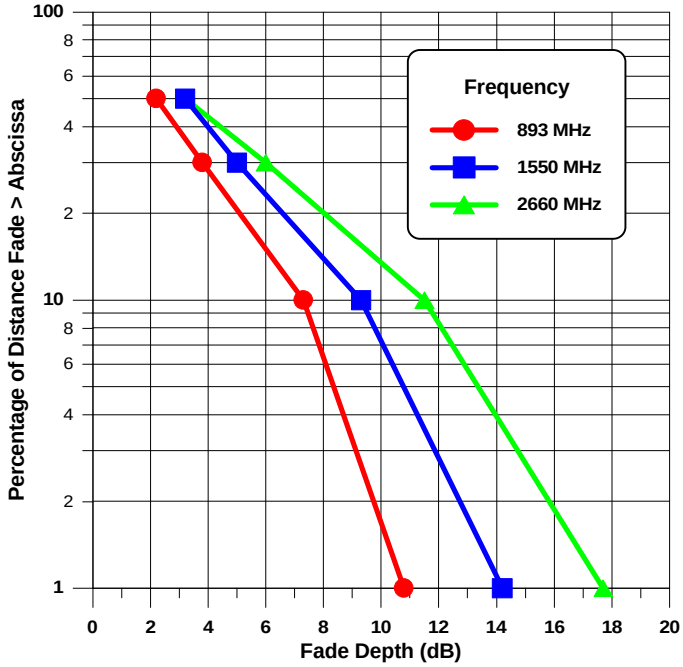

Figure 7-2: Cumulative fade distributions at UHF, L-Band, and S-Band obtained by Bundrock and Harvey [1989] for Melbourne, Australia at an elevation angle of 45° for a tree-lined road with 85% tree density.

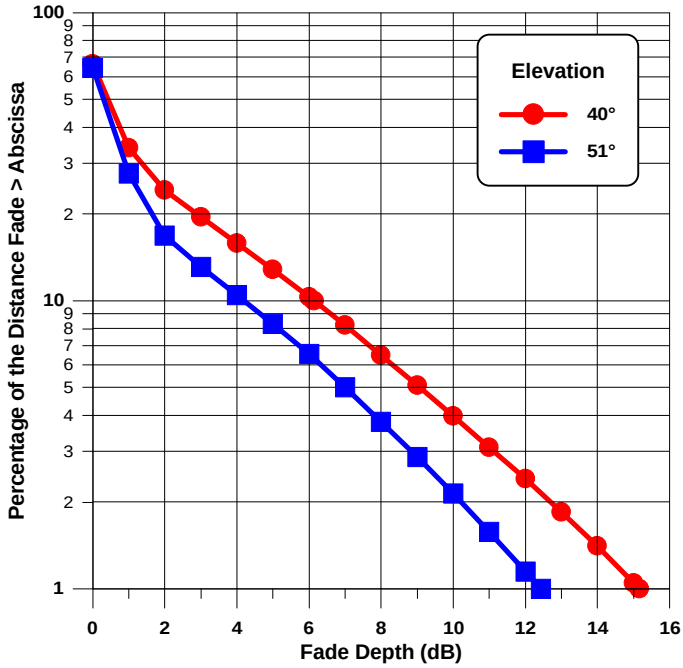

Figure 7-3: Measurements in Australia at 40° and 51° elevation at 1.55 GHz for tree-line roads [Vogel et al., 1992].

7.3 Belgium (PROSAT Experiment)

The PROSAT experiment was instituted by the European Space Agency (ESA) with the objective to accelerate the development of LMSS in Europe [Jongejans et al., 1986]. This experiment involved seven ESA member states; namely Belgium, the Federal Republic of Germany, France, Italy, Spain, the United Kingdom and Norway. The MARECS B-2 satellite was used as the transmitter platform where transmissions were executed at L-Band (1.5 GHz).

In Figure 7-4 is shown the cumulative distribution at 26° elevation for Belgium obtained in January 1984 in a rural area. The area (Ardennes) was hilly and the roadside was lined with bare trees [Jongejans et al., 1986].

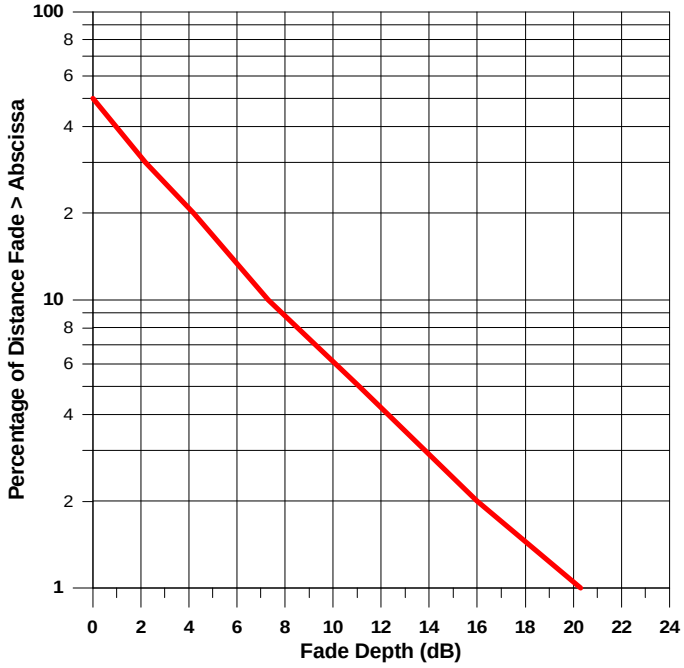

Figure 7-4: Fade distribution at 1.5 GHz derived from measurements at 26° elevation in Belgium in a hilly region with bare trees [Jongejans et al., 1986].

7.4 Measurements in Canada

Canadians were pioneers in the implementation of fade measurements for mobile-satellite system geometries [Butterworth and Matt, 1983; Huck et al., 1983; Butterworth 1984a, 1984b]. Butterworth [1984a, 1984b] describes roadside fade statistics measured at UHF (870 MHz) and L-Band (1.5 GHz) in Ottawa, Ontario, Canada. Various transmitter platforms were employed. These included a tower, a tethered balloon, a helicopter, and the MARECS A satellite. Figure 7-5 shows UHF fade distributions at various elevation angles as derived from helicopter measurements in June 1983 for a rural region in which woodlands constituted 35% of the land area.

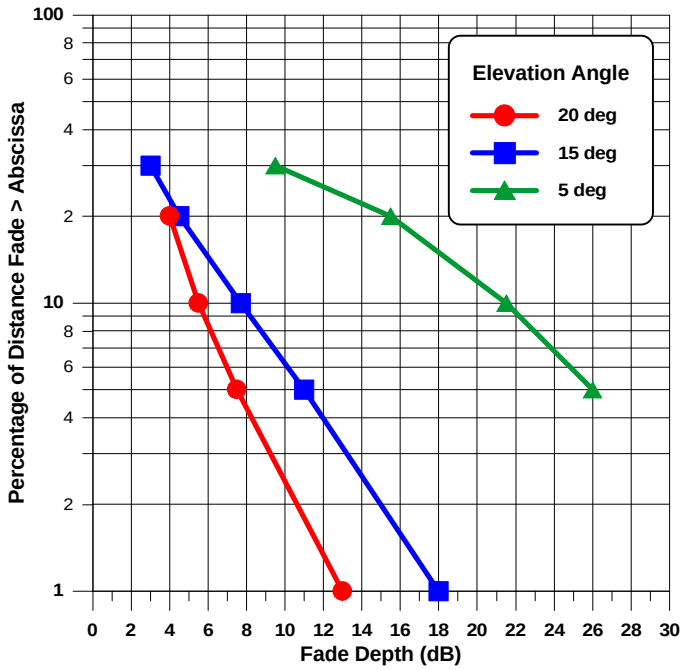

Figure 7-5: Cumulative fade distribution at UHF (870 MHz) in Ottawa, Ontario, Canada derived from helicopter measurements in a rural region (35% woodland) [Butterworth, 1984b].

In Figure 7-6 are shown three distributions obtained from the MARECS A satellite transmissions at 1.5 GHz at a 19° elevation for suburban, and rural/farmland. Butterworth characterized these regions as follows:

- **Suburban:** "an older suburban residential area consisting mainly of one and two-story single-family dwellings."
- **Rural/Forested:** "consisting of hilly terrain covered with immature timber of mixed species, interspersed with occasional cleared areas. The route followed a series of paved provincial highways with one lane for each traffic direction and with gravel shoulders."
- **Rural/Farmland:** "area consisting almost entirely of flat, open fields. About 5% of this route ran through occasional wooded areas. The roads were paved county roads with one lane for each traffic direction and with gravel shoulders."

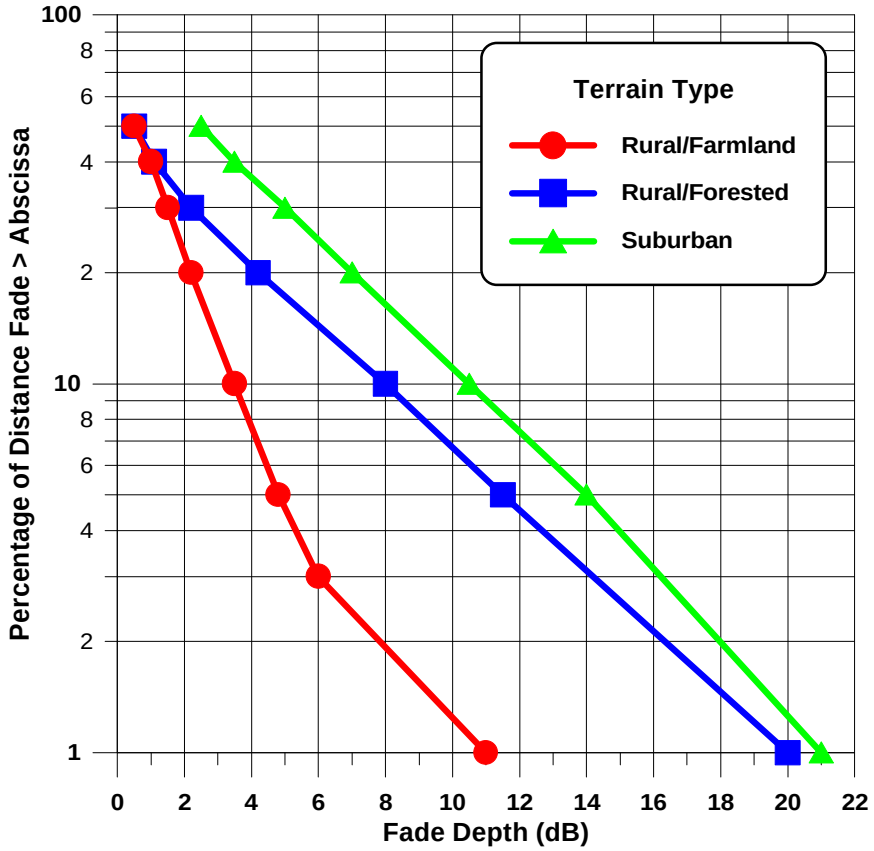

Figure 7-6: Cumulative fade distribution at L-Band (1.5 GHz) in Ottawa, Ontario, Canada obtained from MARECS A satellite measurements in indicated regions at 19° elevation [Butterworth, 1984a].

7.5 Measurements in England

In Figure 7-7 are cumulative fade distributions obtained in England in typical, rural, tree shadowed environments where all the trees had full leaf cover [Renduchintala et al., 1990; Smith et al., 1990]. These results were derived from L-Band transmissions from an antenna mounted on an aircraft and received by a mobile van. Figure 7-7 depicts the distributions for a sequence of runs executed at the elevation angles of 40°, 60° and 80°. As in the case of other investigations, the results demonstrate the strong dependence of fades on elevation angle.

Smith et al. [1993] report on L- (1.6 GHz) and S-Band (2.6 GHz) measurements of fading for mobile scenarios at the higher elevation angles also using an aircraft. Measurements were made for urban, suburban, and tree shadowed environments. Shown in Figure 7-8 and Figure 7-9 are cumulative distributions for tree shadowed environments at L-Band and S-Band, respectively. This environment was defined as follows:

- **Tree Shadowed:** "Mature deciduous trees of varying density and distance from the road. Statistics are for a typical mix of composite cover."

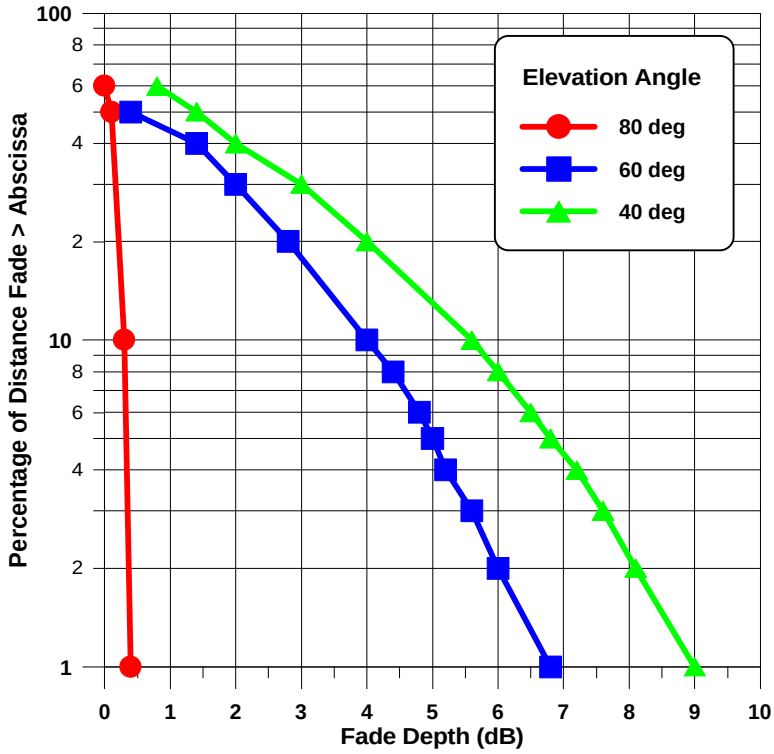

Figure 7-7: Fade distributions (L-Band) for tree shadowed environments in England for different elevation angles [Renduchintala et al., 1990; Smith et al., 1990].

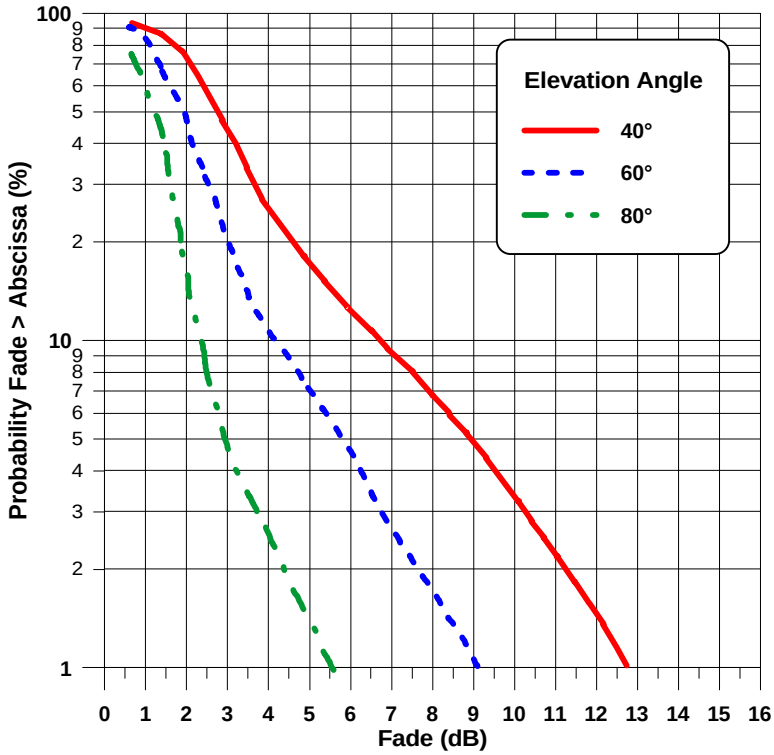

Figure 7-8: Distributions from L-Band measurements (1.6 GHz) at various elevation angles for tree-lined road [Smith et. al, 1993].

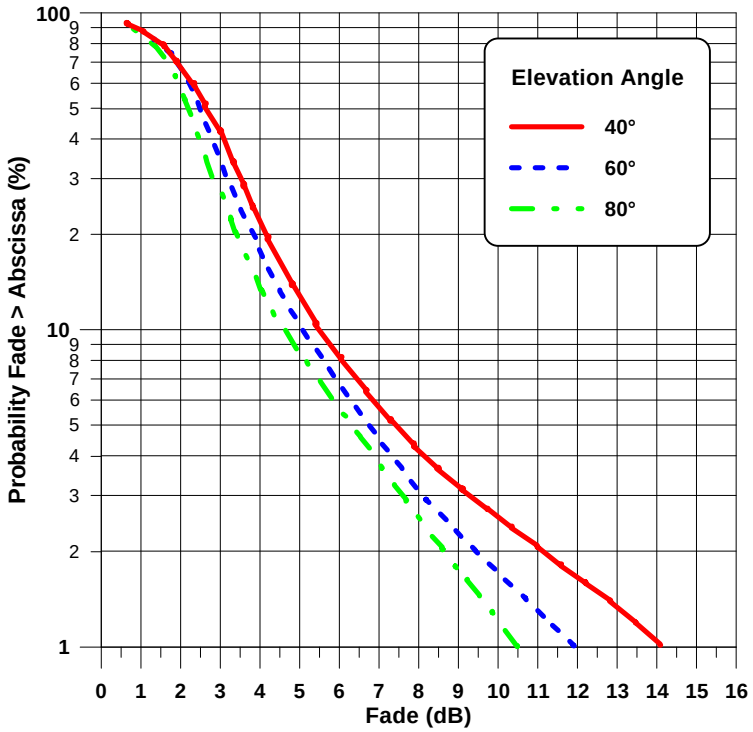

Figure 7-9: Distributions from S-Band measurements (2.6 GHz) at various elevation angles for tree-lined road [Smith et. al, 1993].

Figure 7-10 shows distributions at 60° at L-Band (1.3 GHz), S-Band (2.5 GHz) and K_u-Band (10.4 GHz) for a wooded environment in England as measured using a transmitter on a helicopter platform [Butt et al., 1992]. The measurements were executed along a 7 km "heavily wooded" stretch of a B-type road (less than 4 m wide). Shown in Figure 7-11 are 80° distributions at L-Band and K_u-Band. By way of contrast, Figure 7-12 and Figure 7-13 show similar sets of curves for a "suburban environment."

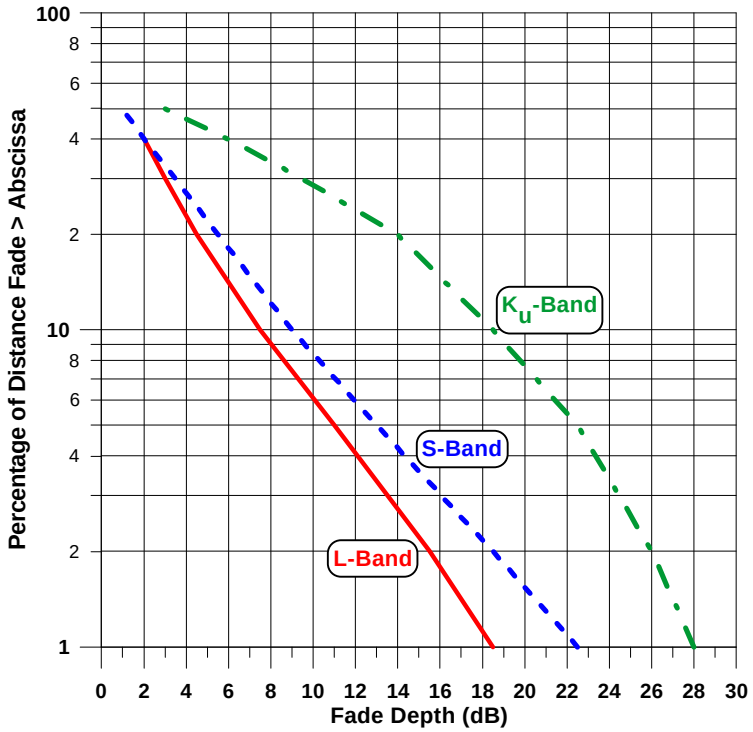

Figure 7-10: Fade distributions at 60° for wooded environment in England at L-Band (1.3 GHz), S-Band (2.5 GHz), and K_u-Band (10.4 GHz) [Butt et al., 1992].

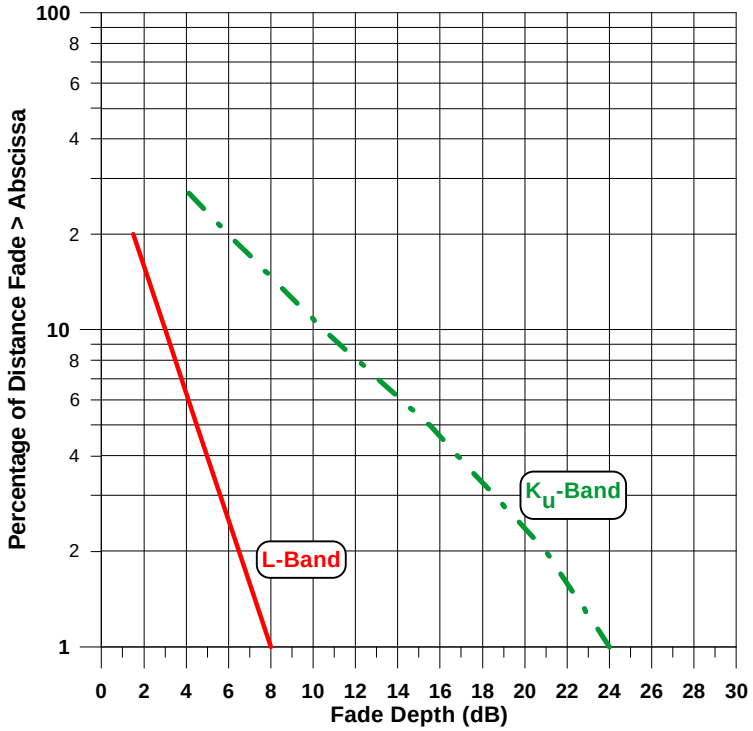

Figure 7-11: Fade distributions at 80° for wooded environment in England at L-Band (1.3 GHz) and K_u-Band (10.4 GHz) [Butt et al., 1992].

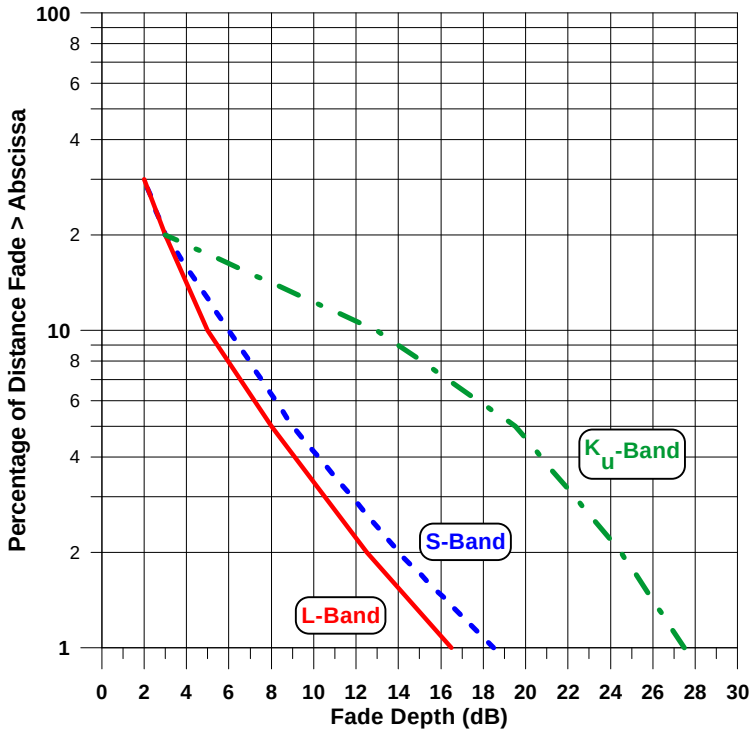

Figure 7-12: Fade distributions at 60° for suburban environment in England at L-Band (1.3 GHz), S-Band (2.5 GHz), and K_u-Band (10.4 GHz) [Butt et al., 1992].

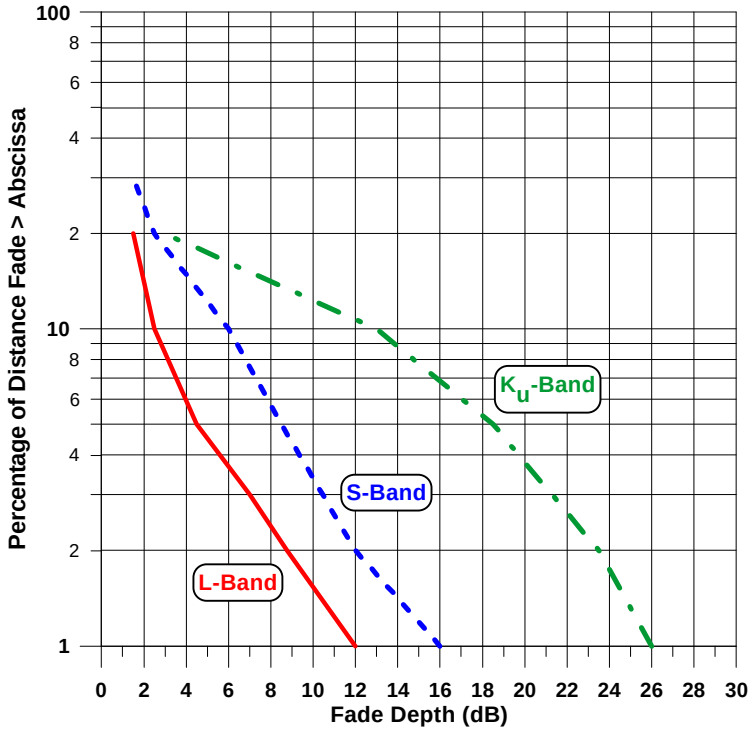

Figure 7-13: Fade distributions at 80° for suburban environment in England at L-Band (1.3 GHz) and S-Band (2.5 GHz), and K_u-Band (10.4 GHz) [Butt et al., 1992].

7.6 France and Germany: European K-Band Campaign

The European Space Agency commissioned a mobile measurement campaign at 18.7 GHz in various types of environments in the Netherlands, France, Germany, and Austria employing the Italsat F1 satellite as a radiating source platform [Murr et al., 1995; Joanneum Research, 1995; Paraboni and Giannone, 1991]. The elevation angles were 30° to 35° and the roads selected were such that the azimuth directions of driving relative to the satellite were 0°, 45°, and 90°. A tracking receiver antenna (2.4° beamwidth) mounted on the roof of a van was utilized in the measurement campaign. Figure 7-14 shows three distributions at azimuths of 0°, 45°, and 90° where the distributions at 45° and 90° coincide. It is interesting to note that although 0° azimuth represents the condition that the satellite was either in front of or in back of the moving vehicle, substantial fades may nevertheless result due to the possibility of overhanging foliage or bends in the road. Figure 7-15 shows distributions for three tree-shadowed cases corresponding to driving azimuths of 0°, 45°, and 90° in Germany. The corresponding measurements were executed in dense needle-tree forests. It is interesting to note that the 45° degree satellite orientation gave larger fades than the 90° case. This may be explained by the fact that because of gaps between the trees greater visibility to the satellite exists at 90° relative to the 45° case. At this latter azimuth, the canopies obstructed gaps between the trees. This was not always the case as is exemplified by the distributions shown in Figure 7-14 obtained for France in a deciduous tree forest. For this case, the 45° and 90° distributions effectively coincide.

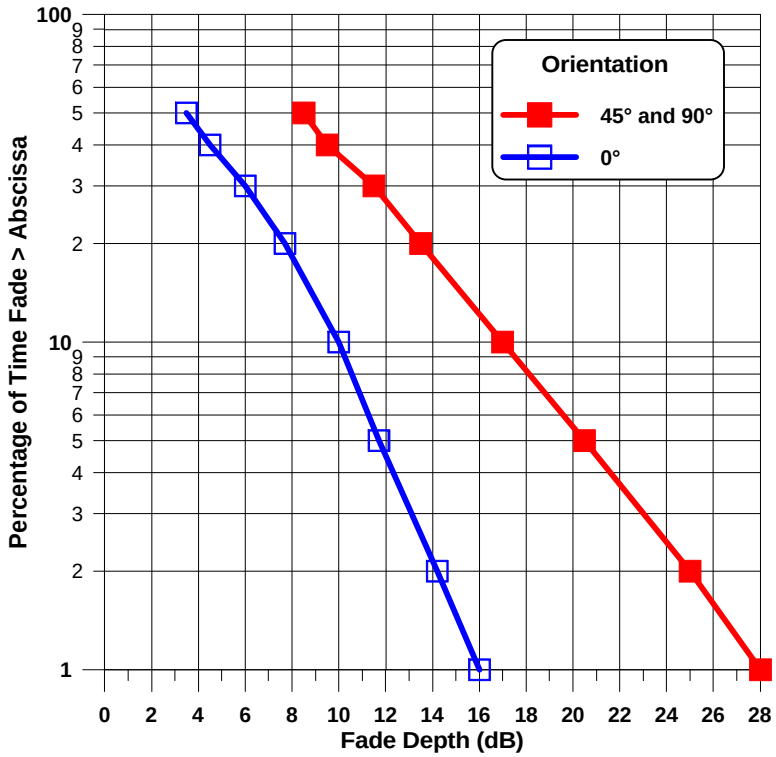

Figure 7-14: Cumulative fade distributions from measurements made in France at 18.7 GHz in a tree-shadowed environment at elevation 30° … 35°. The indicated angles are the driving direction azimuths relative to the satellite [Murr et al., 1995].

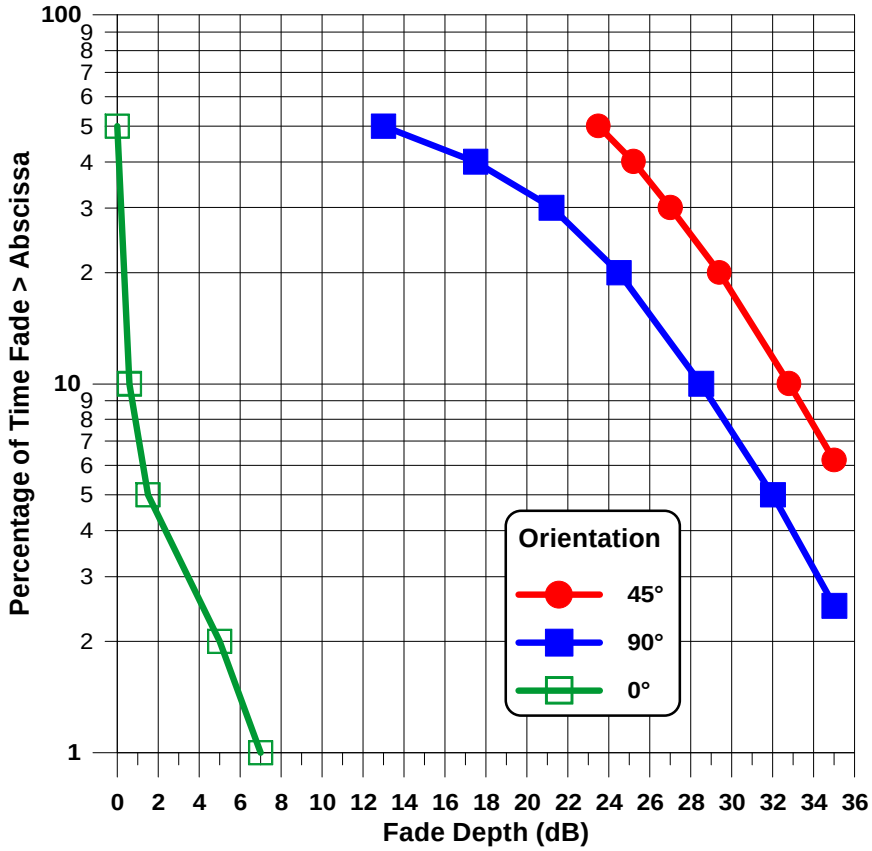

Figure 7-15: Cumulative fade distributions from measurements made in Germany at 18.7 GHz in a tree-shadowed environment at elevation 30° … 35°. The indicated angles are the driving direction azimuths relative to the satellite [Murr et al., 1995].

7.7 Measurements in Japan

Obara et al. [1993] describe 1.5 GHz land mobile satellite measurements in Japan using the Japanese ETS-V satellite as the transmitter platform. Employing a tracking antenna system atop a van, a total distance of approximately 4000 km of primarily expressway-type environments was sampled, where the elevation angle ranged between 40° and 50°. The shadowing environments were comprised of overpasses, tunnels, trees, buildings and guideposts along the highways. These investigators derived 10 distributions corresponding to different road measurements. Eliminating the upper and lower fade extremes of their distributions, Figure 7-16 shows the resulting extreme distributions (of the remaining eight). The distribution having the smaller fades shows a manifestation of short period of extreme fades such as may be caused by signal blockage due to tunnels.

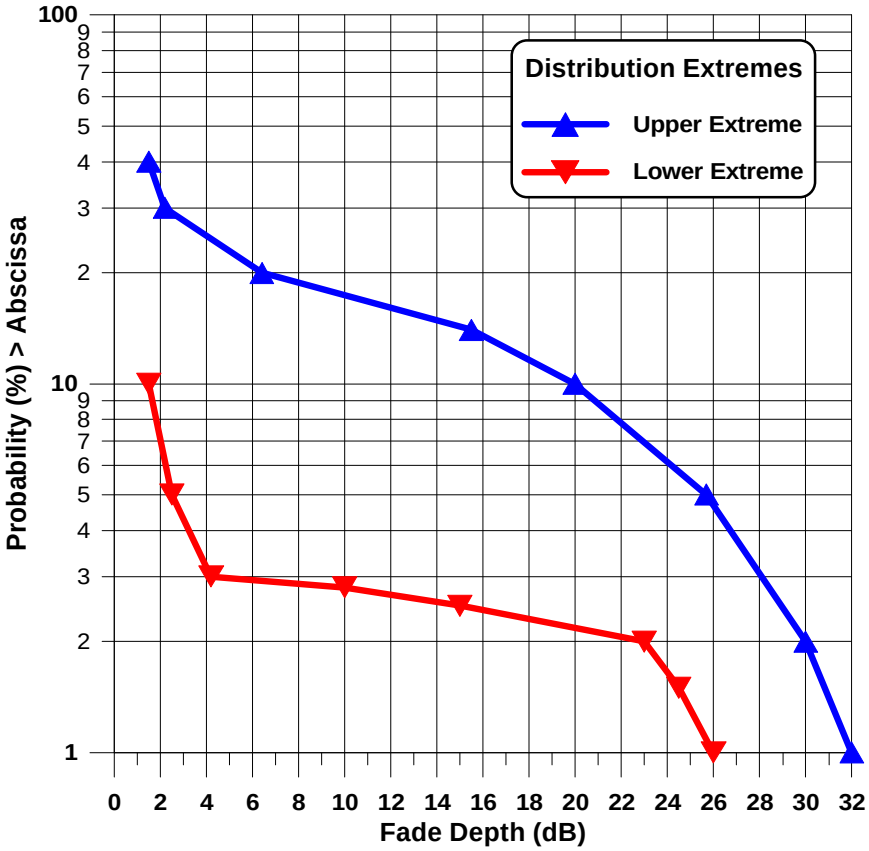

Figure 7-16: Extremes of eight measured distributions in Japan at 1.5 GHz in elevation angle range 40° to 50° in Japan [Obara et al., 1993].

Ryuko and Saruwatari [1991] and Saruwatari and Ryuko [1989] also describe a series of LMSS measurements in Japan employing L-Band (1.5 GHz) transmissions from the Japanese ETS-V satellite which were received by a moving van. Figure 7-17 shows three distributions corresponding to an elevation angle of approximately 46°. The distributions were derived from measurements executed on two expressways and one "old road" running alongside one of the expressways (Kan-etsu). Both expressways traverse flat areas, mountainous terrain, and have many two-level crossings with local roads. The "old road" runs through local urban areas, suburbs, farms, with a number of bridge crossings for pedestrians.

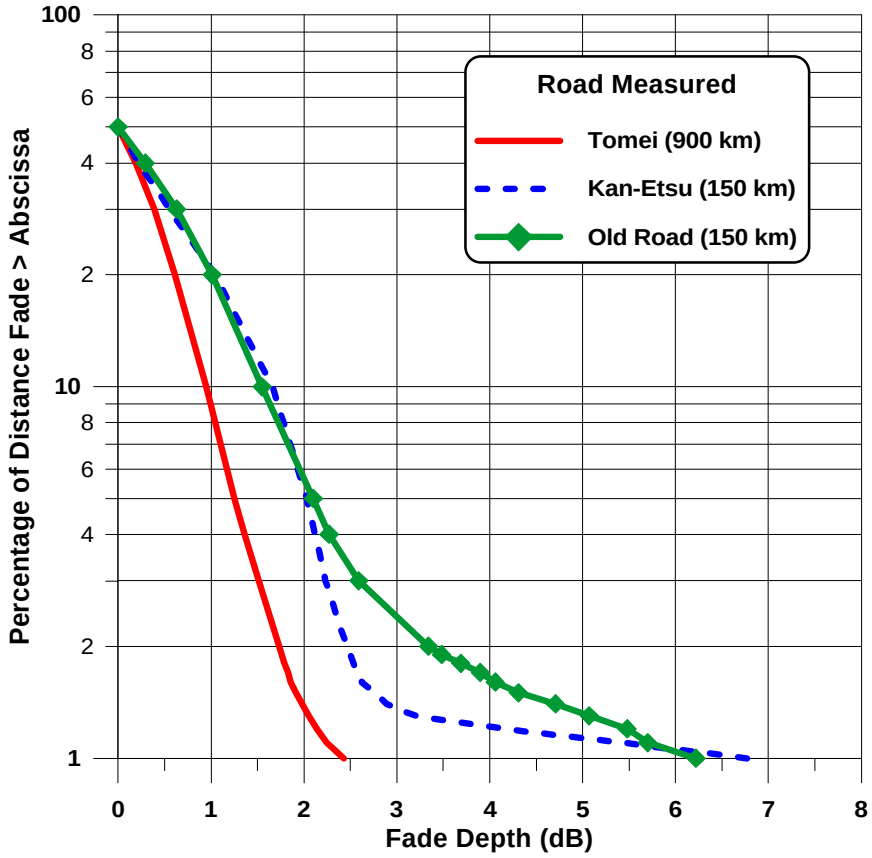

Figure 7-17: Fade distributions at L-Band for two expressways and an "old road" in Japan [Ryuko and Saruwatari, 1991].

7.8 Measurements Performed in the United States

Early LMSS measurements were reported by Hess [1980] who received the vertically polarized components of right hand circular transmissions at 860 MHz and 1550 MHz from the ATS-6 geostationary satellite. Systematic fade measurements were obtained with the receiver system on a moving van as a function of the local environment, vehicle heading, frequency, elevation angle, and street side. Since the circularly polarized transmissions were received with a vertical dipole, the measured signal levels were susceptible to low elevation multipath scattering. Because the distributions described by Hess mainly correspond to urban environments in Denver, his results will not be covered here other than to point out that 25 dB fades were typical for the urban areas. Hess does report, however, that of the measurements made in suburban and rural areas, typical fade levels of 10 dB were measured.

As mentioned previously, systematic propagation measurements were made in the United States by the authors over the period 1983 - 1994. For example, Figure 7-18 through Figure 7-20 show a series of eight measured distributions at UHF (870 MHz) for different roads and driving scenarios in central Maryland at the respective elevation angles of 30°, 45°, and 60° [Goldhirsh and Vogel, 1989]. These distributions were

acquired employing a helicopter as the transmitter platform. In Figure 7-21 through Figure 7-24 are given similar type distributions acquired at L-Band (1.5 GHz) [Goldhirsh and Vogel, 1989; 1995]. In Figure 7-21, the MARECS B-2 geostationary satellite was used as the transmitter platform (elevation = 21°), whereas the other figures were derived from measurements using the helicopter transmitter platform. The legend information in these figures has the following significance. The "star" curve in Figure 7-18 is denoted by 295 S, RL, HR. These symbols represent the case in which the sampled route was 295 south (295 S), the vehicle was traveling in the right lane (RL), and the helicopter was to the right of the driver (HR). The legend information for the other curves has analogous definitions. The solid curve showing no data points in each of these figures corresponds to the EERS model, which is approximately representative of the median of the measured distributions. The variability of the measured distributions is noted to generally be within ± 5 dB vis-à-vis the EERS model.

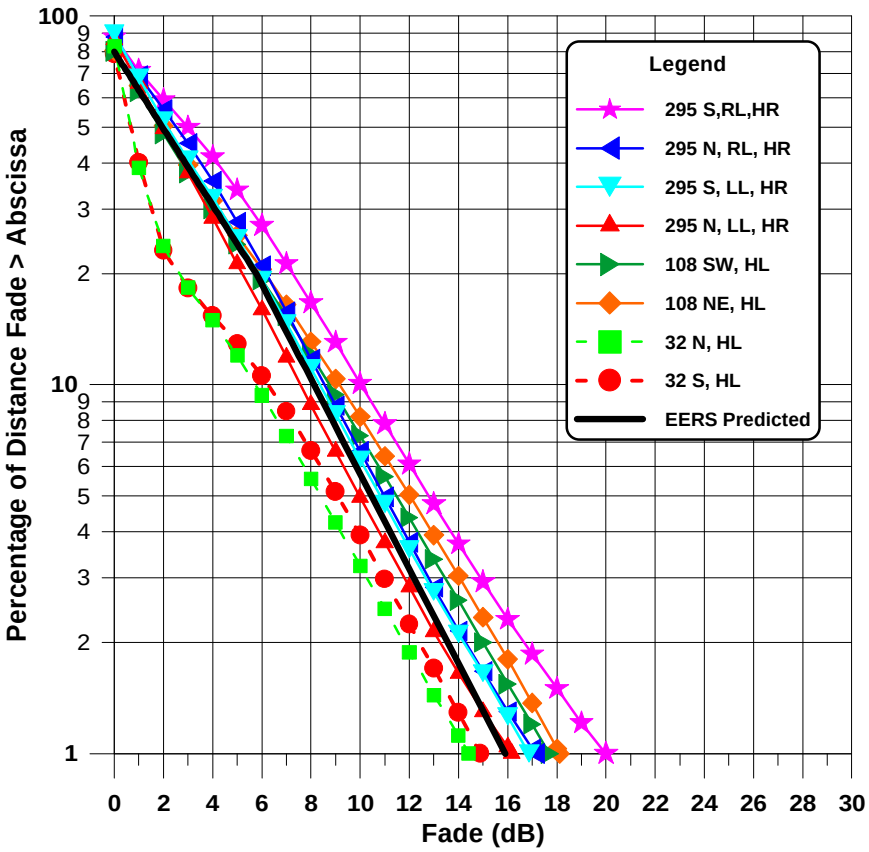

Figure 7-18: Cumulative distributions at UHF (870 MHz) for elevation angle = 30° from mobile measurements made with a helicopter transmitter platform along eight roads in central Maryland [Goldhirsh and Vogel, 1989]. Solid curve is EERS prediction.

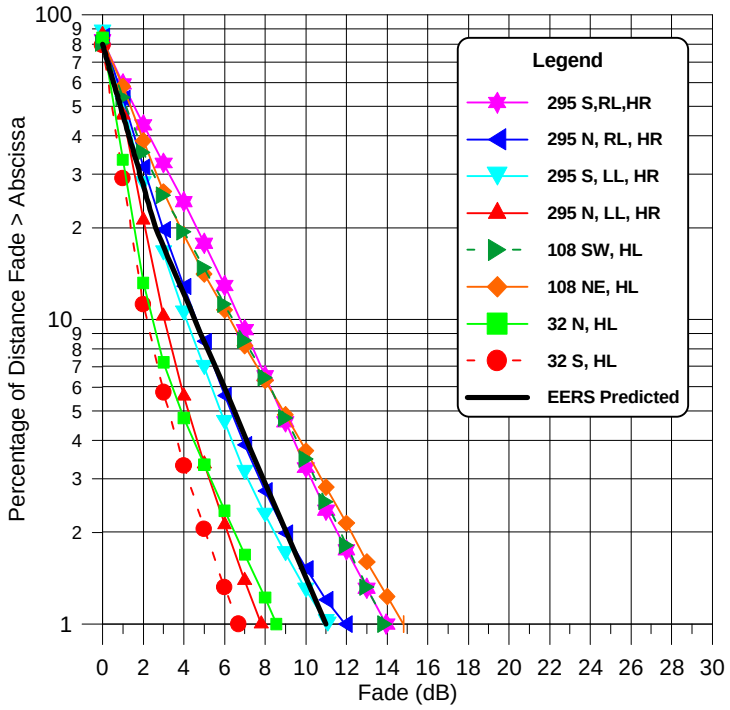

Figure 7-19: Cumulative distributions at UHF (870 MHz) for elevation angle = 45° from mobile measurements made with a helicopter transmitter platform along eight roads in central Maryland [Goldhirsh and Vogel, 1989]. Solid curve is EERS prediction.

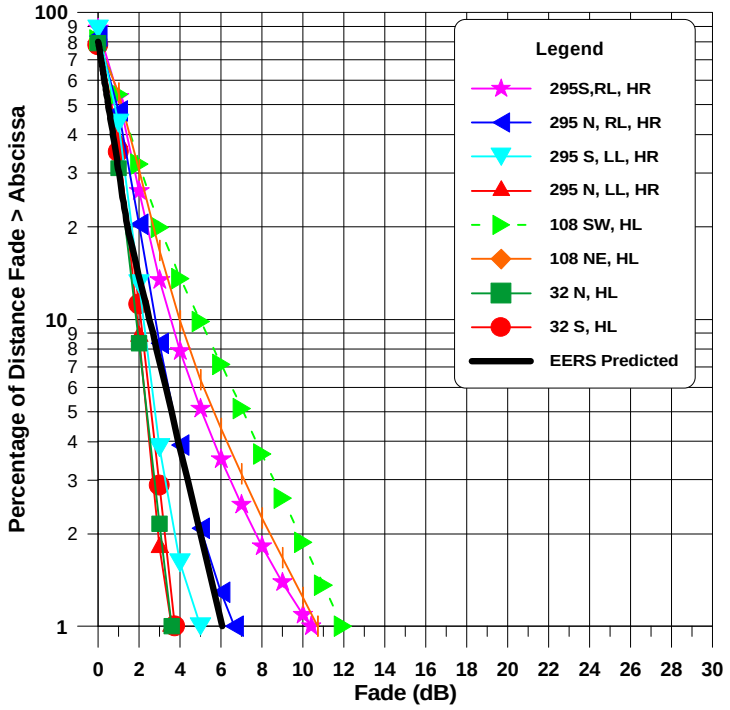

Figure 7-20: Cumulative distributions at UHF (870 MHz) for elevation angle = 60° from mobile measurements made with a helicopter transmitter platform along eight roads in central-Maryland [Goldhirsh and Vogel, 1989]. Solid curve is EERS prediction.

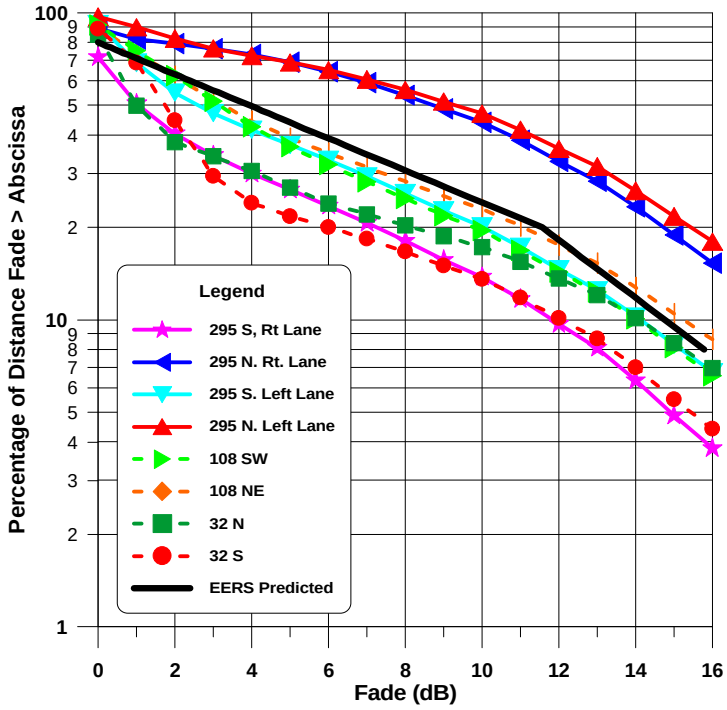

Figure 7-21: Cumulative distributions for eight roads in central Maryland at 1.5 GHz and 21° elevation obtained from measurements with MARECS B-2. Solid curve is EERS model prediction [Goldhirsh and Vogel, 1995].

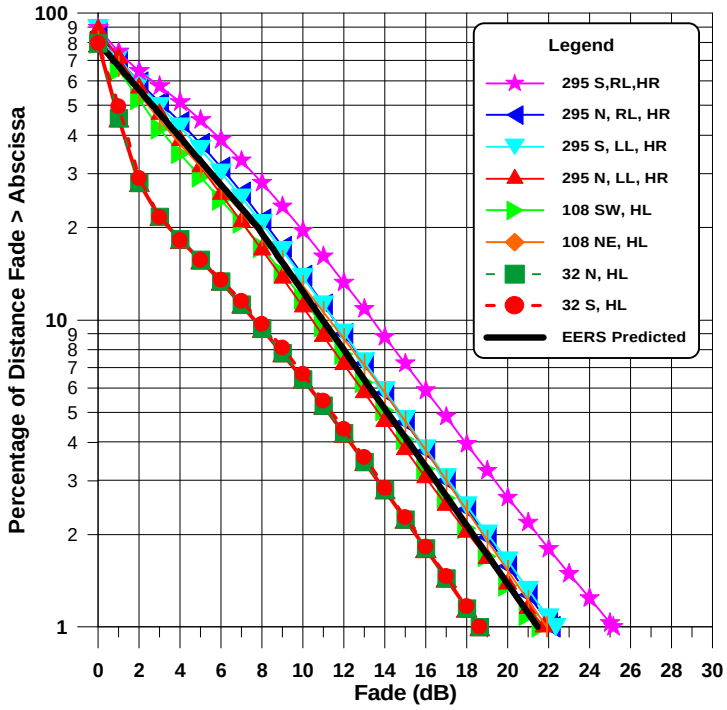

Figure 7-22: Cumulative distributions for eight roads in central Maryland at 1.5 GHz and 30° elevation obtained from measurements employing a helicopter transmitter platform. Solid curve is EERS model prediction [Goldhirsh and Vogel, 1995].

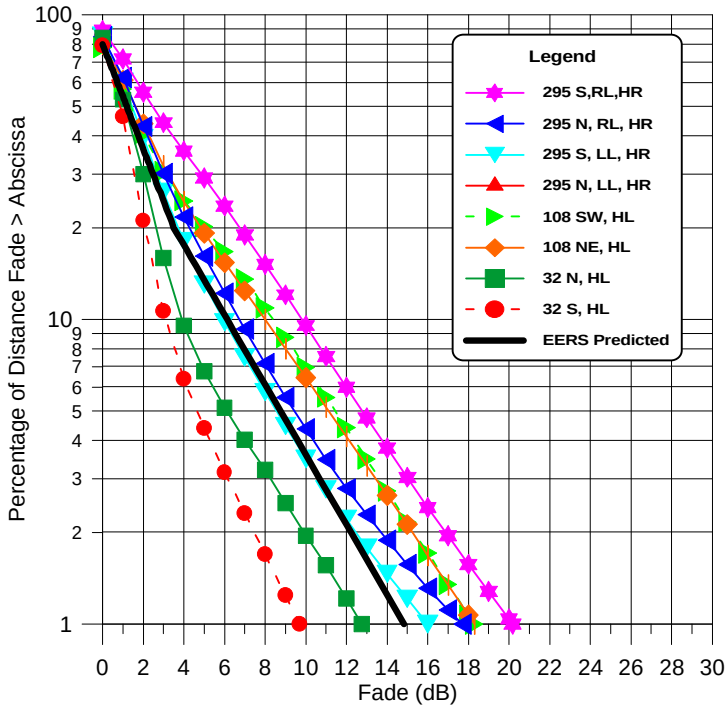

Figure 7-23: Cumulative distributions for eight roads in central Maryland at 1.5 GHz and 45° elevation obtained from measurements employing a helicopter transmitter platform. Solid curve is EERS model prediction [Goldhirsh and Vogel, 1995].

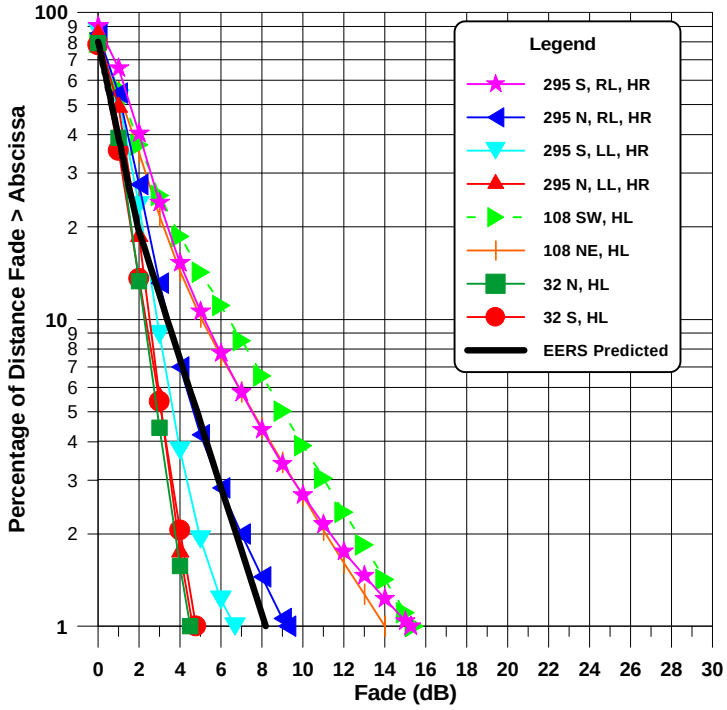

Figure 7-24: Cumulative distributions for eight roads in central Maryland at 1.5 GHz and 60° elevation obtained from measurements employing a helicopter transmitter platform. Solid curve is EERS model prediction [Goldhirsh and Vogel, 1995].

Vaisnys and Vogel [1995] report on measurements conducted on December 15 and 16, 1994 in Pasadena, California. A CW tone at 2.05 GHz emanating from the geostationary Tracking and Data Relay Satellite System (TDRSS) satellite located at 171° West resulted in an elevation of angle of 21°. One of the runs was comprised of a 33 km round trip drive. It passed through a mixed environment consisting of buildings, trees, medium width and wide four-lane streets with trees at varying distances from the roadway, two tunnels, above street-level freeway with occasional overpasses, commercial areas, and residential streets heavily shaded with trees. The fade-time series representation and cumulative fade distribution for this run are given in Figure 7-25 and Figure 7-26, respectively.

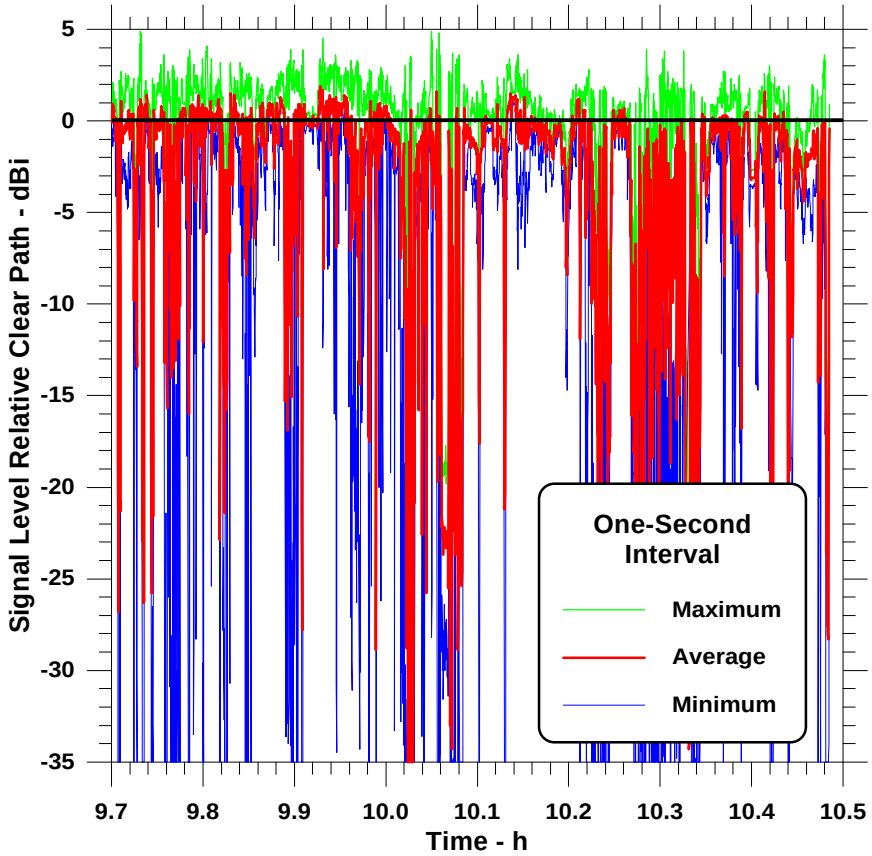

Figure 7-25: Fade-time series for Pasadena 33 km run [Vaisnys and Vogel, 1995].

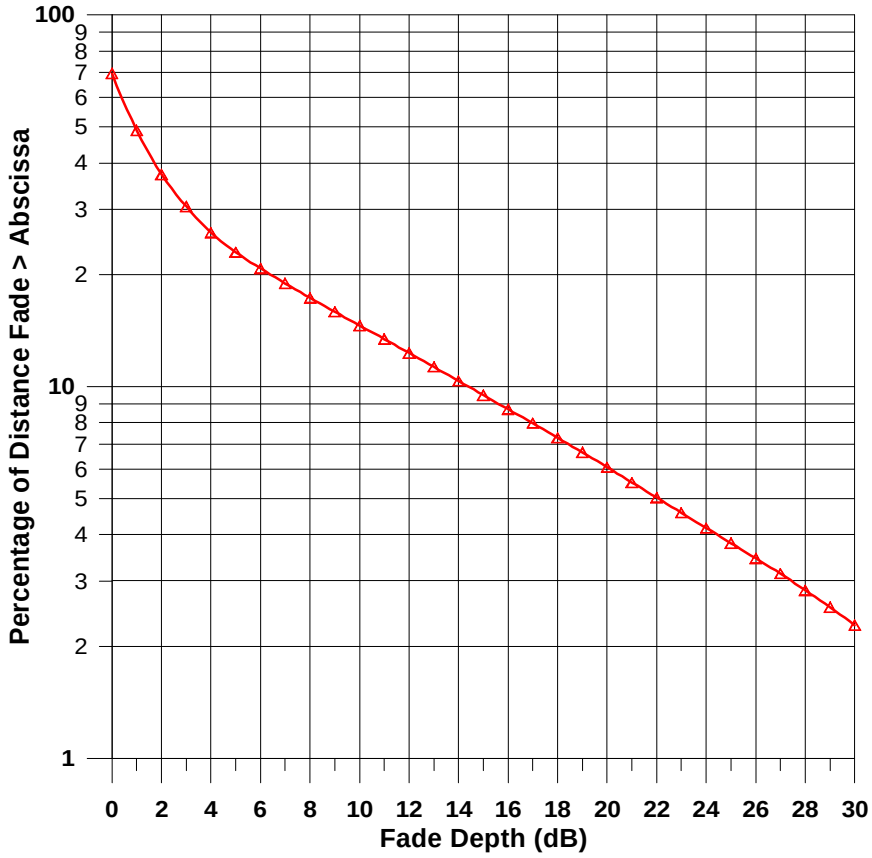

Figure 7-26: Cumulative distribution for Pasadena, California 33 km run [Vaisnys and Vogel, 1995].

Jenkins et al. [1995] received spread spectrum signals from the TDRSS F3 satellite platform located at 61° W and determined cumulative fade distributions at 2.09 GHz for various geographic locations in the western and southwestern United States. The distributions were derived from amplitude measurements of the strongest return observable within each averaged delay profile. Measurements in 21 representative geographical locations in urban/suburban open plain, and forested areas were executed. In Figure 7-27 are shown example distributions for tree lined roads at 18° elevation in Sequoia National Park, California and at 41° elevation in Slidel, Louisiana. The very different characteristics of these distributions are due to the influence of elevation angle and the excessive shadowing and blockage at Sequoia National Park.

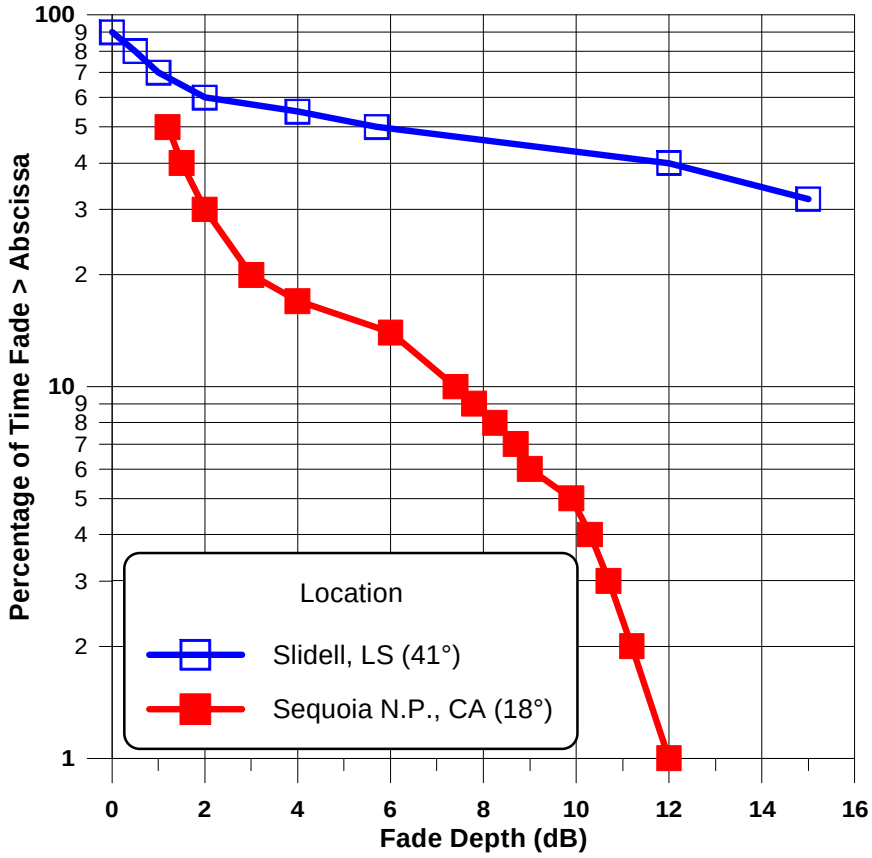

Figure 7-27: Cumulative fade distributions at 2.09 GHz for tree-lined roads at two locations in the United States derived from spread spectrum transmissions [Jenkins et al., 1995].

In Figure 7-28 are shown cumulative distributions derived from measurements at 20 GHz (elevation angle = 46°) employing the Jet Propulsion Laboratory's ACTS Mobile Terminal (AMT) [Rice et al., 1996; Gargione et al., 1995]. The AMT is a "proof of concept breadboard terminal" comprised of a tracking antenna system atop a van and is being used to establish the operational capabilities of 20 GHz and 30 GHz mobile communication systems [Abbe et al., 1996]. Rice et al. defined the road types over which propagation measurements were made in the following way:

- **Category II**: "A broad suburban thoroughfare lined with trees and buildings. The tree canopies cause intermittent blockage and the buildings are either too far removed from the roadside or not tall enough to cause significant blockage."
- **Category III**: "A small, two-lane roadway lined with trees and buildings. The tree canopies often cover the entire roadway and buildings are close enough to contribute to the fading process."

The curves labeled 1 and 3 in Figure 7-28 correspond to the Category II and the curves labeled 4 and 5 represent Category III. Curve 2, given by Gargione et al. [1995], was derived from measurements over a series of roads that encircle the Rose Bowl in Pasadena, California. The road types were characterized as being "surrounded by rolling hills with substantial amounts of foliage."

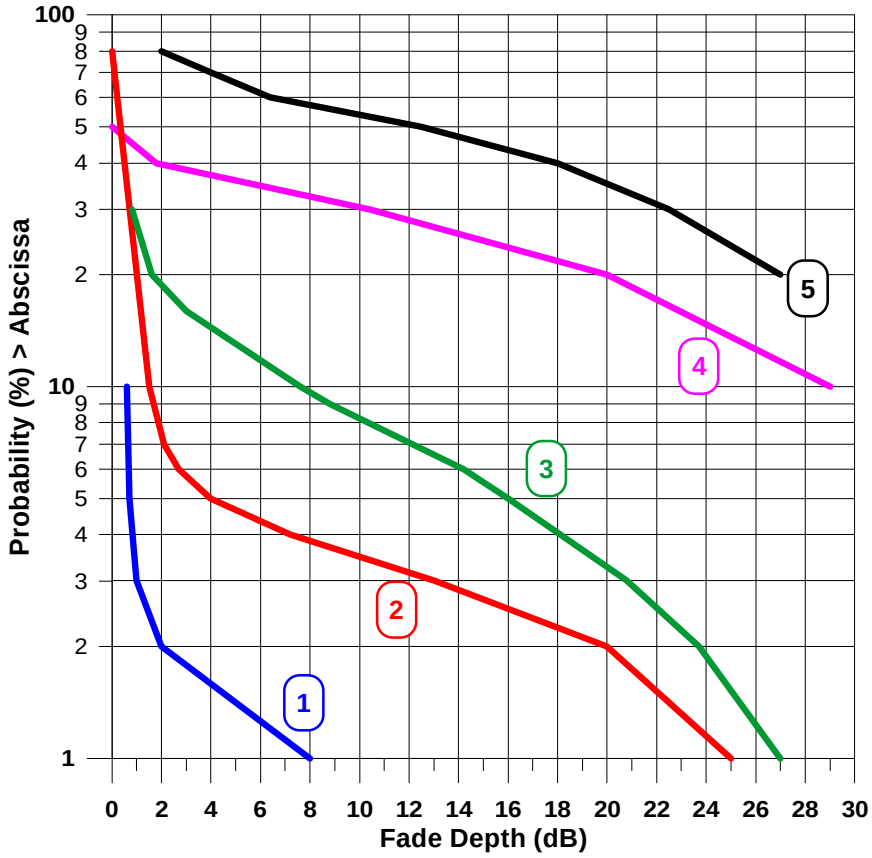

Figure 7-28: Curves labeled 1 and 3 correspond to Category II and curves labeled 4 and 5 represent Category III (defined in text) [Rice et al., 1996]. Curve 2 presented by Gargione et al. [1995], was derived from measurements over a series of roads that encircled the Rose Bowl in Pasadena, California.

The dashed curve in Figure 7-29 represents a 20 GHz measured distribution obtained for a tree-lined road in central Maryland in which the deciduous trees were without foliage and where the tree population was in excess of 55% [Goldhirsh and Vogel, 1995]. This distribution and others described in Figure 7-30 and Figure 7-31 were derived as part of a mobile satellite propagation measurements campaign in the United States employing the Advanced Communications Technology Satellite (ACTS) [Goldhirsh et al, 1995; Goldhirsh and Vogel, 1994]. The solid curve in Figure 7-29 is the corresponding distribution assuming the trees along the same road were in full foliage. This distribution was derived employing a prediction methodology described in Chapter 3. The solid curve in Figure 7-30 is a 20 GHz distribution at 55° elevation measured in Bastrop, Texas along an approximate 10 km stretch of road. It was lined with evergreen trees where the population was in excess of 55% and where there were segments along the road in which the canopies of trees on both sides of the road formed a tunnel of foliage. The dashed curve represents the predicted distribution obtained from the EERS model. Figure 7-31 shows a set of distributions measured in the vicinity of Fairbanks, Alaska along tree-line roads where the elevation angle was 8°. A large variation in the distributions exists because of the varying likelihood of terrain blockage and/or multiple foliage shadowing along some of the roads.

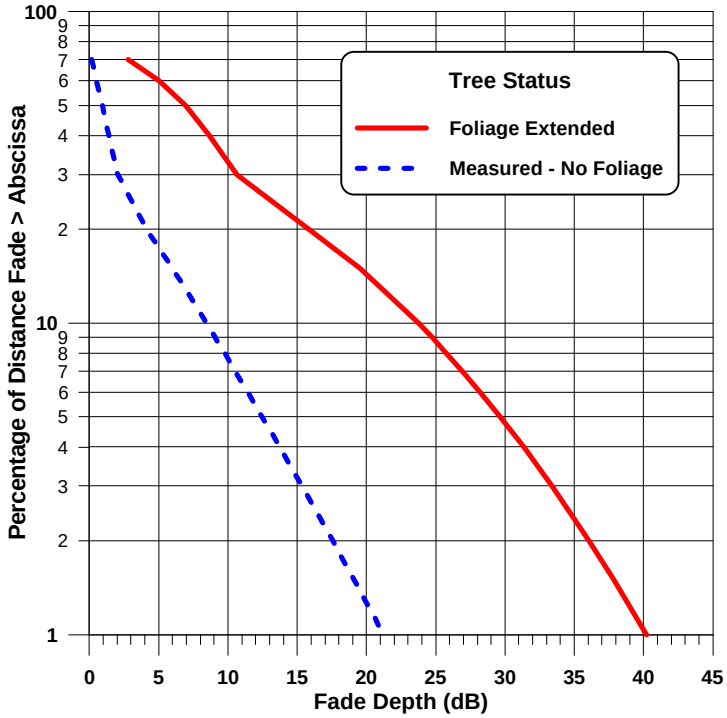

Figure 7-29: Measured distribution in central Maryland at 20 GHz for deciduous trees without leaves (dashed) and foliage predicted distribution (solid) [Goldhirsh and Vogel, 1995].

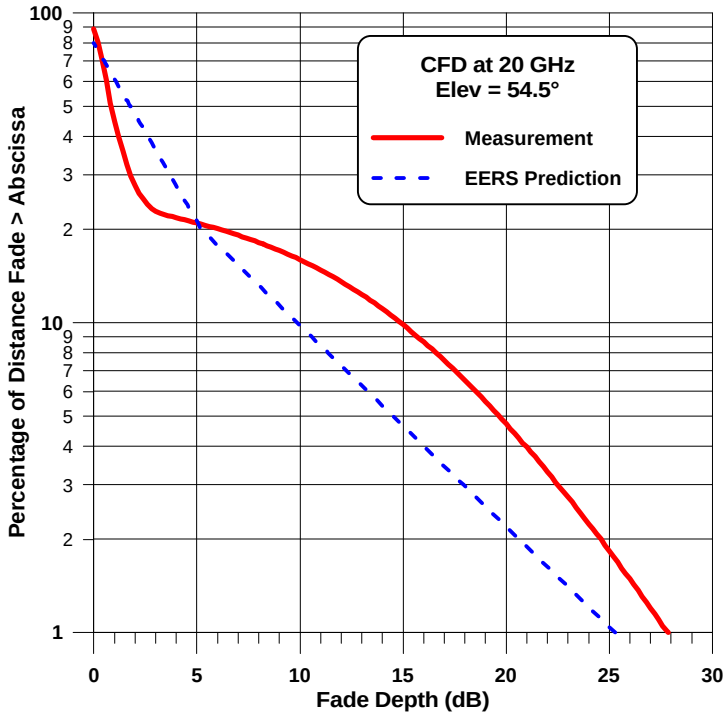

Figure 7-30: Measured cumulative fade distribution at 20 GHz (Bastrop, Texas; elevation = 54.5°). Dashed curve represents EERS prediction.

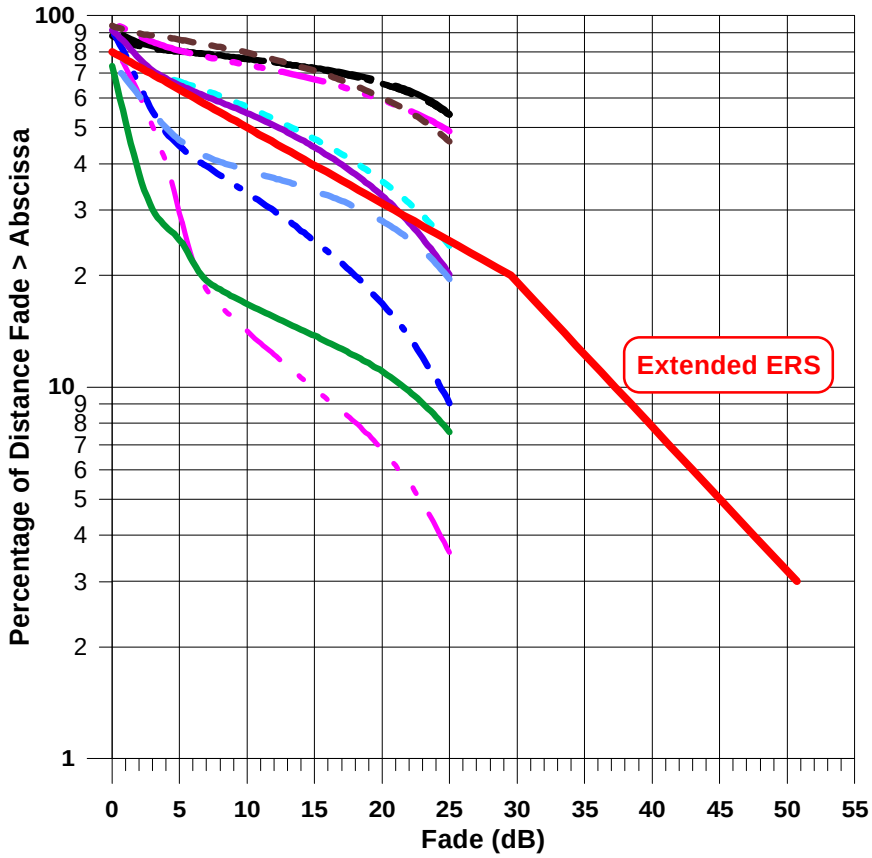

Figure 7-31: Cumulative fade distributions at 20 GHz for roads in vicinity of Fairbanks, Alaska (elevation = 8°). Solid curve extending to 50 dB is EERS prediction.

7.9 Summary Comments and Recommendations

We emphasize here again that the extent of fading is dependent on frequency, elevation angle, bearing to the satellite, the density of foliage cutting the earth-satellite path and the offset of trees from the road. Also affecting the fading are scattering and blockage effects from telephone poles, street signs, and underpasses. Table 7-1 demonstrates the wide range of 1% and 10% attenuation levels. In Table 7-2 are culled the 54 measured distribution entries in terms of frequency and elevation with the indicated fade ranges due to the other causes mentioned above. The last column of this table represents the number of entries obtained from Table 7-1 to arrive at the indicated quantities. The numbers in parentheses correspond to the EERS values. Where angle and/or frequency ranges are given, the EERS value is calculated at the lower elevation angle and larger frequency (worst case). The system designer interested in selecting a design fade margin may use the worst case fade or the mid-value depending upon the individual system constraints. Alternate suggested fade margin levels may be obtained using the indicated EERS values which are dominantly representative of roadside tree shadowing where the trees density exceeds 55%.

Table 7-2: Summary of information derived from Table 7-1 sorted in terms of frequency and elevation angle.

f (GHz)	El (°)	Fade		Number
		P = 1%	P = 10%	
0.87	5	>30 (18)	21.5 (10.5)	1
0.87	15-20	13-18 (18)	5.5-8 (10.5)	2
0.87	30	14-20 (15)	6-10 (7.5)	1
0.87-.893	45	7-15 (10.5)	2-7.5 (4)	2
0.87	60	3-12 (5.5)	2-5 (2.5)	1
1.5	19-26	11-21 (26)	3.5-16 (15.5)	5
1.5-1.55	30	17.5-25 (22)	8-13 (11)	2
1.5-1.6	40-50	2.5-32 (18)	1-20 (8)	7
1.3-1.6	50-60	5-18.5 (13)	2-7.5 (5)	7
1.3-1.6	80	8-12	2-3	3
2.05-2.09	18-21	>30 (31)	>15 (18.5)	2
2.09-2.66	40-45	12-17.7 (22.5)	7-11.5 (10)	3
2.5-2.6	60	12-22.5 (11)	5-9 (10)	3
2.5-2.6	80	10.5-16	4.5-6	2
10.4	60	27.5-28 (17.5)	13-18.5 (7)	2
10.4	80	24-26	10.5-13	2
20	8	>25 (63)	>25 (37)	1
18.7-20	30-38	21-40 (52)	9-33 (27)	4
20	46	8 to >30 (35)	2-30 (14.5)	3
20	54.5	28 (26)	15 (10)	1

7.10 References

Abbe. S. B., M. J. Agan and T. C. Jedrey, [1996], "ACTS Mobile Terminal," *International Journal of Satellite Communications*, Vol. 14, No.3, pp.175-189.

Bundrock, A. and R. Harvey [1989], "Propagation Measurements for an Australian Land Mobile Satellite System," *Australian Telecommunication Research*, Vol. 23, No. 1 pp. 19-25.

Butt, G., B. G. Evans and M. Richharia [1992], "Narrowband Channel Statistics from Multiband Propagation Measurements Applicable to High Elevation Angle Land-Mobile Satellite Systems," *IEEE Journal on Selected Areas in Communications*, Vol. 10, No. 8, October, pp. 1219-1225.

Butterworth, J. S. [1984a], "Propagation Measurements for Land-Mobile Satellite Systems at 1542 MHz," *Communication Research Centre Technical Note 723*, August. (Communication Research Centre, Ottawa, Canada.)

Butterworth, J. S. [1984b], "Propagation Measurements for Land-Mobile Satellite Services in the 800 MHz Band," *Communication Research Centre Technical Note 724*, August. (Communication Research Centre, Ottawa, Canada.)

Butterworth, J. S. and E. E. Matt [1983], "The Characterization of Propagation Effects for Land Mobile Satellite Services," *IEE 3rd International Conference on Satellite Systems for Mobile Communications and Navigation; Conference Publication No. 222*, London, U.K., June 7-9, pp. 51-54.

Gargione, F., B. Abbe, M. J. Agan, T. C. Jedrey and P. Sohn [1995], "Mobile Experiments Using ACTS," *Space Communications (Special Issue on Satellite Mobile and Personal Communications)*, Vol. 13, No. 3 (IOS Press), pp. 193-223.

Goldhirsh, J. and W. J. Vogel [1995], "An Extended Empirical Roadside Shadowing Model for Estimating Fade Distributions from UHF to K-Band for Mobile Satellite Communications," *Space Communications (Special Issue on Satellite Mobile and Personal Communications)*, Vol. 13, No. 3 (IOS Press), pp. 225-237.

Goldhirsh, J., W. J. Vogel and G. W. Torrence, [1995], "Mobile Propagation Measurements in the U.S. at 20 GHz Using ACTS," *International Conference on Antennas and Propagation (ICAP 95)*, Vol. 2, Conference Publication No. 407, Eindhoven, The Netherlands, pp. 381-386.

Goldhirsh, J. and W. J. Vogel [1994], "ACTS Mobile Propagation Campaign," *Proceedings of the Eighteenth NASA Propagation Experimenters Meeting (NAPEX XVIII) and the Advanced Communications Technology Satellite (ACTS) Propagation Studies Miniworkshop*, Vancouver, British Columbia, June 16-17, 1994, pp. 135-150 (JPL Publication 94-19, Jet Propulsion Laboratory, California Institute of Technology, Pasadena, California.)

Goldhirsh, J. and W. J. Vogel [1989], "Mobile Satellite System Fade Statistics for Shadowing and Multipath from Roadside Trees at UHF and L-Band," *IEEE Transaction on Antennas and Propagation*, Vol. 37, No. 4, April, pp. 489-497.

Hess, G. C. [1980], "Land-Mobile Satellite Excess Path Loss Measurements," *IEEE Trans. On Vehicular Tech.*, Vol. VT-29, No. 2, May, pp. 290-297.

Huck, R. W., J. S. Butterworth and E. E. Matt [1983], "Propagation Measurements for Land Mobile Satellite Services," *33rd IEEE Vehicular Technology Conference*, Toronto, pp. 265-268.

Jenkins, J. D., Y. Fan and W. P. Osborne [1995], "Channel Fading for Mobile Satellite Communications Using Spread Spectrum Signaling and TDRSS," *Proceedings of the Nineteenth NASA Propagation Experimenters Meeting (NAPEX XIX) and the Seventh Advanced Communications Technology Satellite (ACTS) Propagation Studies Workshop (APS VII)*, Fort Collins, Colorado, June 14-16, JPL Publication 95-15, pp. 147-158. (Jet Propulsion Laboratory, California Institute of Technology, Pasadena, California.)

Joanneum Research [1995], "Land Mobile Satellite Narrowband Propagation Campaign at Ka Band," *Final Report W.O. #4*, ESTEC Contract 9949/92/NL, January.

Jongejans, A., A. Dissanayake, N. Hart, H. Haugli, C. Loisy and R. Rogard [1986], "PROSAT-Phase 1 Report," *European Space Agency Tech. Rep. ESA STR-216*, May. (European Space Agency, 8-10 Rue Mario-Nikis, 75738 Paris Cedex 15, France.)

Murr, F., B. Arbesser-Rastburg, S. Buonomo and Joanneum Research [1995], "Land Mobile Satellite Narrowband Propagation Campaign at Ka Band," *Proc. International Mobile Satellite Conference (IMSC '95)*, Ottawa, Canada, pp. 134-138.

Obara, N., K. Tanaka, S. Yamamoto and H. Wakana [1993], "Land Mobile Satellite Propagation Measurements in Japan Using ETS-V Satellite," *Proc. International Mobile Satellite Conference (IMSC-93)*, Pasadena, CA, June 16-18, 1993, pp.313-318.

Paraboni, A. and B. Giannone, [1991], "Information for the participation to the ITALSAT Propagation Experiment," Politecnico di Milano Report 91.032.

Renduchintala, V. S. M., H. Smith, J. G. Gardiner and I. Stromberg [1990], "Communications Service Provision to Land Mobiles in Northern Europe by Satellites in High Elevation Orbits - Propagation Aspects," *40th International Conference on Vehicular Technology*, May 6-9, Orlando, Florida (IEEE VTC '90.)

Rice, M., J. Slack, B. Humphreys and D. S. Pinck, [1996], "K-Band Land-Mobile Satellite Channel Characterization Using ACTS," *International Journal of Satellite Communications*, Vol. 14, No.3, pp. 283-296.

Ryuko, H. and T. Saruwatari [1991], "Propagation Characteristics for Land Mobile Satellite Systems in 1.5-GHz Band," *Journal of the Communications Research Laboratory*, Vol. 38, No. 2, pp. 295-302, July.

Smith, H., J. G. Gardiner and S. K. Barton [1993], "Measurements on the Satellite-Mobile Channel at L & S Bands," *Proceedings of the Third International Mobile Satellite Conference, IMSC '93*, June 16-18, Pasadena, California, pp. 319-324.

Smith, H., V. S. M. Renduchintala and J. G. Gardiner [1990], "Assessment of the Channel Offered by a High Elevation Orbit Satellite to Mobiles in Europe - Narrowband Results, Wideband Experiments," *IEE Conference on Radio Receivers and Associated Systems*, Churchill College, Cambridge, UK.

Saruwatari, T. and H. Ryuko [1989], "Propagation Characteristics for Land Mobile Satellite Systems in 1.5 GHz Band," *Proc. Of 1989 International Symposium on Antennas and Propagation (ISAP '89)*, Tokyo, Japan, pp. 769-772.

Vaisnys, A. and W. J. Vogel [1995], "Satellite and Terrestrial Narrow-Band Propagation Measurements at 2.05 GHz," *Proceedings of the Nineteenth NASA Propagation Experimenters Meeting (NAPEX XIX) and the Seventh Advanced Communications Technology Satellite (ACTS) Propagation Studies Workshop (APS VII)*, Fort Collins, Colorado, June 14-16. JPL Publication 95-15, pp. 179-193, (Jet Propulsion Laboratory, California Institute of Technology, Pasadena, California.)

Vogel, W. J., J. Goldhirsh, and Y. Hase [1992], "Land-Mobile-Satellite Fade Measurements in Australia," *AIAA Journal of Spacecraft and Rockets*, Vol. 29, No. 1, Jan-Feb, pp. 123-128.

Vogel, W. J. and J. Goldhirsh [1990], "Mobile Satellite System Propagation Measurements at L Band Using MARECS-B2," *IEEE Trans. Antennas Propagation*, Vol. AP-38, No. 2, February, pp. 259-264.

Chapter 8

Earth-Satellite Propagation Effects Inside Buildings

Table of Contents

Table of Figures

Table of Tables

Chapter 8

Earth-Satellite Propagation Effects Inside Buildings

8.1 Background

Numerous investigations have been reported for the case in which both transmitter and receiver were located within the same building [e.g., Fujimori and Arai, 1997; ITUR, 1995; Polydorou et al., 1995; Tang and Sobol, 1995, Wang et al., 1995, Seidel and Rappaport, 1992, Bultitude et al., 1989; Rappaport, 1989]. Other experiments have been conducted where the transmitter was placed outdoors to simulate antennas mounted close to the ground radiating into nearby buildings [e.g., Cox et al., 1986, 1985, 1984; Hoffman and Cox, 1982]. Few investigators have examined the propagation effects inside buildings for the case in which transmissions originate from a satellite or a source mounted on a platform simulating a satellite. Wells [1977] used transmissions from the geostationary satellite ATS-6 at 860 MHz, 1.5 GHz and 2.6 GHz to determine the average attenuation into wood-frame houses with and without brick veneer at various elevation angles and frequencies. More recently, Vogel and Torrence [1993, 1995a, 1995b, 1995c] described the results of signal loss measurements made interior to a series of buildings. The transmitting antenna was mounted on an outside tower that simulated a satellite platform. The various frequencies considered ranged from 500 to 3000 MHz and measurements of the relative signal losses were made to characterize the spatial, temporal, and frequency variability. Although propagation effects similarities exist for all of the above scenarios, this chapter is primarily concerned with the latter scenario; namely that corresponding to a transmitter on a satellite platform or on a tower simulating a satellite platform with reception measurements made within the building. For this scenario, only results are considered in which outdoor obstacles do not obstruct the line-of-sight path. The indoor results are also presented in the form of signal levels (in dB) relative to those measured immediately outside the structure where an unobstructed line-of-sight existed.

8.2 Satellite Radio Reception Inside Buildings from 700 MHz to 1800 MHz

This section deals with the results of Vogel and Torrence [1993] who arrived at propagation results for measurements inside six buildings comprised of brick, corrugated sheet-metal, wood frame, mobile-home, and reinforced concrete-wall constructions. Their investigation emphasized geostationary satellite transmissions associated with direct broadcasting systems since their receiving antenna had a relatively narrow beamwidth (90°) and was pointed along the line-of-sight to the transmitter. Such an antenna experiences less multipath fading than one that has an azimuthally omni-directional gain characteristic.

8.2.1 Experimental Features

Swept CW signals from 700 MHz to 1800 MHz were radiated from an antenna located on an 18 m tower attached to a van outside these buildings. The part of the receiver system inside the buildings was comprised of the above described antenna on a linear positioner located approximately 1.5 m above the ground and pointed towards the transmitting antenna. Measurements were made for the case in which the receiver antenna was sequentially moved in 5 cm steps (for a total of 80 cm) along any of the three orthogonal directions. The receiver had a resolution bandwidth between 10 KHz and 1 MHz, a carrier to noise ratio of 45 dB, and an overall measurement accuracy of better than 0.5 dB. A summary of the experimental parameters is given in Table 8-1, and a succinct description of each of the site locations (labeled Site 1 through Site 6) is given in Table 8-2.

Table 8-1: Pertinent measurement system parameters of Vogel and Torrence [1993].

Characteristics	Value
Frequency	
Coverage, Δf	700 MHz to 1800 MHz in 1 s
Span	0 Hz to 1100 MHz
Resolution	10 KHz to 1 MHz
Amplitude	
Transmitted Power	10 mw
Range	45 dB
Resolution	0.2 dB
C/N Ratio	64 to 45 dB over Δf
Error	< 0.5 dB
Transmitter and Receiver Antennas	
Type	Cavity Backed Spiral
Polarization	Right-hand Circular
Beamwidth	90° (3 dB)
Gain	-2.5 to 4.5 dB over Δf
Elevation Angle (Receiving)	12° to 48°

Table 8-2: Site descriptions of indoor propagation measurements of Vogel and Torrence [1993].

Site #	Description	Elevation Angle
1	A corner office (6 X 7 m) with two large windows in a single-story building. Walls are of concrete-block masonry with the interior covered with plasterboard. The ceiling is comprised of acoustic tiles suspended at a height of 3 m from metal hangers. A double-glazed optically reflective window is located in the wall toward the transmitter. Roof is flat and consists of concrete panels supported by steel beams. Room is furnished with wooden office furniture. Also referred to as the EERL Building	27.5°
2	A small room in another building (3 X 4 m) with two windows and construction similar to Site 1. Room furnished with metal filing cabinets.	18°
3	A 5 X 5 m corner foyer in another building where a large reflective glass door encompasses half of one outside wall. The external walls are of concrete wall construction, and internal walls have metal frames covered with plasterboard. Also referred to as the Commons.	16°
4	A 3 X 6 m shack with corrugated sheet-metal walls and roof on the outside and plywood on the inside. It has one window on each of the two narrow sides and a metal-covered door centered between two windows on one of the wide sides.	25°
5	An 1870 vintage restored and furnished two-story house with wood siding. The walls are filled with rock wool and covered with plasterboard on the interior and wood siding on the exterior. The gabled roof is covered with wood shingles. Measurements were made in two rooms on the ground floor and one room on the second level. Also referred to as the Farmhouse.	25°
6	A 12 X 2.4 m empty mobile trailer home with sheet-metal exterior and aluminum frame windows with metal screens.	45°

8.2.2 Multipath Interference During Frequency and Position Sweep

An example of maximum and minimum multipath interference (of relative signal level) experienced inside Site 2 is given in Figure 8-1 for a composite frequency sweep and vertical position scan near a window. The set of curves labeled maximum and minimum were derived by executing a frequency sweep between 700 MHz to 1800 MHz for each antenna position and culling out the maximum and minimum signal levels (upper and lower traces) at each frequency. The center thick curve is an example of the signal variability when the antenna position was fixed at an arbitrary position over the frequency interval. The large variability of the signal due to receiver antenna position and frequency changes demonstrates that multipath effects may be significant over the indicated position and frequency intervals. For example, the minimum trace shows signal levels which vary between -5 dB to smaller than -30 dB, the maximum trace shows signal levels which vary between +2 dB and -9 dB, and the fixed antenna position trace shows a variability between 0 to -30 dB.

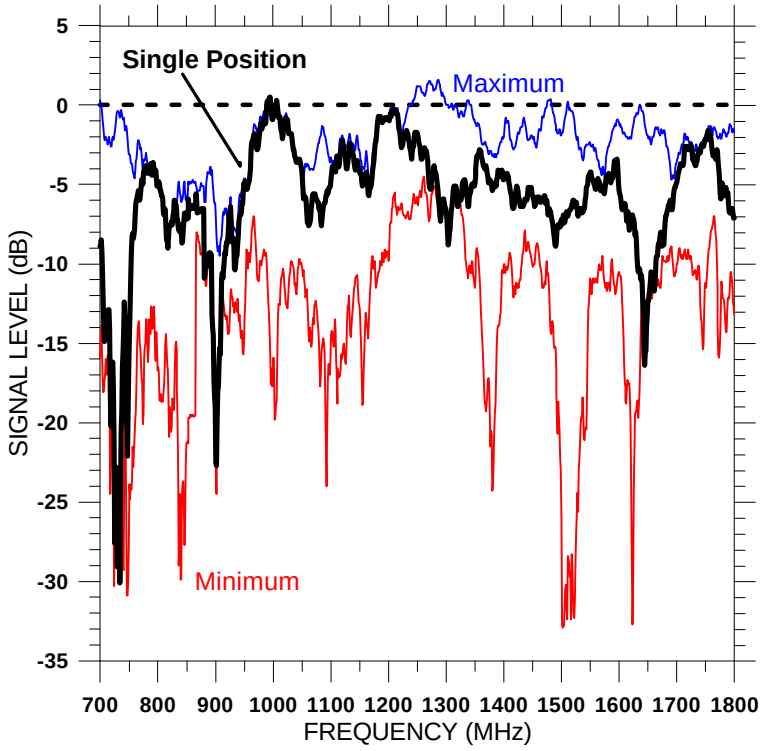

Figure 8-1: Maximum and minimum relative signal levels (thin lines) in a composite vertical scan of 80 cm and frequency sweep over the indicated frequency interval for Site 2. Thick curve corresponds to fixed receiver antenna versus frequency example [Vogel and Torrence, 1993].

8.2.3 Time Delay Distributions

Through the execution of a Fast Fourier Transform of the signal level over the frequency interval examined, estimates of maximum multipath time delays were derived. Cumulative distributions of these time delays are given in Figure 8-2 for three different site locations. It is clear from this figure that 90% of the power have delays smaller than 20 ns, 30 ns, and 80 ns for Sites 2, 4, and 3, respectively, and more than 99% of the power have associated delays smaller than 100 ns for Sites 2 and 4. These results were consistent with power loss measurements employing a series of bandwidths between 1 and 90 MHz over the frequency interval from 700 to 1800 MHz in that negligible bandwidth dependence was found in the loss statistics results.

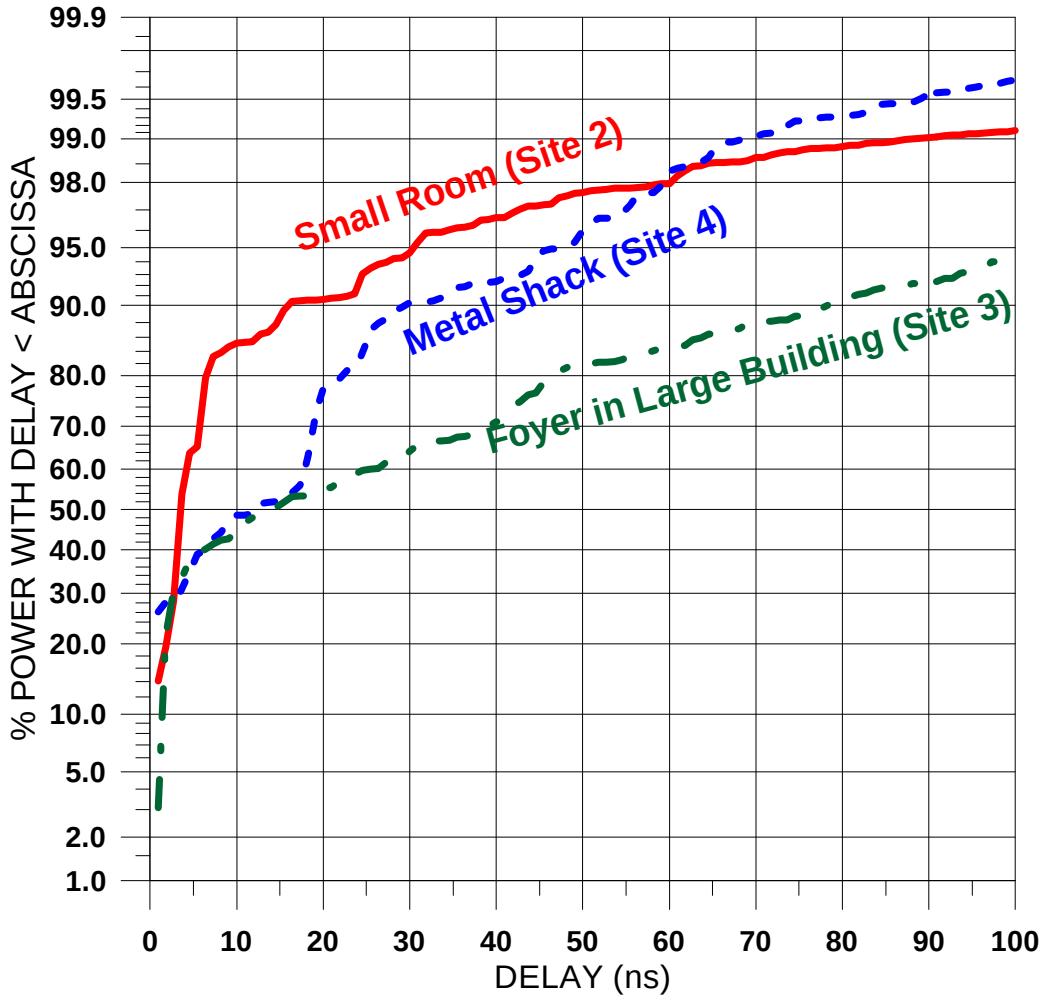

Figure 8-2: Approximate cumulative distributions of time delay at three locations.

8.2.4 Cumulative Distributions of Signal Levels

Figure 8-3 gives the relative signal level versus frequency for a series of fixed probabilities ranging from 1% to 99%. These statistics reflect a database of vertical and horizontal scans at several locations within Site 2 and averaged over bandwidths of 1, 2, 5, 9, 18, 45, and 90 MHz. We note, for example, that 1% of the signal levels exceeded 0 dB at approximately 0.75 GHz to -4 dB at 1.75 GHz, whereas at the probability of 50%, signal levels exceeded -5 to -14 dB at these respective frequencies. The general trend of the probability contour is such that the losses increase with increasing frequency.

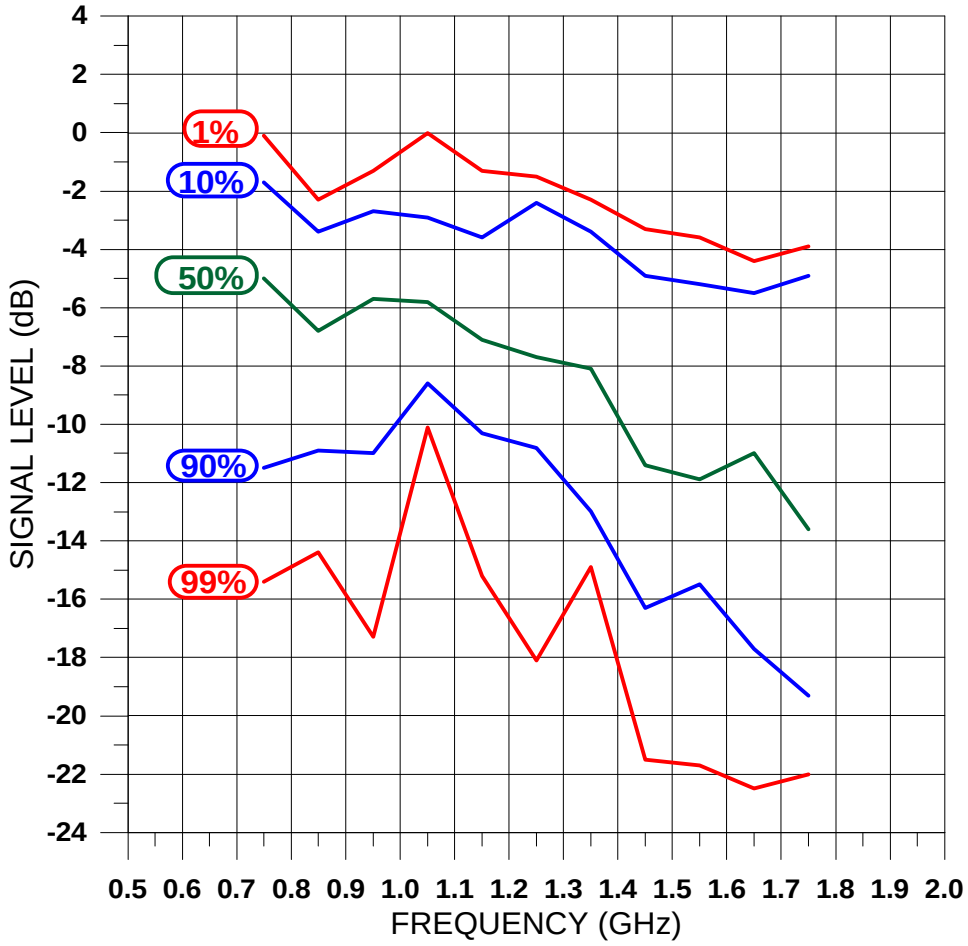

Figure 8-3: Cumulative probabilities of relative signal level as a function of frequency for Site 2. The database reflects measurements taken at 16 positions for 80 cm vertical scans at several locations and seven bandwidths

The cumulative distributions of the relative dB signal losses were found to follow a Gaussian distribution for the cases in which the loss values were binned for the composite of values. The composite of values were obtained at the different frequencies and at the different locations within a particular building (from 8 to 20 locations were considered within a given building). In Table 8-3 are given the mean and standard deviations associated with the best-fit Gaussian distributions for each of the sites (building locations) at defined "average" and "best" cases. The "average" case was obtained by taking the linear average loss over a series of bandwidths ranging from 1 MHz to 90 MHz (1, 2, 5, 9, 15, 45, and 90 MHz) within each 100 MHz bin interval over the frequency span 700 MHz to 1800 MHz. In determining the "average" the results were also combined for each of 16 antenna positions (5 cm displacement per position) and at each location within a given site (eight to twenty locations per site). The "best" case corresponds to statistics associated with that location within the position scan that resulted in the smallest losses. Site 6 showed the largest mean loss of approximately -25 dB as this building was a mobile trailer with a sheet metal exterior and aluminum frame windows having metal screens. At all other locations, the measurements of Vogel and Torrence were obtained in a less severe attenuation environment. Neither Ricean nor

Rayleigh distributions provided a better fit than the Gaussian distribution. Also given in Table 8-3 are the overall averages (of the averages) including the worst site (Site 6) and excluding it. It is noted, for example, that the average for all sites is 12.7 dB with a standard deviation of 5.5 dB. When Site 6 is excluded, the overall average is 10.2 dB with a standard deviation of 5.8 dB.

Table 8-3: Mean and standard deviation of best fit Gaussian distributions for frequency and spatial averaging.

Site	Average Case		Best Case	
	Mean (dB)	STD (dB)	Mean (dB)	STD (dB)
1	-7.9	5.5	-4.2	4.2
2	-9.1	4.4	-5.4	4.2
3	-15.4	8.4	-9.7	6.7
4	-9.7	6.3	-5.2	4.9
5	-9.0	4.5	-5.4	3.7
6	-24.9	3.8	-19.8	3.4
Average (Sites 1 to 6)	12.7	5.5	8.3	4.5
Average (Sites 1 to 5)	10.2	5.8	6.0	4.7

Table 8-4 lists the median of the relative power levels at all the site locations for the "average and "best" cases (defined previously) over the frequency interval 750 MHz to 1750 MHz. The smallest and largest median power levels are given over this frequency for each of the cases as well as the overall averages "with" and "without" the worst case Site 6 (last two rows). It is noted that Sites 3 and 6 had the most severe fading. Site 3 experienced more than 15 dB fading when the line-of sight path passed through a reflective glass door. The overall averages of the largest fade medians are less than -14.8 dB and -13 dB with and without Site 6.

Table 8-4: Relative median power levels over frequency interval 750 MHz to 1750 MHz.

Site #	Average Case (dB)		Best Case (dB)	
	Smallest	Largest	Smallest	Largest
1	-5	-11	-2	-6
2	-5	-14	-2	-5
3	-17	-18	-12	-13
4	-9	-11	-5	-6
5	-5	-11	-3	-5
6	-20	< -24	-16	-22
Average (1-6)	-10.2	<-14.8	-6.7	-9.5
Average (1-5)	-8.2	-13.0	-4.8	-7.0

8.2.5 Frequency Dependence of Probability

The dependence of exceedance probability on frequency (f) and relative signal loss (SL) at frequencies from 750 MHz to 1750 MHz has been found to follow the least square relation

$$P = a + b \times f \ , \tag{8-1}$$

where

$$a = a_0 + a_1 \times SL , \tag{8-2}$$

$$b = b_0 + b_1 \times SL , \tag{8-3}$$

and where a_0, a_1, β_0, β_1 are tabulated in Table 8-5 for the various site locations. Also tabulated in Table 8-5 is the RMS error of P in percent. Example distributions are given for Site 2 at 750 MHz, 1.25 GHz and 1.75 GHz in Figure 8-4.

Table 8-5: Best fit coefficients for the model cumulative distributions (8-1).

Site	a_0	a_1	β_0	β_1	RMS Error in P (%)
1	66.2	5.3	16.0	-0.54	4.0
2	74.1	7.0	20.3	-1.2	8.4
3	105.7	3.1	-7.8	-0.34	2.8
4	97.8	6.2	-3.8	-1.5	3.4
5	67.2	5.2	224.9	-0.1	6.1

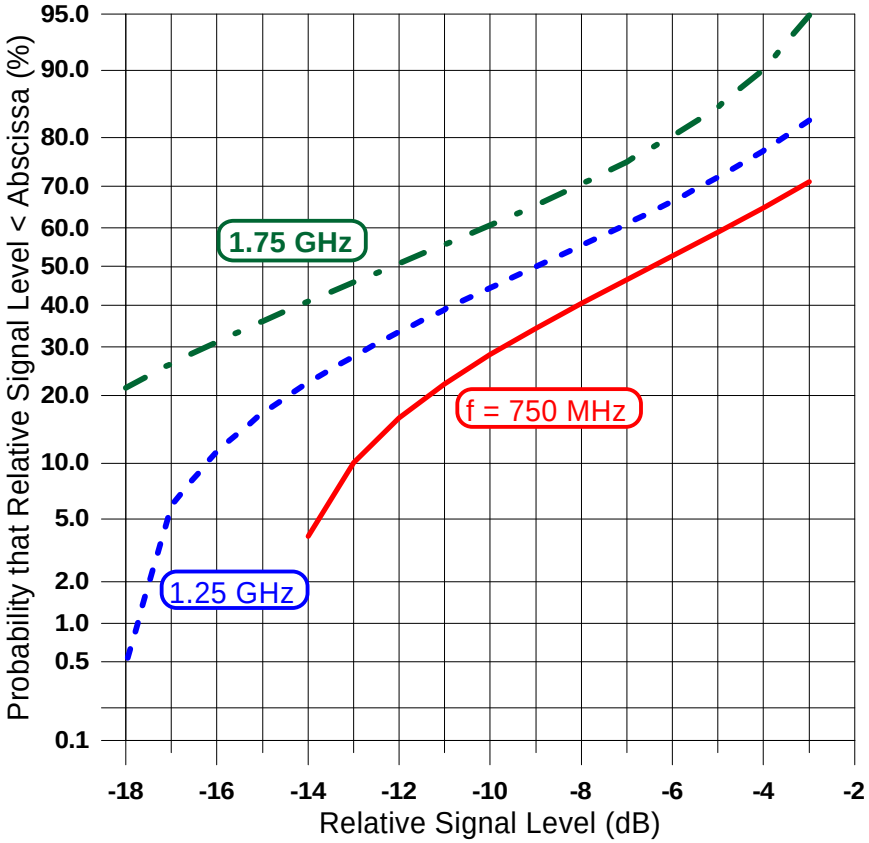

Figure 8-4: Example cumulative distributions of relative signal loss for Site 2 based on model described by (8-1) through (8-3).

8.2.6 Space Diversity Considerations

Vogel and Torrence measured the position spacing between the minimum (troughs) and maximum (crests) signal levels for all buildings and found the median value to be between 35 cm and 45 cm and to be independent of frequency. An example of power level versus spacing at a series of six frequencies spaced 5 MHz apart is given in Figure 8-5. It is noted that the relative power loss varies approximately between 0 dB and -30 dB from crest to trough. Taking averages over frequency of the distances between signal minima and maxima, this distance was found to be Gaussian distributed with a mean near 41 cm with a standard deviation of 17 cm. No significant differences were observed for movement along the vertical or horizontal directions. The above results suggest optimal separation distances of antennas when space diversity concepts are employed.

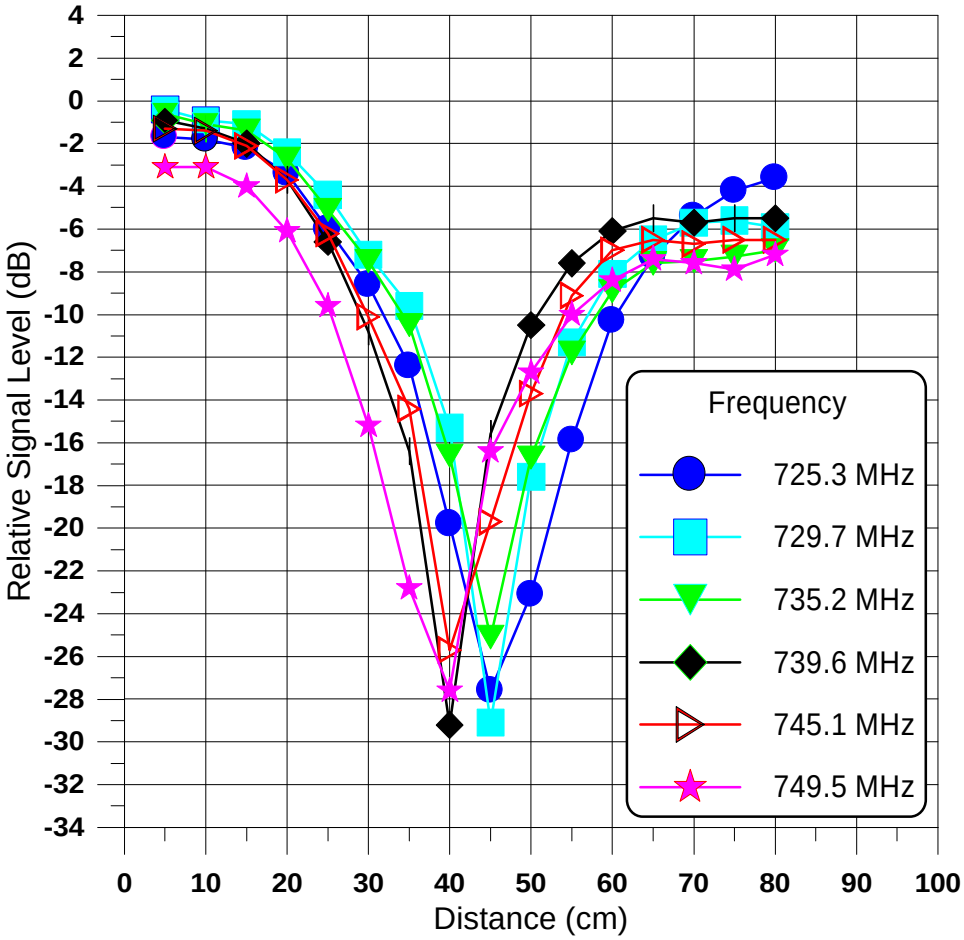

Figure 8-5: Relative signal level versus vertical measurement distance at six frequencies spaced approximately 5 MHz apart. (Site 2).

8.2.7 Bandwidth Distortion Considerations

At relative signal levels down to approximately -15 dB, the multipath delays tended to be less than 100 ns consistent with the results in Figure 8-2. We may imply from this result that contemplated systems with bandwidths of up to about 1 MHz should not be adversely affected by signal distortion. Vogel and Torrence executed an investigation to establish the expected levels of signal distortion one might encounter by examining the losses at various bandwidths ranging from 2 MHz to 90 MHz. The signal distortion was described in terms of the standard deviation of the deviations relative to the mean signal loss at each bandwidth. Since the standard deviation was found to be frequency insensitive, the results were combined over each frequency interval considered (e.g., 700 to 800 MHz, 800 to 900 MHz, … 1700 to 1800 MHz), and are shown plotted in Figure 8-6 for the "average" and "best" cases for Site 4. It is noted that at a 2 MHz bandwidth the standard deviation is approximately 0.5 dB, whereas the deviations become considerably larger at 90 MHz, ranging from 2.5 to 3.5 dB.

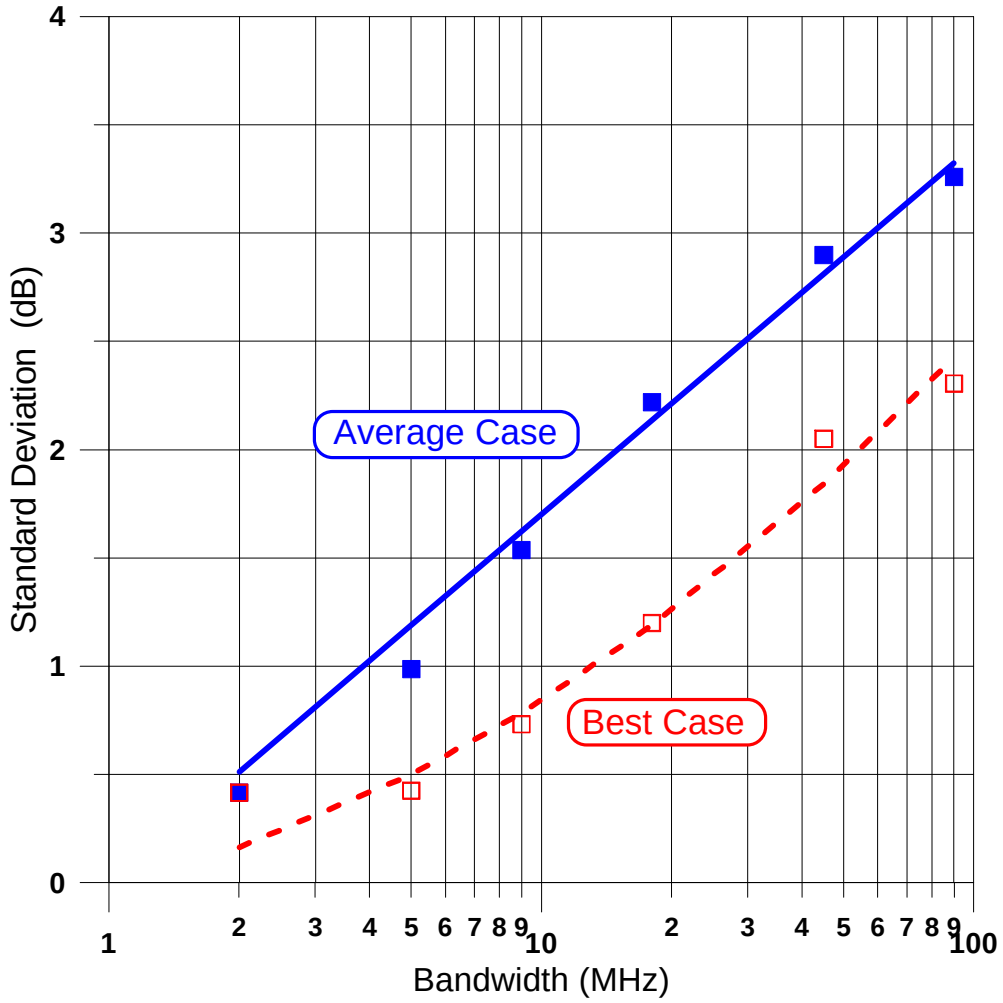

Figure 8-6: Standard deviation versus bandwidth for Site 4 for the "average" and "best" cases.

The standard deviation was found to follow the regression relations for each site as given by:

Average Case

$$STD = a \log(BW) \tag{8-4}$$

Best Case

$$STD = b \log(BW) + g (\log(BW))^2 \tag{8-5}$$

where α, β, γ, are tabulated in Table 8-6 for the various site locations, STD is the standard deviation given in dB, and BW is the bandwidth given in MHz (2 to 90 MHz).

Table 8-6: Parameter values for standard deviation versus bandwidth as given by (8-4) and (8-5).

Site			
1	1.6	0.12	0.61
2	1.6	0.03	0.56
3	2.6	2.82	-0.31
4	1.7	0.42	0.42
5	1.4	-0.02	0.55
6	2.4	1.9	0.31

8.3 Slant-Path Building Penetration Measurements at L- and S-Band

In this section, we describe the results of another campaign of Vogel et al. [1995a, 1995b] who executed L- and S-Band slant path fade measurements in six different buildings employing a tower-mounted transmitter and a dual frequency receiver system. Separate circularly polarized antennas were used at the receiving end of the link. The objective of this set of measurements was to provide inside building signal loss information associated with personal communications satellite design. In particular, the correlation of fading inside buildings between frequencies near 1620 MHz and 2500 MHz was examined. The measurements described in the previous section [Vogel and Torrence, 1993] were targeted towards the application of broadcasting from geostationary satellites as they used a relatively directive receiving antenna in their measurements. In the effort described here, azimuthally omni-directional antennas were employed which interact to a greater degree with the multipath environment.

8.3.1 Experimental Description

The measurement system is comprised of a single transmitting antenna located approximately 20 m from the ground atop a tower mounted on a van. Transmissions were executed in one of two modes. Mode 1 corresponded to the case in which transmission occurred at simultaneous fixed frequencies of 1618 and 2492 MHz. Mode 2 corresponded to the case in which simultaneous radiation occurred at two swept frequency ranges, namely, 1580-1780 MHz and 2330-2530 MHz. The L- and S-Band receiving antennas were spaced 5 cm apart and both were mounted on a positioner (described in the previous section) capable of automatically scanning either in the vertical or horizontal at 5 cm increments over a range of 80 cm (16 positions). As mentioned, the receiving antennas had patterns that were azimuthally omni-directional with a peak gain at about 30° in elevation. When Mode 1 was selected, the processed outputs were relative power level versus time for L- and S-Band with a time sampling rate of 100 Hz. When Mode 2 was selected, processing resulted in frequency spectra over ±80 MHz relative to the center frequencies of 1680 and 2430 MHz with about 1 MHz resolution and obtained over a 0.1 s sweep duration. In this mode, 160 sample pairs for L- and S-Band were saved to a computer file for every sweep lasting 0.1 s. Subsequent to the

co-polarized measurements, the experimental procedures were repeated with cross-polarized receiving antennas in order to establish the efficacy of frequency reuse employing multiple polarizations.

Measurements were made into six different buildings during the Fall of 1994. The names of these buildings, pertinent construction details, and the path elevation angles are given in Table 8-7. EERL, The Commons, and the Farmhouse were previously referred to by Vogel and Torrence [1993] (Section 8.2) as Sites 1, 3, and 5, respectively in Table 8-2.

The van with processing instrumentation and mounted tower was placed outside of each of the buildings, and transmissions from the radiating antenna simulated those emanating from a satellite. Each experiment included a calibration procedure during which the co-polarized power level was measured outside the building. This co-polarized power level was used as a relative reference (clear line-of-sight) of the power measurement interior to the building.

Table 8-7: Building characteristics and measurement parameters.

Building Name	Year of Construction	Construction Type	Roof Type	Avg. El.(°)	Distance Meas. (m)
Commons	1987	concrete tilt wall	tar	16	16
EERL Office	1944	block brick	tar	30	8.8
Farmhouse	1880	wood frame	wood shingle	57	19.2
House	1958	wood frame	composition	40	12
Motel	1980	brick	composition	26	8
Store	1967	steel frame	tar	37	16

8.3.2 Stability of Measurement

An example of a 50 second time series of power is given in Figure 8-7 for L- and S-Bands for the Commons for both co-polarized and cross-polarized levels at fixed antenna positions. The standard deviation for the case shown is less than 0.2 dB at L-Band and S-Bands. Similar stability measurements were executed at the five other sites and the overall average of the standard deviations was less than 0.5 dB at both frequencies. This variability is a measure of the uncertainty in the measurements and reflects system stability, possible transmitter motion, people motion, and ambient interference.

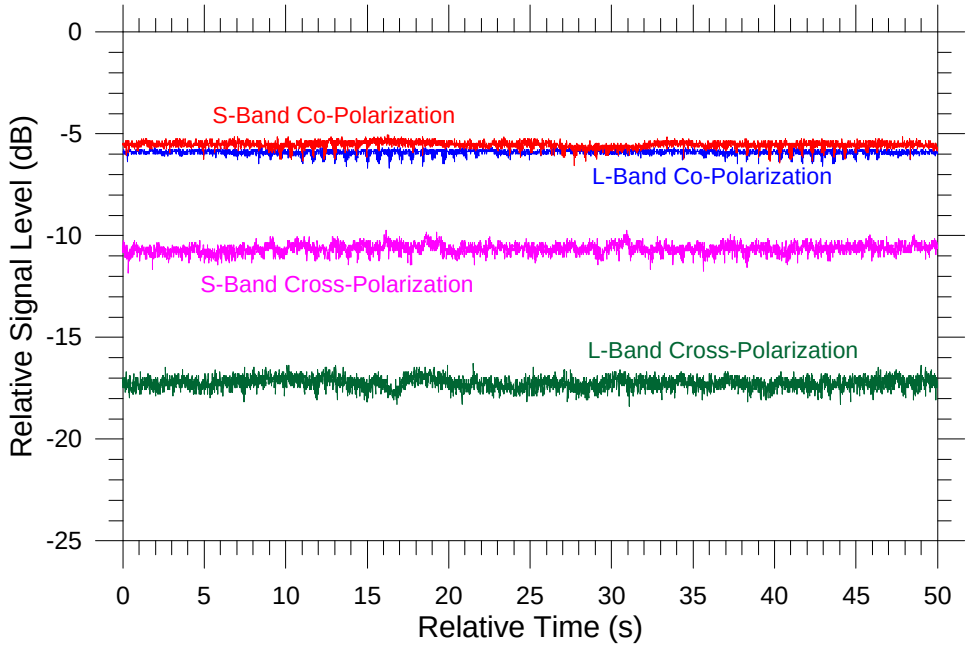

Figure 8-7: Example of 50 s time series of relative signal level measured at the Commons for both co-polarized and cross-polarized levels and fixed antenna positions.

8.3.3 Space Variability

Figure 8-8 illustrates the spatial variation of power levels received at 1618 and 2492 MHz with co-polarized and cross-polarized antennas as a function of position inside the Commons Building, and Figure 8-9 summarizes the statistics for the median, 5%, and 95% levels for all the site locations. Table 8-8 lists the median values for the L- and S-Band frequencies as well as the overall average median at these wavelengths. Table 8-9 and Table 8-10 also summarize the mean and standard deviation for the six site locations for the co-polarized and cross-polarized cases, respectively. We note from Table 8-8 and Table 8-9 that the overall average median and mean power levels show 1.0 dB and 0.5 dB larger fades at S-Band relative to L-Band. In fact, for some of the sites the fading at L-Band is larger than at S-Band. We may conclude from these results that a small difference in the fading exists at the two frequencies.

The relative attenuation at L- and S-Bands is complicated in that the fading into buildings depends both on the absorption by building materials and the reflection and scattering properties of the building skeleton and ambient obstacles. A steel mesh, for example, may be less transmissive at the longer L-Band wavelength than at the shorter S-Band wavelength, resulting in smaller attenuation for the latter. On average, the overall mean powers (over all site locations) are -14.6 dB and -15.1 dB at L- and S-Bands, respectively, with a standard deviation of 6.5 dB at both wavelengths. It is also interesting to note that the power losses are for the most part uncorrelated, as the average correlation coefficient is 0.28.

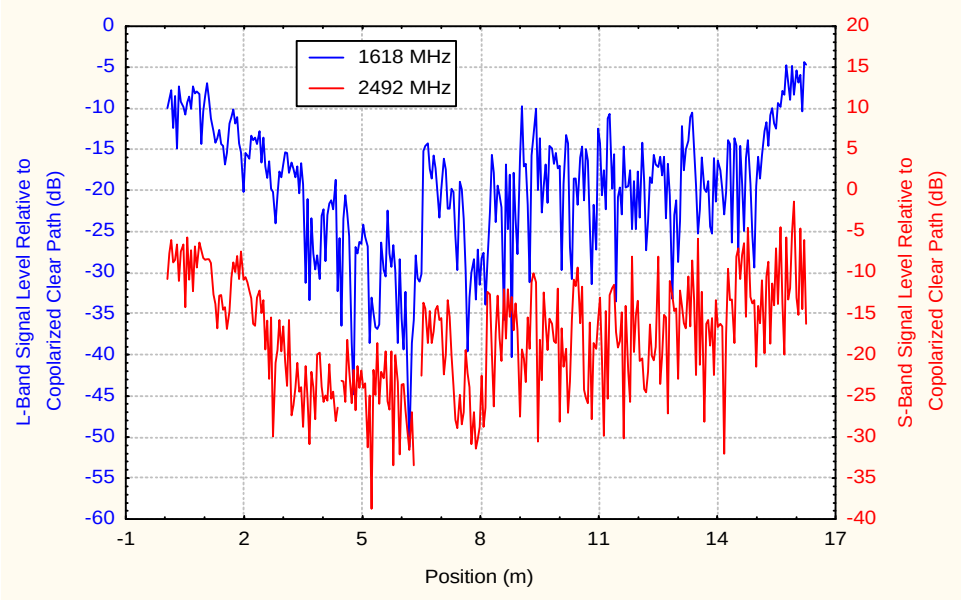

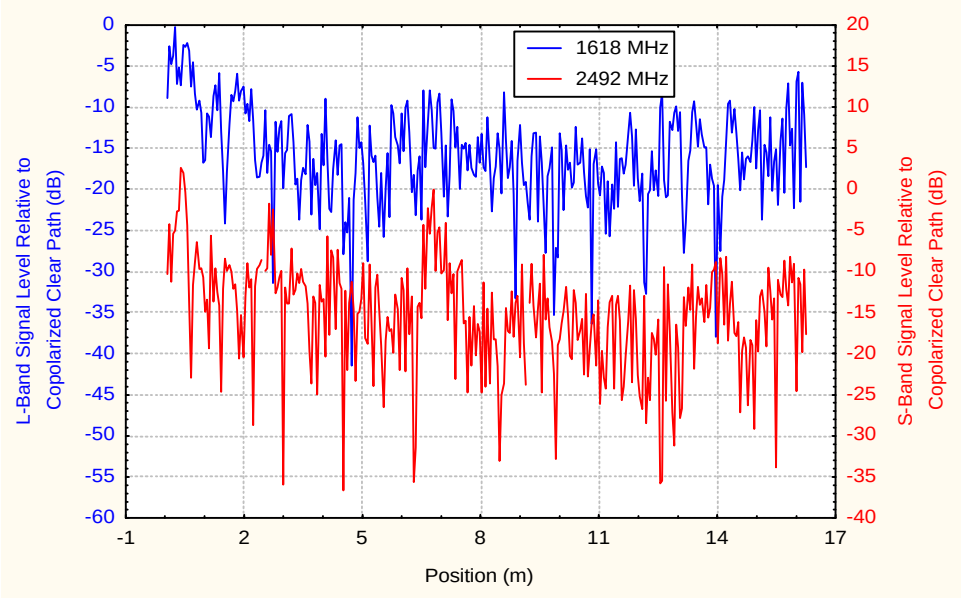

Figure 8-8: Received power levels at 1618 MHz and 2492 MHz inside the Commons. The co-polarized and cross-polarized levels are the upper and lower figures, respectively. The upper traces represent L-Band (left scale) and lower traces S-Band (right scale).

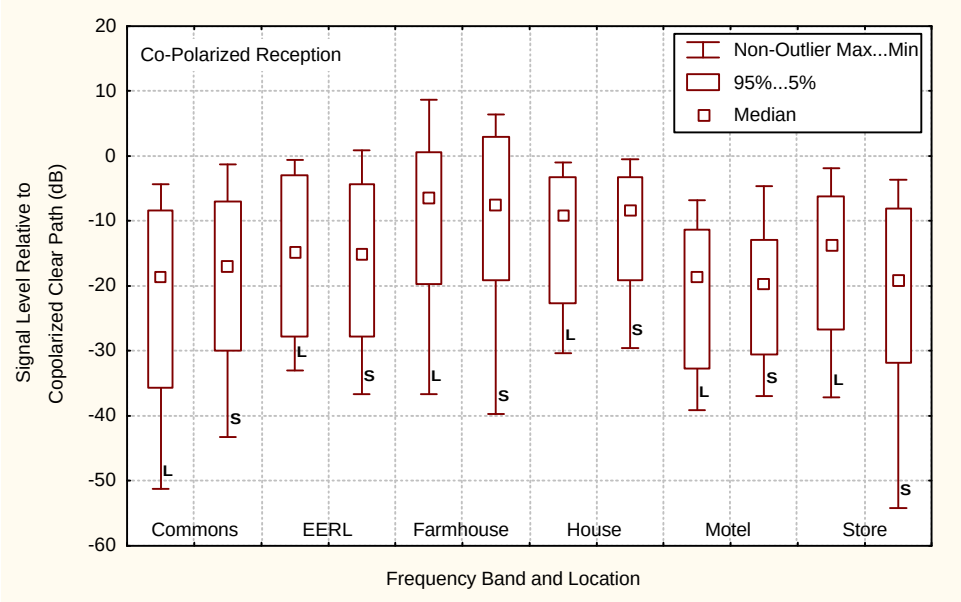

Figure 8-9: Summary of statistics at L- and S-Band giving median, 95%, and 5% levels of the relative power losses inside the six buildings for the case in which the antennas were moved horizontally over multiple 80 cm intervals.

Table 8-8: Summary of medians of the relative signal loss inside the six buildings at L- (1618 MHz) and S-Band (2492 MHz).

Site	Median Fade (dB)	
	L-Band	S-Band
Commons	-18.6	-17.1
EERL	-14.7	-15.1
Farmhouse	-6.5	-7.5
House	-9.1	-8.4
Motel	-18.5	-19.7
Store	-13.7	-19.2
Average	-13.5	-14.5

The overall averaged cross-polarized relative power levels are only 2.3 and 1.6 dB smaller than the corresponding co-polarized power levels at L- and S-Band, respectively (Table 8-9 and Table 8-10). For example, the average relative cross-polarized power levels at L- and S-Bands are -16.9 dB and -16.7 dB, whereas the average relative co-polarized levels are -14.6 dB and -15.1 dB. These results suggest that the isolation between polarizations inside buildings is small, obviating the possibility of employing intra-system frequency re-use for gaining additional spectral capacity, although not the possibility of inter-system frequency re-use for achieving higher isolation between different satellite communications systems.

Table 8-9: Summary of statistics associated with spatial variations of L- (1618 MHz) and S-Band (2492 MHz) co-polarized relative power levels during spatial scans inside buildings.

Building	L-Band		S-Band		Correlation
	Mean (dB)	STD (dB)	Mean (dB)	STD (dB)	
Commons	-19.9	8.1	-18.0	7.2	0.56
EERL	-15.0	6.9	-15.6	6.9	0.34
Farmhouse	-7.4	6.1	-7.9	7.1	0.28
House	-10.6	5.7	-9.6	5.1	0.13
Motel	-19.8	6.3	-20.1	5.6	0.05
Store	-14.7	6.2	-19.5	7.3	0.34
Average	-14.6	6.5	-15.1	6.5	0.28

Table 8-10: Summary of statistics associated with spatial variations of L- (1618 MHz) and S-Band (2492 MHz) cross-polarized relative power levels during spatial scans inside buildings.

Building	L-Band		S-Band		Correlation
	Mean (dB)	STD (dB)	Mean (dB)	STD (dB)	
Commons	-16.0	6.1	-15.5	7.1	0.21
EERL	-18.1	5.4	-16.0	5.4	0.01
Farmhouse	-10.3	8.0	-11.6	8.7	0.54
House	-16.2	5.6	-15.4	5.8	0.12
Motel	-21.0	6.0	-19.8	5.1	0.16
Store	-20.0	6.4	-22.0	6.0	0.15
Average	-16.9	6.25	-16.7	6.35	0.20

Table 8-11 summarizes the statistics associated with the instantaneous differences in the S-and L-Band powers received during the spatial scans at the various site locations. The difference power level was found to be Gaussian distributed as depicted by the example given in Figure 8-10. The mean difference indicates whether on average there is a bias of the power levels at one frequency relative to the other. We note that on average, the bias ranges from +1.9 dB for the Commons to -4.8 dB for the Store sites, with an overall average bias of approximately -0.6 dB. For all sites, the standard deviations are significantly larger than the respective means. The relative lack of correlation between the instantaneous L- and S-Band fades suggests the difficulty of applying power control to a link operating in this environment.

Table 8-11: Statistics associated with power differences between co-polarized S-Band and L-Band for spatial scans at each of the site locations.

Building	Mean Difference (dB)	STD (dB)
Commons	1.9	7.2
EERL	-0.6	7.9
Farmhouse	-0.5	7.9
House	1.0	7.2
Motel	-0.30	8.2
Store	-4.8	7.8
Average	-0.55	7.7

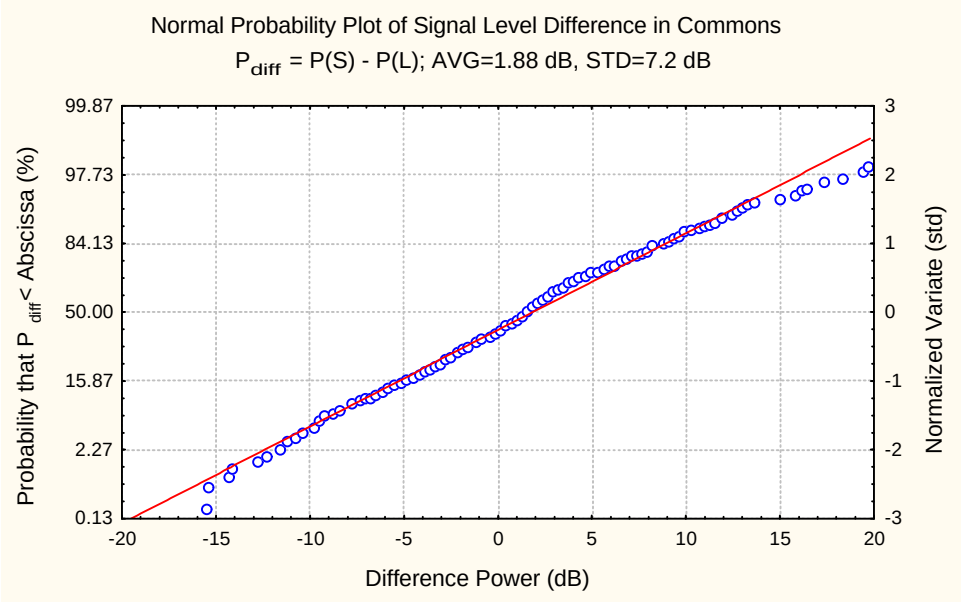

Figure 8-10: Cumulative probability distribution of signal level difference of the instantaneous S-Band minus the L-Band powers. The indicated straight line implies a Gaussian distribution with a mean and standard deviation of 1.9 dB and 7.2 dB, respectively.

8.3.4 Frequency Variability

Rapid changes of the power with frequency occur only when the average power level is comparable to the diffusely scattered power. This concept is illustrated in the frequency scan example in Figure 8-11 which shows the power levels relative to the center frequencies of 1680 MHz and 2430 MHz obtained at the EERL Building. Four cases were selected from all positions, namely frequency scans with mean relative received power levels of -20, -15, -10, and -5 dB. It is noted that when the mean signal level is -5 dB, the variability of the signal level over the 160 MHz band is relatively small (e.g., -3 dB maximum and -10 dB minimum for both L- and S-Bands). On the other hand, the

-20 dB mean level shows signal loss deviations that are significantly larger over the frequency scan (e.g., -12 dB maximum and -38 dB minimum at L-Band).

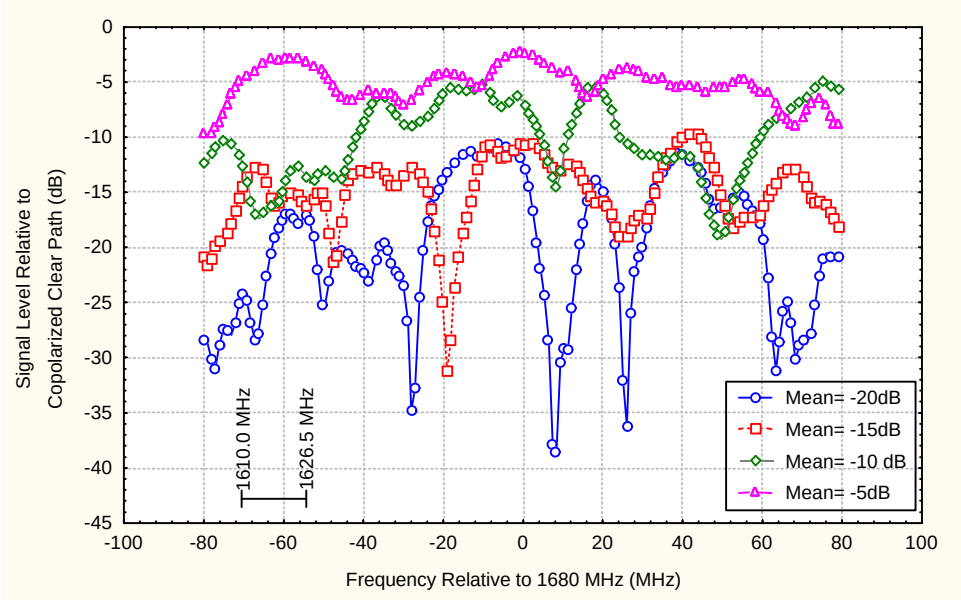

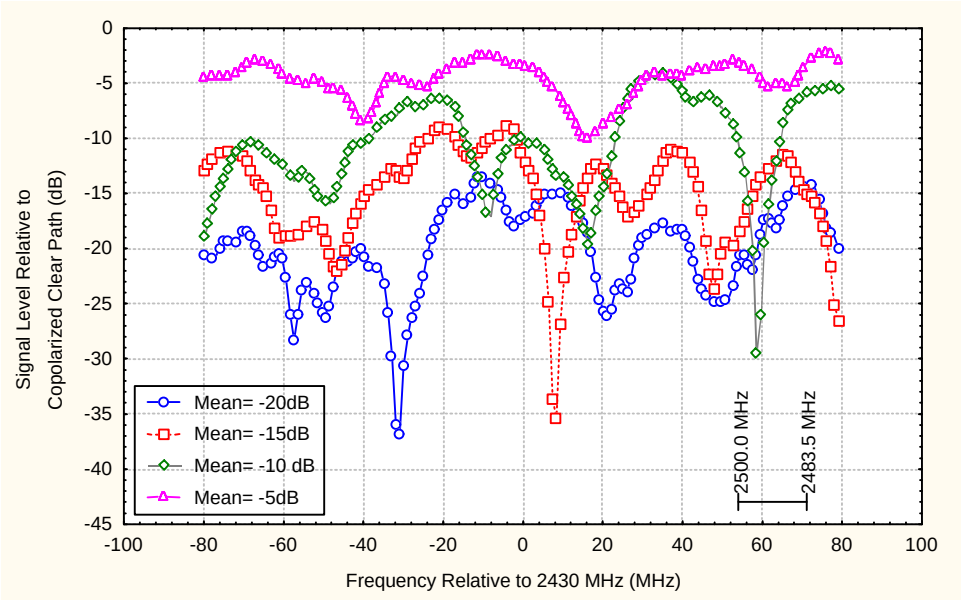

Figure 8-11: Relative power loss variation with frequency at L-Band (upper figure) and S-Band (lower figure) for various mean power levels over the 160 MHz bandwidth.

An indicator of the frequency variability is the fade slope as a function of frequency defined by

$$FS = \frac{dS}{df} \quad \text{(dB/MHz)}, \tag{8-6}$$

where *dS* is the change in the received co-polarized power over the 1 MHz frequency interval *df*. A regression expression has been established relating the standard deviation of the fade slope to the mean signal level μ_{SL} over the frequency span for each of the buildings at both L- and S-Band. This expression is given by given by

$$s_{FS} = a + bm_{SL} + cm_{SL}^2, \tag{8-7}$$

where *a*, *b*, *c* are tabulated in Table 8-12 for the L- and S-Band wavelengths. Summary statistics describing the mean and standard deviation of the fade slopes at the various site locations are given in Figure 8-12. It is noted from Figure 8-12 that the median fade slopes (upper figure) varies between 0.5 and 1.3 dB/MHz and the corresponding median standard deviations (lower figure) vary between 1.8 and 0.7 dB/MHz. We conclude from these levels that for a resolution of 1 MHz the frequency distortion is expected to be small over the frequency range 1680 to 2430 MHz.

Table 8-12: Tabulation of standard deviation parameters in (8-7) for different site locations at L- and S-Band.

Location	L-Band			S-Band		
	a	*b*	*c*	*a*	*b*	*c*
Commons	-0.589	-0.11	0.000	-0.52	-0.123	-0.001
EERL	0.323	0.038	0.004	0.296	0.027	0.003
Farm	0.298	-0.047	0.003	0.196	-0.014	0.003
House	0.169	-0.015	0.002	0.237	0.026	0.004
Motel	0.531	0.063	0.004	0.342	0.047	0.004
Store	0.379	0.008	0.004	0.549	0.057	0.004

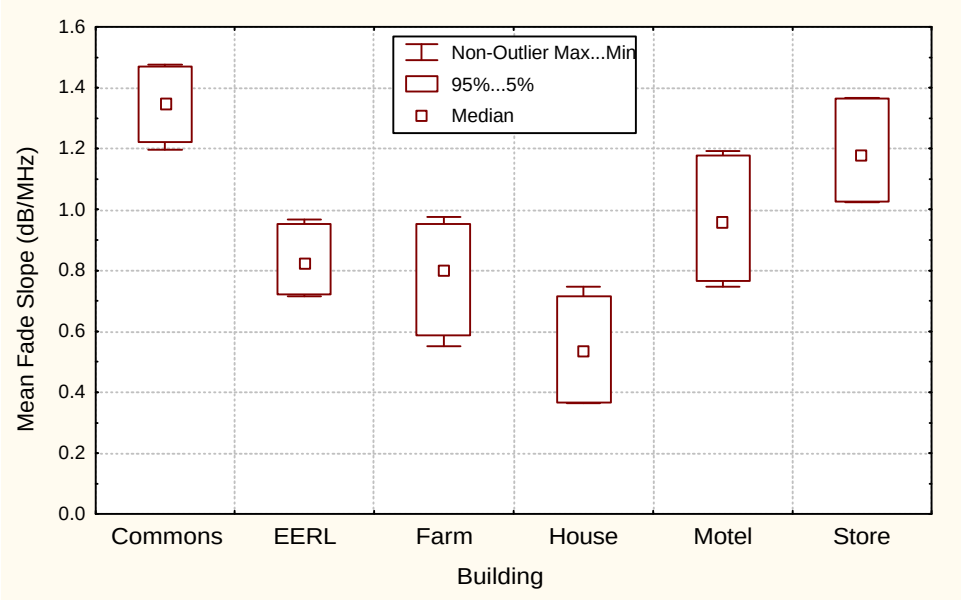

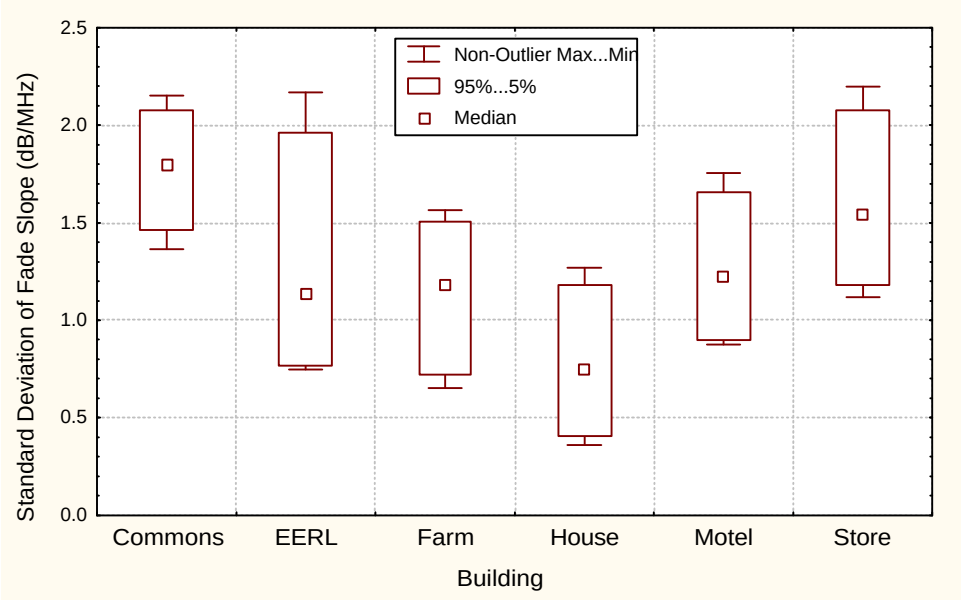

Figure 8-12: Summary statistics giving the median, 95% and 5% levels of the mean fade slope (upper figure) and the standard deviation of the fade slope (lower figure) at the various site locations.

8.4 Slant-Path Building Attenuation Measurements from 0.5 to 3 GHz

In this section we describe the results of Vogel and Torrence [1995c] who executed a comprehensive set of measurements in which they examined attenuation levels over swept frequencies ranging from 500 MHz to 3000 MHz into a set of six buildings. These results extend those of Vogel and Torrence [1993] who examined fading within buildings

over the frequency range 700 MHz to 1800 MHz (described in Section 8.2). In the effort described here, Vogel and Torrence used a similar experimental configuration employing an antenna mounted on a tower which simulated transmissions from a satellite platform and which radiated right hand circular polarization signals (RHCP). The receiving antenna received RHCP over a beamwidth of 90° in both the vertical and horizontal principal planes. As in the previous experiment, the receiving antenna inside each of the buildings was located on a positioner that moved it in 5 cm increments over 16 spatial positions (80 cm).

8.4.1 Experimental Description

The major components of the experiment of Vogel and Torrence were a 20 m crank-up transmitter tower mounted on a van, a vector network analyzer (VNA), a personal computer (PC), and a linear positioner. One of the two wideband antennas was mounted atop the tower outside a building and the other at the positioner inside where the relative signal levels (in dB) were determined. As previously described, the relative signal levels were determined by comparing the levels measured interior to each of the buildings with the reference levels measured for the unobstructed line-of-sight case outside. The PC controlled the VNA and linear positioner, and stored the data from the VNA. The relative signal frequency was swept between 500 MHz to 3000 MHz at 1 MHz increments and the data were analyzed at a step bandwidth of 0.2% of the frequency. At the low frequency end, the sampling increment was therefore 1 MHz (500 MHz x 0.002) and at the high end it was 6 MHz (3000 MHz x 0.002). Measurements were made into six different buildings during the Spring of 1995. The names of these buildings and pertinent parameters are summarized in Table 8-13. The Commons, EERL, the Farmhouse and the Motel were sites also used in the L- and S-Band investigations [Vogel and Torrence, 1995a; 1995b] described in Section 8.3. Photographs of the exterior buildings and floor layouts with measurement locations within each of the buildings listed in Table 8-13 are given by Vogel and Torrence [1995c].

Table 8-13: Building names and pertinent characteristics.

Building Name	Year of Construct.	Type	# of Stories	Roof Type	Avg. El. (°)	No. of Locat.
Commons Entry	1987	concrete wall	1	tar	18	7
EERL	1944	block brick	1	tar	38	6
Farmhouse	1880	wood frame	2	metal	33	12
House	1976	wood frame	2	metal	41	10
MER	1992	glass, concrete	2	tar	26	9
Motel	1980	brick	2	composition	37	8

8.4.2 Average Signal Levels over Frequency Band and Positions

Figure 8-13 summarizes the overall relative signal loss results at the various building locations. The mean, standard deviation, minimum and maximum values were obtained

after averaging the signal loss over the frequency band at each position (e.g., average at approximately 900 frequency values). The averages of these means were then taken over all locations (e.g., 16 positions of positioner times number of locations within the building as given in last column of Table 8-13). Table 8-14 lists the mean value and standard deviations given in Figure 8-13. The overall average is shown to be -11.9 dB with an average standard deviation of 7.4 dB (last row of table). The mean relative signal losses vary between -5 dB (in Farmhouse) and -19.5 dB in the House. Although both have metal roofs, the House also has an aluminum heat shield in all exterior walls. The other four buildings fall into the range of approximately -9 dB to -13 dB. These results also include data in which the receiving antenna was located in an open door or window in sight of the transmitter.

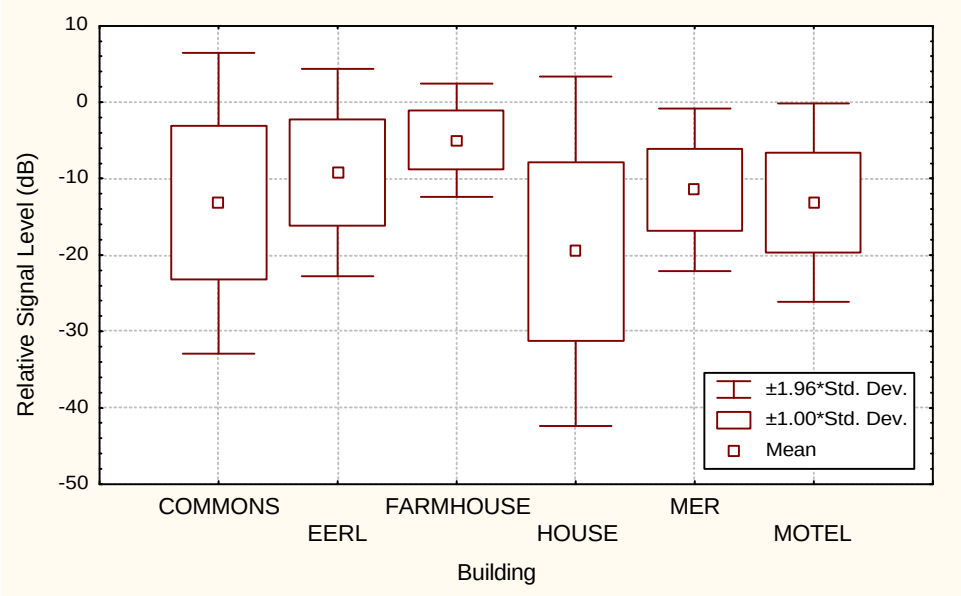

Figure 8-13: Relative signal level statistics at each of the building locations.

Table 8-14: Listing of the mean and standard deviations when relative signal loss is averaged over position and frequency (0.5 to 3.0 GHz).

Site	Mean (dB)	Standard Deviation (dB)
Commons	-13.2	10.0
EERL	-9.2	6.9
Farmhouse	-5.0	3.8
House	-19.5	11.6
MER	-11.5	5.4
Motel	-13.1	6.6
Overall Average	-11.9	7.4

8.4.3 Distance and Frequency Dependence

Figure 8-14 shows an example describing the relative signal level versus position at four frequencies extending over approximately 1 GHz to 3 GHz for the Commons. We note the relative signal varies between -15 to -30 dB for scenarios in which the direct path penetrates a concrete wall (e.g., 0 to 3 m). It increases to the range of -5 to +5 dB as the antenna moves across the window area and ends up outside the open door (e.g., 4 to 5.5 m). By contrast, an extreme case is depicted in Figure 8-15 for the House that shows levels ranging from -25 dB to -45 dB. These low fade levels are presumed to occur because the construction includes a metal roof and a tight energy conserving aluminum heat shield under the cedar exterior.

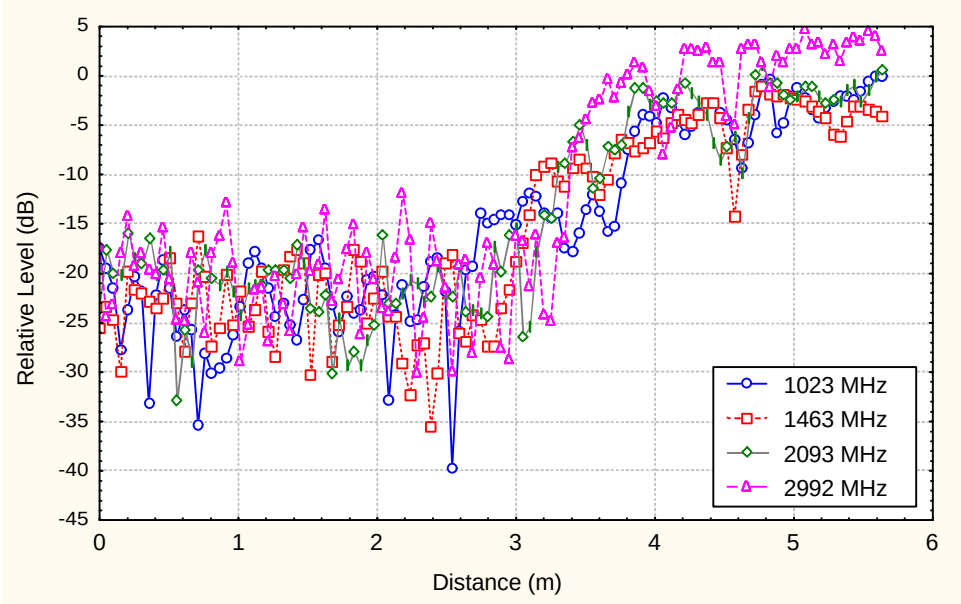

Figure 8-14: Relative signal level versus position at four frequencies in the Commons.

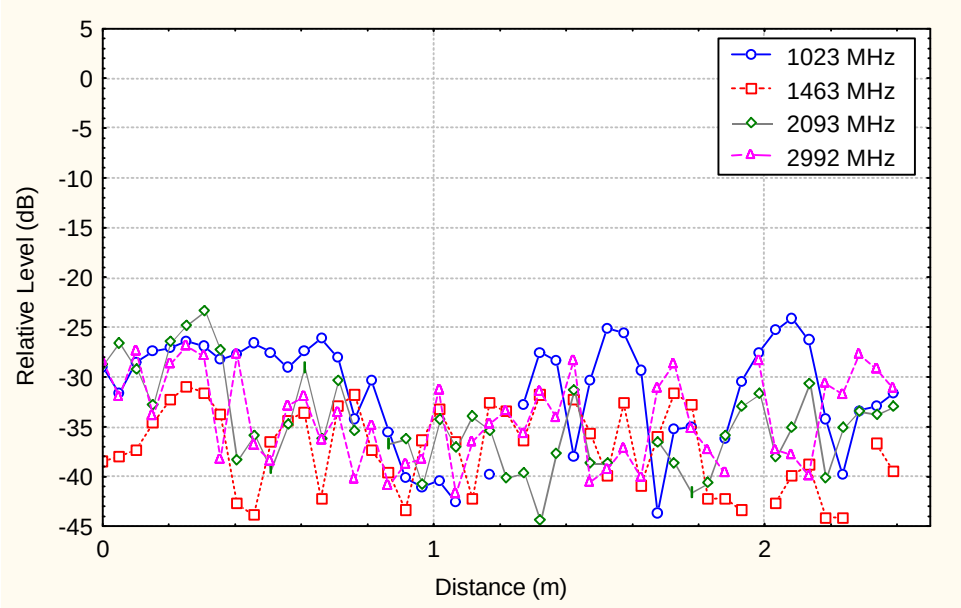

Figure 8-15: Relative signal level versus position at four frequencies in the House.

8.4.4 Spatial Autocorrelation Characteristics

The autocorrelations were calculated at approximately 900 frequency samples for lags from 0 m to 3.2 m. Figure 8-16 gives an example of the spatial autocorrelations versus frequency for the EERL Building at a lag of 50 cm. The overall data do not exhibit a clear frequency dependence in spite of the fact that the wavelength at 500 MHz is 60 cm whereas it is only 10 cm at 3 GHz. The median value of the autocorrelations in Figure 8-16 is 0.37. The autocorrelation as a function of distance at 1625 MHz is plotted in Figure 8-17 for the Commons, EERL, and the Farmhouse. In Table 8-15 are listed the median decorrelation distances (i.e., distance at which autocorrelation equals 0.37) for each of the building sites. It is noted that the overall average is 0.71 m.

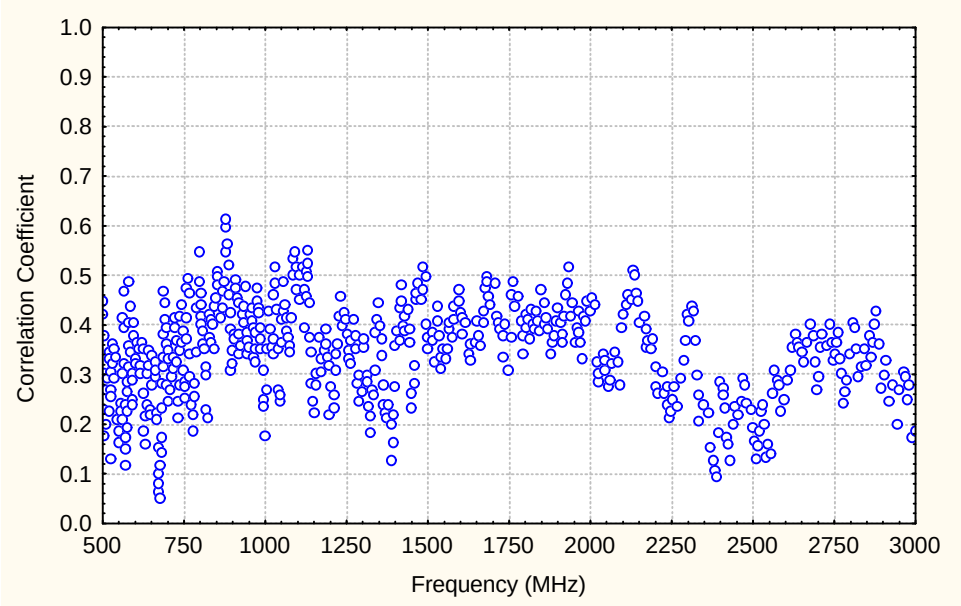

Figure 8-16: Spatial autocorrelation versus frequency at a lag of 50 cm for EERL.

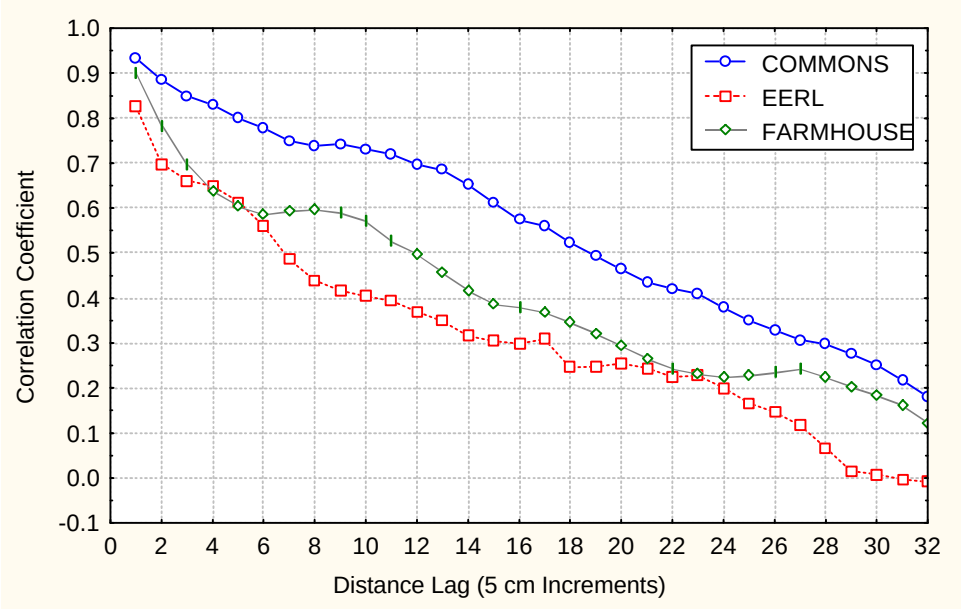

Figure 8-17: The spatial autocorrelation at 1625 MHz versus distance lag in Commons, EERL, and Farmhouse. The abscissa distance is the indicated number times 0.05 m.

Table 8-15: Median decorrelation distances at each building location.

Building	Median Decorrelation Distance (m)
Commons	1.1
EERL	0.5
Farmhouse	0.85
House	0.55
MER	0.7
Motel	0.55
Overall Average	0.71

8.4.5 Relative Signal Loss Versus Frequency

An example of the trend of the relative signal loss versus frequency over the interval 500 MHz to 3000 MHz at a fixed location in the Farmhouse is given in Figure 8-18. The trend slope of -0.006 dB/MHz is shown to exist over the frequency interval between 500 MHz and 3000 MHz. The trend slope should not be confused with the smaller scale frequency slope *FS* given by (8-6) which characterizes the change of signal level per MHz of bandwidth. The indicated trend slope in Figure 8-18 implies that over the frequency interval of 2500 MHz (500 MHz to 3000 MHz) the attenuation trend is such that the signal level is diminished by approximately 15 dB. An overall summary of the trend slope statistics is given in Figure 8-19 where all positions within each building are considered. We note that the Farmhouse represents an extreme case for the trend loss as all the other sites have significantly smaller values.

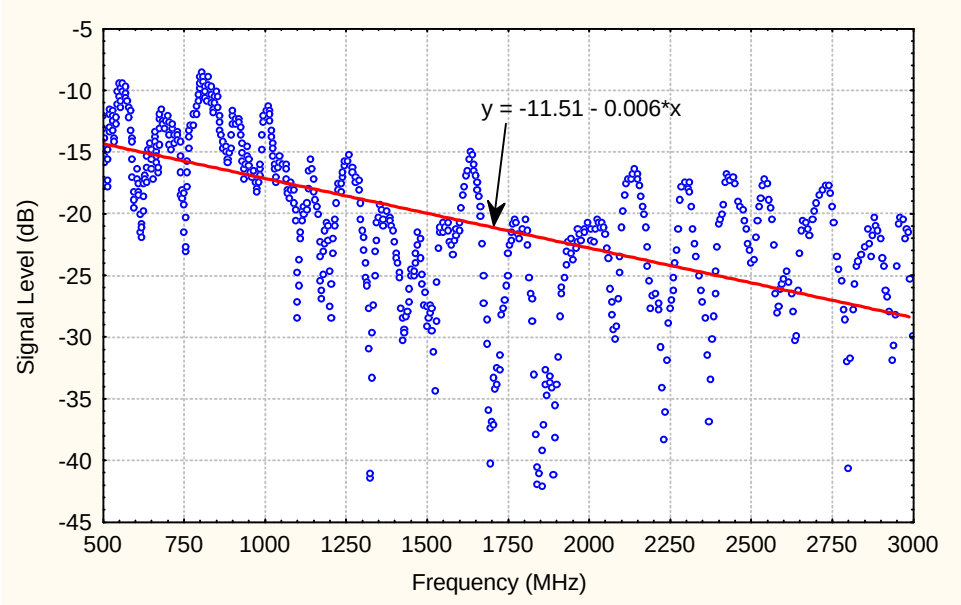

Figure 8-18: Dependence of relative signal level with frequency in the Farmhouse. The trend slope is shown to be -0.006 dB per MHz.

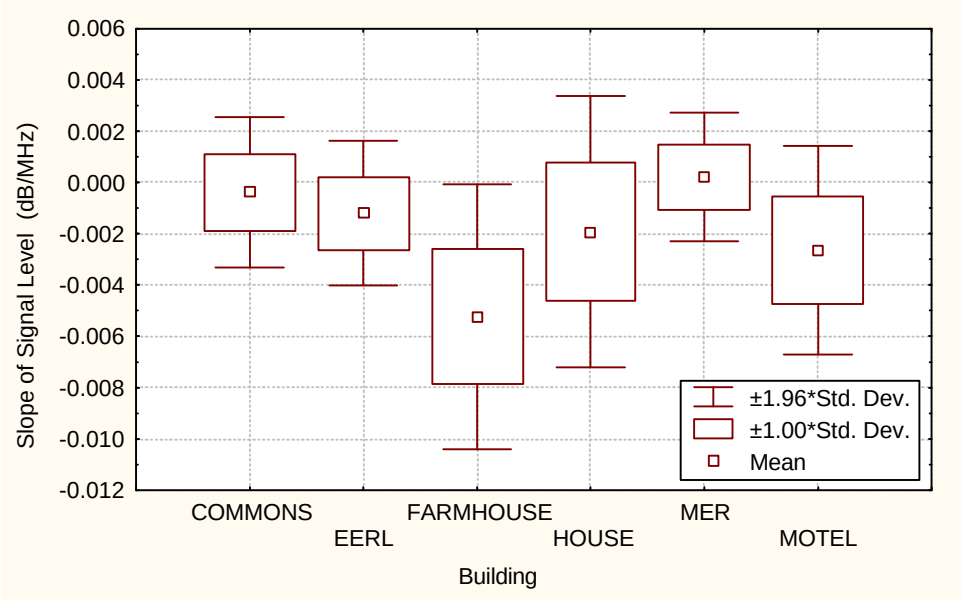

Figure 8-19: Summary of trend slope statistics in the six building.

The autocorrelation of frequency variability reveals information regarding systems which attempt to mitigate fading employing power control on the uplink (mobile to satellite) at one frequency using knowledge of the fade on the downlink (satellite to mobile) at another frequency. An example of the autocorrelation at a given receiver location is plotted for each building in Figure 8-20. At 500 MHz, the lag of 10, for example, implies a bandwidth separation of 10 x 0.002 x 500 MHz = 10 MHz. At 3000 MHz, the lag of 10 implies a bandwidth separation of 60 MHz. The lag of 10 gives an autocorrelation of approximately 0.6 for the Farmhouse and 0.1 for the motel (extremes). Table 8-16 summarizes the median decorrelation bandwidths (decorrelation = $\boldsymbol{e}^{-1}$ = 0.37) when all positions are accounted for within each of the buildings. The overall average of the median decorrelation is 2.4% of the frequency for the case in which the farmhouse is not included and 5.4% when the farmhouse is included.

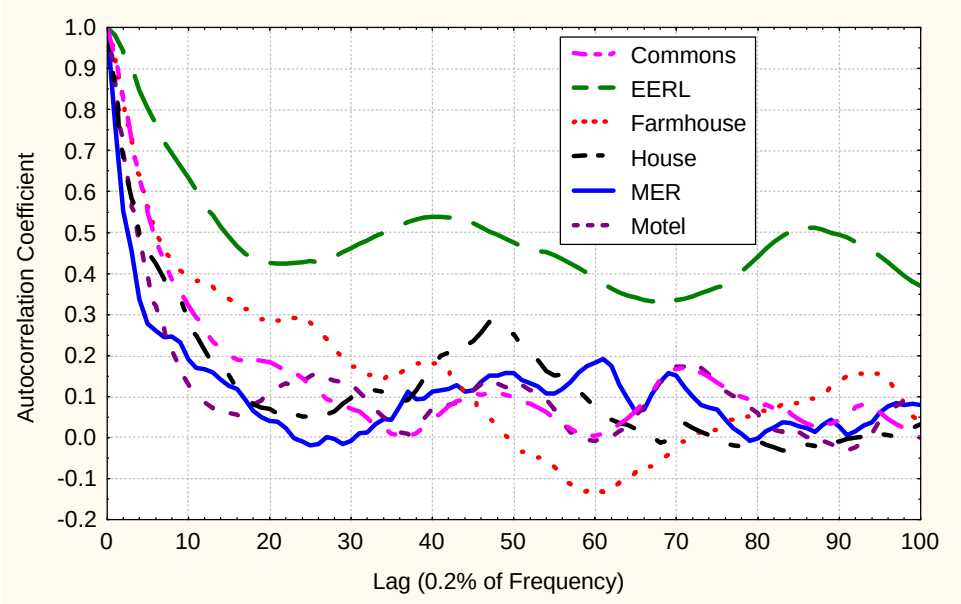

Figure 8-20: The frequency autocorrelation at a fixed location in each building for frequency lags from 0 to 20%. The lag of 10, for example, implies 10•0.002•*f* (MHz).

Table 8-16: Summary of median decorrelation bandwidths when all positions within each building are considered.

Building	Median Decorrelation Bandwidth (% frequency)
Commons	2.0
EERL	3.6
Farmhouse	20.2
House	1.6
MER	1.2
Motel	3.8
Overall Average without Farmhouse	2.4
Overall Average with Farmhouse	5.4

8.5 Building Attenuation at UHF, L- and S-Band Via Earth-Satellite Measurements

In this section are described building attenuation measurements at 860 MHz, 1550 MHz, and 2569 MHz using the Application Technology Satellite No. 6 (ATS-6) as the radiating platform [Wells, 1977]. Transmissions at each of the frequencies were right-hand circularly polarized and the receiving antenna was a vertically polarized azimuthally omni-directional conical monopole located above a short ground plane. Measurements were made on several wood-frame siding houses and several wood frame brick-veneer houses in five geographic locations. The elevation angles at these location were 36.1°

(Duluth, MN), 42.3° (Boulder, CO), 44.7° (Kansas City, MO), 49.6° (Little Rock, AK), and 55.4° (Houston, TX). A series of measurements were made at different locations within each house (e.g., 16) and related to measurements made outside the house to obtain the relative attenuation. The average attenuation and standard deviation for each house were subsequently determined.

8.5.1 Experimental Results

Wells emphasizes in his results: (1) two building types; wood siding and brick veneer, (2) two insulation types; ceiling, and ceiling and walls, and (3) two room exposure types; one or more exposed walls and no exposed walls. An exposed wall implied that the line-of-sight path passed through a single wall, whereas an unexposed wall scenario implied that another room or another wall sheltered the wall. A four factor model including frequency (4 levels), construction type (2 levels), insulation type (2 levels), and room position (2 levels) was developed and summarized by the listing in Table 8-17.

To obtain the overall attenuation for a particular structure from Table 8-17, we execute the following example steps: (1) The "Average Value" of 6.3 dB is added to values described in subsequent steps. (2) For a frequency of 2.569 GHz, we add +1.16 dB to the average value. (3) For a brick veneer construction, we add +0.58 dB. (4) For a structure with insulation in both ceiling and walls, add +0.8 dB. (5) For a room with unexposed walls, add +0.30 dB. The overall attenuation is 9.14 dB for the above combination of effects. Wells culls out several "high attenuation" structures. These are two mobile homes (average attenuation of 23.6 dB) and two wood frame houses with interior walls and ceiling comprised of plasterboard backed with aluminum foil (average attenuation of 17.1 dB). Wells also shows that no significant attenuation occurs as a function of elevation angle.

Wells summarized the above results as follows: (1) On average, the signal level varied by 0.6 dB as a function of position of a room within each house. (2) Houses having brick veneer gave rise to a 1.2 dB higher attenuation than houses with wood siding. (3) Insulation in ceiling and walls caused about 1.6 dB higher attenuation than insulation in ceiling only. (4) Insulation and plasterboard with aluminum backing caused attenuations between 14.6 to 22 dB. (5) The attenuation at 2.569 GHz was approximately 2.9 dB larger than at 860 MHz. (6) Horizontal polarization at 860 MHz gave approximately 1.8 dB higher attenuation than vertical polarization.

Table 8-17: Average attenuation contributions at UHF, L, and S-Band [Wells, 1977].

Parameter	Characteristic	Attenuation Contribution (dB)
Frequency	2.569 GHz	1.16
	1.550 GHz	0.39
	0.860 GHz (V)	-1.69
	0.860 GHz (H)	0.14
Construction	Wood Siding	-0.58
	Brick Veneer	0.58
Insulation	Blown-In Ceiling	-0.80
	Ceiling and Walls	0.80
Room Position	Exposed Walls	-0.30
	No Exposed Walls	0.30
Overall Average	6.3 dB	

8.6 Attenuation of 900 MHz Radio Waves by Metal Building

Hoffman and Cox [1982] describe attenuation measurements within a highly attenuating building in which the walls and roof were covered with corrugated overlapped steel sheets. The building contained a double door with windows covered with a 2.5 cm wire mesh. Secondary metal window screens (two in front) and metal screen doors also existed. Four-1.2 m cube volumes were sampled within the building. Signals emanated at 900 MHz from a vertically polarized corner reflector antenna. The antenna was located on a line perpendicular to the front of the building and was at a height of 3 m above the ground. The receiver antenna was a half-wavelength skirted coaxial antenna mound vertically on a wooden scanning mechanism. Linear 1.2 m long scans were made parallel to the front wall of the building at 0.9, 1.5, and 2.1 m heights. Attenuation distributions were found to be approximately Rayleigh distributed with medians ranging from 26 dB to 32 dB within small areas. The overall median attenuation for the entire building was 29 dB.

8.7 Summary and Concluding Remarks

8.7.1 Required Fade Margins

Table 8-18 summarizes the levels of the relative power losses in terms of the overall averages of the means, standard deviations and the medians for all sites investigated with the exception that the results of Site 6 in the first row has not been included. (Note that the references by Vogel and Torrence are denoted as V&T). This site (characterized in Table 8-2 was considered an extreme attenuating environment and therefore is not considered. The results in each row of Table 8-18 were culled from the listed tables

(fourth column), and the originating reference is listed in the last column. Similar type results are given in Table 8-19 for the site location with the highest fading (again with the exception of Site 6 as mentioned above). We may conclude that; (1) fade margins of at least 30 dB (e.g., mean loss plus two standard deviations) are required to achieve relatively reliable communications for most cases vis-à-vis the overall average fading, and (2) 40 dB are required for the worst case sites.

Table 8-18: Summary of relative power losses in terms of overall average of worst case fading (all site average with exception of Site 6 for the first row).

Mean (dB)	Standard Dev. (dB)	Median Loss (dB)	Tables	Freq. Interval (GHz)	Reference
-10.2	5.8	-13.0	Table 8-3, Table 8-4	0.7-1.8	V&T [1993]
-15.1	6.5	-14.5	Table 8-9, Table 8-8	1.6, 2.5	V&T [1995a,b]
-11.9	7.4		Table 8-14	0.5-3.0	V&T [1995c]
-9.1	3.0		Table 8-17	0.86-2.57	Wells [1977]

Table 8-19: Summary of relative power losses in terms of worst site location.

Site	Mean (dB)	Standard Deviation (dB)	Median Loss (dB)	Frequency Interval (GHz)	Reference
Commons	-15.4	8.4	-18.0	0.7-1.8	V. &T. [1993]
Commons	-19.9	8.1	-18.6	1.6, 2.5	V. & T. [1995a,b]
House	-19.5	11.6		0.5-3.0	V. & T. [1995c]

8.7.2 Fading Dependence on Frequency

8.7.2.1 Small and Large Bandwidths Effects

The relative signal level may dramatically vary as the frequency is swept over intervals of 100 MHz due to multipath variability. An example of this variability is depicted by the fixed position frequency sweep in Figure 8-1, where the signal varies from -25 dB to 0 dB over the frequency interval 900 MHz to 1000 MHz, respectively. On the other hand, the trend fading over larger bands between 0.5 GHz to 3.0 GHz is generally small when the short frequency scale fluctuations are averaged. It may be deduced from Figure 8-19, that for five of the six sites the fade increased by only 3 dB and less over a 1 GHz frequency span. This fade increase is considered small compared to the smaller scale variability of fading over 100 MHz as shown in Figure 8-18. Wells [1977] also showed from direct earth-satellite measurements that small increases of the average fading occurred over the frequency interval between 0.86 and 2.57 GHz. From Table 8-17, the overall average fade increase over this band is indicated to be less than 3 dB.

Vogel and Torrence [1995a, 1995b] have characterized the short-term frequency variability as a function of the fade slope *dS/df* expressed in dB/MHz. This descriptor, which characterizes the change in the received power level over a 1 MHz bandwidth, is quantified in Figure 8-12. Values of the mean fade slopes range between 0.5 to 1.3 dB/MHz for the various building locations. These slopes should only be used over bandwidths of approximately 1 MHz.

8.7.2.2 Cumulative Distribution Dependence on Frequency

Vogel and Torrence [1993] developed a model giving the frequency dependence on the cumulative probability distribution of the relative signal loss for each of the sites. This model is given by Equations (8-1) through (8-3) where tabulations of the indicated coefficients are listed in Table 8-5.

8.7.2.3 Distortion Due to Bandwidth

Vogel and Torrence [1993] described the signal distortion in terms of the standard error relative to the mean signal loss over bandwidths ranging from 2 MHz to 90 MHz. Figure 8-6 shows that at 2 MHz, the standard error is 0.5 dB whereas the deviations range from 2.5 to 3.5 dB at 90 MHz. These results imply that relatively small distortions of the signal should be expected for bandwidths between 1 to 10 MHz. These results are consistent with time delay calculations as given in Figure 8-2.

8.7.2.4 Frequency Correlation

The autocorrelation of the relative signal loss was described as a function of the lag in frequency from 0 to 20% of the frequency (Figure 8-20) by Vogel and Torrence [1995c]. The median decorrelations (between 0.5 GHz and 3 GHz) were found to vary between 1.2 to 20.2% of the frequency with an overall average of 5.4%. Excluding the extreme case (Farmhouse), the median decorrelation varied between 1.2% and 3.8% with an overall average of 2.4% (Table 8-16). Such information is useful for establishing the efficacy of uplink power control at one frequency given knowledge of the power at another frequency.

8.7.3 Fading Effects Due to Antenna Position

8.7.3.1 Antenna Spacing between Maximum and Minimum Signal Levels

Vogel and Torrence [1993] determined the median antenna spacing between antenna positions giving maximum and minimum relative signal levels. The median position was found to be between 35 and 45 cm independent of frequencies between 0.7 and 1.8 GHz. The example in Figure 8-5 shows signal variability approaching 30 dB over this position interval. The spacing interval (between minima and maxima) was found to be Gaussian distributed with a mean of approximately 41 cm and a standard deviation of 17 cm. This mean distance suggests an optimum spacing that might be employed for space diversity systems.

8.7.3.2 Signal Variability Due to Antenna Positioning

Table 8-9 lists the standard deviations of the relative signal loss due to spatial variations of 80 cm at L- and S-Bands (1618 MHz and 2492 MHz). The standard deviations vary between 5.7 and 8.1 dB at L-Band with an overall average of 6.5 dB. At S-Band the standard deviations vary between 5.1 dB and 7.3 dB with an overall average of 6.5 dB. Figure 8-8 shows an example of the instantaneous spatial variability as a function of location within a specific site (Commons). It is noted that within a 1 m interval, fluctuations of the signal level of 20 dB are possible.

8.7.3.3 Spatial Decorrelation Distances

Autocorrelation calculations by Vogel and Torrence [1995c] were carried out for lags between 0 to 3.2 m in the frequency interval between 0.5 to 3.0 GHz. The median decorrelation distance varied between 0.5 m to 1.1 m with an overall average of 0.71 m, (Table 8-15).

8.7.4 Effects Caused by the Human Body

Vogel and Torrence [1993] found in the frequency interval of 700 MHz to 1800 MHz, that typically, people moving near the receiving antenna but outside the antenna Fresnel region, produced variations of less than 0.5 dB. On the other hand, a person blocking the transmission produced fades of 6 to 10 dB at an average location in the site rooms. The ITU-R [1995] reports that at 1.7 GHz, a person moving into the line-of-sight path causes 6 to 8 dB attenuation in the received power level. When a hand-held terminal is used, the proximity of the antenna to the user's head and body affect the received signal level. For example, at 900 MHz, measurements with a dipole antenna showed the received signal strength to decrease in the vicinity of 4 to 7 dB when the terminal was held at the waist, and 1 to 2 dB when the terminal was held against the head.

8.8 References

Bultitude, R. J. C., S. A. Mahmoud, W. A. Sullivan [1989], "A Comparison of Indoor Radio Propagation Characteristics of 910 MHz and 1.75 GHz," *IEEE Journal of Selected Areas in Communications*, Vol. 7, No. 1, January, pp. 20-30.

Cox, D. C., R. R. Murray, H. W. Arnold, A. W. Norris, and M. F. Wazowics [1986], "Cross-Polarization Coupling Measured for 800 MHz Radio Transmission In and Around Houses and Large Buildings," IEEE Transactions on Antennas and Propagation, Vol. AP-34, No. 1. January, pp. 83-87.

Cox, D. C., R. R. Murray, and A. W. Norris [1984], "800 MHz Attenuation Measured in and around Suburban Houses," Bell Labs Tech. J., Vol. 63, pp. 921-954.

Cox, D. C., R. R. Murray, and A. W. Norris [1985], "Antenna Height Dependence of 800 MHz Attenuation Measured in Houses," IEEE Transactions on Vehicular Technology, Vol. VT-34, No. 2, May, pp. 108-115.

Fujimori, K. and H. Arai [1997], "Polarization Characteristics Under Indoor Micro/Pico Cell Environments," 10th International Conference on Antennas and Propagation, Edinburgh, UK, 14-17 April, Conference Publication No. 436, pp. 2.302-2.310.

Hoffman, H. H., and D. C. Cox [1982], "Attenuation of 900 MHz Radio Waves Propagating into a Metal Building," IEEE Transactions on Antennas and Propagation, Vol. AP-30, No. 4, July, pp. 808-811.

ITU-R [1995], "Propagation Data and Prediction Models for the Planning of Indoor Radiocommunications Systems and Radio Local Area Networks in the frequency Range 900 MHz to 100 GHz," International Telecommunications Union, Radiocommunications Study Group, Document 3/2-E, 8 January, (Doc. 3K/TEMP/39(Rev.2).

Polydorou, A., G. Stratakos, C. Capsalis, and N. Uzunoglu [1995], "Comparative Study of Millimeter Wave Propagation at 30 GHz and 60 GHz in Indoor Environment," International Journal of Infrared and Millimeter Waves, Vol. 16, No. 10, pp. 1845-1862.

Rappaport, T. S. [1989], "Characterization of UHF Multipath Radio Channels in Factory Buildings," IEEE Transactions on Antennas and Propagation, Vol. 37, No. 8, August, pp. 1058-1069.

Seidel, S. Y. and T. S. Rappaport [1992], "914 MHz Path Loss Prediction Models for Indoor Wireless Communications in Multifloored Buildings," IEEE Transactions on Antennas and Propagation, Vol. 40, No. 2, February, pp. 209-217.

Tang, Y. and H. Sobol [1995], "Measurements of PCS Microwave Propagation in Buildings," Applied Microwave and Wireless, Winter, pp. 38-60.

Vogel, W. J., G. W. Torrence, and H. P. Lin [1995a], "Into Building Fading at L- and S-Band For Satellite PCS," Proc. of the 19th NASA Propagation Experimenters Meeting (NAPEX XIX) and the Seventh Advanced Communications Technology Satellite (ACTS) Propagation Studies Workshop (APSW VII), (JPL Publication 95-15), Fort Collins, Colorado, June 14-16. (Jet Propulsion Laboratory, California Institute of Technology, Pasadena, California).

Vogel, W. J., G. W. Torrence, and H. P. Lin [1995b], "Slant-Path Building Penetration Measurements at L- and S-Band, EERL Technical Report EERL-95-301, 23 March (The University of Texas, Electrical Engineering Research Laboratory, 10100 Burnet Road, Austin, Texas 78758).

Vogel, W. J. and G. W. Torrence [1995c], "Slant-Path Building Penetration Measurements from 500 to 3000 MHz, EERL Technical Report EERL-95-10A, 30 October (The University of Texas, Electrical Engineering Research Laboratory, 10100 Burnet Road, Austin, Texas 78758-4497).

Vogel, W. J and G. W. Torrence [1993], "Propagation Measurements for Satellite Radio Reception Inside Buildings," IEEE Transactions on Antennas and Propagation, Vol. 41, No. 7, July, pp. 954-961.

Wang, L. Q., N. E. Evans, J. B. Burns, and J. G. W. Mathews [1995], "Fading Characteristics of a 2.3 GHz Radio Telemetry Channel in a Hospital Building," Medical Engineering Physics, Vol. 17, No. 5., pp. 226-231.

Wells, P. I. [1977], "The Attenuation of UHF Radio Signals by Houses," IEEE Transactions on Vehicular Technology, Vol. VT-26, No. 4, November, pp. 358-362.

Chapter 9

Maritime-Mobile Satellite Propagation Effects

Table of Contents

Table of Figures

Table of Tables

Chapter 9
Maritime-Mobile Satellite Propagation Effects

9.1 Introduction

Problems that may affect maritime-mobile satellite communications are

- blockage from ship-structures along the Earth-satellite path,
- multipath from ship structures
- multipath from the ocean at low grazing angles when low-gain antennas are used
- fading due to ionospheric or tropospheric scintillations at low elevation angles
- Faraday rotation effects
- tropospheric refractive effects at low elevation angles such as ducting.

This chapter deals primarily with multipath fading from the ocean when low gain antennas are employed at low elevation angles for ship-satellite scenarios. The other effects enumerated above are either beyond the scope of this text or are described elsewhere.

9.2 Early Multipath Experiments

9.2.1 Ship to Satellite Fading Measurements

Early measurements of multipath effects at 1.5 GHz for ship to satellite communications scenarios were reported by Fang et al. [1982a, b]. The measurements were executed with a terminal on a ship transmitting to and receiving from the MARISAT F-1 satellite located at 15°-west longitude (over the Atlantic Ocean). The antenna diameter was 1.2 m (approximately 12° beamwidth) and the system G/T was –4 dB/K. Elevation angles

ranged from 15° to 0°. Measurements were performed over a period 40 hours during which the ship was en route from Norfolk, VA to Texas City, Texas. Time-division multiplexing (TDM) carriers for Teletype and voice carriers for telephone and data transmissions were monitored and analyzed. These signals were monitored at the shore station, Southbury, Connecticut, and the ship terminal. The frequencies for these signals were within 1.537 and 1.541 GHz. At satellite elevation angles below 2°, the mean carrier reduction and peak-to-peak fluctuations were noted to be severe. For example, down to two degrees, the peak-to-peak fluctuations of the carrier to noise ratio were smaller than 4 dB. These fluctuations followed the two-component multipath model from a calm sea relatively well after a 1-dB bias was added for gaseous fading. Below 2° elevation, the peak-to-peak fluctuations increased to levels as high as 10 dB and deviated considerably from the two-component multipath model. Cumulative signal distributions relative to the mean values demonstrated that peak-to-peak fluctuations exceeded 10 dB with a probability of 42% in the angular interval of 0.5-2°. The spectrum properties of a 10-minute sample at 2° elevation indicated the presence of turbulent-type scattering in the troposphere or ionosphere. Measurements showed that in passing from 10° to 5° elevation angle, a mean carrier to noise ratio drop of less than 2 dB was observed. The maximum fade level at 5° caused by signal fluctuations was less than 6.5 dB 99% of the time. On the other hand, at an elevation angle of 10°, the fading was less than 4.4 dB for 99% of the time.

9.2.2 Evolution of a Simplified Multipath Fading Prediction Model

A number of investigators have analyzed the characteristics of multipath fading due to sea surface reflections. Karasawa and Shiokawa [1984a] applied the Kirchhoff approximation theory and developed a model for the coherent and incoherent scattered power as a function of sea surface conditions for L-Band. Using their developed model, fade depths were determined as a function of elevation angle, wave height and antenna gain. They showed that at an elevation angle of 5°, the fade depth under rough sea conditions was dependent on small antenna gains and had little dependence on wave height. For example, at 5° elevation and 99% of the time, the fade depth varied between 4.5 to 6.5 dB for an antenna gain of 20 dBi; ($BW \approx 17°$, BW is the half power beamwidth). The fade depth varied between 7 to 9 dB for an antenna gain of 15 dBi ($BW \approx 30°$) and 8 dB to 10.5 dB for an antenna gain of 10 dBi ($BW \approx 53°$). These results assume wave heights smaller than 4 m. In a later paper, Karasawa and Shiokawa [1986] reported on a series of measurements using shore-to-shore, satellite-to-shore and satellite-to-ship paths and antennas with gains from 13 dBi (BW = 37°) to 21 dBi (BW = 15°). Based on these and other measurements and previously developed concepts, simplified prediction models were developed by them [Karasawa and Shiokawa; 1988, 1987] and adopted by the ITU-R [1994, pp. 352-354]. These simplified models are described in Section 9.3.

9.3 Characteristics of Multipath Fading Due to Sea Surface Reflection

9.3.1 Fundamental Concepts

We use here the developments of Karasawa and Shiokawa [1988] in describing fundamentals of fading due to sea surface reflections. Their model adopted concepts described by Sandrin and Fang [1986] who proposed a method for determining the fading depth using a multipath power diagram as a function of antenna gain, elevation angle and Nakagami-Rice statistics [ITU-R-1994, pp. 59-61]. Although the model of Karasawa and Shiokawa was confirmed for circular polarization, it is believed also applicable for horizontal and vertical polarizations with appropriate caveats.

Multipath reflections from the sea are comprised of "specular" and "diffuse" contributions, also referred to as "coherent" and "incoherent" components, respectively. For calm seas, the specular component dominates but decreases rapidly for increasingly rough seas. The total power received is obtained by combining the power contributions of coherently scattered and incoherently scattered waves, and the direct wave component. Under calm sea conditions, the forward-scattered wave is composed entirely of the coherent component that can be estimated by

$$P_{CO} = \left| \vec{E}_i R D_r^* \right|^2 , \tag{9-1}$$

where $\vec{E}_i$ is the incident wave vector and where *i* denotes either the horizontal or vertical components (*H*,*V*) and * denotes the complex conjugate. That is,

$$\vec{E}_i = (E_{iH}, E_{iV}) . \tag{9-2}$$

Also, *R* is the Fresnel reflection coefficient matrix of the sea given by

$$R = \begin{pmatrix} R_{HH} & R_{HV} \\ R_{VH} & R_{VV} \end{pmatrix}, \tag{9-3}$$

where for the calm sea case, $R_{HV} = R_{VH} = 0$. D_R is the directivity of the antenna in the direction of the specular reflection point and given by

$$D_R = \begin{pmatrix} D_H \\ D_V \end{pmatrix}. \tag{9-4}$$

The intensity of the coherent and incoherent components depends on the roughness of the sea expressed by the roughness parameter *u* given by

$$u = \frac{4p}{l} h_o \sin(q_o) , \tag{9-5}$$

where l is the wavelength in m, q_o is the elevation angle to the satellite, h_0 is the RMS wave height in m related to the significant wave height *H* by

$$h_o = H/4 . \tag{9-6}$$

The significant wave height is the average height of waves corresponding to the highest one-third of the actual waves that pass a fixed point. When the sea is rough, the incoherent and coherent components of the scattered powers, P_I, P_C may be expressed in terms of the coefficients $h_I(u)$ and $h_C(u)$ defined such that

$$P_I(u) = h_I^2(u) P_{CO} \tag{9-7}$$

and

$$P_C(u) = h_C^2(u) P_{CO} , \tag{9-8}$$

where P_{CO} is given by (9-1). The mean total power of the reflected waves is thus given by

$$P_r(u) = h^2(u) P_{CO} \quad with \quad h^2 = h_C^2(u) + h_I^2(u) . \tag{9-9}$$

The coherent component h_C is related to the roughness parameter u by the relation [Beckmann and Spizzichino, 1963],

$$h_C = \exp(-u^2 / 2) . \tag{9-10}$$

For $u > 1$, Miller et al. [1984] showed the results to be consistent with the measurements of Beard [1961] (for u up to 3) where h_C is defined by

$$h_C = \exp(-u^2 / 2)\, I_o(u^2 / 2) \tag{9-11}$$

and where I_0 is the zero-order modified Bessel function. Karasawa and Shiokawa demonstrated from their measurements at 1.5 GHz using right-handed circular polarization that

$$\begin{aligned} h^2 &\approx h_C^2 + h_I^2 \approx 1 \quad for \quad 0 \le u < 2 \\ h^2 &\approx h_I^2 \approx 1 \quad for \quad 2 \le u \le 10 \end{aligned} . \tag{9-12}$$

Combining (9-12) with (9-10) or (9-11) enables h_I^2 to be explicitly expressed by

$$h_I^2 = 1 - \exp(-u^2) \tag{9-13}$$

or

$$h_I^2 = 1 - \left[\exp(-u^2 / 2) I_o(u^2 / 2)\right]^2 . \tag{9-14}$$

The measurements of Karasawa and Shiokawa were sufficiently scattered such that they fell within the bounds of both (9-13) and (9-14).

The level of the maximum coherent component P_{CO} of the reflected wave may be determined by varying the antenna height on board the ship during calm sea conditions. By determining the level difference between the minimum and maximum signals (for a calm sea), the intensity of the coherent component of the scattered wave relative to the direct wave component can be evaluated. The intensity of the incoherent component of the scattered wave may be obtained through the assumption that the incoherent signal follows a Nakagami-Rice distribution. Figure 9-1 shows the relation between the fading depth and the mean total multipath power relative to the direct signal power assuming this distribution. Karasawa and Shiokawa [1984] define the "fading depth" as the dB difference between the signal level of the direct incident wave and a threshold level that the resultant signal level exceeds with a probability of P percent of the time. The individual curves denote the indicated probability of exceeding the ordinate fading depth. Shipborne experiments carried out by Karasawa and Shiokawa [1988] have corroborated use of this distribution for values of $u \geq 2$. As an illustration of the dependence of u on wave-height, Figure 9-2 is a plot of u given by (9-5) versus the RMS wave height h (upper abscissa) and significant wave height H (lower abscissa). We note that at $q_o = 5°$, $u \geq 2$ implies $H > 1.5$ m and $h > 0.4$ m.

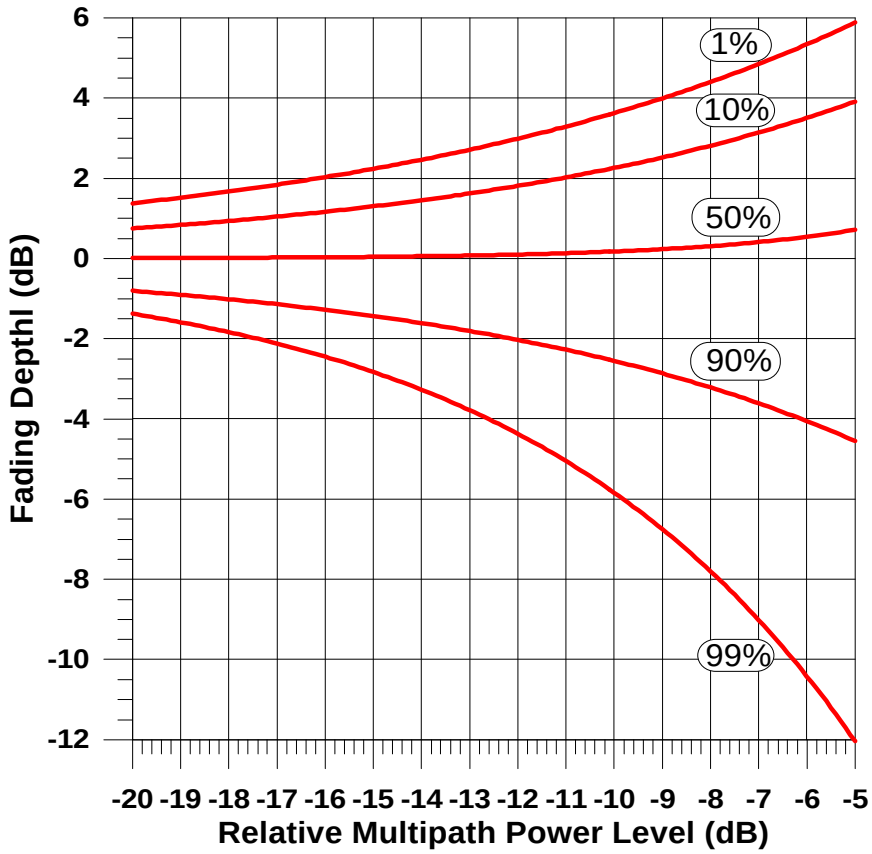

Figure 9-1: Fading depth versus total multipath power relative to the direct signal level for different exceedance probabilities (of the incoherent level) based on the Nakagami-Rice distribution.

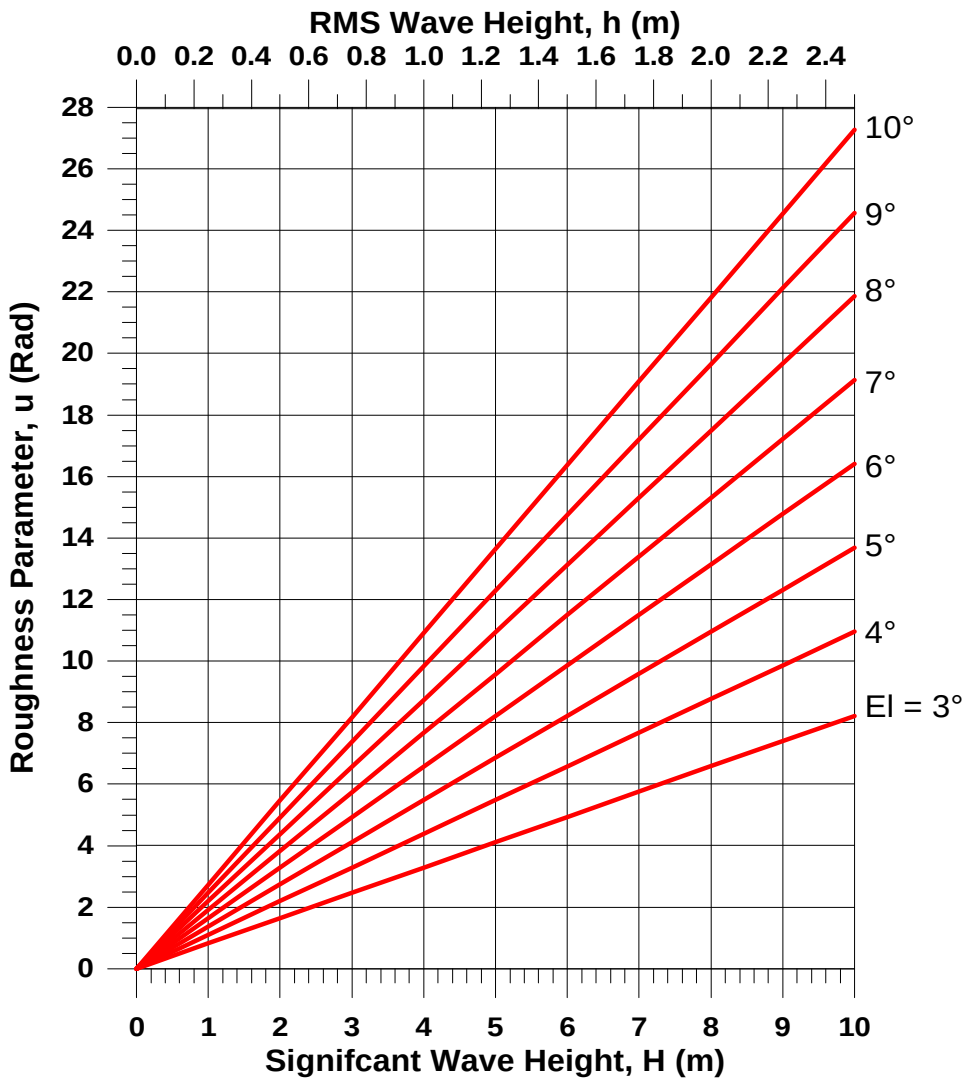

Figure 9-2: Roughness parameter versus significant wave height (lower abscissa) and RMS wave height (upper abscissa).

9.3.2 Prediction Method of Karasawa and Shiokawa

We describe here the prediction model of Karasawa and Shiokawa [1988] (also adopted by the ITU-R [1994, pp. 352-354]) for evaluating the fading depth due to sea surface multipath reflections. The individual steps in executing this model follow:

Step1: Confirm the applicable parameters for which the method is valid. These are:

- Frequency range from 1 to 2 GHz (nominal frequency is 1.5 GHz).
- Polarization is circular or horizontal. Vertical polarizations may be used for elevation angles above 8°. Below 8°, noticeable errors may exist for vertical polarization due to Brewster angle complications.
- Elevation angle q_o is within the interval given by

$$3^o \le q_o \le \frac{BW}{4}. \tag{9-15}$$

- The sea condition is such that the roughness parameter u defined as:

$$u = \frac{4p}{l} h \ \sin(q_o) \tag{ -16}$$

is given by

$$2 \le u \quad 10, \tag{9-17}$$

where l is the wavelength in m, q_o is the elevation angle to the satellite, h_0 is the RMS wave height in m related to the significant wave height H by

$$h_o = H/4. \tag{9-18}$$

Employing Figure 9-2, (9-17) implies for instance, at 5° elevation

$$1.5 \le H \le 7.3 \quad or \quad 0.4 \le h_o \le 1.8 \quad (m). \tag{9-19}$$

Step 2: Find the relative antenna gain D_r (in dB) in the direction of the specular reflection point on the sea. The relative antenna gain is approximately given by

$$D_r = -4 \times 10^{-4} (10^{G_o/10} - 1) q_r^{\ 2}, \tag{9-20}$$

where G_0 is the antenna gain in dBi (dB above isotropic), and

$$q_r = 1.5 q_o \tag{9-21}$$

when the beam center is in the direction of the satellite. The factor of 1.5 (as opposed to 2) is used since a significant portion of the multipath energy comes from the region between the true specular reflection point and the horizon [Karasawa and Shiokawa, 1984a].

Step 3: Obtain the Fresnel reflection coefficient R_{ij} (in dB), where i represents the polarization of the incident wave and j is the polarization of the reflected wave. These reflection coefficients are tabulated for the sea at 1.5 GHz in Table 9-1 for horizontal polarization R_{HH}, vertical polarization R_{VV}, and circular polarization R_{CC}. The Fresnel reflection coefficients may also be calculated using the formulas of Beckmann and Spizzichino [1963].

Step 4: Calculate the correction factor C_q in dB given by

$$C_q = 0 \ dB \quad for \quad q_o \ge 7° \tag{9-22}$$

and

$$C_q = (q_o - 7)/2 \; dB \quad for \quad q_o < 7^\circ \tag{9-23}$$

Step 5: Find the mean power of sea reflected waves P_r (in dB) relative to the direct power. This is given by

$$P_r = D_r + R_{ij} + C_q \;\; (\text{dB}) \tag{9-24}$$

Step 6: Find the fading depth A (relative to the direct power) from Figure 9-1 by setting the multipath power calculated from (9-24) to the abscissa. Least square fits of the individual curves in Figure 9-1 follow the form

$$A = a \exp\left(-\frac{P_r}{b}\right) \text{(dB)}, \tag{9-25}$$

where the parameters a , b in (9-25) are tabulated in Table 9-2 for different exceedance percentages.

In Figure 9-3 through Figure 9-9 are given the fading depths versus the elevation angle for antenna gains of 0, 5, 10, 15, 18, 20, and 25 dBi, respectively. These curves were derived executing the above-described steps at 1.5 GHz, assuming circular polarization.

9.3.3 Example Calculation

Consider the following example:

$$\begin{aligned} &f = 1.5\,GHz \\ &G_o = 10\,dB \\ &q_o = 6^o \\ &Polarization = Circular \end{aligned} \tag{9-26}$$

It is desired to find the signal level variation (relative to the direct power) at the 99% exceedance probability level. For circular aperture antennas, the half power beamwidth BW in (9-15) is approximately given by

$$BW = \sqrt{r}\,\frac{180}{10^{G_o/20}} \;\; (\text{deg}), \tag{9-27}$$

where r is the antenna efficiency factor (between 0 and 1). Assuming a nominal value of 0.6 for r , $BW \approx 44^\circ$. Hence (9-15) is satisfied. We tacitly assume the conditions (9-16) and (9-17) are also satisfied. Injecting G_0 = 10 dB and $q_r = 1.5, q_o = 9^\circ$ into (9-5), we obtain D_r = -0.29 dB. Substituting $q_o = 6^\circ$ into (9-23) results in $C_q = -0.5$ dB. The reflection coefficient for circular polarization is given by R_{CC} = -6.19 dB from Table 9-1 at $q_o = 6^\circ$. Substituting the above values into (9-24) gives the mean power of sea reflected waves P_r = -6.98 dB. Finally, substituting $a = -24.8271, b = -6.9088$ from

Table 9-2 (P = 99%) into (9-25) results in a fading depth relative to the direct signal of A = -9.0 dB. Figure 9-1 at $q_o = 6°$ gives the same value for the fading depth at the 99% level.

Table 9-1: Fresnel reflection coefficient values of the sea at 1.5 GHz for various polarizations

Elevation, q (deg)	Polarization		
	Horiz., R_{HH} (dB)	Vertical, R_{VV} (dB)	Circular R_{CC} (dB)
1	-0.03	-2.86	-1.34
2	-0.06	-5.83	-2.52
3	-0.09	-9.05	-3.57
4	-0.12	-12.58	-4.52
5	-0.15	-16.01	-5.39
6	-0.18	-17.41	-6.19
7	-0.21	-16.01	-6.94
8	-0.24	-13.95	-7.64
9	-0.27	-12.19	-8.3
10	-0.30	-10.81	-8.92
11	-0.33	-9.7	-9.52
12	-0.36	-8.81	-10.09
13	-0.39	-8.07	-10.64
14	-0.42	-7.46	-11.16
15	-0.45	-6.93	-11.67
16	-0.48	-6.48	-12.17
17	-0.51	-6.09	-12.65
18	-0.54	-5.74	-13.12
19	-0.57	-5.44	-13.58
20	-0.60	-5.16	-14.03

Table 9-2: Parameters a, b at the given probabilities that fit (9-25) derived from the Nakagami-Rice distribution.

Probability (%)	a	b
1	9.5414	-10.3467
10	6.7844	-9.0977
50	2.9286	-3.5705
90	-8.1119	-8.6521
99	-24.8271	-6.9088

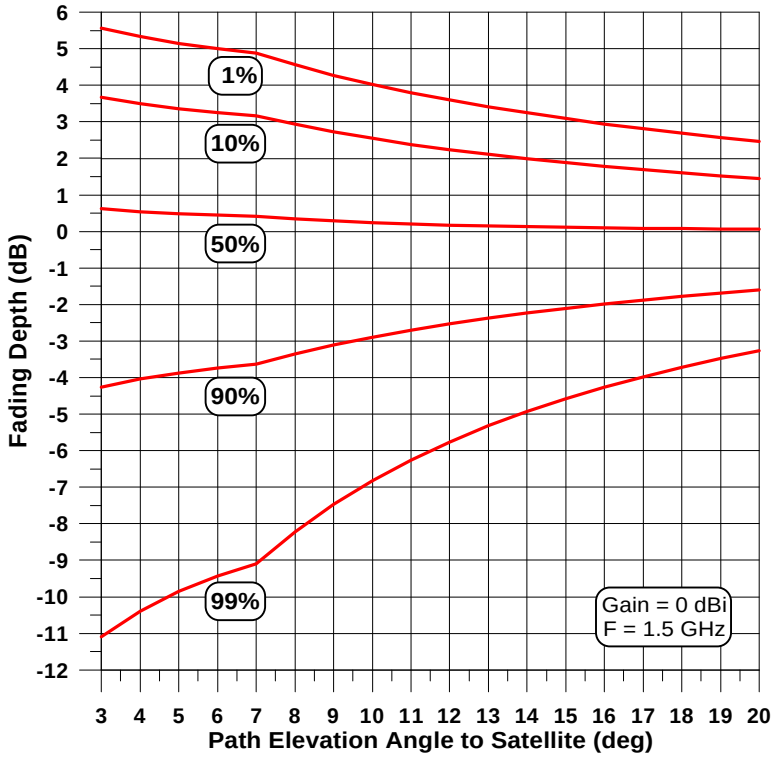

Figure 9-3: Fading depth versus path elevation angle at different exceedance probabilities assuming an antenna gain G_0 = 0 dBi, 1.5 GHz and circular polarization.

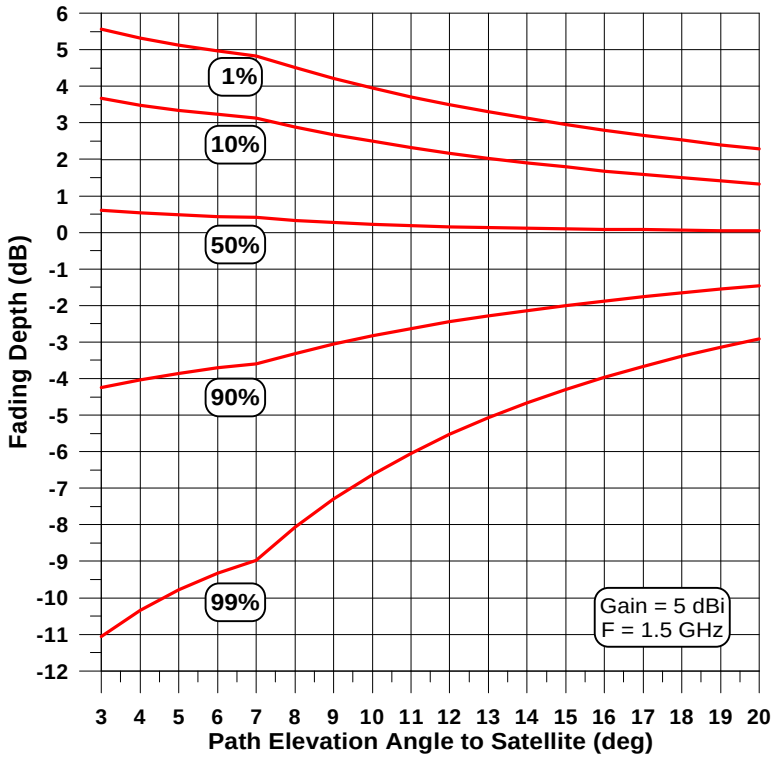

Figure 9-4: Fading depth versus path elevation angle at different exceedance probabilities assuming an antenna gain G_0 = 5 dBi, 1.5 GHz, and circular polarization.

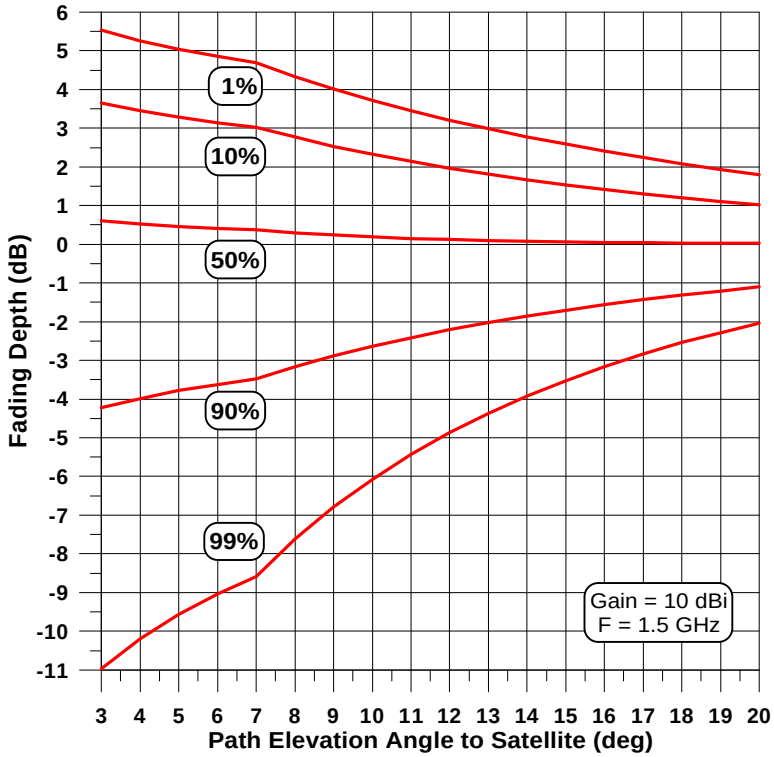

Figure 9-5: Fading depth versus path elevation angle at different exceedance probabilities assuming an antenna gain G_0 = 10 dBi, 1.5 GHz, and circular polarization.

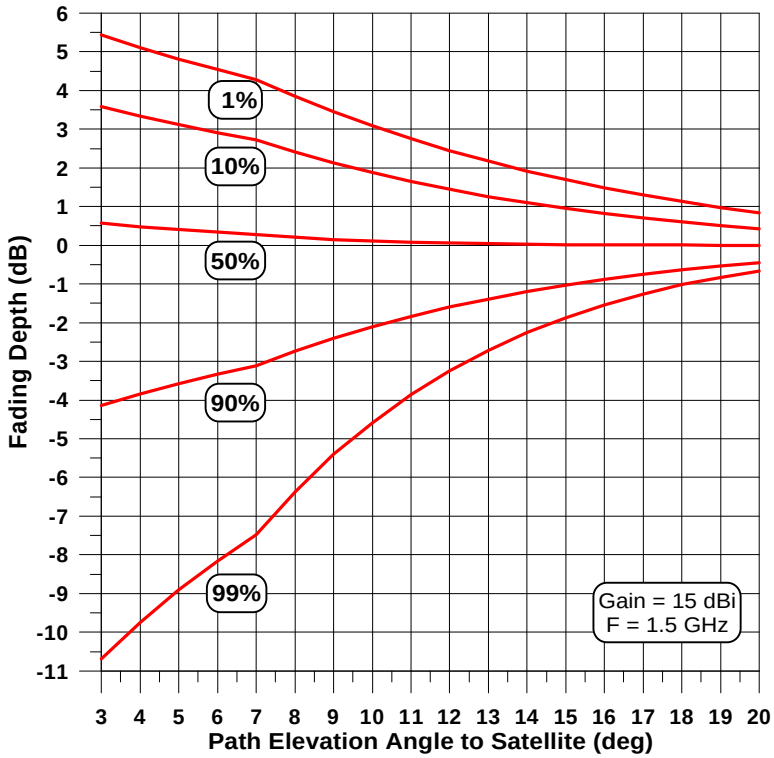

Figure 9-6: Fading depth versus path elevation angle at different exceedance probabilities assuming an antenna gain G_0 = 15 dBi, 1.5 GHz, and circular polarization.

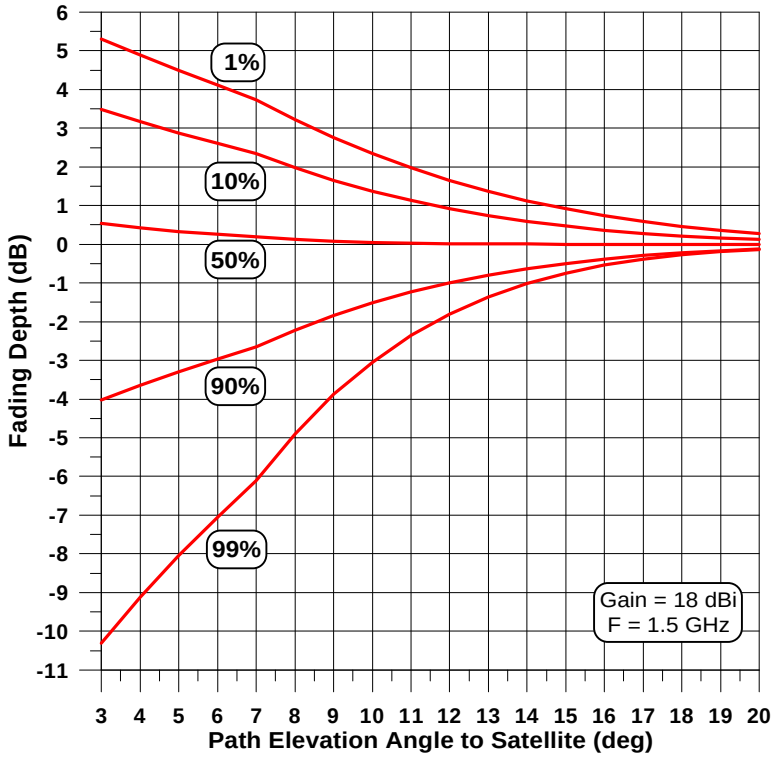

Figure 9-7: Fading depth versus path elevation angle at different exceedance probabilities assuming an antenna gain G_0 = 18 dBi, 1.5 GHz, and circular polarization.

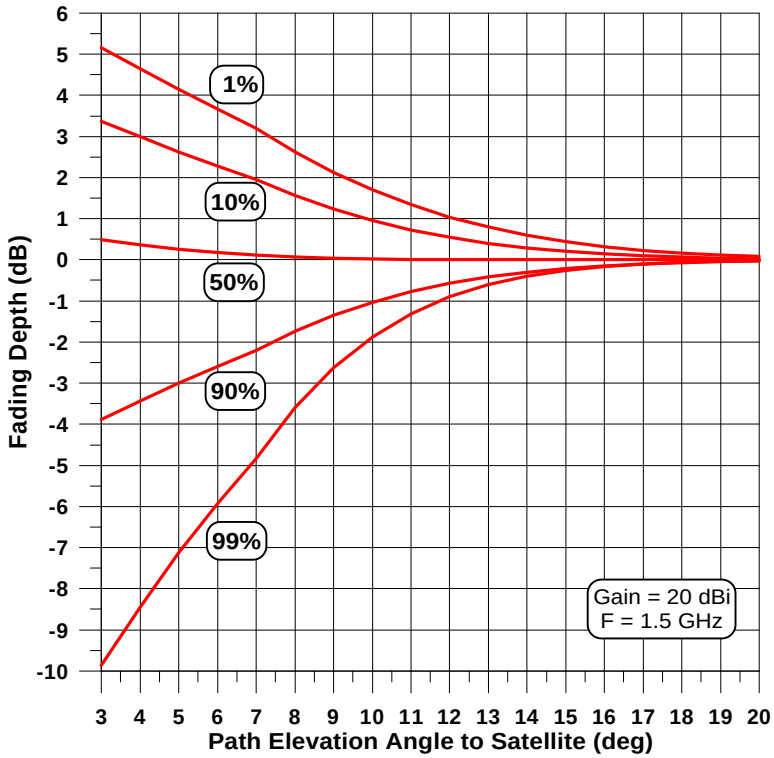

Figure 9-8: Fading depth versus path elevation angle at different exceedance probabilities assuming an antenna gain G_0 = 20 dBi, 1.5 GHz, and circular polarization.

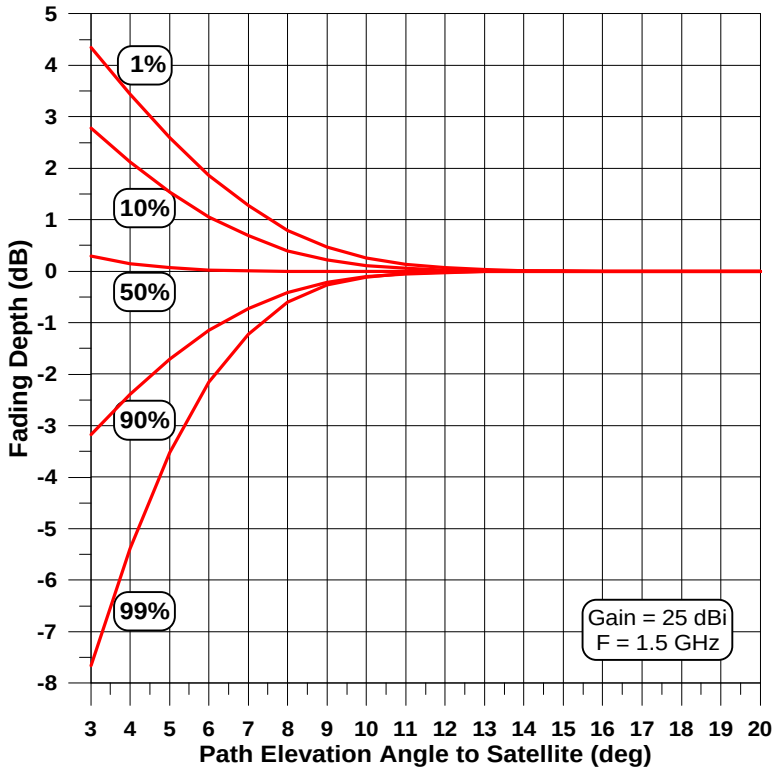

Figure 9-9: Fading depth versus path elevation angle at different exceedance probabilities assuming an antenna gain G_0 = 25 dBi, 1.5 GHz, and circular polarization.

9.4 Model of Fade Durations Due to Sea Reflections

Karasawa and Shiokawa [1987] analyzed multipath fading due to sea surface reflections at L-Band (1.54 GHz) and determined mean values of fade durations T_D and fade occurrence intervals T_I from the fading power spectrum. The fade duration T_D is defined as the time interval between the instant the signal amplitude falls below a particular level and the instant it reaches that level again (Figure 9-10). The fade occurrence interval T_I is defined as the interval of time between the instant the signal intensity drops below a specified level R_p to the instant it falls below that same level again (Figure 9-10). The signal level R_p in Figure 9-10 is assigned the exceedance percentage P.

Karasawa and Shiokawa [1987] arrived at a simple model for the mean values of T_D and T_I which was also adopted by the ITU-R [1994, pp. 354-356]. The mean value of the fade occurrence interval at the fade exceedance percentage P is denoted by $\langle T_I(P) \rangle$ and is given by

$$\langle T_I(P) \rangle = \langle T_I(50\%) \rangle \exp\left(\frac{m(P)^2}{2} \right), \tag{9-28}$$

where $\langle T_I(50\%)\rangle$ is the mean value of the fade occurrence interval at the fade exceedance percentage of 50% and *m(P)* is given by (9-31). The mean value of the fade duration at the fade exceedance *P* or $\langle T_D(P)\rangle$ may be calculated by

$$\langle T_D(P)\rangle = \langle T_I(P)\rangle\left(1-\frac{P}{100}\right). \tag{9-29}$$

The mean fade occurrence interval at $P = 50\%$ may be calculated using

$$\langle T_I(50\%)\rangle = \frac{\sqrt{3}}{f_{-10}}, \tag{9-30}$$

where f_{-10} is called the "-10 dB spectral bandwidth." This corresponds to the bandwidth over which the power density decays to –10 dB relative to the peak power density (characterized in Figure 9-11). The parameter *m(P)* in (9-28) is evaluated using the following equations.

$$\begin{aligned} m(P) &= 2.33 - 0.847a - 0.144a^2 - 0.0657a^3 \\ a &= \log(100-P) \qquad for \quad 70\% \le P \le 99.9\% \end{aligned} \tag{9-31}$$

The bandwidth f_{-10} was derived from a theoretical fading model of Karasawa and Shiokawa [1984b] and is plotted as a function of elevation angle in Figure 9-11 at 1.5 GHz for two maritime conditions. The upper bound (denoted by f_{-10U}) corresponds to a significant wave height of 5 m, ship velocity of 20 knots, with a roll of 30°. The lower bound (f_{-10L}) corresponds to a significant wave height of 1 m, ship velocity of 0 knots, with 0° roll. Least square fits of the lower and upper curves in Figure 9-11 have the form

$$f_{-10U,L} = a + b\exp\left(\frac{q_o}{c}\right). \tag{9-32}$$

The values of *a,b,c* are tabulated in Table 9-3 for the upper bound f_{-10U} and lower bound f_{-10L}.

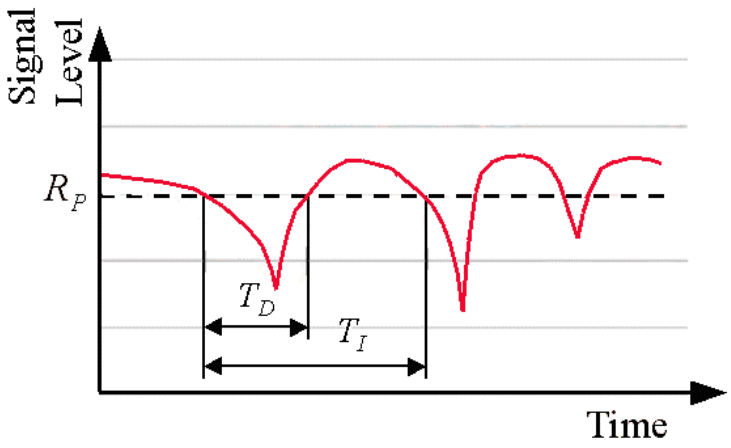

Figure 9-10: Definitions of "fade duration" T_D and "fade occurrence interval" T_I. These are defined at the signal level R_p that is exceeded P(%) of the time.

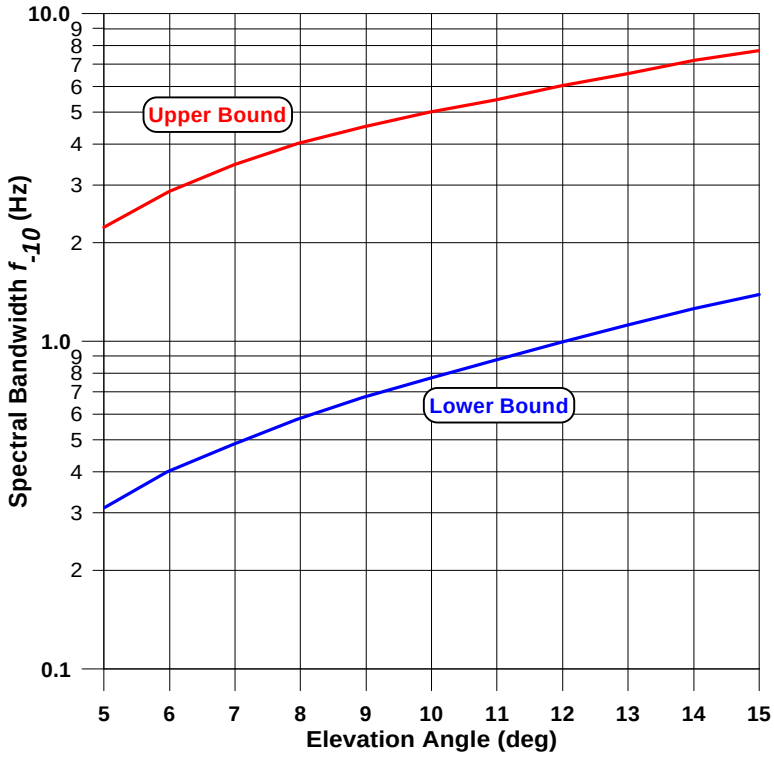

Figure 9-11: Spectral bandwidth f_{-10} of 1.5 GHz multipath fading due to sea surface reflection based on a theoretical model [Karasawa and Shiokawa; 1984b]. The upper bound f_{-10U} corresponds to a significant wave height of 5 m, ship velocity of 20 knots, with a roll of 30°. The lower bound f_{-10L} corresponds to a significant wave height of 1 m, ship velocity of 0 knots, with 0° roll.

Table 9-3: Values of parameters *a, b, c* for upper lower bounds of –10 dB spectral bandwidth (9-32).

f_{-10}	**a**	**b**	**c**
Upper Bound f_{-10U}	-1140489.7	1140489.4	-2129739.7
Lower Bound f_{-10L}	-0.99312632	0.97234278	-16.718273

9.4.1 Example Calculation

It is desired to find the mean fade occurrence interval $\langle T_I(P)\rangle$ and the mean fade duration $\langle T_D(P)\rangle$ under the following conditions:

$$P = 95\% \tag{9-33}$$

and

$$q_o = 5^\circ . \tag{9-34}$$

Step 1: Evaluate a and *m(P)*.

Substitute *P* given by (9-33) into (9-31) and evaluate a and *m(P)*. We obtain

$$a = 0.699, \quad m(P) = 1.645 . \tag{9-35}$$

Step 2: Evaluate the upper and lower bounds of the –10 dB spectral bandwidth f_{-10}.

Substituting coefficients of Table 9-3 into (9-32) for q_o given in (9-34), we obtain

$$f_{-10U} = 2.378, \quad f_{-10L} = 0.318 \tag{9-36}$$

Step 3: Evaluate the mean fade occurrence interval at *P*=50%.

Substituting (9-36) into (9-30), we obtain

$$\langle T_I(50\%)\rangle_U = 0.7285, \quad \langle T_I(50\%)\rangle_L = 5.4435 , \tag{9-37}$$

where the subscripts *U, L* denote the upper and lower bounds of f_{-10} in (9-36), respectively.

Step 4: Evaluate $\langle T_I(95\%)\rangle$ at the upper and lower bound of f_{-10}.

Substituting $\langle T_I(50\%)\rangle$ given in (9-37) and *m(P)* given in (9-35) into (9-28),

$$\langle T_I(95\%)\rangle_U = 2.8s, \quad \langle T_I(95\%)\rangle_L = 21.1s \tag{9-38}$$

Step 5: Evaluate $\langle T_D(95\%)\rangle$ at the upper and lower bounds of f_{-10}.

Substituting (9-33) and (9-38) into (9-29),

$$\langle T_D(95\%)\rangle_U = 0.14s, \quad \langle T_D(95\%)\rangle_L = 1.05s \tag{9-39}$$

In Figure 9-12 through Figure 9-14 are given pairs of curves showing the spread of the mean fade occurrence interval $\langle T_I(P)\rangle$ versus elevation angle at the aforementioned maritime bounds for exceedance probabilities of multipath fading P of 99%, 95%, and 90%, respectively. In Figure 9-15 through Figure 9-17 are given analogous sets of curves for the mean fade durations $\langle T_D(P)\rangle$. Consistent with the fact that higher exceedance percentages imply greater multipath fading, the spread (difference between upper and lower bound values for a fixed elevation angle) of the mean fade occurrence interval is greater at the higher percentages (larger fades) and smaller at the lower percentages (smaller fades). Analogously, the mean fade duration spread is smaller at the higher percentages (greater fading) and larger at the smaller percentages (smaller fading).

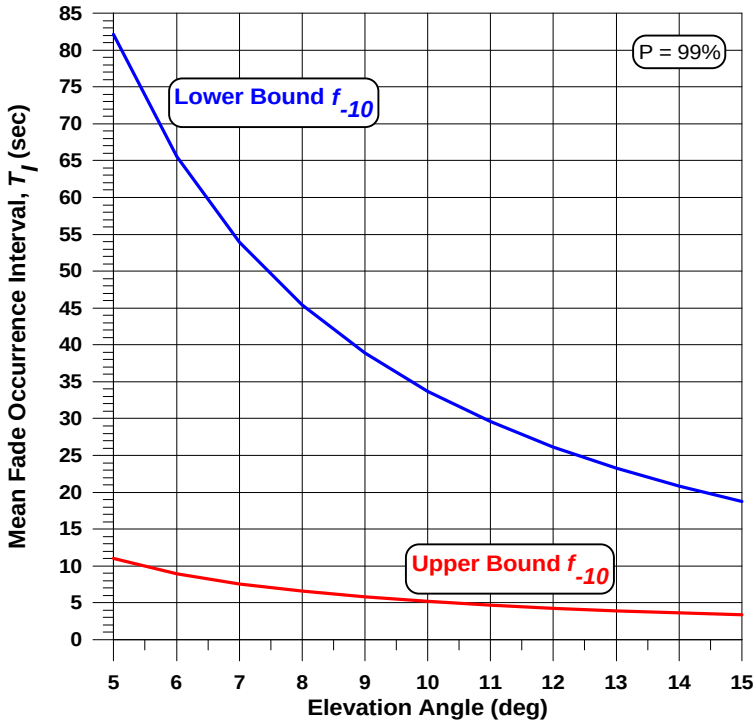

Figure 9-12: Bounds of mean fade occurrence interval $\langle T_I(P)\rangle$ for multipath fade exceedance percentage P = 99% at L-Band.

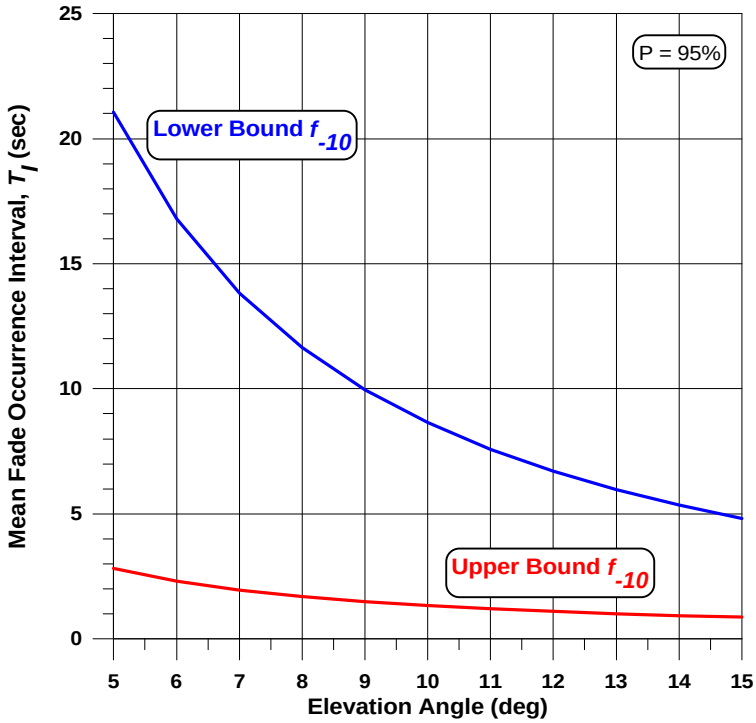

Figure 9-13: Bounds of mean fade occurrence interval $\langle T_I(P) \rangle$ for multipath fade exceedance percentage P = 95% at L-Band.

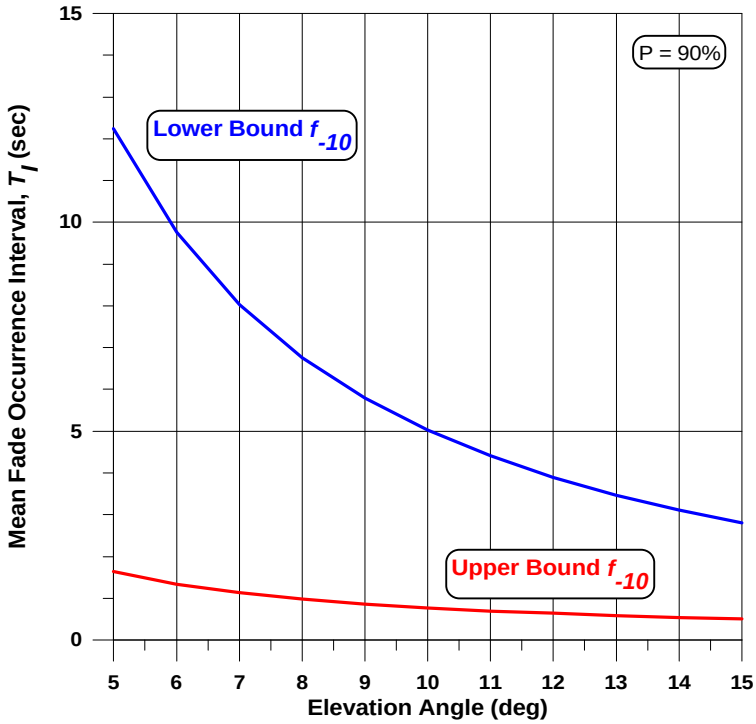

Figure 9-14: Bounds of mean fade occurrence interval $\langle T_I(P) \rangle$ for multipath fade exceedance percentage P = 90% at L-Band.

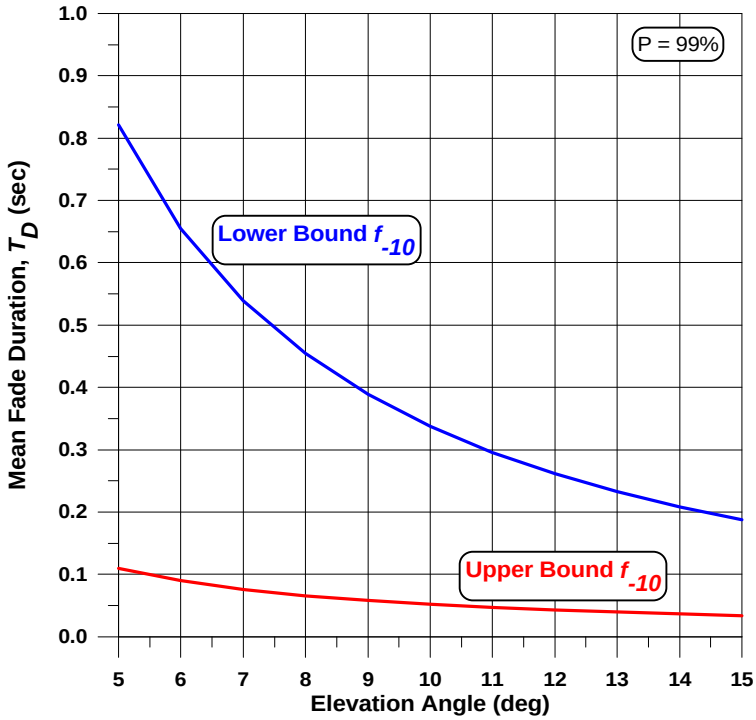

Figure 9-15: Bounds of mean fade duration $\langle T_D(P) \rangle$ for multipath fade exceedance percentage P = 99% at L-Band.

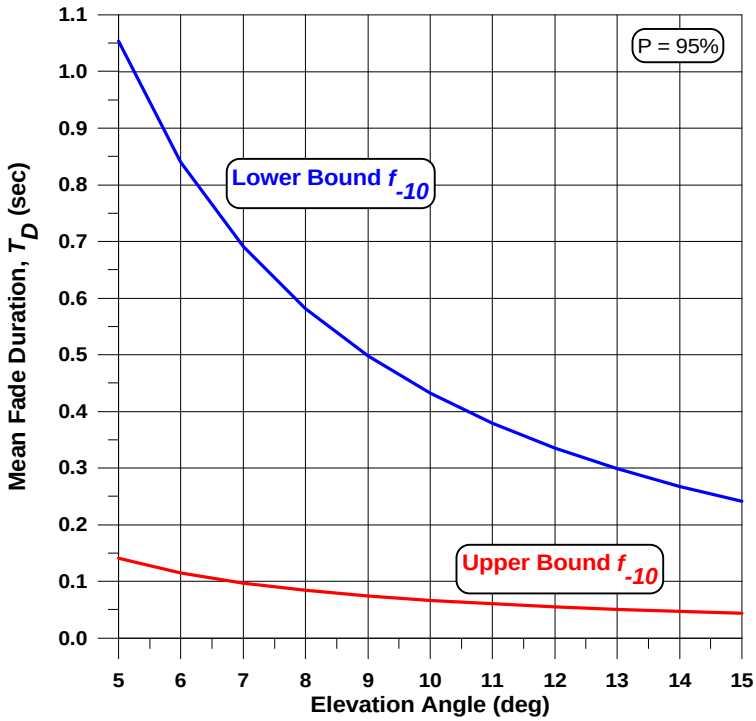

Figure 9-16: Bounds of mean fade duration $\langle T_D(P) \rangle$ for multipath fade exceedance percentage P = 95% at L-Band.

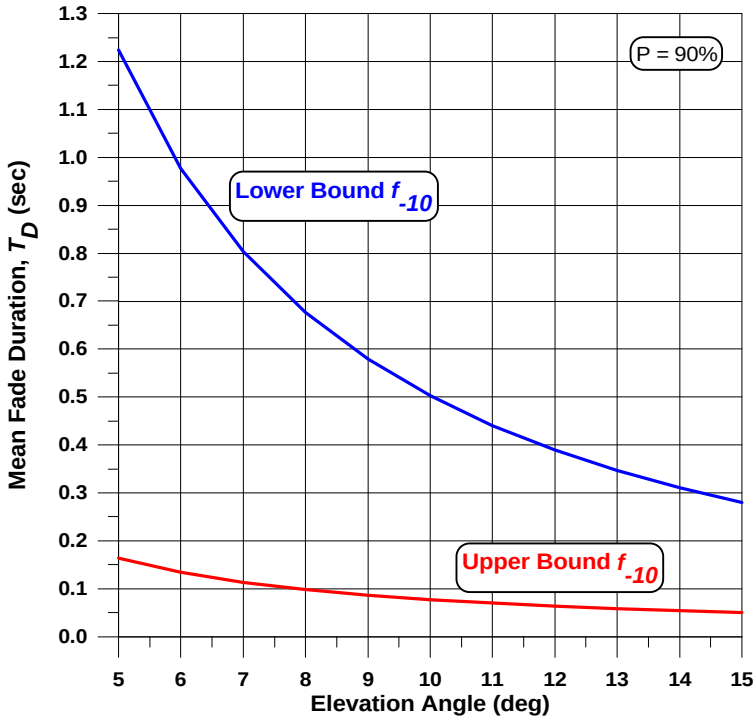

Figure 9-17: Bounds of mean fade duration $\langle T_D(P) \rangle$ for multipath fade exceedance percentage P = 90% at L-Band.

9.5 Multipath from Rough Seas and Frequency Dependence on Multipath Fading

9.5.1 Rough Sea Model

Karasawa et al. [1990] executed an analysis in which multipath fading from very rough seas (with significant wave heights H greater than 3 m) is examined. They developed a model that takes account of the effect of smaller-scale waves superimposed onto the dominant wave. They make use of the fact that the spectrum of ocean waves caused by wind may be approximated by the Pierson-Moskowitz spectrum [1964] and that ocean waves have the characteristics of gravity waves. The RMS slope of the sea surface is calculated and applied to a theoretical model for estimating fade depths. A series of curves is presented of the 99th percentile of fading depth versus significant wave height H for the following combinations of antenna gain and elevation angle (15 dBi, 5°), (21 dBi, 5°), and (15 dBi, 10°). The analytically derived multipath fading for "wind-wave" and "swell" conditions are compared with results derived from the experiments of Karasawa et al. [1986]; Matsudo et al., [1987], and Ohmori et al. [1985]. They show that the fading depth tends to reach a peak for H between 1 and 2 m. The multipath fading peaks are approximately 8 dB, 5 dB, and 4 dB for the above combinations of antenna gain and elevation angle, respectively, consistent with their wind-wave model. For larger H, the multipath fading decreases slightly for wind-waves conditions and remains relatively

unchanged for swell conditions. The multipath fading due to swell gives greater contributions by as much as 4 dB, 2 dB, and 1 dB (for the different combinations of gain and elevation angle) vis-à-vis the wind-wave contribution.

9.5.2 Dependence on Frequency

The analysis by Karasawa et al. [1990] alluded to above enable a computation of the relation between frequency, significant wave height and fading depth. A set of fade isopleths at the 99% probability exceedance level were calculated by them and have been depicted in Figure 9-18 for an elevation angle of 5°, circular polarization, and antenna gain of 15 dBi assuming wind-wave conditions [CCIR, 1990 (p.525-526)]. The left side of the dashed line denotes the region where both coherent and incoherent multipath may contribute whereas the right side of the dashed line is the region where the coherent component is negligible.

In the region where incoherent multipath is dominant, (e.g., to the right of the dashed line), the fading depth versus significant wave height decreases with increasing significant wave height. This is evident in Figure 9-19, which represents a plot of fading depth versus significant wave height at 10 GHz, 5 GHz, and 3 GHz extracted from the curves of Figure 9-18.

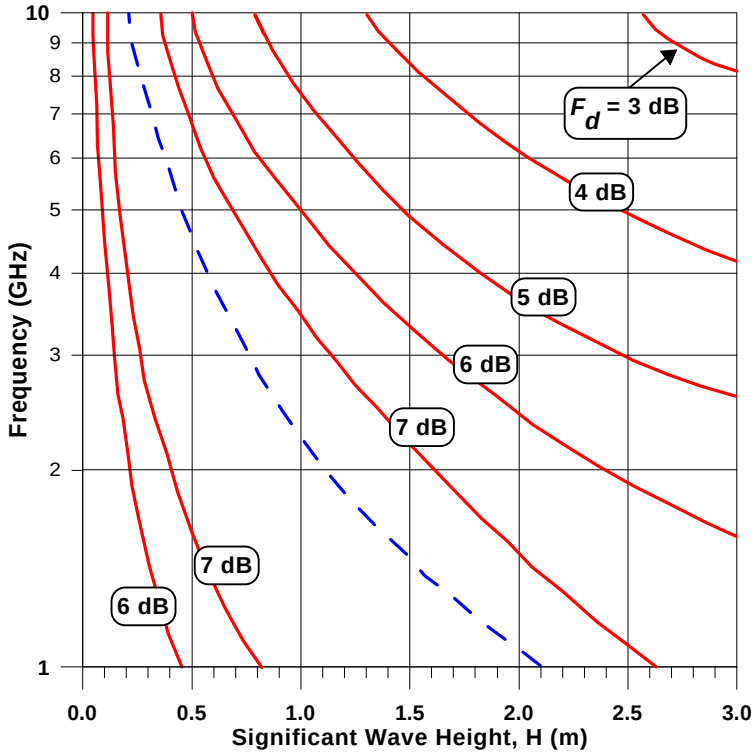

Figure 9-18: Calculation of contours of fading depth at the 99% probability exceedance level for variable frequencies and significant wave heights assuming an elevation angle of 5°, circular polarization, antenna gain of 15 dBi, and wind-wave sea conditions are assumed dominant. The region to the left of the dashed line corresponds to where the coherent and incoherent components of multipath reflections may contribute.

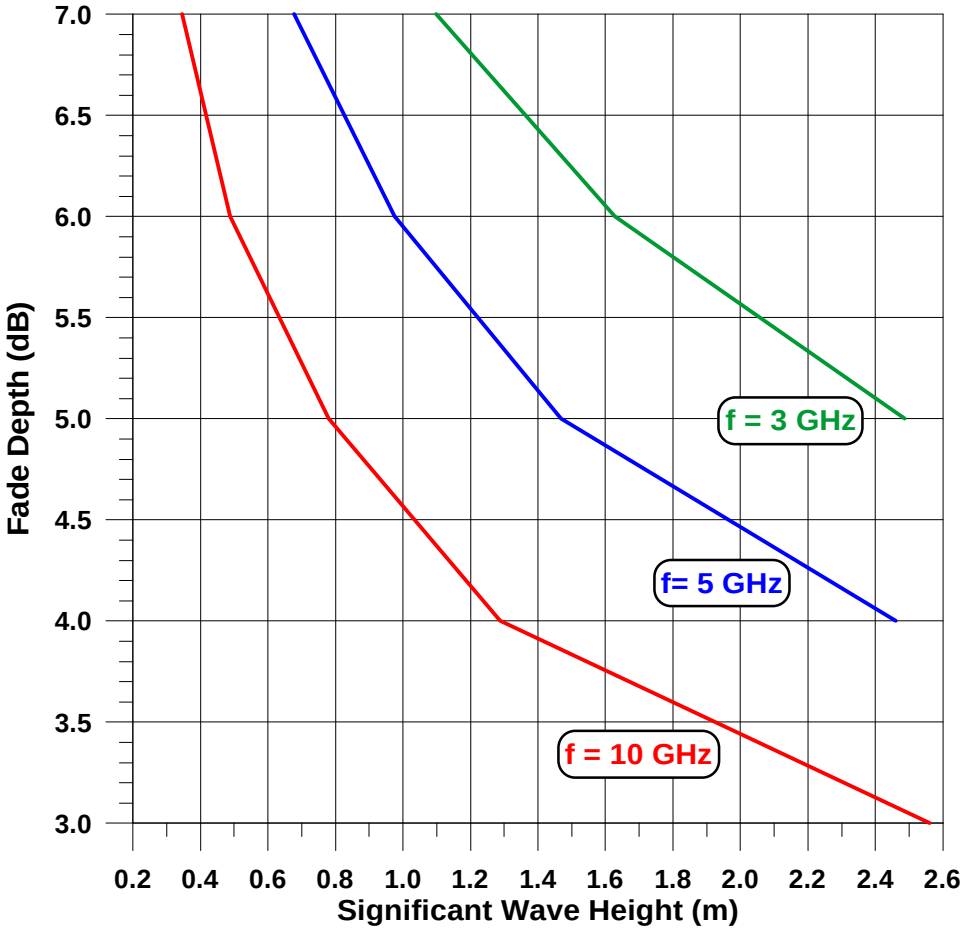

Figure 9-19: Fading depth versus significant wave height at 3 GHz, 5 GHz, and 10 GHz extracted from Figure 9-18 in the region where incoherent multipath dominates.

9.6 Other Maritime Investigations

9.6.1 Experimental Measurements in Japan during 1980 and 1983

Ohmori et al. [1985] report on experimental results at sea shores at Wakasa Bay and Echizen Cape in Fukui Prefecture, Japan in 1980 and 1983. In the 1980 experiment, L-Band (1.54 GHz) and VHF (250 MHz) transmitter systems were placed at the top of a 300 m mountain (Mt. Tennou-san). The receiver was located on the shore (3800 m distance) of an intervening body of water. The 1983 experiment involved reception of a time-division-multiplexing carrier at 1.538 GHz radiated from the geostationary INMARSAT satellite located above the India Ocean. In both experiments the elevation to the radiating source was 5° and circular polarization was used. A wave rider buoy measured the sea wave height. Measurements were performed by these investigators in calm seas (RMS wave height h of approximately 0.06 m and rougher seas (h = 0.4 to 0.9 m). Cumulative fading distributions at L-Band (using a short backfire antenna) for rougher sea conditions showed that 99%, 95%, and 90% of the times the fading signals

were greater than –6 dB, -4 dB, and –3 dB, respectively for the case when h = 0.91 m. There results showed that the fading depth peaked at h = 0.4 m and diminished slightly at greater wave-heights.

9.6.2 Extension of the Kirchhoff Classical Model

Sobieski and Guissard [1993] extended the Kirchhoff classical approach for mobile maritime satellite propagation using the boundary perturbation method (BPM) [Brown, 1980; Guissard and Sobieski, 1987]. They evaluated carrier to specular and carrier to multipath ratios and compared these results with those derived by measurements and by other models. Comparing their calculations with results from other measurement campaigns, they obtained generally good agreement.

9.6.3 K/Ka-Band Maritime Experiments

Perrins and Rice [1997] describe shipboard measurements employing the Advanced Communication Technology Satellite (ACTS) Mobile Terminal (AMT) [Abbe et al., 1996]. The link was comprised of a ground terminal at the Jet Propulsion Laboratory in Pasadena, California and the mobile terminal on board the USS Princeton in the eastern Pacific Ocean (October 1996), where the ACTS steerable spot beam was employed. The transmit gain of the AMT (30 GHz) is a minimum of 20 dBi with a 12° elevation beamwidth for elevation angles between 30° and 60°. The receive gain at 20 GHz is a minimum of 18.8 dBi over a 12° elevation beamwidth for elevation angles between 30° and 60°. The minimum receive system G/T is better than –6 dB/K over the elevation beamwidth. The AMT antenna is mechanically steerable in both azimuth and elevation.

Analysis of pilot tone data received by the AMT showed that negligible variations of the signal arose due to ocean multipath. This is consistent with the relatively narrow beamwidth (12°) and the fact that the elevation angle was always above 40°. During the measurement campaign, six significant fades above 10 dB were noted. The deepest fades (in excess of 30 dB) occurred just after the ship changed direction after a long turn; suggesting the antenna tracker may have been the source of the fades [Perrins and Rice, 1997]. For the ship oriented azimuth angles associated with the maneuvers, the line-of-sight was clear for elevation angles as low as 30°. Hence, it did not appear that shadowing by the superstructure accounted for the observed fades.

9.7 Summary and Recommendations

9.7.1 Fading Depth Due to Sea Surface Reflections

Figure 9-3 through Figure 9-9 may be used to estimate the multipath fading depth at L-Band (1 to 2 GHz) for the indicated exceedance percentages, antenna gain, and elevation angle assuming circular polarization. These curves were generated using the step by step procedure given by (9-15) through (9-21) for circular polarization. Horizontal polarization may alternately be employed using the tabulations of Table 9-1.

Vertical polarization may be employed at elevation angles above 8°. At lower angles, errors due to Brewster angle effects may arise.

9.7.2 Fading Depth Durations and Occurrence Intervals

The procedures outlined by (9-28) through (9-32) may be employed to establish the bounds of the mean fading occurrence interval and the mean fading depth for circular polarization at L-Band. Figure 9-12 through Figure 9-14 depict the bounds for the mean fading occurrence interval as a function of elevation angle at fade exceedance percentages of 99%, 95%, and 90%, respectively. Figure 9-15 through Figure 9-17 give the bounds for the mean fade duration intervals as a function of elevation angle at the same percentages.

9.7.3 Fading Depth Dependence on Frequency and Significant Wave Height

Figure 9-18 and Figure 9-19 describe the dependence of fading at different frequencies as a function of significant wave height. Figure 9-18 shows contours of fading depth isopleths at frequencies ranging from 1 to 10 GHz and significant wave heights up to 3 m. Figure 9-19 gives the fading depths versus significant wave height at 3 GHz, 5 GHz, and 10 GHz derived from Figure 9-18.

9.8 References

Abbe, B., M. Agan, and T. Jedrey [1996], "ACTS mobile terminals," *International Journal of Satellite Communications*, Vol. 14, No. 3, pp. 175-190, January.

Beard, C. I. [1961], "Coherent and Incoherent Scattering of Microwaves from the Ocean," *IEEE Transactions on Antennas and Propagation*, Vol. AP-9, Sept.

Beckmann, P. and A. Spizzichino [1963], "The Scattering of Electromagnetic Waves from Rough Surfaces," Elmsford, NY: Pergamon.

Brown, G. S. [1980], "Backscattering from a Gaussian-distributed perfectly conducting rough surface," *IEEE Transactions on Antennas and Propagation*, Vol. AP-26, pp. 472-482, May (see correction in ibidem, Vol. AP-28, pp. 943-946, Nov. 1980).

CCIR [1990], "Propagation Data for Maritime Mobile-Satellite Systems for Frequencies Above 100 MHz," *Reports of the CCIR, Annex to Volume V, Propagation in Non-Ionized Media*, Report 884-2, pp. 515-535. (International Radio Consultative Committee, XVIIth Plenary Assembly, Dusseldorf, 1990; International Telecommunications Union, Geneva, 1990).

Fang, D. J., F. T. Tseng and T. O. Calvit [1982a], "A Low Elevation Angle Propagation Measurement of 1.5 GHz Satellite Signals in the Gulf of Mexico," *IEEE Transactions on Antennas and Propagation*, Vol. AP-30, No. 1, Jan., pp. 10-15.

Fang, D. J., F. T. Tseng, and T. O. Calvit [1982b], "A Measurement of the Marisat L-Band Signals at Low Elevation Angles Onboard Mobil Aero," *IEEE Transactions on Communications*, Vol. COM-30, No. 2, Feb., pp. 359-365.

Guissard, A. and P. Sobieski [1987], "An approximate model for the microwave brightness temperature of the sea," *Int. J. Remote Sensing*, Vol. 8, No. 11, pp. 1607-1627, Nov.

ITU-R [1994], "Propagation Data Required for the Design of Earth-Space Maritime Mobile Telecommunication Systems," *Recommendation 680-1, International Telecommunication Union, ITU-R Recommendations*, 1994 PN Series Volume, Propagation in Non-Ionized Media.

Karasawa, Y. and T. Shiokawa [1984a] "Characteristics of L-Band Multipath Fading Due to Sea Surface Reflection," *IEEE Transactions on Antennas and Propagation*, Vol. AP-32, No.6, June, pp. 618-623.

Karasawa, Y and T. Shiokawa [1984b], "Spectrum of L-band Multipath Fading Due to Sea Surface Reflection," *Trans. IECE Japan*, Vol. J67-B, No. 2 pp. 171-178.

Karasawa, Y., M. Yasunaga, S. Nomoto, and T. Shiokawa [1986], "On-board experiments on L-band multipath fading and its reduction by use of the polarization shaping method," *Trans. IECE Japan*, Vol. E69, No. 2, pp. 124-131.

Karasawa, Y., and T. Shiokawa [1987] "Fade Duration Statistics at L-Band Multipath Fading Due to Sea Surface Reflection," *IEEE Transactions on Antennas and Propagation*, Vol. AP-35, No.8, August, pp. 956-961.

Karasawa, Y. and T. Shiokawa [1988], "A Simple Prediction Method for L-Band Multipath Fading in Rough Sea Conditions," *IEEE Transactions on Communications*, Vol. 36, No. 10, October, pp. 1098-1104.

Karasawa, Y., T. Matsudo, and T. Shiokawa, and T. Shiokawa [1990], "Wave Height and Frequency Dependence of Multipath Fading Due to Sea Reflection in Maritime Satellite Communications," *Electronics and Communications in Japan*, Part 1, Vol. 73, No. 1, pp. 95-106.

Matsudo, M., Y. Karasawa, M. Yasunaga, and T. Shiokawa [1987], "Results of on-board experiment for reduction technique of multipath fading due to sea surface reflection (IV)," *Paper of Tech. Group on Antennas and Propagation, IEICE Japan*, Vol. AP87-23.

Miller, A. R., R.M. Brown, and E. Vegh [1984], "New Derivation for the Rough Surface Reflection Coefficient and for the Distribution of Sea-Wave Elevations," *IEE Proc.*, Vol. 131, Pt. H, pp. 114-115, April.

Ohmori, S., A. Irimata, H. Morikawa, K. Kondo, Y. Hase and S. Miura [1985], "Characteristics of Sea Refection Fading in Maritime Satellite Communications," *IEEE Transactions on Antennas and Propagation*, Vol. AP-33, No. 8, August, pp.838-845.

Pierson, W. J. and L. Moskowitz [1964], "A proposed spectral form for fully developed wind seas based on the similarity theory of S. A. Kitaigorodskii," *Journal of Geophysical Research*, Vol. 69, No. 24, pp. 5181-5190.

Perrins, E., and M. Rice [1997], "Propagation Analysis of the ACTS Maritime Satellite Channel," *Proceedings of the Fifth International Mobile Satellite Conference*, Pasadena, California, June 16-18, pp. 201-205.

Sandrin, W. A., and D. J. Fang [1986], "Multipath Fading Characterization of L-Band Maritime Mobile Satellite Links," *COMSAT Technical Review*, CTR-86-306, Vol. 16, No. 2, Fall, pp. 319-338.

Sobieski, P. and A. Guissard [1993], "Sea Surface Scattering Calculations in Maritime Satellite Communications," *IEEE Transactions on Communications*, Vol. 41, No. 10, October, pp. 1525-1533.

Chapter 10

Optical Methods for Assessing Fade Margins

Table of Contents

Table of Figures

Table of Tables

Chapter 10
Optical Methods for Assessing Fade Margins

10.1 Background

Until recently, several measurement methods were used by investigators for assessing fade margins for the following types of land-mobile earth-satellite scenarios: (1) propagation paths with clear line-of-sight in a multipath environment, (2) paths through shadowing media such as canopies of trees, and (3) paths which are blocked by buildings or structures. The methods involved radiation from transmitter platforms on towers, aircraft, and satellites that are stationary and non-stationary. Although significant information has been derived from these measurements as described in the other chapters of this text, the methods are generally labor intensive and expensive as they require a transmitter platform, vehicle tracking systems, and complex receiver/data acquisition system which are frequency and bandwidth dependent. More recently, Akturan and Vogel [1997] and Vogel [1997] describe a unique measurement technique for estimating fade margins. The method involves photographing the roadside image of ambient structures, image reduction and analysis, and application of existing models assuming a known constellation of satellites. The methods involved in imaging, photographing, and analyzing the ambient scene are also referred to in this chapter as "photogrammetry". The models are associated with scenarios pertaining to propagation for (1) clear line-of-sight with multipath reflections, (2) the shadowed state [Loo, 1985], and (3) the blocked state [Karasawa et al. 1995]. In this chapter we describe the various experiments, methodologies for reduction and analysis, and subsequent results that have hitherto been derived employing this optical method. The "shadowed state" is here defined as a condition where propagation takes place over the first Fresnel zone through a medium which attenuates the signal (such a tree canopy). The "blocked state" is defined as the condition where the propagation path within the first Fresnel zone is completely obstructed such as by a building or a mountain, and the mechanism of signal reception is accomplished through diffraction and multipath.

10.2 General Methodology

The method consists of the following steps: (1) Images seen through a fisheye lens are photographed at potential user locations. (2) Clear, shadowed, or blocked path states are extracted as a function of look angle. (3) Path states are combined for single or multiple satellite scenarios with frequency-appropriate statistical fade models to predict fade distributions and diversity performance as a function of elevation angle. Measurements of optical brightness along the line-of-sight path have demonstrated a statistical link between fading and optical intensity [Vogel and Hong, 1988]. The images are acquired with a 35-mm camera with a fisheye lens having a full 90° field of view in elevation and 360° in azimuth. The camera may be mounted on a vehicle, hand carried, or fixed on a tripod. A compass is used to align the top of each frame towards north. Resulting slides are scanned into a personal computer and subsequently analyzed.

Figure 10-1 shows an example of a fish-eye lens image in an urban location in Austin, Texas where the zenith is at the center [Akturan and Vogel, 1995]. The 24-bit color image is reduced to an 8 bit gray-scale and it is unwrapped from a circular image (zenith at center) to a rectangular one with the zenith at the top. An image histogram is constructed based on the gray scale value of 32,400 pixels (360° azimuth times 90° elevation, where each pixel size is 1° by 1°. The second derivative of the image histogram, after filtering, is used to estimate the gray-level threshold value separating sky and obstacles [Bovik, 1991]. A binary ski/no-sky image is subsequently produced and used to calculate the elevation angle for each azimuth at which the sky becomes visible (e.g., the skyline). The corresponding skyline of the unwrapped image of Figure 10-1 is shown in Figure 10-2 with the abscissa representing the azimuth (relative to north at 0°) and the ordinate is the corresponding elevation angle.

Figure 10-1: Example of fisheye lens image in Austin, Texas

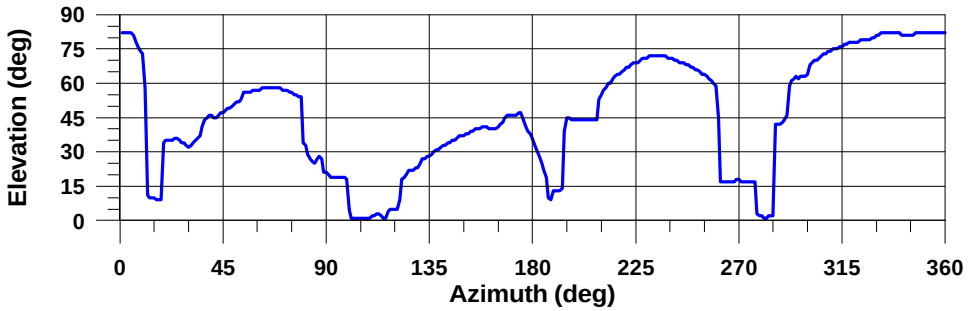

Figure 10-2: Skyline derived from image shown in Figure 10-1.

10.3 Skyline Statistics of Austin and San Antonio, Texas

Using the methodology described in Section 10-2, databases for four locations were derived by Akturan and Vogel [1995a]. The locations consisted of a rural and suburban area in Austin, Texas and central business districts in Austin and San Antonio, Texas. For the rural case, 39 images were acquired along a sparsely tree-lined road at a spacing of approximately one image per mile. In the suburb, 86 images were taken in a neighborhood with single-family houses and relatively small trees. In the central business district (CBD) of Austin and San Antonio, 106 and 96 images were obtained, respectively. The mean, standard deviation, and the 90th percentile (percentage of angles below) elevation angles were averaged in each environment and are summarized in Table 10-1. A small difference exists between the results of the rural and suburban Austin cases. Neither the suburban nor the rural environments had significant tree shadowing. The suburb area was comprised of one- and two-story houses. The 90th percentile of the skyline elevation angle follows a normal distribution, except in the suburb. San Antonio and Austin have similar skyline statistics for the central business district.

Table 10-1: Average skyline statistics for four locations derived by optical methods.

Location	Mean Elevation (°)	Stand. Dev. (°)	90% (Angles Below)
Rural Austin	5.3	3.7	10.9
Suburban Austin	7.4	5.8	16.6
Austin CBD	25.8	20.2	55.2
San Antonio CBD	27.7	18.1	53.5

As an example, the skyline histogram for the central business district of San Antonio is given in Figure 10-3. This histogram follows with good approximation the log normal fit,

$$f(q) = \frac{1}{(q/c)s\sqrt{2p}} \exp\left[\frac{-\left(\ln(q/c) - m\right)^2}{2s^2}\right], \qquad (10\text{-}1)$$

where q is the elevation angle (°), m and s are the mean and standard deviation of $\ln(q/c)$, respectively, and c is a scaling factor. The values of these parameters are summarized in Table 10-2.

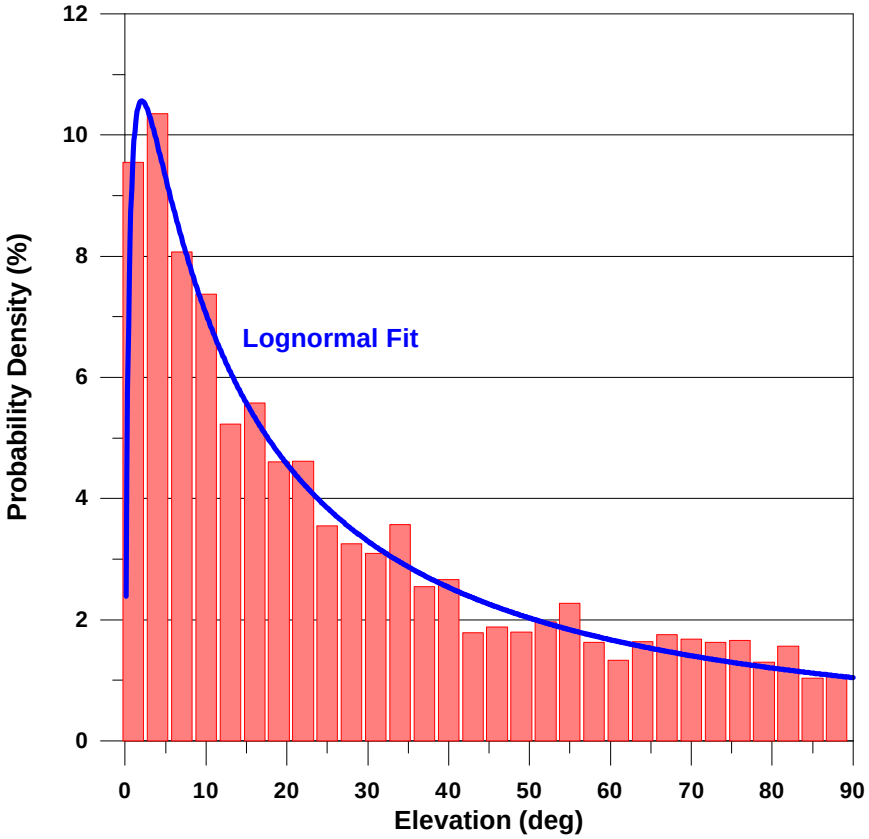

Figure 10-3: Skyline elevation angle histogram for San Antonio, Texas.

Table 10-2: Parameters associated with lognormal fits associated with histograms of the type given in Figure 10-3 and percent visibility above 10°.

Location	Mean (m)	Stand. Dev. (s)	c	Percent Visibility Above 10°
Rural Austin	0.39	0.84	2.96	98%
Suburban Austin	0.44	0.80	2.81	95%
Austin CBD	1.74	1.52	3.13	77%
San Antonio CBD	2.30	1.75	4.46	68%

As an another example of the useful information that may be derived employing the measurements described above, the last column in Table 10-2 gives the percent visibility above 10° at the various locations. We note that in the central business district of Austin and San Antonio, only 77% and 68% of the sky are visible above 10°, respectively. The analysis was executed assuming the binary states “blocked” or “clear.” In the following section, a methodology is given that includes multipath effects and shadowing.

10.4 Clear, Shadowed and Blocked Propagation States

Fading for mobile satellite communications can be modeled by assuming that distinct signal level statistics pertain to three major propagation states, i.e., when the line-of-sight is clear with multipath contributions, shadowing by foliage, and blocked by buildings. Karasawa et al. [1994] fitted L-Band satellite fade data obtained in urban Japan at 32° elevation to a cumulative probability distribution consisting of a weighted linear combination of fading density functions developed by Rice, Loo, and Rayleigh. This linear combination is expressed by

$$f_n(v) = C\ f_{Rice}(v) + S\ f_{Loo}(v) + B\ f_{Rayleigh}(v), \tag{10-2}$$

where *C, S, B* are probabilities of clear, shadowed, and blocked states, and f_v denotes the probability density function (PDF) for the signal envelope. The Ricean density distribution is given by

$$f_{Rice}(v) = 2Kv\ \exp\left[-K(v^2+1)\right] I_o(2Kv), \tag{10-3}$$

Loo's density function [Loo, 1985] is given by

$$f_{Loo}(v) = 8.686\sqrt{\frac{2}{p}}\frac{Kv}{s}\int_0^\infty \frac{1}{z}\exp\left[-\frac{(20\log(z)-m)^2}{2s^{\,2}} - K(v^2+z^2)\right] I_0(2Kvz)dz, \tag{10-4}$$

and the Rayleigh density function is given by

$$f_{Rayleigh}(v) = 2Kv\exp(-Kv^2), \tag{10-5}$$

where n is the received voltage relative to the clear path voltage, *K* is the ratio of the direct power received to the multipath power, $I_0(n)$ is the modified Bessel function with argument$n$, m is the mean of $\log(n)$, and s is the standard deviation of $\log(n)$. It should be noted that (10-2) does not account for any specular reflection or any building diffracted power for blocked conditions.

Satellite beacon and photogrammetrically measured values of *K* for the three fade states are tabulated in Table 10-3. Employing earth-satellite measurements at 1.5 GHz and 32° elevation for urban Tokyo, Karasawa et al. [1994] estimated values of *C, S, B* of 0.55, 0.1, 0.35, respectively. The "path-state mixture vector" for this case is defined as

$$\overline{M} = <0.55, 0.1, 0.35>. \tag{10-6}$$

For the fit using (10-6), the RMS fade prediction error over the 5% to 95% interval is 1.3 dB (3rd column, last row in Table 10-3). The measured (Δ) and modeled (short dashed) cumulative fade distributions (CDF) of Karasawa et al. [1994] are plotted in Figure 10-4. Shown to the right of the distribution are error curves defined as the difference between the measured and modeled dB values. A peak error of approximately 3 dB occurs at a

probability of 34%. Also shown in Figure 10-4 is the "fitted" distribution (long-dashed curve) based on the photogrammetrically measured path state mixture corresponding to the measurements of Akturan and Vogel [1997], who found a path-state mixture vector of

$$\overline{M} =< 0.51, 0.07, 0.42 > . \tag{10-7}$$

To achieve a best fit, the values of the parameters of (10-2) through (10-5) were adjusted (4th column of Table 10-3) for the two most prevalent states (C and B). The "fitted" three-state model gives a peak error of 2.5 dB (Figure 10-4) and an RMS error of 1.1 dB over the 5% to 95% range.

Table 10-3: Fade parameters of the three-state fade model.

Fade State	PDF Type	Karasawa [Karasawa et al., 1994]	"Fitted" 3-State	Urban 3-State
C	**Rice**			
	K	6.3 (8 dB)	5.9 (7.7 dB)	5.9 (7.7 dB)
S	**Loo**			
	K	20 (13 dB)	20 (13 dB)	20 (13 dB)
	m	10 (10 dB)	10 (10 dB)	10 (10 dB)
	s	2 (3 dB)	2 (3 dB)	2 (3 dB)
B	**Rayleigh**			
	K	100 (20 dB)	49 (16.9 dB)	
B	**Loo**			
	K			501 (27 dB)
	m			100 (20 dB)
	s			5.4 (7.3 dB)
	RMS Error	1.3 dB	1.1 dB	0.5 dB

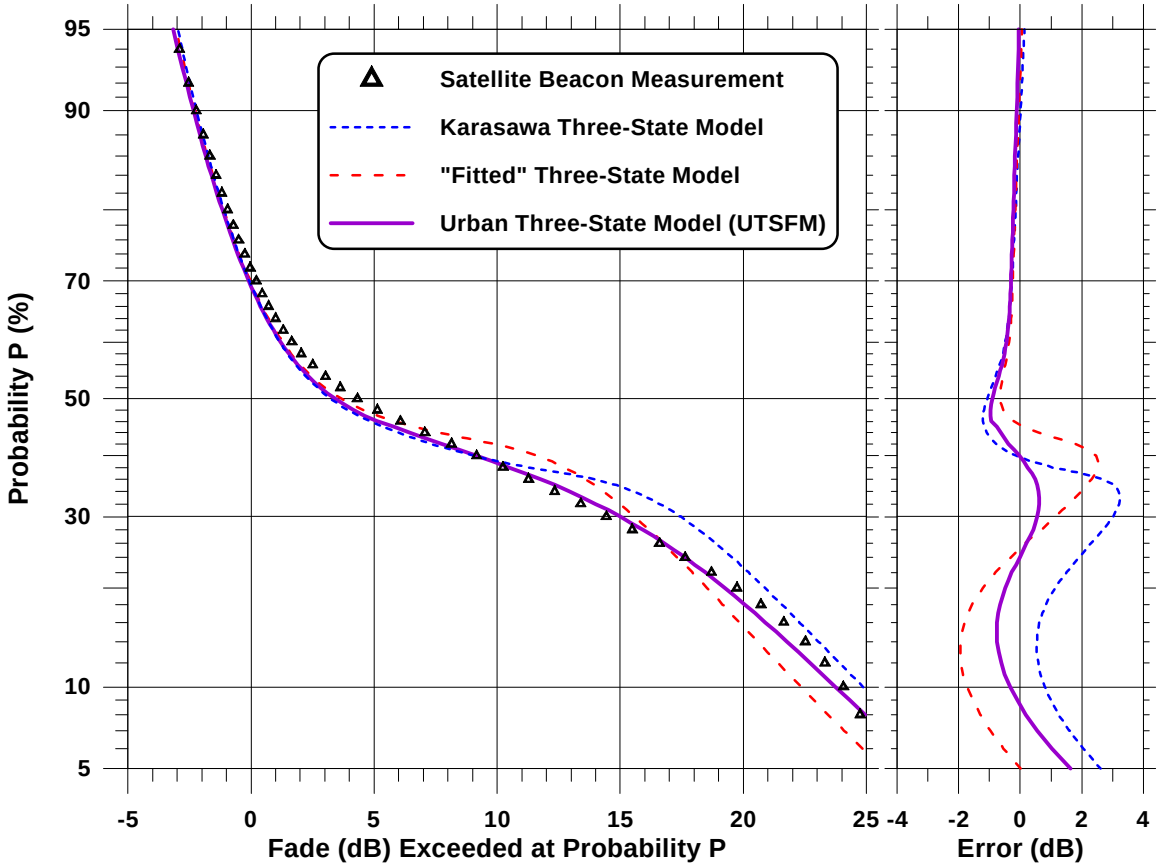

Figure 10-4: The left set of curves denotes measured and modeled fade distributions in Japan (urban regions) at 32° elevation and f = 1.5 GHz. The right-hand curves represent the fade differences between the measured and modeled distributions at different percentages.

In Figure 10-4, the major qualitative difference between the measured and the modeled CDF is that the modeled CDFs are much flatter than the measured one in the fade range from 3 to 13 dB. The terraced shape of the CDF has been observed on open rural freeways, where the unobstructed line-of-sight and strong multipath sources are both blocked at the same time by overpasses for a certain fraction of the distance. In this case, it is appropriate to use the Rayleigh distribution to describe the blocked state. On the other hand, when the signal is blocked in the urban environment, specular reflections from nearby illuminated building surfaces and diffracted rays are likely to also be received. To account for these effects, the distribution in the urban blocked state was changed from Rayleigh to Loo using the values given in the last column of Table 10-3. This CDF (solid curve) is plotted in Figure 10-4 and gives a peak error smaller than 1.5 dB (Figure 10-4) and a corresponding RMS error of 0.5 dB. At the terrace part of the curve, the maximum error is approximately 0.5 dB.

10.5 Urban Three-State Fade Model (UTSFM)

Employing concepts described in Section 10.4, an Urban Three-State Fade Model was developed by Akturan and Vogel [1997]. This model, hereafter referred to by the acronym UTSFM, has the form

$$f_n(n,a) = C(a)\ f_{Rice}(n) + S(a)\ f_{Loo}(n) + B(a)\ f_{Loo}(n), \qquad (10\text{-}8)$$

where in (10-8) is the elevation angle. Using photogrammetric measurements in urban Japan, henceforth generically referred to as "Tokyo" although other Japanese cities were also involved, Akturan and Vogel [1997] have characterized *C, S, B* as a function of a. These values, which have been averaged over the 360° azimuth, are tabulated in Table 10-4. In Figure 10-5 are plotted a family of CDF's employing (10-8), the values in Table 10-4 at the mid-range of the angular intervals, and the parameters in the right-hand column of Table 10-3. We note the dramatic effect elevation angle has on fade at any given fixed exceedance probability level. For example, at the 10% level, the fades range between approximately 6 dB at 82° and 28 dB at 7°. Between 12° and 67° at the 10% level, the fade increases at a rate of approximately 0.2 dB per degree (e.g., from 15 dB to 25.5 dB). All the curves in Figure 10-5 contain a terraced shape region between approximately 5 to 13 dB where a relatively small percentage change takes place. Such a result indicates that increasing the fade margin beyond approximately 5 dB may not "pay off" until 13 dB is exceeded. The curves in Figure 10-5 may be employed at any urban location (for L-Band) under the assumption that the path-state mixture vector is given by (10-7), implying the urban environment of Tokyo is similar to the urban location being modeled.

Table 10-4: Tabulation of azimuth averaged values of *C, S* and *B* in (10-8) for different elevation angle intervals for Tokyo, Japan.

Elevation Angle Interval (°)	*C*	*S*	*B*	Elevation Angle Interval (°)	*C*	*S*	*B*
0-4	0.02	0.03	0.95	45-49	0.67	0.05	0.27
5-9	0.07	0.06	0.86	50-54	0.72	0.05	0.23
10-14	0.17	0.08	0.75	55-59	0.76	0.04	0.20
15-19	0.28	0.08	0.64	60-64	0.80	0.03	0.17
20-24	0.37	0.08	0.56	65-69	0.83	0.03	0.14
25-29	0.44	0.07	0.48	70-74	0.86	0.03	0.11
30-34	0.51	0.07	0.42	75-79	0.89	0.02	0.09
35-39	0.58	0.06	0.36	80-84	0.92	0.02	0.06
40-44	0.63	0.06	0.31	85-89	0.93	0.02	0.06

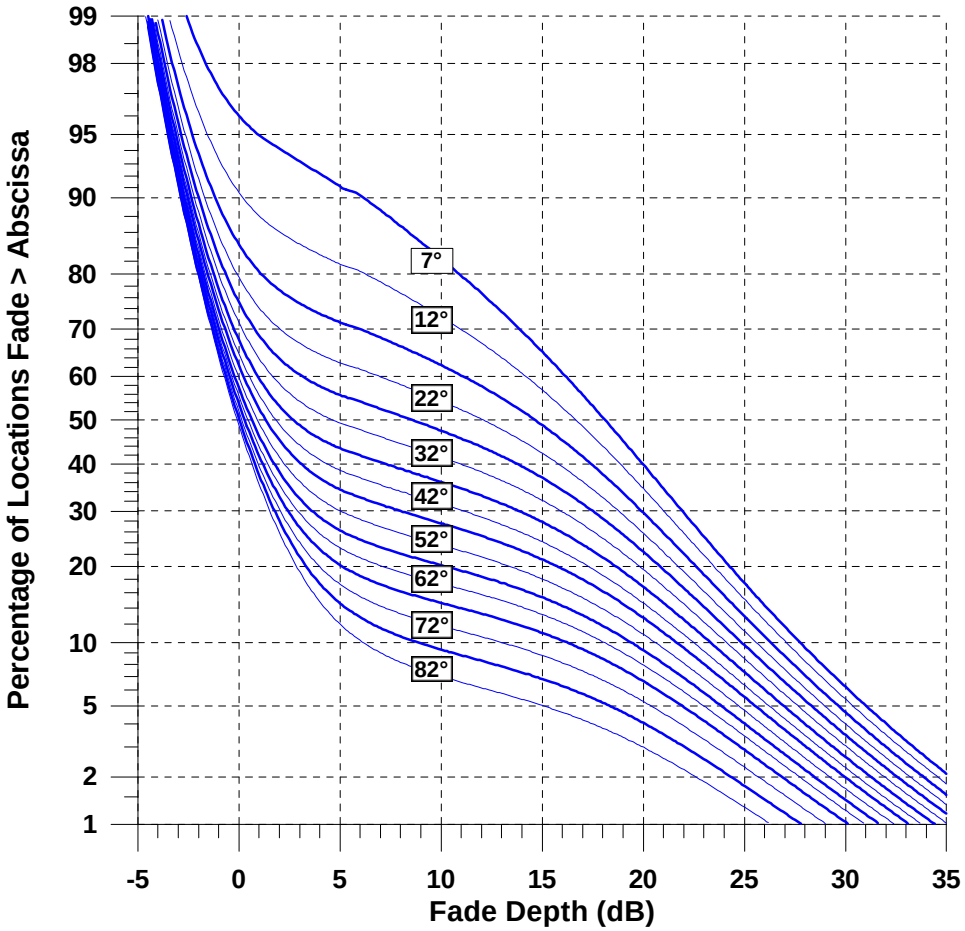

Figure 10-5: Cumulative fade distributions at 1.5 GHz for a family of elevation angles for urban Japan. Curves were derived using the UTSFM described in text. Indicated elevation angles are centered within $\pm 2°$ intervals.

10.6 Estimation of Urban Fading for the Globalstar Constellation

Akturan and Vogel [1997] and Vogel [1997] estimated urban fading for a real mobile satellite system using azimuths and elevations for the Globalstar constellation [Schindall, 1995]. This constellation consists of 48 satellites orbiting in eight planes (six satellites per plane) inclined at 52° with a period of 114 minutes. A satellite is said to be potentially visible if the elevation angle is above 10°. The azimuths and elevations to each satellite were calculated at 18-second intervals over a 24-hour period. In other words a total of 4800 satellite constellations (24x3600/18) were considered for each photogrammetric image. Since a total of 236 images were taken, the statistical database in which the cumulative distributions were calculated is comprised of a sample size in excess of 10^6 constellations (4800x236).

10.6.1 Cumulative Fade Distributions for Urban Areas In Tokyo, London, and Singapore

Assuming that the urban environment of Tokyo (mid-latitude $\approx 35.5°$) is globally representative and has similar skyline statistics as other urban areas, cumulative fade distributions were derived for London, England having a higher latitude ($\approx 51.5°$) and Singapore (Island of Singapore), at the equatorial latitude ($\approx 1°$). Based on photogrammetric measurements and the known satellite constellations (of Globalstar), at each of these locations the average state mixtures of the "highest" and "best" were determined for all images and the entire period. The values of *C, S, B* are listed in Table 10-5 for both of these cases. The "highest" satellite configuration is a form of satellite diversity where communications is sequentially switched (every 18 s in the case considered here) to the satellite that gives the largest elevation angle of the earth-satellite path; regardless of whether it is "blocked" or "shadowed." The "best" satellite configuration switches first to the satellite that has a "clear line-of-sight." If such a satellite does not exist in the constellation, switching takes place to a satellite that is "shadowed." If neither the "clear" or "shadowed" line of sight is available, then the line-of-sight path is blocked.

Table 10-5: List of values of "path-state vector" components *C, S, B* for Globalstar constellation in London, Tokyo, and Singapore.

Location	Highest Satellite			Best Satellite		
	C	*S*	*B*	*C*	*S*	*B*
London	0.689	0.086	0.225	0.817	0.081	0.102
Tokyo	0.583	0.103	0.314	0.782	0.095	0.124
Singapore	0.567	0.110	0.323	0.668	0.121	0.211

In Figure 10-6 are plotted the cumulative fade distributions for the "highest" satellite cases for the above mentioned cities. The cumulative fade distribution for London shows the smallest fades because the elevation angles to the satellites are generally greater. It is noted that 15 dB is exceeded at 20% (London) to approximately 30% (Singapore and Tokyo) of locations (or of time) for the "highest" satellite scenario.

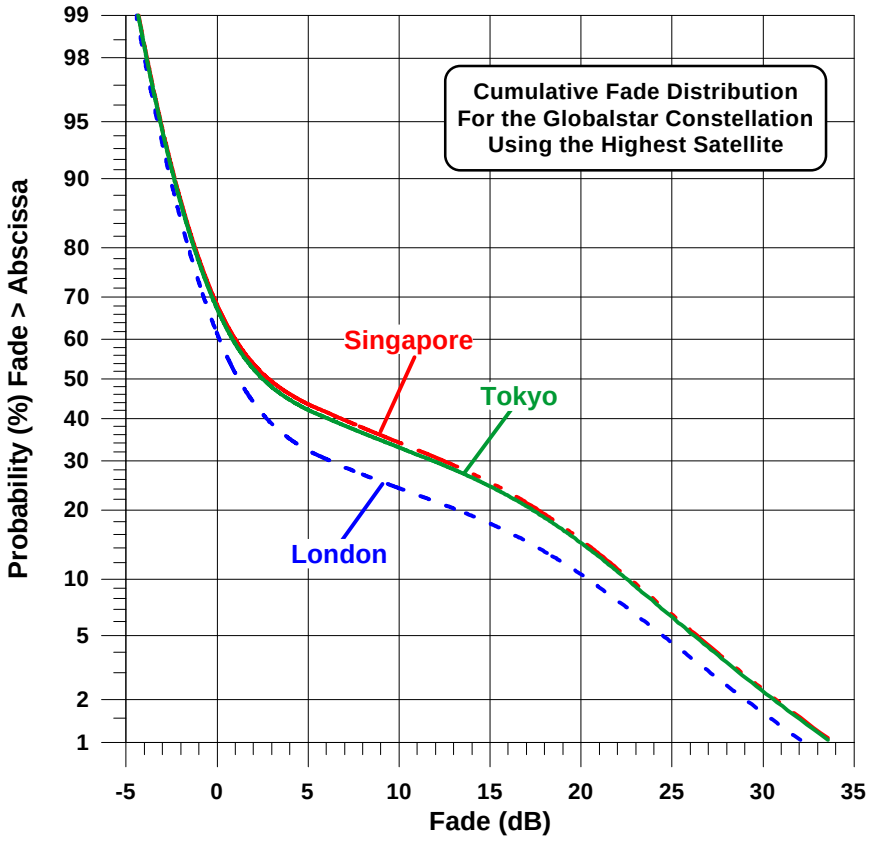

Figure 10-6: Cumulative fade distribution for Globalstar satellite constellation associated with "highest" satellite diversity scenario. The path state vector components for London, Tokyo, and Singapore are given in Table 10-5.

10.7 Statistics of Potentially Visible Satellites in Various States

In order to establish *a priori* an optimum communications strategy for any given land-mobile satellite system, it is desirable to have knowledge of the statistics associated with the "states" of the "potentially visible" satellites. In this section, we describe such a statistic assuming the Globalstar system of satellites at the geographic locations of Tokyo, London, and Singapore. As mentioned, "potentially visible" is defined as a satellite at an elevation angle above 10°.

Figure 10-7 through Figure 10-9 are three-dimensional bar charts describing satellite constellation and path-state mixture statistics for Tokyo, London, and Singapore, respectively. The vertical scale signifies the joint probability (in percent) that the indicated numbers of satellites are potentially visible with the shown state mixture. The scale labeled "Mixed State" represents the various combinations of states for up to four potentially visible satellites. For example, CCSB corresponds to the states clear, clear, shadowed, and blocked for four potentially visible satellites. When three satellites are potentially visible, we take the first three states; namely, clear, clear, and shadowed. For the two-satellite case, this nomenclature implies the clear, clear state, and for one satellite, it represents the clear state. The indicated "All" state denotes all the satellites

that are potentially visible (satellites above 10°) regardless of the state. For example (for London) shows there is zero probability that only one satellite is visible for any of the states indicated. On the other hand, the probabilities are approximately 30%, 50%, and 20% that two, three, and four satellites are potentially visible, respectively. The joint probabilities that one, two, three, and four satellites are potentially visible and that they have clear states (i.e., CCCC) are approximately 0%, 10%, 5%, and 1%, respectively.

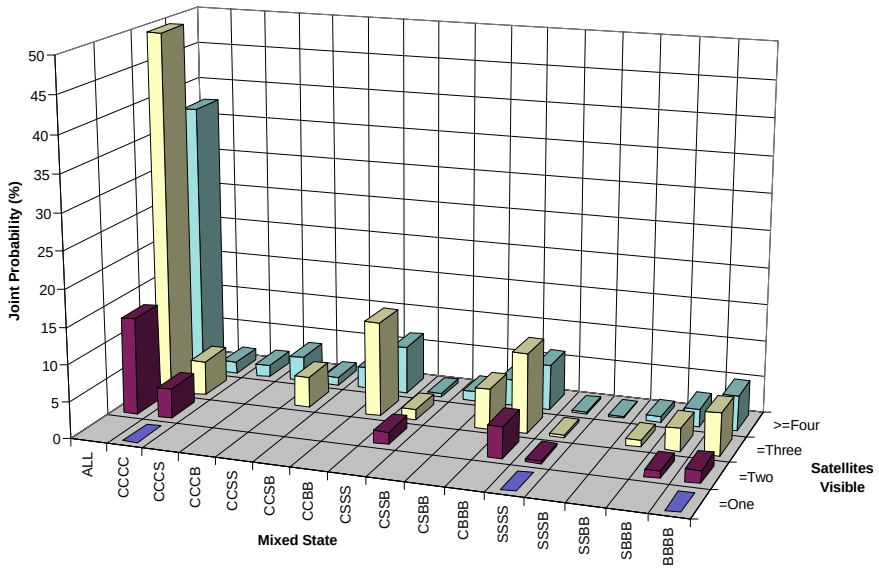

Figure 10-7: The joint probability for state mixtures of two, three, and four potentially visible satellites assuming the Globalstar constellation for observations made in Tokyo.

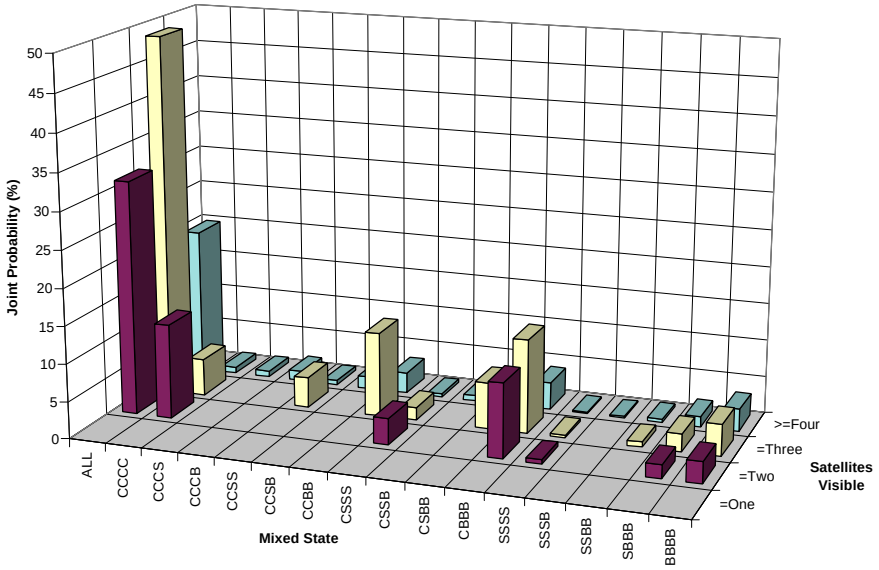

Figure 10-8: The joint probability of state mixtures of two, three, and four potentially visible satellites assuming the Globalstar constellation for observations made in London.

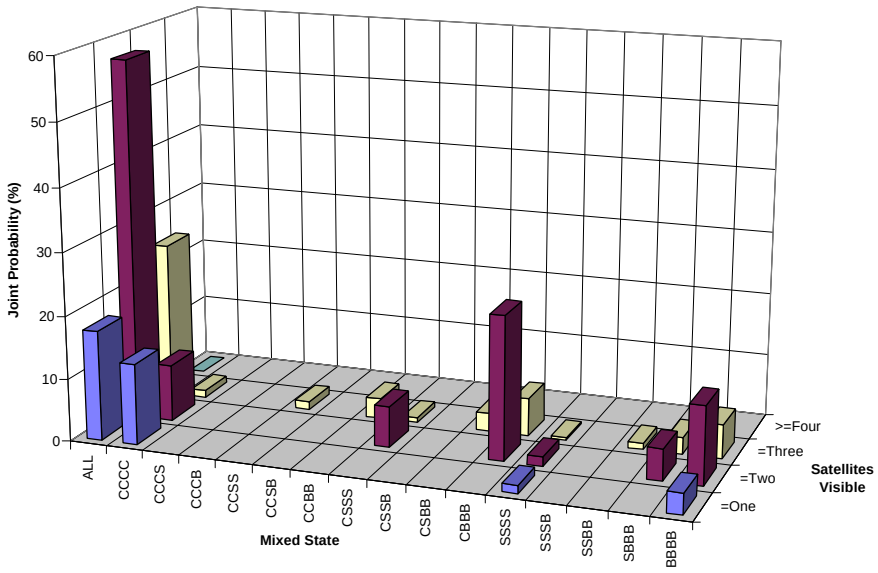

Figure 10-9: The joint probability of state mixtures for two, three, and four potentially visible satellites assuming the Globalstar constellation for observations made in Singapore.

10.8 Satellite Diversity

The geometry of the satellites in their constellation and the nature of the associated states corresponding to each satellite position at any instant of time suggest the employment of satellite diversity. Although satellite diversity using the Globalstar constellation has been previously described in Chapter 6 (Section 6.6), for purposes of completeness and chapter continuity, we again review the results here.

10.8.1 Single and Joint Fade Distributions

In Figure 10-10, Figure 10-11 and Figure 10-12 are given a series of cumulative fade distributions for Tokyo, London, and Singapore assuming the Globalstar constellation relative to each geographic location. The distributions in each of these figures correspond to different types of satellite diversity communications systems. The distribution for the "Highest Satellite" is derived from a satellite diversity scenario where communications are switched to the satellite that assumes the highest elevation angle in the respective constellation, regardless of the path-state. The distribution labeled "Best Satellite" is also derived from multiple satellites where switching takes place relative to the satellite giving the smallest fade. In calculating this distribution, a decision for "best satellite" was made every 18 seconds before "hand over" was executed. At the 10% probability, the fades exceeded are 15 dB, 13 dB, and 19 dB for Tokyo, London, and Singapore, respectively. The average elevation angles for the constellation of satellites for Tokyo and Singapore are similar (40° and 38°, respectively). Nevertheless, Singapore tends to show larger fades for the "Best" and multiple satellite scenarios because of the

reduced choice of potentially visible satellites near the equator (e.g., compare Figure 10-7 and Figure 10-8 with Figure 10-9).

The distribution labeled "2 Best Satellites" represents the joint distribution associated with the two satellites giving jointly the "smallest fades". At any instant of time, different pairs of satellites may fall under the "2 Best Satellite" category. The distributions labeled "3 Best Satellites" and "4 Best Satellites" are analogously defined. The above joint distributions were derived assuming "combining diversity" where the signals received are "added," as opposed to "hand-off" where the satellite with the "highest" signal is processed. It is apparent that relatively small differences in fade margin reduction exist at the 10% probability in comparing the multiple satellite case with the "Best Satellite" distribution at the three locations. For example, in comparing the "Best-Satellite" with the "4-Best Satellite" distributions at the 10% probability, a less than 5 dB improvement exists at all three locations. Somewhat larger improvements occur at the 1% probability level, however the fade margins even for multiple satellite diversity becomes prohibitively high.

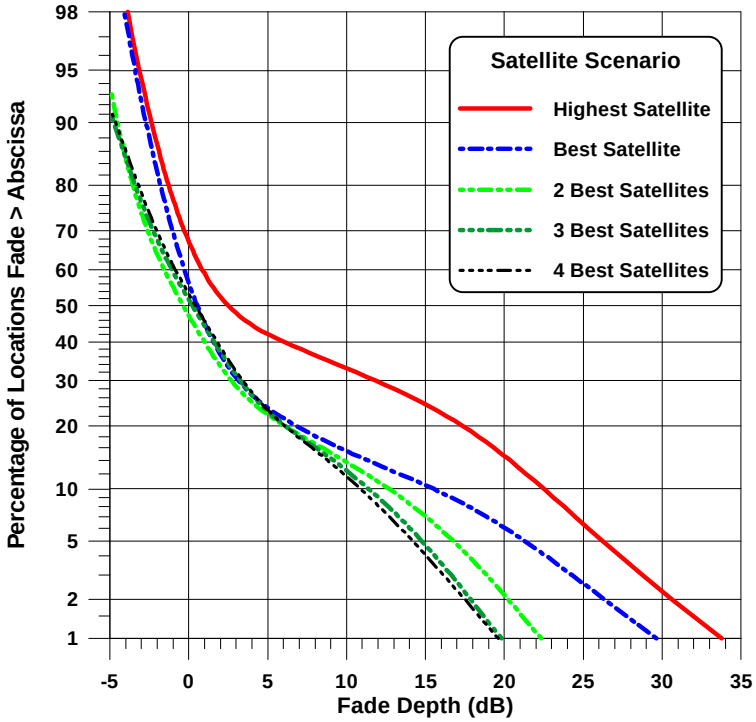

Figure 10-10: Cumulative fade distributions for Tokyo, Japan at L-Band (1.5 GHz) for the simulated Globalstar constellation. The joint distributions for multiple satellites correspond to "combining diversity."

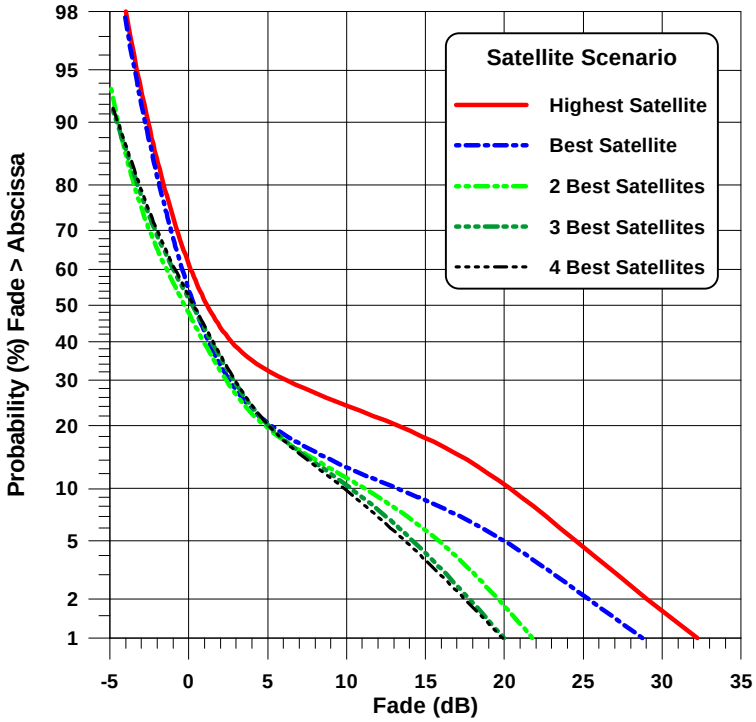

Figure 10-11: Cumulative fade distributions for London, England at L-Band (1.5 GHz) for the simulated Globalstar constellation. The joint distributions for multiple satellites correspond to "combining diversity."

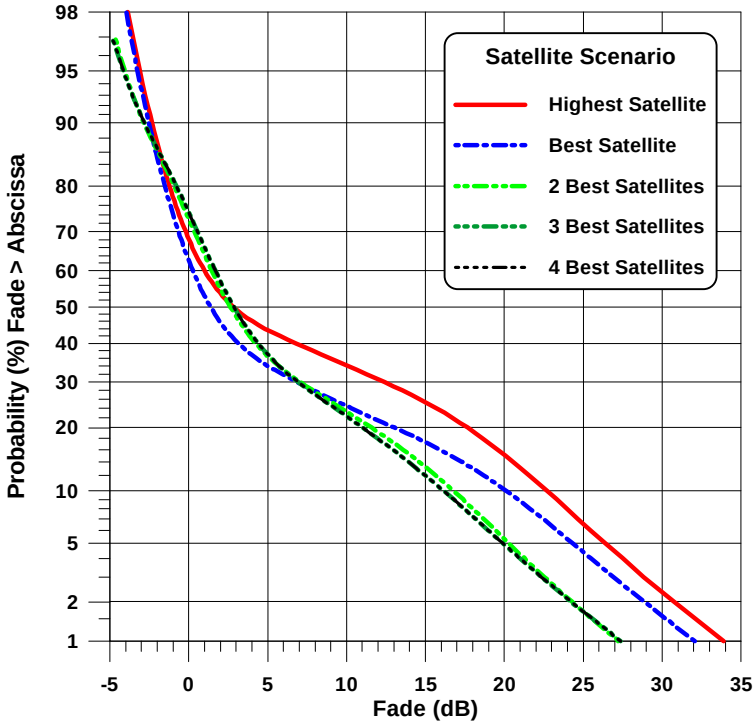

Figure 10-12: Cumulative fade distributions for Singapore at L-Band (1.5 GHz) for the simulated Globalstar constellation. The joint distributions for multiple satellites correspond to "combining diversity."

10.8.2 Diversity Gain Versus Probability for Tokyo, London, and Singapore

In Figure 10-13 is given the diversity gain versus probability for the "Best-Satellite" and the joint distribution multiple satellite cases for Tokyo. Two types of diversity gains are shown plotted; namely one corresponding to "handoff" (solid) and the other to "combining" (dashed) as previously described. The diversity gain is defined here as the fade difference between the highest satellite and any of the other scenario distributions at a fixed probability level. For example, at the 10% probability in Figure 10-10, the Highest-Satellite and Best-Satellite fade levels exceeded are approximately 22 dB and 15 dB, respectively. The difference in these fade levels corresponds to a diversity gain of 7 dB at a probability of 10% as noted in Figure 10-13. The diversity gains for the other distributions are analogously derived.

The following results may be gleaned from Figure 10-13: (1) The diversity gain differences (at any probability) between "handoff" and "combining" methodologies are generally smaller than 1 dB. (2) For probabilities down to approximately 20%, the "Best Satellite" diversity gain is within 1.5 dB of the other multiple satellite cases. (3) At the 10% level, the multiple satellite cases give 3 to 5 dB improvement in the diversity gain relative to the Best Satellite**.**

The London diversity gain curves are similar to those of Tokyo except approximately 1 to 2 dB lower because the "Highest" satellite reference distribution is shifted to the left (as shown in Figure 10-6). This occurs predominantly because the average satellite elevation of the highest satellite is 52° for London as compared to 40° for Tokyo.

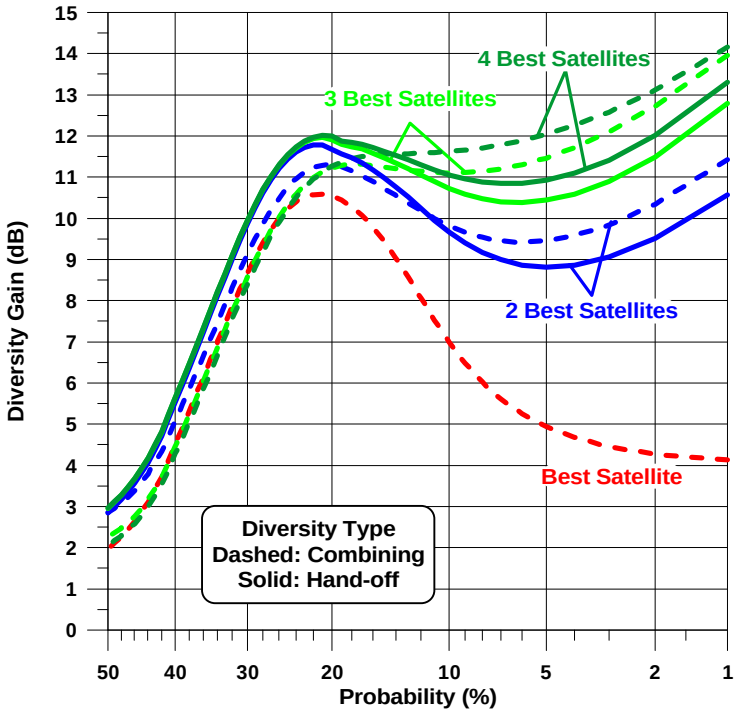

Figure 10-13: Path diversity gains at 1.5 GHz derived from distributions for the simulated Globalstar constellation with "combining" and "handoff" diversity for Tokyo, Japan.

Figure 10-14 shows an analogous set of diversity gains for Singapore. Although the average elevation angle (38°) to the highest satellite is approximately the same as in Tokyo (40°), the corresponding diversity gains are only about half of those achieved in the more northern latitudes. This occurs because of the reduced choice of potentially visible satellites at the equator.

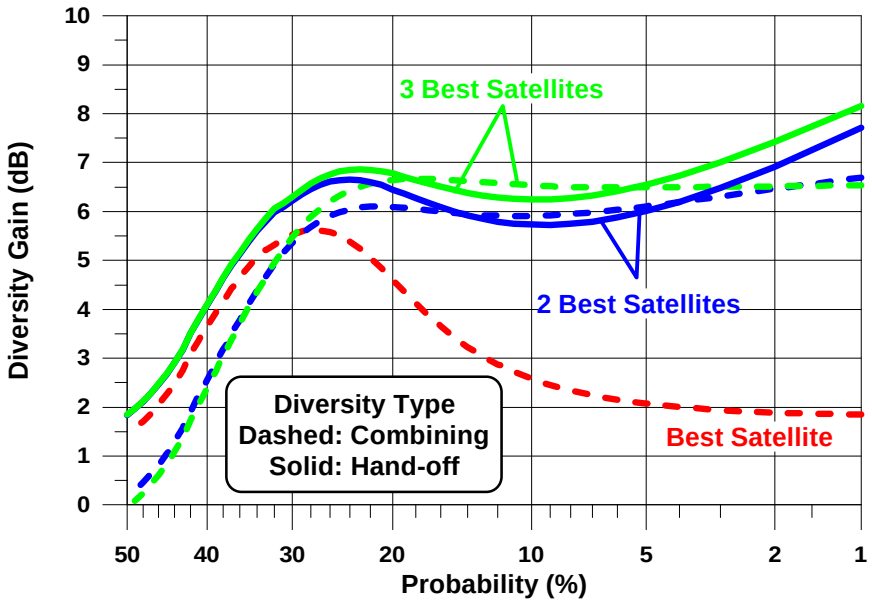

Figure 10-14: Path diversity gains at 1.5 GHz derived from distributions for the simulated Globalstar constellation with "combining" and "handoff" diversity for Singapore.

10.9 Summary Comments and Recommendations

A method by Akturan and Vogel [1994, 1995, 1995a, 1995b, 1997], Vogel [1997] has been described in this chapter to assess fade margins for outdoor mobile satellite systems. This photogrammetric method involves taking fisheye lens images at potential user locations and analyzing the images for the presence of clear sky, tree shadowing, or blockage by solid obstacles. This method works for the following reasons: (1) Propagation effects for Satellite-Personal-Communications Systems (SPCS) are imposed by the physical environment within a short range from a mobile user's terminal. (2) Analysis of the propagation conditions is straightforward since the earth-satellite path is elevated and the path-state is related to the ambient structure environment (as opposed to terrestrial scenarios where propagation occurs via multipath from hidden multipath structures). (3) The statistical properties of the received signal levels can be described by a few physically reasonable distributions that are a function of the fade-state. (4) Suitable parameters for the distributions have already been evaluated for a limited number of cases (as described in this chapter).

A model known as the Urban Three-State Fade Model (UTSFM) is described here. This model may be used for urban environments similar to that of Tokyo. The model

gives a family of cumulative fade distributions for satellite elevation angles ranging between 2° and 87° as shown in Figure 10-5.

Assuming the Globalstar constellation of satellites, cumulative fade distributions for various diversity scenarios are given in Figure 10-10, Figure 10-11 and Figure 10-12 for Tokyo, London, and Singapore. Corresponding diversity gain results for both "combining" and "hand-off" diversity are given in Figure 10-13, and Figure 10-14. These curves were derived under the assumption that London and Singapore has the same urban state characteristics as Tokyo (measured). These figures show that combining diversity may buy approximately 1 dB in fade margin relative to hand-off diversity.

It is recommended that detailed measurements of the state characteristics are made at other locations around the world and cumulative fade distributions are derived independently without relying on the assumptions of the Tokyo measurements. Until such results are available the results given in this chapter should be used along with the stated caveats.

10.10 References

Akturan, R. and W. J. Vogel [1994], "Photogrammetric Mobile Satellite Service Prediction," Proceedings of the Eighteenth NASA Propagation Experimenters Meeting (NAPEX XVIII) and the Advanced Communications Technology Satellite (ACTS) Propagation Studies Mini-Workshop, Vancouver, British Columbia, June 16-17, pp. 159-163. (JPL Publication 94-19; Jet Propulsion Laboratory, California Institute of Technology, Pasadena, California).

Akturan, R. and W. J. Vogel [1995], "Optically Derived Elevation Angle Dependence of Fading for Satellite PCS," Proceedings of the Nineteenth NASA Propagation Experimenters Meeting (NAPEX XIX) and the Seventh Advanced Communications Technology Satellite (ACTS) Propagation Studies Workshop (APSW VII), Fort Collins, Colorado, June 14-16, pp. 127-132. (JPL Publication 95-15; Jet Propulsion Laboratory, California Institute of Technology, Pasadena, California).

Akturan, R. and W. J. Vogel [1995a], "Photogrammetric Mobile Satellite Service Prediction," Electronics Letters, February 2, Vol. 31, No. 31, pp. 165-166.

Akturan, R. and W. J. Vogel [1995b], "Elevation Angle Dependence of Fading for Satellite PCS in Urban Areas," Electronics Letters, December 7, 1995, Vol. 31, No. 25, pp. 2156-2157.

Akturan, R. and W. J. Vogel [1997], "Path Diversity for LEO Satellite-PCS in the Urban Environment," IEEE Transactions on Antennas and Propagation, Vol. 45, No. 7, pp. 1107-1116.

Bovik, A. C. [1991], "Digital Image Processing," The University of Texas at Austin, Austin, Texas.

Karasawa, Y., K. Minamisono, and T. Matsudo [1995], "A Propagation Channel Model for Personal Mobile-Satellite Services," in Proceedings of Progress of Electromagnetic Research Symposium of the European Space Agency (ESA), Noordwijk, The Netherlands, July, pp. 11-15.

Loo, C. [1985], "A Statistical Model for a Land Mobile Satellite Link," IEEE Transactions on Vehicular Technology, 1985, VT-34, Vol. 3, pp. 122-127.

Schindall, J. [1995], "Concept and Implementation of the Globalstar Mobile Satellite System," Proceedings of 4th International Mobile Satellite Conference, Ottawa, Canada, June, pp. A11-A16.

Vogel, W. J., [1997], "Satellite Diversity for Personal Satellite Communications-Modeling and Measurements," Tenth International Conference on Antennas and Propagation (ICAP 97)," Vol. One, Conference Publication, No. 436, pp. 1269-1272.

Vogel, W. J., and U. S. Hong [1988], "Measurement and Modeling of Land Mobile Satellite Propagation at UHF and L-Band," IEEE Transactions on Antennas and Propagation, Vol. AP-36, No. 5, pp. 707-719.

Chapter 11

Theoretical Modeling Considerations

Table of Contents

Table of Figures

Table of Tables

Chapter 11
Theoretical Modeling Considerations

11.1 Background

Modeling serves a variety of purposes for characterizing land mobile satellite propagation. Without the availability of data, a heuristic propagation model is desirable in order to design propagation experiments that measure important signal characteristics without imposing instrumentation limitations. Once data are available, specialized models can be developed to explain the observed signal variations and their dependence on a wide range of experimental parameters, such as the environment topography, link elevation angle, vehicle speed, or receiver antenna pattern. As empirical or analytical models reach maturity, they can be employed to evaluate system performance under specified conditions or to simulate the actual operation for LMSS scenarios with a particular choice of modulation and coding. Good models based on a thorough understanding of the causes of signal degradation can then be used as aids in optimizing system design and to explore fade mitigation strategies.

Much work has been done to characterize the signal variations observed in terrestrial land mobile propagation at UHF [Jakes, 1974; Lee, 1986]. While some of the same basic concepts of signal statistics apply also to LMSS, significant differences exist and require the development of LMSS specific models. Satellite systems are usually power limited because it is expensive and/or impractical to operate high-power transmitters and high-gain antennas in space. Such systems therefore function with relatively low fade margins at or near the line-of-sight signal level. On the other hand, terrestrial systems can apply higher power levels and do not need to establish a line-of-sight signal path. They normally operate by utilizing the scattered multipath signals. In contrast, satellite systems must utilize the line-of-signal component for communications, and multipath scattering represents interference.

In response to the needs of experimenters and system designers, several distinct types of LMSS models have been developed. Three classes of models are described in the following paragraphs. They are classified here as (1) empirical regression fits to data, (2) probability distribution models, and (3) geometric-analytic models. The empirical

regression fits to data models describe probability distributions of fades based on experimental measurements. The second class, probability distributions models, are based on the utilization of a composite of several probability density functions customarily used in radio wave propagation; namely, Rayleigh, Ricean, and lognormal statistics. Among these, some combine densities based on physical reasoning about the propagation process, while others add the use of fade state or fade state transition probabilities. The third class of models employs geometrical analytical procedures for predicting the effects of single and multiple scatterers.

The choice as to which model is most appropriate depends very much on the intended application and which propagation phenomenon one wants to predict. Of the different types, empirical models do not provide insight into the physics of propagation processes, but they characterize the sensitivity of the results to important parameters. Statistical models build upon an understanding of the processes that cause signal variations, but with simplifying assumptions. Analytical models attempt to describe a particular propagation scenario deterministically, but then have to use statistics to extend the results to realistic situations.

In this chapter, we present background information associated with the important elements of model development. Also described are the dominant LMSS propagation models of the above types, their input and output parameters, as well as their advantages and limitations.

11.2 Background Information Associated with Model Development

11.2.1 Diffusely Scattered Waves

To explain signal variations specific to LMSS transmissions between a satellite and a moving vehicle, the interactions of two important signal components have to be considered: line-of-sight and diffusely scattered waves. We ignore the ground reflected waves since it is presumed that for LMSS scenarios, any energy directed towards the antenna near the horizontal will be outside its beamwidth and be filtered out by the low gain pattern function values.

The direct wave may be approximated by a plane wave propagated along the line-of-sight path, with most of the power transmitted through the first Fresnel zone. It may be completely obscured by obstacles such as mountains, buildings, or overpasses, or partially shadowed by roadside trees or utility poles. Absorption, diffraction, scattering, or a combination thereof may explain the shadowing process. The frequency of the direct wave is also shifted by an amount proportional to the relative speed between the satellite and the vehicle.

A scenario for diffuse scattering for mobile reception may be described as follows. Transmissions from a satellite illuminate obstacles in the vicinity of the vehicle resulting in reflected energy emanating from multiple scatterers. Waves from these scatterers arrive at the receiving antenna with random polarizations, amplitudes, and phases, and the individual contributions are delayed by the amount of time corresponding to the extra

path traveled. In addition, the individual contributions undergo a Doppler shift proportional to the relative speed between any particular scatterer and the vehicle. It is limited to a band of frequencies relative to the zero speed center frequency given by

$$\Delta f_D = \pm \frac{v}{l} \tag{11-1}$$

where v is the vehicle speed in m/s and l is the wavelength in m. The positive sign denotes an increase in frequency that occurs when the vehicle moves towards the illuminated obstacle. The negative sign corresponds to a decrease in frequency occurring when the vehicle moves away from the illuminated object. This, of course, represents a worst case scenario that may occur at locations where there are sharp bends in the road. As an example, a vehicle traveling at 25 m/s ($\approx$55 mph) receiving L-Band (1.5 GHz or l = 0.2 m), will experience Doppler shifts limited to ± 125 Hz.

11.2.2 Faraday Rotation

Faraday rotation effects [Davies, 1990; Flock, 1987] are potential contributors to signal strength variations which can be neglected for LMSS systems which employ circular polarization and L-Band or above frequencies. The ionosphere contains free electrons in the relatively static Earth's magnetic field. This combination causes polarization rotation of linearly polarized waves as given by (for f > 100 MHz)

$$f = 1.35 \cdot 10^6 \frac{B_e \cdot TEC}{f^2} \quad (^\circ), \tag{11-2}$$

where f is the frequency in Hz and B_e is the effective earth's magnetic field in Webers/m^2 assumed constant as a simplifying assumption and defined by

$$B_e = B \cos q_B, \tag{11-3}$$

where B is the true Earth's magnetic flux density at a location in the ionosphere along the Earth-satellite path and q_B is the angle between the direction of propagation and the earth's magnetic flux density vector. TEC is the total electron content (number of electrons/m^2) given by

$$TEC = \int N \, dl \quad (number\ of\ electrons / m^3), \tag{11-4}$$

where l is the path length through the ionosphere and N (number of electrons/m^3) is the electron density along the path. Assuming extreme values of TEC and B_e given by [ITU-R, 1986b (Report 263-6)] and for an angle of transversal of 30°

$$TEC = 1.86 \cdot 10^{18} \qquad (\text{number/m}^2), \tag{11-5}$$

$$B_e = 0.43 \cdot 10^{-4} \qquad \text{(Webers/m}^2\text{)}, \tag{11-6}$$

polarization rotations of 142.7° and 48.0° occur at f = 870 MHz and f = 1.5 GHz, respectively. It is apparent that at UHF frequencies, significant signal loss due to polarization mismatch may occur. As mentioned, this is normally avoided by transmitting and receiving circular polarized signals since the receiving antenna is insensitive to the same polarization shifts of the orthogonal linear components comprising the circular polarized wave. At L-Band and higher frequencies, Faraday rotation may generally be ignored.

11.2.3 Ground Specular Reflection

This type of specular reflection is generated on the ground near the vehicle, where the ray from the reflection point to the antenna is below the horizontal. This coherent reflection comes from an area around the intercept point the size of approximately the first Fresnel zones. Its strength, relative phase shift, and polarization depend on the roughness and dielectric properties of the ground and are elevation angle sensitive. In a system utilizing a low-gain antenna (e.g., a dipole) which can geometrically see the specular point and also has gain in that direction, destructive interference between the specular reflection and the direct wave can produce deep fades [ITU-R, 1986a (Report 1008); Flock, 1987].

The antennas contemplated for use in LMSS are either low-cost, medium gain, fixed pointed or higher-cost, high gain, tracking antennas. A typical medium gain antenna is a crossed drooping dipole, which has azimuthally omni-directional gain of about 4 dB from 15° to 60° elevation. At lower elevation angles, its gain decreases rapidly, thus providing protection against specular reflections from the ground near the vehicle and multipath from elevated objects at larger distances. A high-gain antenna, typically a mechanically or electronically scanned array, achieves even greater rejection of multipath power and a concomitant narrowing of the Doppler spectrum. Placing the antenna on the center of the vehicle roof, which acts as a ground plane, helps to direct the pattern upwards. This further enhances the isolation from ground specular scatter.

For circular polarization, rejection of the reflected multipath energy occurs when the grazing angle is greater than the Brewster angle. At these angles the sense of rotation of the reflected energy is reversed and hence opposite that of the receiving antenna. These grazing angles are in the range of 15° to 35° for very wet to very dry land, respectively [Reed and Russel, 1966].

11.3 Empirical Regression Models

Empirical regression models are represented by fade distributions derived from experimental measurements at different frequencies, elevation angles, vehicle headings, sides of road, types of terrain, and extent of shadowing. They all have the common advantage of being based on actual data and hence they may be used with a certain degree of confidence for the prediction of fade distributions over similar types of roads. Although they are derived from "time-series" of fading events, this information is lost in

the estimation of fade distributions. The physics associated with the empirical models exist to the extent that the models are based on the categorized measureables, such as frequency, elevation angles, heading, and percentage of shadowing due to trees.

The common disadvantage associated with these models is that difficulties may exist in extrapolating these models to cases not considered; such as other "road-types' or frequencies outside the interval of scaling.

11.3.1 Large-scale - Small-scale (LS-SS) Coverage Model

The first propagation experiments targeted towards land mobile satellite communications were conducted by observing 860 MHz and 1550 MHz transmissions emanating from NASA's ATS-6 spacecraft [Hess, 1980]. Using the database from measurements taken over about 1200 km in or near nine cities of the Western and Midwestern United States, an empirical model was derived relating the probabilities of exceeding fades for large-scale (LS) and small-scale (SS) "coverages." Coverage in broadcasting is defined either in terms of percentage of locations within an area or percentage of time at a particular location that there exists satisfactory service. For LMSS scenarios, signal level variations as a function of time are produced by vehicular motion. The model under discussion (denoted by LS-SS) describes statistics from measured data for small and large spatial scales. Small-scale coverage (as defined by Hess) represents a driving interval of 100 m. For a vehicle speed of 25 m/s ($\approx$55 mph), this converts to a time interval of 4 seconds or the time interval of a short conversational sentence. For each 100 m interval, Hess derived a cumulative fade distribution given by

$$P_{Si}(A, A_q) = P_{Si}[A < A_q], \tag{11-7}$$

where the right hand side of (11-7) is read as "the probability that the attenuation A is smaller than a designated attenuation level A_q, for the i^{th} small-scale distribution." The "large-scale" distribution function PL may be derived as follows. We first construct a large family of small-scale distributions of the type depicted by (11-7) on a graph. We next intersect each of these distributions by a fixed percentage (e.g., P_S = 90%) and arrive at a family of fade levels A_q from which a new cumulative fade distribution may be derived. We call this new cumulative distribution the "large-scale" case and represent it by

$$P_L(A) = P_L[A < A_q | P_S]. \tag{11-8}$$

The right hand side may be read as "the probability that the attenuation A exceeds a designated threshold level A_q, given the condition that the small-scale probability P_S assumes a particular value (P_S = 90% for the given example). The physical significance that may be attributed to (11-8) is that it predicts the probability that the fade will be less than a particular fade level over many kilometers of driving, assuming a given P_S which denotes likelihood of successful reception over a 100 m driving distance.

Families of distributions of the type given by (11-7) and (11-8) were derived from data collected for different vehicle environments and path geometries. A normal

distribution was fit to (11-8) from which a "mean excess path loss, m," and "standard deviation, s," was derived. The model equations of Hess for P_S = 90% valid in the range of P_L from 50% to 90% are given by

$$A(P_L) = m + k(P_L)s \ , \tag{11-9}$$

where

$$m = a_0 + a_1 ENV + a_2 HEAD + a_3 FREQ + a_4 SIDE + a_5 ELEV \ , \tag{11-10}$$

$$s = b_0 + b_1 ENV + b_2 HEAD + b_3 FREQ + b_4 SIDE + b_5 ELEV \ . \tag{11-11}$$

In (11-9), k is the number of standard deviations for various values of P_L and are given by

$$k = \begin{cases} 0 & P_L = 50\% \\ 1.28 & P_L = 90\% \\ 1.65 & P_L = 95\% \\ 2.33 & P_L = 99\% \end{cases} . \tag{11-12}$$

The model parameters ENV, HEAD, FREQ, SIDE, and ELEV are defined in Table 11-1. We note that the model contains the following elements: (1) the local environment (ENV) such as urban, semi-urban (commercial) and suburban, (2) the vehicle heading (HEAD) with respect to the satellite azimuth, (3) the frequency (FREQ); UHF or L-Band, (4) the side (SIDE) of the road driven (satellite located across opposing lane or not) and (5) the elevation angle (ELEV) to the satellite. The downtown area of a city, with many tall buildings and a rectangular street grid would be characterized as urban. Streets lined by shopping centers as well as by businesses with off-street parking lots are classified as commercial, and areas with small one- or two-story houses along moderately tree-lined roads define the suburban environment. Data acquired in rural surroundings are included in the suburban category. The coefficients for the mean fade m and slope s, given in (11-10) and (11-11), respectively, are summarized in Table 11-2 along with their standard errors.

The overall standard errors of m and s are

$$S.E.(m) = 3.65 \, dB \ , \tag{11-13}$$

$$S.E.(s) = 2.5 \, dB \ . \tag{11-14}$$

In order to extend the small-scale coverage from the modeled value of P_S = 90% as given by (11-9) to (11-11) and Table 11-2 to other values of P_S, we use the following formulation:

Urban and Commercial

$$A(P_L, P_S) = \begin{cases} (P_S - 90) \cdot 0.6 + A(P_L) & 95\% \geq P_S \geq 90\% \\ (P_S - 90) \cdot 0.2 + A(P_L) & 95\% \leq P_S < 90\% \end{cases} \quad (11\text{-}15)$$

Suburban-Rural

$$A(P_L, P_S) = (P_S - 90) \cdot 0.1 + A(P_L) \quad 95\% \leq P_S \leq 90\% \quad (11\text{-}16)$$

Table 11-1: Parameter Definition and Values for Hess Model.

Parameter	Range of Values
ENVironment	1 = Urban, 0 = Commercial, -1 = Suburban/Rural
HEADing	$-\cos(2(Az_{Vehicle} - Az_{Satellite}))$
FREQuency	1 = UHF, 1.8 = L-Band
SIDE of road	+1 = Satellite across road, -1 = On same side
ELEVation	15° to 50°

Table 11-2: Coefficients in LS-SS Fade Model.

Mean Fade, m			Standard Deviation, s		
Coefficient	Value (dB)	Std. Error (dB)	Coefficient	Value (dB)	Std. Error (dB)
a_0	9.55		b0	3.75	
a_1	4.46	0.42	b1	2.62	0.29
a_2	3.41	0.61	b2	0.98	0.42
a_3	1.66	0.91	b3	0.046	0.62
a_4	-0.35	0.36	b4	-0.24	0.25
a_5	-0.052	0.045	b5	0.04	0.031

11.3.1.1 Example: LS-SS Model

To illustrate the procedures by which we execute the LS-SS model, consider the following example. Assume that a receiver can recover the LMSS coded errors as long as the small-scale coverage is at least P_S = 70%. The system operates at L-Band in a suburban area with an elevation angle to the satellite of 45°. It is desired to determine the required fade margin to achieve a large-scale probability of P_L = 95%.

We assume a worst case heading and condition of roadside, with the satellite at a right angle to and right of the vehicle. Hence, we employ the following parameter values from Table 11-1:

ENV	=	-1	(Suburban/Rural)
HEAD	=	+1	($Az_{Vehicle}$ - $Az_{Satellite}$ = 90°)
FREQ	=	1.8	(L-Band)
SIDE	=	-1	(Satellite Same Side)
ELEV	=	45°.	

(11-17)

Substituting the above into (11-10) and (11-11), we obtain

$$m = 9.5\,dB\,, \tag{11-18}$$

$$s = 4.33\,dB\,. \tag{11-19}$$

Substituting (11-18), (11-19) and k = 1.65 (from (11-12) for P_L = 95%) into (11-9) results in

$$A = 16.5 \text{ dB for } P_S = 90\% \tag{11-20}$$

The fade given by (11-20) corresponds to a large-scale probability of P_L = 95% and small-scale probability of P_S = 90%. To convert the above to the desired small-scale probability P_S = 70 %, substitute (11-20) into (11-16). Hence

$$A = 14.5 \text{ dB for } P_S = 70\%. \tag{11-21}$$

In Figure 11-1 is given a family of curves of the large-scale cumulative distributions P_L for elevation angles of 20°, 30°, and 45° with small-scale probabilities of P_S = 90%, 70%, and 50%. This figure corresponds to an overall driving condition as each curve represents the average of four distributions; right side of road, left side of road and difference in vehicle-satellite azimuth directions of 90° and 0°. We note that P_L is relatively insensitive to elevation angle but is highly sensitive to P_S.

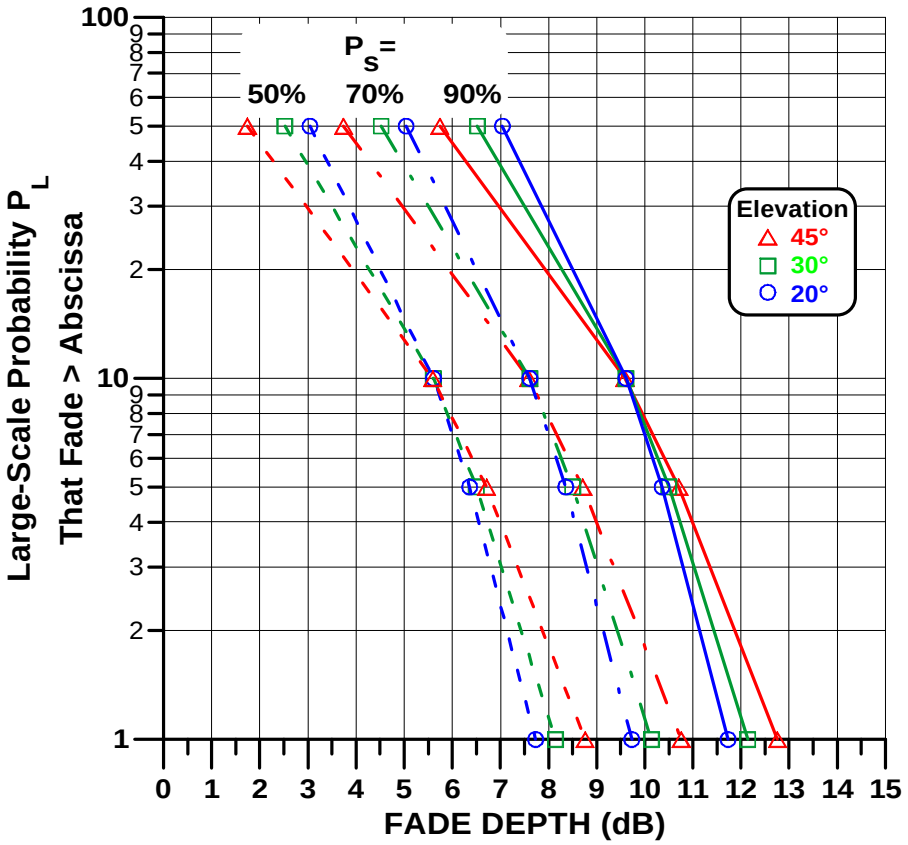

Figure 11-1: Probability distributions for LS-SS model for family of elevation angles and indicated small-scale probabilities P_S.

11.3.1.2 Discussion

The LS-SS model of Hess is derived from an extensive database of measurement results, which is especially weighted for urban to suburban environments. It is simple to use and has realistic parameterization for the most important environmental variables.

The model was derived from data taken with linearly polarized quarter wavelength whip antennas. Such a system will not provide isolation from ground specular reflections, as do low-gain LMSS type antennas previously described. While shadowing loss measurements were not affected by the antenna choice, multipath and specular effects were most likely enhanced. This may have caused overprediction of signal variations especially in open rural areas where shadowing is statistically less significant than multipath. It is also important to note that the experiment emphasized urban over rural areas, making predictions from the database for rural areas less reliable.

11.3.2 Extended Empirical Roadside Shadowing Model

Since the empirical roadside shadowing (ERS) and extended empirical roadside shadowing (EERS) models were addressed in Chapter 3, the model details will not be described here. A short summary discussion is presented in the following paragraphs.

11.3.2.1 Discussion

The EERS model is based on extensive measurements in rural and suburban environments in central Maryland, southwest U.S., the West Coast of the U.S., and Alaska. Helical antennas, parabolic dishes and waveguide apertures were used during reception. The model is based on systematically repeated measurements at 870 MHz, 1.5 GHz, and 20 GHz at elevation angles ranging from 7° to 60°. The fade distributions are simple to calculate. They are a manifestation of an overall average fade condition for both left and right side driving and various degrees of roadside shadowing (55% to 75%). The model has been independently validated to within a few dB employing measurements in Australia.

Because of the limited dynamic range of the measurements, only the median distribution of many 90-second intervals could be determined and modeled. The higher percentile distributions (e.g., 90th or 95th) were beyond the measurement range of the equipment in the 80% to 1% range of fade exceedance. The variability of the distributions could therefore not be modeled. As is the case with the LS-SS model, the EERS model does not provide information about fade dynamics and therefore cannot be used to generate simulated data. This model is also biased in favor of the geometric condition where maximum shadowing occurs; namely, the line-of-sight path is dominantly directed perpendicular to the line of roadside trees. The model is valid in the range of elevation angles from 7° to 60° but may be extended to angles as high as 80° using the methodology described in Chapter 3.

11.4 Probability Distribution Models

Probability functions used to describe LMSS propagation are the Rayleigh and Ricean for multipath effects and the lognormal for shadowing. These statistics are useful to the extent that they accurately describe the shadowing and multipath scenarios.

Models of these types correspond to homogeneous cases for which line-of-sight fading and multipath are simultaneously present, or only multipath is present under the conditions of no shadowing or complete blockage. They do not account for scenarios in which the vehicle may pass from shadowing to non-shadowing conditions (causing bursts of fading and non-fading) typical at higher elevation angles (e.g., 45°) in rural and suburban environments.

Their usefulness is also based on the ability to tailor parameters of the distributions to actual measurements. The parameters of importance are standard deviation, mean, percentage of shadowing, and ratio of line-of-sight to multipath power. These parameters are however tuned to “light” or “heavy” shadowing, “zero to frequent” percentage of shadowing, and “urban”, “suburban”, or “highway scenes.” They represent a “rough” tuning to the model, which is based on measurements at fixed elevation angles. It is, for example, difficult to relate these models to other elevation angles, which are known to critically influence fading. Furthermore, it is difficult to extract from these statistics “time-series” of fading events for simulation purposes without the employment of experimental data.

In the following section is given an overview of the density functions used in modeling procedures. A further characterization is given by the ITU-R [ITU-R, 1986a (Report 1007)].

11.4.1 Density Functions Used In Propagation Modeling

11.4.1.1 Ricean or Nakagami-Rice Density Function

The voltage phasors from all the reflection sources can be combined into two independent orthogonal vectors x and y, the in-phase and quadrature components, having normal envelopes and uniform phase distributions. When received together with a direct signal voltage a, the two-dimensional probability density of the received voltage can be expressed as

$$f_{xy}(x,y) = \frac{1}{2p\sigma^2}\exp\left[-\frac{(x-a)^2+y^2}{2\sigma^2}\right], \tag{11-22}$$

where σ is the standard deviation of the voltage. The signal envelope represents the length of the voltage vector z, given by

$$z = \sqrt{x^2+y^2}\,, \tag{11-23}$$

from which we derive the Ricean density $f_z(z)$ [Papoulis, 1965]

$$f_z(z) = \frac{z}{\sigma^2}\exp\left[-\frac{(z^2+a^2)}{2\sigma^2}\right]I_0\left(\frac{za}{\sigma^2}\right), \tag{11-24}$$

where I_0 is the 0^{th} order modified Bessel function.

The normalized line-of-sight power is given by

$$P'_{los} = a^2 \tag{11-25}$$

and the average (normalized) multipath power is given by

$$P'_{mp} = 2\sigma^2, \tag{11-26}$$

where we denote the powers by a prime to distinguish it from probability. The ratio of these two powers defines the K value that characterizes the influence of multipath scattering on the signal distribution. Hence,

$$K = \frac{P'_{los}}{P'_{mp}} = \frac{a^2}{2\sigma^2}\,. \tag{11-27}$$

Usually, the K factor is quoted in terms of dB. That is,

$$K(dB) = 10\log\left(\frac{P'_{los}}{P'_{mp}}\right) = 10\log\left(\frac{a^2}{2s^2}\right). \tag{11-28}$$

It is apparent from (11-27) that the lower the relative level of the multipath power, the larger the K value, and conversely. Further normalizing P'_{los} such that $P'_{los} = 1$, reduces the Ricean density (11-24) to a single parameter density function of the voltage, which can be written as a function of K by

$$f_z(z) = 2Kz\exp\left(-K(z^2+1)\right)I_0(2Kz), \tag{11-29}$$

where

$$K = \frac{1}{2s^2}. \tag{11-30}$$

11.4.1.2 Rayleigh Density Function

The Rayleigh density is a special case of the Ricean distribution and arises when no line-of-sight power is received. Setting a = 0 in (11-24) results in

$$f_z(z) = \frac{z}{s^2}\exp\left[-\frac{z^2}{2s^2}\right]. \tag{11-31}$$

Even though no direct signal is received, the Rayleigh density can also be defined in terms of a $\overline{K}$ -factor as

$$\overline{K} \equiv \frac{1}{2s^2}. \tag{11-32}$$

Substituting (11-32) into (11-31) gives

$$f_z(z) = 2\overline{K}z\exp\left(-\overline{K}z^2\right). \tag{11-33}$$

Note that the Rayleigh distribution has but a single parameter (namely, s or $\overline{K}$). For Rayleigh scattering, the average scattered power is variable, but the standard deviation on a dB scale is constant and equal to 5.57 dB. As a rule of thumb, based on the Central Limit Theorem, at least six random scattering sources are required to produce a Rayleigh (or Ricean) distribution [Papoulis, 1965].

11.4.1.3 Lognormal Density Function

Shadowing is a manifestation of the absorption and scattering of the incident direct wave by roadside trees or other obstacles as it is transmitted via the line-of-sight between the satellite and the mobile terminal. The cumulative distribution function of the received power expressed in dB can often be fit to a straight line when plotted on a normal probability scale. The voltage variation due to shadowing is then lognormal. The lognormal density function for a random variable z can be derived from the normal density function for x by using

$$x = \ln(z). \tag{11-34}$$

In this case the lognormal density of z has the form

$$f_z(z) = \frac{1}{sz\sqrt{2p}} \exp\left[-\frac{(\ln(z) - m)^2}{2s^2} \right], \tag{11-35}$$

where m and s are the mean and standard deviation of ln(z), respectively. Since the power x is usually expressed in dB, the relation between x (in dB) and z is

$$x = 10\log(z) \qquad \text{z = power (watts)} \tag{11-36}$$

or

$$x = 20\log(z) \qquad \text{z = voltage (volts).} \tag{11-37}$$

The lognormal density function of power when z is the power in watts is

$$f_z(z) = \frac{4.343}{sz\sqrt{2p}} \exp\left[-\frac{(10\log(z) - m)^2}{2s^2} \right] \qquad \text{z = power (watts),} \tag{11-38}$$

where m and s are the mean and standard deviation of $10\log(z)$, respectively. The lognormal density function of power when z is voltage is

$$f_z(z) = \frac{8.686}{sz\sqrt{2p}} \exp\left[-\frac{(20\log(z) - m)^2}{2s^2} \right] \qquad \text{z = voltage (volts),} \tag{11-39}$$

where m and s are the mean and standard deviation of $20\log(z)$, respectively.

11.4.2 Loo's Distribution Model

A statistical model for land mobile satellite propagation based on probability density functions of multipath and shadowing propagation has been developed by Loo [1985; 1987]. The following assumptions are made: (a) the receiver voltage due to the diffusely

scattered power is Rayleigh distributed, and (b) the voltage variations due to attenuation of the line-of-sight signal are lognormally distributed. The two voltages are considered correlated as attenuation by trees is caused by both absorption and scattering. The model employs the parameters $\overline{K}$ as given by (11-32), as well as the mean *m* and standard deviation *s* previously defined for lognormal fading. The mean scattered power in the model is set constant at a level that depends on the severity of the shadowing relevant to a particular environment. While the line-of-sight attenuation is constant, a conditional Ricean distribution of the signal envelope holds. The overall probability density is found by integration of the conditional density multiplied by the lognormal probability of the line-of-sight envelope. The resulting probability density function of the signal envelope is

$$f_v(v) = \frac{\sqrt{2}\overline{K}v}{s\sqrt{p}} \int_0^\infty \frac{1}{z} \exp\left[-\frac{(\ln(z)-m)^2}{2s^2} - \overline{K}\left(v^2+z^2\right)\right] I_0\left(2\overline{K}vz\right) dz \,. \tag{11-40}$$

For signal voltages much greater and much less than the standard deviation of the Rayleigh process, the density function is lognormal or Rayleigh, respectively, and can be simplified to

$$f_v(v) = \frac{1}{sv\sqrt{2p}} \exp\left[-\frac{(\ln(v)-m)^2}{2s^2} \right] \qquad v >> \frac{1}{\sqrt{\overline{K}}} \tag{11-41}$$

and

$$f_v(v) = 2\overline{K}v \exp\left(-\overline{K}v^2\right) \qquad v << \frac{1}{\sqrt{\overline{K}}} \,. \tag{11-42}$$

At intermediate values of v, $f_v(v)$ is found by numerical integration, where the use of the polynomial approximations for I_0 given in Abramowitz and Stegun [1964] as Eqs. 9.8.1 and 9.8.2 is helpful because they reduce integrand overflow problems. With $t = x/3.75$, for

$-3.75 \le x \le 3.75$ use

$$\begin{aligned} I_0(x) = {} & 1 + 3.5156229t^2 + 3.0899424t^4 + 1.2067492t^6 \\ & + 0.2659732t^8 + 0.0360768t^{10} + 0.0045813t^{12} + e \,, \\ & |e| < 1.6 \cdot 10^{-7} \end{aligned} \tag{11-43}$$

and for

$3.75 \le x \le \infty$ use

$$\begin{aligned}\sqrt{x}\exp(-x)I_0(x) = {} & 0.39894 + 0.01328592t^{-1} + 0.00225319t^{-2} \\ & -0.00157565t^{-3} + 0.00916281t^{-4} \\ & -0.02057706t^{-5} + 0.02635537t^{-6} \\ & -0.01747633t^{-7} + 0.00392377t^{-8} + e \\ & |e| < 1.9\cdot 10^{-7}\end{aligned}, \qquad (11\text{-}44)$$

to evaluate $\exp(-x)I_0(x)$. Inserting the latter into (11-40) results in the numerically somewhat more friendly expression

$$f_v(v) = \frac{\sqrt{2}\overline{K}v}{s\sqrt{p}}\int_0^\infty \frac{1}{z}\exp\left[-\frac{(\ln(z)-m)^2}{2s^2} - \overline{K}(v-z)^2\right]\exp(-2\overline{K}vz)I_0\left(2\overline{K}vz\right)dz, \qquad (11\text{-}45)$$

although carrying out the integration still requires care.

Table 11-3: Parameters for Loo's Model

Shadowing Class	Rayleigh Scatter	Lognormal Shadowing	
	$\overline{K}$ (dB)	*m*	*s*
Infrequent light	6.3	0.115	0.115
Frequent heavy	18.8	-3.91	0.805
Overall	4.0	-0.69	0.23

The probability that the received voltage is less than or equal to *v* is

$$F_v(v) = \int_0^v f_v(u)\,du \qquad (11\text{-}46)$$

from which the cumulative distribution function A in dB is found using

$$A = 20\log(v) \qquad (11\text{-}47)$$

Values of the model parameters were derived by Loo from propagation data measured over a helicopter to vehicle link with 15° elevation angle in a rural environment with two classes of shadowing: infrequent light and frequent heavy. The parameters are summarized in Table 11-3 for environments with infrequent light shadowing, such as a road with occasional sparse trees and frequent heavy shadowing, i.e., a road with many large trees with overhanging crowns.

11.4.2.1 Level Crossing Rate and Average Fade Duration

In addition to describing the fade cumulative distribution function, Loo's model also provides insight into the dynamics of fading by deriving statistical relations for the level crossing rate (*LCR*) and the average fade duration (*AFD*). The level crossing rate is the expected rate at which the signal envelope crosses a specified signal level with a positive slope. The average fade duration is the expected time or distance the signal envelope is continuously below the specified signal level. The inverse of the level crossing rate is the sum of the average fade and non-fade durations. The derivation, based on earlier work by Rice and Jakes, hinges on the statistical independence between the signal envelope and its time derivative, which is assumed to be a Gaussian process both for Ricean and lognormal fading. The *LCR* is normalized by the maximum possible Doppler shift

$$f_{\max} = \frac{v}{l}, \tag{11-48}$$

where v is the vehicle speed and l is the wavelength. The normalized level crossing rate LCR_n, is based on the wavelength, independent of speed, and can be written as

$$LCR_n = \frac{LCR}{f_{\max}} = \sqrt{2p}\sqrt{1-r^2}s\ ^2\ \frac{\sqrt{s\ ^2 + 2r s\ s + s^2}}{s\ ^2\left(1-r^2\right)+4r s\ s} f_v(v), \tag{11-49}$$

where r, now a fourth parameter of Loo's model, is the correlation coefficient for the rate of change of the envelope due to multipath and shadowing effects. Typically, the correlation coefficient r was in the range from 0.5 to 0.9 for the data set used by Loo.

The *AFD* can be found from LCR_n, by

$$AFD = \frac{1}{LCR_n}\int_0^L f_v(v)\,dv \tag{11-50}$$

With supporting helicopter data at 870 MHz and satellite data at 1542 MHz and for elevation angles from 5° to 30°, it was shown that the signal phase and the rate of change of the phase can be treated as Gaussian processes [Loo, 1987]. Values of the mean and standard deviation of the phase were 7.5° and 12.6° at 870 MHz, and 7.5° and 26° at 1542 MHz, respectively.

11.4.2.2 Discussion

The Loo model provides a description of primary and secondary fade statistics for LMSS scenarios based on four parameters derived from measurements performed in Canada. As all of the measurements were made at elevation angles below 30°, model parameters for higher elevation angles are not available.

11.4.3 Total Shadowing Model

Another statistical model characterizing the fade distribution applicable to LMSS propagation has been devised by Lutz et al. [1986]. As in Loo's model, Ricean, Rayleigh, and lognormal probability densities are combined and model parameters are derived from least-square error fits to measured data. However, there are significant differences in the way the three distributions are assigned to the two major propagation phenomena, scattering and shadowing. As described in the previous section, Loo combines a constant intensity Rayleigh distributed scattering voltage with a lognormally shadowed line-of-sight signal voltage. Lutz et al., on the other hand, consider two distinct propagation link states; shadowing, and no shadowing. In the unshadowed state, the envelope statistics are assumed to be Ricean with constant *K*-factor due to the superposition of the direct wave with constant intensity multipath echoes. When the propagation link is shadowed by roadside trees, the line-of-sight is assumed to be totally obscured and most of its power converted into scattered waves, leaving only multipath signals with Rayleigh statistics, but their average strength is modeled as lognormally distributed. Loo modulates the Ricean *K*-factor by shadowing the line-of-sight component. Lutz, in the shadowed state, varies the intensity of the Rayleigh scattering process, or the $\overline{K}$ -factor, in the absence of any line-of-sight signal. In Lutz's model, the probability density of the received voltage for the unshadowed fraction (1-S) of the driving distance is Ricean. When expressed in terms of the received power P', it has the form

$$f_{P',Rice}(P') = K \exp\left[-K\left(P'+1\right)\right] I_0\left(2K\sqrt{P'}\right), \tag{11-51}$$

where unity line-of-sight power is assumed and K is the ratio of line-of-sight to average multipath power. That is

$$K = \frac{1}{P'_{mp}}. \tag{11-52}$$

For the shadowed fraction *S* of the total distance, the power is Rayleigh distributed and has the following form when expressed in terms of the received power, *P'*

$$f_{P',Rayleigh}(P') = \overline{K} \exp\left(-\overline{K}P'\right), \tag{11-53}$$

where $\overline{K}$ is the reciprocal of the average multipath power as given by (11-32). Lutz et al. postulate this multipath power Rayleigh intensity $1/\overline{K}$ to be lognormally distributed. The density can be expressed in terms of the $\overline{K}$ -factor, the mean *m*, and the standard deviation *s* of $10\log\left(\overline{K}\right)$ as

$$f_{\overline{K}}(\overline{K}) = \frac{4.343}{\overline{K}s\sqrt{2p}} \exp\left[-\frac{\left(10\log\left(\overline{K}\right)-m\right)^2}{2s^2}\right], \tag{11-54}$$

where

$$m = E\left[10\log\left(\overline{K}\right)\right] \tag{11-55}$$

and

$$s = \left\{E\left[\left(10\log\left(\overline{K}\right)\right)^2\right] - m^2\right\}^{\frac{1}{2}}, \tag{11-56}$$

where E denotes the "expected value."

The overall probability density of the received power follows by combining (11-51) and (11-53) with (11-54)

$$f_{P'}(P') = (1-S)\, f_{P',Rice}(P') + S\int_0^\infty f_{P',Rayleigh}\left(P'\middle|\overline{K}\right) f_{\overline{K}}\left(\overline{K}\right) d\overline{K} \tag{11-57}$$

The cumulative distribution of the fractional distance the fade exceeds *A* dB is found by evaluating (11-57). Model parameters were determined by Lutz et al. from regressions to satellite measurements performed in various environments with a 24° elevation angle. They are summarized in Table 11-4 for a vehicle antenna with a hemispherical pattern. Good fits of the model to the measured cumulative distribution functions of the attenuation were obtained.

11.4.3.1 Discussion

The Lutz et al. experiments were carried out using three different receiving antennas. The shadowing parameter *S* derived from the corresponding data sets was found to be dependent on the antenna, which indicates a coupling of S to multipath propagation. Had the model been a true representation of LMSS propagation, *S* would be independent of the antenna pattern.

Table 11-4: Typical Parameters for Total Shadowing Model of Lutz et al. [1986]

Environment	S	K (dB)	m (dB)	s (dB)
Urban	0.60	3	-10.7	3.0
Suburban	0.59	9.9	-9.3	2.8
Highway	0.25	11.9	-7.7	6.0

11.4.4 Lognormal Shadowing Model

Smith and Stutzman [1986] also incorporated the idea into a model that different statistics should be used to describe LMSS signal variations depending on whether the propagation path is shadowed or unshadowed. They developed a model, which assigns Rayleigh, Ricean and lognormal behavior of the received signal voltage in a manner similar to Loo's model. In the unshadowed state, the received signal consists of the sum of the direct signal and a constant average intensity Rayleigh voltage due to the diffusely

scattered multipath echoes. The resulting signal amplitude has a Ricean probability density characterized by a constant ratio of direct to scattered power. In the shadowed state, the amplitude of the line-of-sight signal is assumed to have lognormal statistics. When combined with constant level diffuse multipath, the probability density (11-40) derived by Loo applies.

The overall probability density of the received voltage is developed analogously to the derivation of (11-57) as

$$f_v(v) = (1-S)\,2Kv\exp\left[-K\left(v^2+1\right)\right]I_0(2Kv) + S\,\frac{8.686\sqrt{2\overline{K}}v}{s\sqrt{p}} \times \int_0^\infty \frac{1}{z}\exp\left[-\frac{\left(20\log(z)-m\right)^2}{2s^2} - \overline{K}\left(v^2+z^2\right)\right] I_0\left(2\sqrt{\overline{K}}vz\right)dz \tag{11-58}$$

where S, K, $\overline{K}$, m, and s are the five model parameters already described in the previous section.

Table 11-5: Parameter Values for the Lognormal Shadowing Model

Parameter	Range of Values	Remarks
K	22 to 13 dB	Low to high multipath, unshadowed
$\overline{K}$	21 to 18 dB	Low to high multipath, shadowed
m	-1 to -10 dB	Light to heavy shadowing
s	0.5 to 3.5 dB	Light to heavy shadowing
S	0.0 to 1.0	No shadowing to frequent shadowing

The parameters given in Table 11-5 were determined by a least square error fit of the statistical model to propagation data collected using a helicopter as the source platform.

11.4.4.1 Discussion

As was the case for the other statistical models, the lognormal shadowing model has been fit to measured cumulative fade distributions quite well. One would expect an increased multipath power level to go hand-in-hand with shadowing conditions. The small range and low level found for $\overline{K}$ seem to indicate that the model does not adequately uncouple shadowing and scattering. The range of applicability of the model vis-à-vis elevation angle has also not been specified.

Because of the complexities in evaluating (11-58), a much simpler empirical model (in the next section) was derived from the statistical results by curve fitting procedures.

11.4.5 Simplified Lognormal Shadowing Model

This model [Barts and Stutzman, 1991; Barts et al., 1987] has the inputs S, K, $\overline{K}$, m, and s, which have been defined in the previous two sections and assume the values

summarized in Table 11-5. The resultant probability distribution model is expressed in terms of the contributions for the "no shadowing" and "shadowing" cases in the following way

$$P(A > A_q) = P_{ns}(1 - S) + P_s S\,, \tag{11-59}$$

where P_{ns} is the probability distribution for the case of no shadowing of the line of sight and is given by

$$P_{ns}(A > A_q) = \exp\left[-\frac{(A + U_1)}{U_2}\right], \tag{11-60}$$

where the parameters U_1 and U_2 are functions of K and are given by

$$U_1 = 0.01K^2 - 0.378K + 3.98 \tag{11-61}$$

and

$$U_2 = 331.35K^{-2.29}\,. \tag{11-62}$$

In (11-59), P_s is the probability distribution for the case of shadowing of the line of sight and is

$$P_s(A > A_q) = \left(\frac{50 - A_q}{V_1}\right)^{V_2}, \tag{11-63}$$

where the parameters V_1 and V_2 are given by the following functions of $\overline{K}$ as well as the mean m and standard deviation s of the lognormal signal

$$V_1 = -0.275\,\overline{K} + 0.723\,m + 0.336\,s + 56.979 \tag{11-64}$$

$$V_2 = \left(-0.006\,\overline{K} - 0.008\,m + 0.013\,s + 0.121\right)^{-1} \tag{11-65}$$

Typical fade predictions calculated from (11-59) have been plotted in Figure 11-2 for light and heavy as well as in Figure 11-3 for medium heavy shadowing, for infrequent (S=0.25), moderate (S=0.5) and frequent (S=0.75) shadowing occurrences. In the worst case scenario corresponding to heavy and frequent shadowing, the calculated fade probabilities may exceed 1.0, but should be limited to that value.

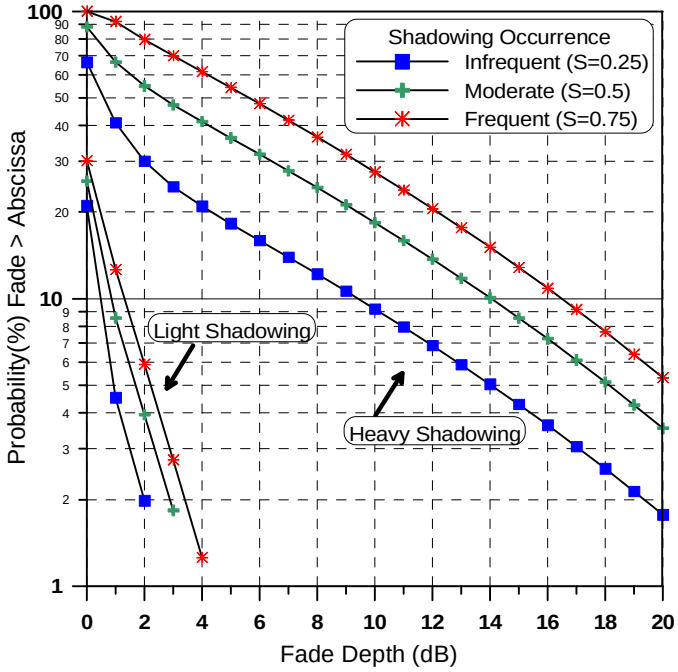

Figure 11-2: Typical fade distributions calculated from the Simplified Lognormal Shadowing Model for light $(K = 22dB, \overline{K} = 18dB, m = -1dB, s = 0.5dB)$ and heavy $(K = 13dB, \overline{K} = 12dB, m = -10dB, s = 3.5dB)$ shadowing, and for infrequent (I; S = 0.25), moderate (M; S = 0.5), and frequent (F; S = 0.75) shadowing occurrences.

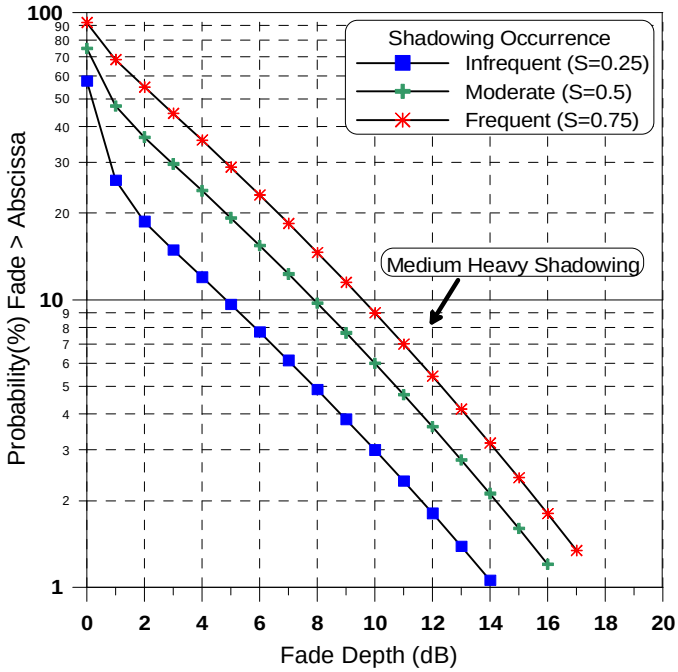

Figure 11-3: Typical fade distributions calculated from the Simplified Lognormal Shadowing Model for medium $(K = 17.5dB, \overline{K} = 15dB, m = -5.5dB, s = 2dB)$ shadowing, and for infrequent (I; S = 0.25), moderate (M; S = 0.5), and frequent (F; S = 0.75) shadowing occurrences.

11.4.5.1 Discussion

The model has been shown to fit measured fade distributions, when the propagation parameters were determined by tailoring the data to the model. Calculation procedures are straightforward.

11.4.6 Models With Fade State Transitions

11.4.6.1 Two- and Four-State Markov Modeling

Cygan et al. [1988] used a 2-state Markov model (Gilbert-Elliot model) for non-shadowed (good) and shadowed (bad) channel conditions and a 4-state Markov model, also with good and bad states and qualified by either short or long duration, to predict error rates in the land mobile satellite channel. Channel states are related to the presence or absence of shadowing conditions and both models describe the transition probabilities between states. Model parameters are determined from data collected in L-Band satellite propagation experiments carried out in a variety of environments at elevation angles between 21° and 24°. The data set on which the parameters are based is the same as the one used for the derivation of the total shadowing model.

The 2-state model has a total of four parameters, of which two are signal level dependent error rates and two are state transition probabilities. A summary of its parameters for three propagation scenarios is given in Table 11-6. The derived bad lengths appended to the table may be reasonable in the urban environment where much of the shadowing is due to blockage by buildings. For tree shadowing prevalent in the suburban environment, the 2-state model is lacking in predicting the effects of many short fades observed in real channel measurements.

Table 11-6: Parameters for 2-State Model

Parameter	Remark	Urban	Suburban	Highway
P_{GB}	Transition probability from “good” to “bad” state	3.95×10^{-4}	2.1×10^{-4}	2.96×10^{-5}
P_{BG}	Transition probability from “bad” to “good” state	1.05×10^{-4}	1.54×10^{-4}	1.29×10^{-4}
e_G	Error rate in “good” state	2.1×10^{-4}	3.4×10^{-4}	1.1×10^{-4}
e_B	Error rate in “bad” state	0.317	0.298	0.194
L_G	Derived “good” length (m)	24	45	704
L_B	Derived “bad” length (m)	88	60	161

At the price of being more calculation intensive, the 4-state model is capable of providing a more realistic statistical simulation of error bursts. It has a total of thirteen parameters, of which eight are state transition probabilities, two express the transitional durations between short and long, good or bad states, and three are measures for the error probabilities in all good as well as short and long bad states. Typical values of the transitional durations for good/bad states are 0.46/1.85 m for urban, 0.92/0.65 m for suburban, and 5.2/2.5 m for highway driving, respectively. Error probabilities range

from $1 \cdot 10^{-4}$ to $3.5 \cdot 10^{-4}$ for the good states to 0.16 … 0.37 for the bad states, with the short bad state's error rate about 30% below the long bad state. While the discussion of error probabilities is beyond the scope of this text, these models give an indication of the level of complexity that may be required for successfully modeling the LMSS channel.

11.4.6.2 Markov Transitions, Multipath And Fade Depth Model

By combining three distinct concepts into one LMSS propagation model, Wakana [1991] has modeled fading and its spatial characteristics. Fading due to multipath is rendered by Ricean statistics (11-29), while fading of the line-of-sight signal due to tree shadowing is described in terms of a Markov model for the transitions between fade states and an attenuation algorithm for the fade depth. Like the 4-state model described above, this Markov model considers transition probabilities between four fade states: fade or non-fade, short or long, but with a total of only six as opposed to eight independent parameters. Of two attenuation models introduced, one linking the attenuation to the fade state, the other to the fade duration, the former alternative was used. Besides the six state transition probabilities, four other parameters are required. They are the Ricean K-factor for the multipath scattering, attenuation levels for short and long fades, and a lowpass filter time constant to smooth the transitions between fade and non-fade states. The ten model parameters were determined for a specific suburban propagation path geometry with an optimization procedure performed on data collected in a helicopter experiment. Simulated data produced using these parameters are qualitatively similar to real data when time series are compared and have, of course, similar cumulative distributions of fades, fade durations, and non-fade durations. Typical parameter values are in the range of 0.13 to 0.97 for the transition probabilities, 10.7 dB attenuation for both fade states, a 13 dB K-factor, and a 22 Hz lowpass filter cut-off frequency, corresponding to a spatial filter of about 1 m.

Variations of the signal level at near line-of-sight power, which may be due to diffraction at the fade state transition zone and specular reflection from the ground near the vehicle have not been considered in the model development and therefore are not replicated by the simulator. Until parameters are determined for a variety of environments and elevation angles, the modeling results cannot readily be applied to other propagation geometries.

11.5 Geometric Analytic Models

Geometric analytic models are useful for gaining physical insight of the mechanism of fading and characteristics of signal retrieval. They may also be used to achieve time-series fades that may be interfaced with simulation techniques. Unfortunately, the complexities of “real life” scenarios do not lend themselves to analytic models and only simplified and idealized scenarios are considered.

11.5.1 Single Object Models

11.5.1.1 Point Scatterer Multipath

Frequently, signal variations observed in satellite land-mobile propagation experiments can be correlated with the receiving vehicle passing in the vicinity of a generator of multipath scattering, such as a utility pole or roadside sign. To increase understanding of these multipath reflections observed from a moving platform, a physical model based on the geometry of a single point scatterer has been developed [Vogel and Hong, 1988]. While the model does not address the major limitation of LMSS, shadowing, it provides a tool to study the dependence of signal variations observed under clear line-of-sight conditions on parameters such as antenna pattern, path azimuth and elevation angles, distance of multipath sources, and bandwidth.

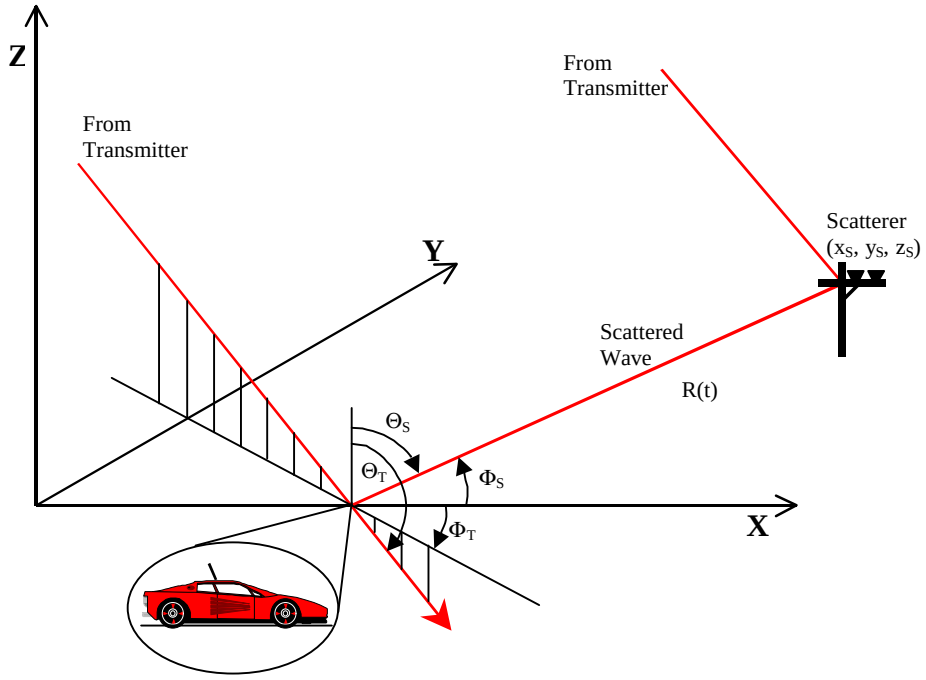

Figure 11-4: Propagation geometry for single object scattering in which a vehicle traveling at a speed *v* carries an antenna with a given pattern along the x-axis.

A sketch of the propagation scenario considered is shown in Figure 11-4, in which a vehicle carries an antenna with a given pattern along the x-axis with speed *v*. A plane wave transmitted from a satellite propagates into the direction (Q_T, F_T). In addition to the line-of-sight wave, the vehicle also receives one multipath component scattered by an object at (x_S, y_S, z_S). The vector sum of the two waves constitutes the received signal. In order to achieve simplicity in the numerical evaluation of the model, the following assumptions were made: (1) there is only one scatterer, (2) it scatters isotropically, and (3) the receiving antenna's gain is azimuthally omni-directional. The formula developed by Vogel and Hong [1988] for the received electric field strength E_r is

$$E_r(t) = E_0\, D(\Theta_T)\exp(jw_0 t - b) \times \left\{ T + \frac{\sqrt{s}\, D(\Theta_S)}{2\sqrt{p}\, R(t) D(\Theta_T)} \exp\left[j \frac{2p}{l} (a(t) - p - R(t)) \right] \right\}, \quad (11\text{-}66)$$

where b is the phase shift given by

$$b = \frac{2p}{l} vt \sin(\Theta_T)\cos(\Phi_T). \quad (11\text{-}67)$$

Alos, a(t) is the path length from the wave through the origin to the antenna given by

$$a(t) = t \sin(\Theta_T)\cos(\Phi_T), \quad (11\text{-}68)$$

p is the path length from the wave plane through the origin to the scatterer given by

$$p = x_S \sin(\Theta_T)\cos(\Phi_T) + y_S \sin(\Theta_T)\sin(\Phi_T), \quad (11\text{-}69)$$

and where

E_0 line-of-sight field strength, V/m

$D(\Theta_T)$ antenna voltage directivity versus elevation Θ_T,

w_0 transmitter frequency, Hz

T transmission of direct wave:
1 = no shadowing, 0 = complete blockage,

s bistatic cross section of scatterer, m^2

$R(t)$ path length between antenna and scatterer, m

l wavelength, m.

This model has been shown to produce time series of received data that closely match those observed, if appropriate parameters are used. One such example is shown in Figure 11-5 and Figure 11-6, which respectively show experimentally received and calculated signal level and phase for an L-Band receiver using a crossed drooping dipole antenna and moving at 24 m/s. The transmitter azimuth and elevation angles are 150° and 35°, respectively. The scattering object is a wooden utility pole about 3 m to the right of and 4 m above the vehicle with a 32 m^2 radar cross section. The model predicts higher fluctuations before and after passing the pole, an indication that the scattering in reality is not isotropic.

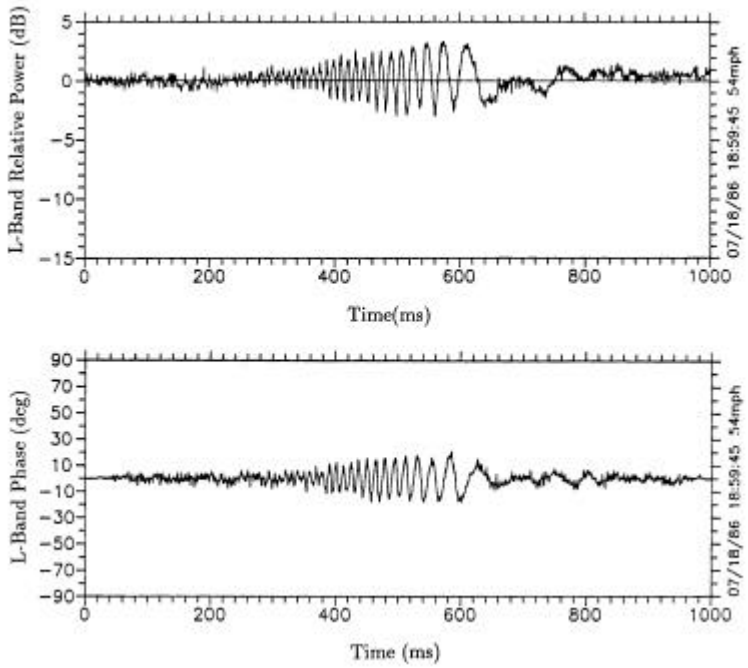

Figure 11-5: Measured L-Band signal level and phase fluctuations as a function of time relative to arbitrary reference as receiving vehicle passes by a wooden utility pole with a metal crossbar. The vehicle's closest approach to the pole occurs at about 0.6 s.

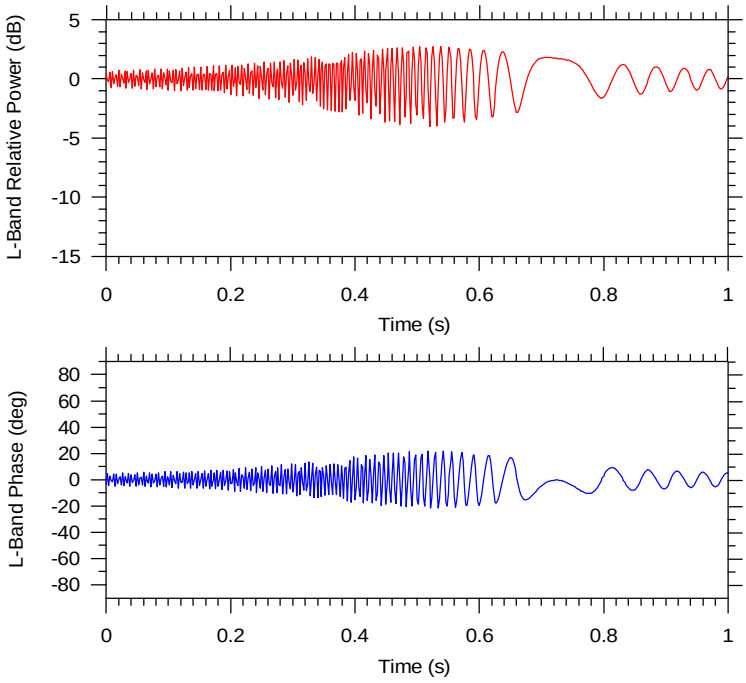

Figure 11-6: Calculated L-Band signal level and phase fluctuations as a function of time for the geometry of Figure 11-5.

Evaluating the model over a range of parameters, the following has been empirically determined:

- The peak-to-peak fluctuations of the received signal level (dB) due to multipath vary with the inverse of the square root of the satellite elevation angle.
- The multipath power (dB) varies as the inverse distance to the scatterer taken to the 4/3 power.
- Assuming two frequencies (at L-Band) are simultaneously received, the RMS deviation of the dB power difference between signal levels at the respective frequencies is proportional to the frequency difference. Employing this result, amplitude dispersion is found to be negligible for narrow band (bandwidth < 10 kHz) LMSS systems.

11.5.1.2 Fresnel Approaches to Tree Shadowing

Several simplifying methods have been used to assess the effect of shadowing by a single tree. Modeling a tree trunk as a very long opaque strip of equal width, a diffraction pattern was obtained by LaGrone and Chapman [1961] and compared to measurements at UHF frequencies. Taking account of the tree crown, two different two-dimensional tree models have been studied, both capable of achieving rough quantitative agreement with observations of tree shadowing. One assumed a tree to be composed of a number of finite, canted opaque strips of varying width and length, representing the silhouette of a tree with branches of various sizes [Vogel and Hong, 1988]. Attenuations of up to about 12 dB were calculated at L-Band versus 8 dB at UHF. Spatial fluctuations in the shadow of the tree were found to be faster with higher signal frequency and closer proximity to the tree during a simulated drive-by scenario. The maximum fade was proportional to the logarithm of the number of limbs. In the second approach [Yoshikawa and Kagohara, 1989], the tree crown was modeled as a triangle which obscures a wedge of the first Fresnel zone. By comparisons with measurements, the results have been shown to correctly explain the average decrease of attenuation with increasing distance of the receiver from the tree.

11.5.2 Multiple Object Scattering Models

11.5.2.1 Two-Dimensional Model

A two-dimensional geometric LMSS propagation model by Amoroso and Jones [1988] considered 1000 scatterers randomly distributed in an annular region with an outer radius of 2000 m and an inner radius of 400 m, corresponding to an average area per scatterer of 12,000 m^2. The model has been used to correctly predict multipath Doppler spectra, both for omnidirectional and directive antennas. The simulated fading record of unmodulated carrier power for an omni-directional antenna shows unrealistic peak-to-peak variations of over 20 dB, however. This is the consequence of (1) using a two-dimensional approach, which eliminates realistic elevation angle and antenna effects, and (2) the avoidance of any scatterers in proximity to the vehicle, which in field measurements have been shown to dominate the signal variations in the absence of shadowing. The model therefore also overestimates delay spread.

11.5.2.2 Three-Dimensional Model

An extension to the single scatterer multipath model of Vogel and Hong [1988] allows a vehicle to be driven through a region with many randomly distributed, point-source multipath scatterers [Vishakantaiah and Vogel, 1989]. The output of the drive simulator yields time series of signal amplitude and phase as well as Doppler spectra, all for user-specified conditions. These outputs, in turn, can be used to calculate system performance parameters. The simulator does not consider shadowing, and this limits its application to very low fade margin systems, where multipath-fading effects determine system performance most of the time.

In order to obtain the total field at the receiver due to many scatterers, the vector sum of the constant incident field and all the scattered fields *e* is formed similarly to (11-66) and the relative total power and phase are calculated from

$$Power_{total} = \sqrt{\left(1 + \sum e_{real}\right)^2 + \left(\sum e_{imag}\right)^2} \tag{11-70}$$

and

$$Phase_{total} = \arctan\left(\frac{\sum e_{imag}}{1 + \sum e_{real}}\right), \tag{11-71}$$

where the summation includes the real or imaginary parts of each scatterer's response *e* to the incident wave.

The model was validated by comparing the predicted power and phase assuming a single scatterer to the results from measurements, both with similar parameters as well as by comparing the calculated power spectral density to the one expected [Clarke, 1968]. Figure 11-7 demonstrates that the model produces the correct Doppler spectrum, centered on the received carrier frequency. The shape shows the typical signature of mobile multipath propagation, a sharply band-limited spectrum with maximum power at the edges. The frequency deviation of the scattered wave (±120 Hz) agrees with the value expected from the geometry. The signal level output of the model shows a peak-to-peak variation of less than 1.5 dB assuming 1000 scatterers located in an annular region with radii of 400 and 2000 m, a drooping dipole antenna, and the height of the scatterers randomly distributed between 0 and 10 m. This peak-to-peak variation is in agreement with measurements made in locations where no scatterers are in the immediate vicinity of the vehicle.

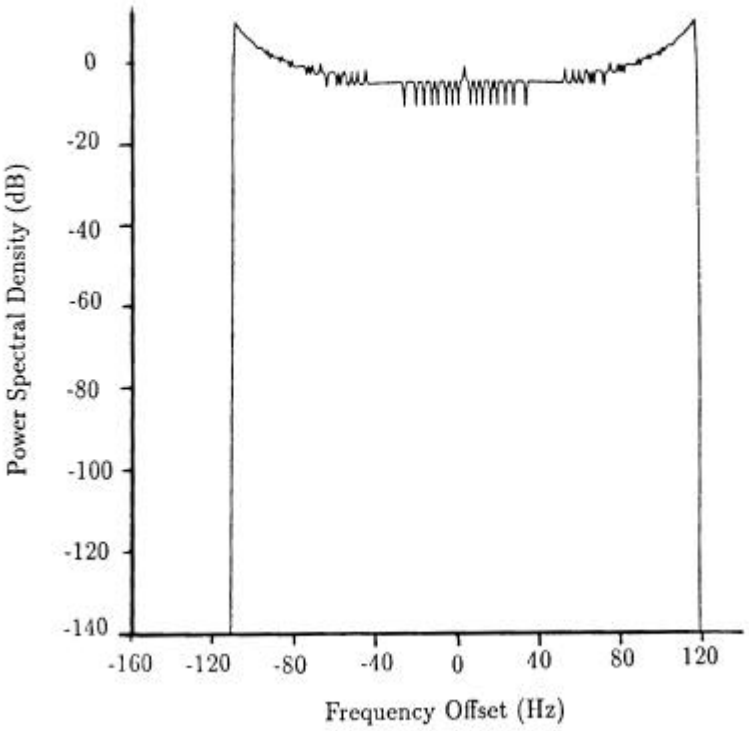

Figure 11-7: Calculated Doppler spectrum due to single multipath reflector averaged over one second, while the vehicle is driving past the scatterer.

Similar cases to the one above, except for an outer radius of 500 m and the much higher average area per scatterer of 625 m^2, were examined with inner clearance radii from 30 to 400 m. The result demonstrates that multipath phenomena for LMSS scenarios are significant only if the scatterers are located close to the vehicle. The standard deviation of the logarithmic amplitude decreases monotonically with increasing inner clearance from 0.22 dB to 0.07 dB.

As an outgrowth of geometric modeling, it has been ascertained that when higher gain antennas are employed, the side of the road on which the scatterer is located influences the multipath fading [Vishakantaiah and Vogel, 1989]. For example, assuming an antenna with 80° half-power beamwidth in both the azimuth and elevation planes, the multipath fading was 10 dB when a simulated scatterer (e.g., a utility pole) was placed between the vehicle and the satellite. Only 1 dB multipath fading occurred when the vehicle was between the scatterer and the satellite. Filtering of the signal by the antenna pattern diminished fading for the latter case. On the other hand, when an azimuthally omni-directional antenna was used, no change in the multipath fading (e.g., 10 dB) was observed for the two cases. In an environment with many scatterers at random heights and cross sections, the reduction of the fade fluctuations arising from lower versus higher gain antennas is not as extreme, but still significant. For the case of 500 scatterers (having random heights and cross-sections) located at distances between

10 m to 300 m, the peak-to-peak fade fluctuations were reduced from 3.6 dB (for the lower gain antenna) to 0.8 dB (for the higher gain antenna).

11.5.2.3 Discussion

Two-dimensional simulation models overestimate multipath, because the elevation angle selectivity of the receiving antenna is neglected. Therefore they cannot be used to predict amplitude, phase, or bandwidth effects realistically. The three-dimensional simulator demonstrates that only scatterers in the immediate vicinity of the receiver matter. As a consequence, the delay spread spectrum is narrow and has no detrimental impact on contemplated systems with channel bandwidths of 10 kHz.

Time-series produced with this model will give more realistic inputs to systems that analyze bit error performance than those based on statistical assumptions only as long as the no-shadowing condition holds.

11.6 Summary and Recommendations

The salient conclusions associated with model execution and development may be summarized as follows:

1. When the propagation path is unshadowed, Ricean statistics apply most of the time, although the K-factor cannot strictly be assumed constant.
2. Signal variations in the clear path case are due to scattering from objects such as trees and utility poles in the vicinity of the vehicle, as weighted by the vehicle antenna pattern. Where these objects recede from or come closer to the vehicle, the K-factor decreases or increases, respectively.
3. When a single scatterer dominates, as might be the case with a utility pole, Ricean statistics are no longer applicable and a geometrical analytical model must be used. This case is treated in Section 11.5.1.
4. Statistics of clear path K-factor variations have not been considered in any of the models.
5. Signal fluctuations for LMSS scenarios that are solely due to multipath scattering at path elevation angles above about 15° are less than 2 or 3 dB for 99% of the distance, consequently there may not be a need to have a more accurate description of "unshadowed propagation" than that given by applying Ricean multipath scattering models as given by (11-29) or by using geometric-analytic models of the type described in Section 11.5.
6. When the line-of-sight is completely blocked by continuous obstacles such as mountains, buildings, or overpasses, not enough power is contributed by multipath scattering to enable any communication through a satellite system with a commercially feasible fade margin of around less than 20 dB. In this case LMSS cannot be functional at all and what is required is some knowledge of the probability

of blockage and its duration for specific path geometry. No separate statistical evaluations for the incidence of blockage are currently available.

7. In view of items 5 and 6, the major propagation model of interest should describe the condition of shadowing of roadside trees where complete blockage does not occur.
8. Simulation of time series of fade data for various conditions of tree shadowing is a requirement for analytically addressing fade mitigation techniques such as antenna diversity and error correction schemes.

Based on the results to date as examined in this text, the following represents a list of recommendations to fill the present modeling gaps for LMSS scenarios.

1. A comparative assessment of the various statistical models described in this Chapter is recommended.
2. In the absence of 1, the authors recommend the following:

   (a) Designers interested in cumulative fade distributions should employ empirical models such as the EERS (Chapter 3) or the Simplified Lognormal Model (Section 11.4.5), which are derived directly from measured data.

   (b) Designers interested in fade durations and fade rates should employ Loo's model (Section 11.4.2) or one of its variants (e.g., see Chapter 10) which appears to be the most mature.
3. Empirical models describing cumulative fade distributions should be developed from databases associated with the following locations:

   (a) Regions in which elevation angles range between 0° to 8°. At angles near grazing, (e.g., northern latitudes), scintillations and refractive effects due to the troposphere may influence the fade statistics.

   (b) Regions where ionospheric scintillations are prevalent such as in the tropics (e.g., geostationary satellite communications) or auroral regions for cases in which communications exist with polar orbiting satellites.

Note: Systematic measurements and modeling of wide-band delay spread characteristics, a recommendation of the first edition of this document, have been executed by several groups of investigators. The results will be included in the next revision.

11.7 References

Abramowitz, M. and I. A. Stegun [1964], *Handbook of Mathematical Functions*, NBS Applied Mathematics Series, Vol. 55, U.S. Govt. Printing Office, Washington, D.C., 20402.

Amoroso, F. and W. W. Jones [1988], "Modeling Direct Sequence Pseudonoise (DSPN) Signaling with Directional Antennas in the Dense Scatterer Mobile Environment," *38th IEEE Vehicular Technology Conference*, Philadelphia, PA, pp. 419-426, 15-17 June.

Barts, R. M. and W. L. Stutzman, [1991] "Modeling and Simulation of Mobile Satellite Propagation," *IEEE Trans. Antennas and Propagation*, Vol. 40, No. 4, pp. 375-382, April.

Barts, R. M., W. L. Stutzman, W. T. Smith, R. S. Schmier, and C. W. Bostian [1987], "Land Mobile Satellite Propagation Modeling," *Proc. of the 1987 IEEE A&P Society International Symposium*, Vol. 1, pp 20-23.

Clarke, R. H. [1968], "A Statistical Theory of Mobile-Radio Reception," *Bell System Technical Journal*, Vol. 47, No. 6, July-August, pp. 957-1000.

Cygan, D., M. Dippold and J. Finkenzeller [1988], "Kanalmodelle für die Satellitengestützte Kommunikation Landmobiler Teilnehmer," *Archiv für Elektronik und Übertragungstechnik*, Vol. 42, No. 6, pp. 329-339.

Davies, K. [19901, *Ionospheric Radio*, IEE/Peter Peregrinnus Ltd., London, U.K.

Flock, W. L. [1987], "Propagation Effects on Satellite Systems at Frequencies Below 10 GHz; A Handbook for Satellite System Design (Second Edition)," *NASA Reference Publication* 1108 (02), December.

Hess, G. C. [1980], "Land-Mobile Satellite Excess Path Loss Measurements," *IEEE Trans. on Vehicular Tech.*, Vol. VT-29, No. 2, pp. 290-297, May.

ITU-R, formerly CCIR [1986a], *Recommendations and Reports of the CCIR*, Volume V, Propagation in Non-Ionized Media, International Telecommunications Union, Geneva, Switzerland.

ITU-R, formerly CCIR [1986b], *Recommendations and Reports of the CCIR*, Volume VI, Propagation in Ionized Media, International Telecommunications Union, Geneva, Switzerland.

Jakes, W. C., Jr. (Editor) [1974], *Microwave Mobile Communications*, Wiley, New York.

LaGrone, A. H. and C. W. Chapman [1961], "Some Propagation Characteristics of High UHF Signals in the Immediate Vicinity of Trees," *IRE Trans. on Antennas and Propagat.*, Vol. AP-9, September, pp. 487-491.

Lee, W. C. Y. [1986], *Mobile Communications Design Fundamentals*, H. W. Sams and Co., Indianapolis, Indiana.

Loo, C. [1985], "A Statistical Model for A Land Mobile Satellite Link," *IEEE Trans. on Vehicular Tech.*, Vol. VT-34, No. 3, August, pp. 122-127.

Loo, C. [1987], "Measurements and Models of A Land Mobile Satellite Channel and Their Applications to MSK Signals," *IEEE Trans. on Vehicular Tech.*, Vol. VT-35, No. 3, August, pp. 114-121.

Lutz, E., W. Papke, and E. Ploechinger [1986], "Land Mobile Satellite Communications Channel Model, Modulation and Error Control," *Seventh International Conference on Digital Satellite Communications*, 12 - 16 May, pp. 537-543.

Papoulis, A. [1965], *Probability, Random Variables, and Stochastic Processes*, McGraw-Hill, New York.

Reed, H. R., and C. M. Russel [1966], *Ultra High Frequency Propagation*, Boston Technical Publishers, Inc., Cambridge, MA.

Smith, W. T. and W. L. Stutzman [1986], "Statistical Modeling for Land Mobile Satellite Communications," *Virginia Tech Report EE Satcom 86-3*, Virginia Tech, Blacksburg, VA, August.

Vishakantaiah, P. and W. J. Vogel [1989], "LMSS Drive Simulator for Multipath Propagation," *Proc. of NAPEX XIII*, San Jose, CA, 29-30 June, pp. 42-47 (Jet Propulsion Laboratory Publication JPL 89-26).

Vogel, W. J., and U.-S. Hong [1988], "Measurement and Modeling of Land Mobile Satellite Propagation at UHF and L-band," *IEEE Trans. Antennas Propagat.*, Vol. AP-36, No. 5, pp. 707-719, May.

Wakana, H. [1991], "A Propagation Model for Land-Mobile-Satellite Communication," *1991 North American Radio Science Meeting and IEEE/APS Symposium*, The University of Western Ontario, London, Ontario, Canada, June 24-28.

Yoshikawa, M., and M. Kagohara [1989], "Propagation Characteristics in Land Mobile Satellite Systems," *39th IEEE Vehicular Technology Conference*, 1-3 May, pp. 550-556.

Chapter 12
Summary of Recommendations

Table of Contents

Table of Figures

Table of Tables

Chapter 12
Summary of Recommendations

The major recommendations of the individual chapters are succinctly summarized here along with caveats and suggestions for future work. Elaboration of the formulations including pertinent references may be found in the designated chapters.

12.1 Introduction (Chapter 1)

An overview of the contents of the individual chapters in this text is given. Also included is a description of how to access the contents of this document from the World Wide Web at http://www.utexas.edu/research/mopro/index.html. The authors encourage the readers to send their suggestions and comments to them by accessing this address.

12.2 Average Foliage Attenuation Due to Trees: Static Case (Chapter 2)

Attenuation levels and formulations for stationary earth-satellite paths passing through canopies of trees are described. Canopy attenuation at frequencies ranging from 870 MHz to 20 GHz is considered.

12.2.1 Average and Median Foliage Attenuation Due to Tree Canopies

The average measured attenuations due to tree canopies for multiple tree-types are as follows: (a) 11 dB at 870 MHz with a 3 dB RMS, (b) 11 dB at 1.6 GHz with a 5 dB RMS. At 20 GHz, the median canopy attenuation is 23 dB. The RMS deviations are based on multiple measurements for different tree types, densities of foliage, and variable path lengths through the foliage.

12.2.2 Frequency Scaling

The following frequency scaling formulation has been validated at frequencies of 870 MHz, 1.5 GHz, 3 GHz and 20 GHz

$$A(f_2) = A(f_1) \cdot \exp\left\{1.5 \cdot \left[\left(\frac{1}{f_1}\right)^{0.5} - \left(\frac{1}{f_2}\right)^{0.5}\right]\right\}, \quad (12\text{-}1)$$

where $A(f_1)$, $A(f_2)$ are expressed in dB and represent equal probability attenuations at frequencies f_1, f_2 (GHz), respectively. In the scaling from L-Band (1.6 GHz) to K-Band (19.6 GHz), the expression (12-1) was found to hold over percentages between 1.5% to 20% with a maximum deviation of 2 dB. The concept of "percentage" for the static tree case represents "the percentage of optically shadowed locations over which measurements were made."

12.2.3 Effects of Canopy Branches and Foliage

At UHF (870 MHz), branches of canopies are the dominant cause of attenuation, whereas at K-Band (20 GHz), the leaf part of the tree is the major cause. For example, assume that 5 dB attenuation exists for the no-foliage condition at UHF or K-Band. When leaves are present, the attenuation in dB nominally increases at UHF by a factor of 1.35 to 6.8 dB, whereas at K-Band it increases by a factor of 3.5 to 17.5 dB.

The following static formulations were found applicable:

For $5\,dB \le A(no\ \ foliage) \le 14\,dB$ at $f = 870\,MHz$

$$A(\ foliage) = 1.35 \cdot A(no\ foliage)\,. \quad (12\text{-}2)$$

For $5\,dB \le A(no\ \ foliage) \le 25\,dB$ at $f = 20\,GHz$

$$A(\ foliage) = 0.351 + 6.825 \cdot [A(no\ \ foliage)]^{0.578}, \quad (12\text{-}3)$$

where $A(\ foliage)$, $A(no\ \ foliage)$ are the equal probability values of the attenuation (in dB) for the foliage and non-foliage conditions, respectively.

12.2.4 Suggestions for Future Efforts

Measurements in the interval between 4 GHz and 20 GHz are not available. Static canopy attenuation measurements for earth-satellite scenarios should therefore be made at the intermediate frequencies (e.g., C-Band, X-Band and K_u Band) to extend the validity of (12-1). This formulation may further be extended for frequencies above 20 GHz.

12.3 Attenuation Due to Roadside Trees: Mobile Case (Chapter 3)

Attenuation distributions are presented for scenarios involving a mobile vehicle with an antenna mounted on its roof receiving satellite signals along tree-lined roads. The results presented here are framed in terms of the "percentage of the distance driven over which

the attenuation exceeds given fade margins," also referred to as the "cumulative fade distribution."

12.3.1 The Extended Empirical Roadside Shadowing Model

This model (presently an ITU-R Recommendation) estimates the cumulative fade distribution for mobile-satellite scenarios with the following caveats. (1) The earth-satellite path is approximately orthogonal to the line of roadside trees. (2) The percentage of optical shadowing is in the range of 55% to 75%. (3) Exceedance probabilities range between 1% and 80%. (4) Elevation angles range from 7° to 60°. (5) The frequency interval of validity is 0.8 GHz to 20 GHz. (6) The fade uncertainty in the distribution at any given probability is ± 5 dB for elevation angles exceeding 20°. (7) Below 20° the uncertainty may be larger because of the likelihood of blockage from terrain and other obstacles. This model has been adopted by the ITU-R and the steps for implementation are as follows:

Step 1: Calculate the fade distribution at L-Band ($f_L = 1.5$ GHz), valid for percentages of distance traveled of $20\% \geq P \geq 1\%$, at the desired path elevation angle, $60° \geq \theta \geq 20°$ using:

$$A(P, \theta, f_L) = -M(\theta)\ln(P) + N(\theta), \tag{12-4}$$

where

$$M(\theta) = 3.44 + 0.0975\,\theta - 0.002\theta^2, \tag{12-5}$$

$$N(\theta) = -0.443\,\theta + 34.76, \tag{12-6}$$

and q is the elevation angle in degrees.

Step 2: Convert the fade distribution (12-4) at $f_L = 1.5$ GHz, valid for $20\% \geq P \geq 1\%$, to the desired frequency f (GHz) where $0.8\,GHz \leq f \leq 20\,GHz$ using:

$$A(P, \theta, f) = A(P, \theta, f_L)\exp\left\{1.5 \cdot \left[\left(\frac{1}{f_L}\right)^{0.5} - \left(\frac{1}{f}\right)^{0.5}\right]\right\} \tag{12-7}$$

Step 3: Extend the fade distribution to percentages of distance traveled in the range $80\% \geq P > 20\%$ using:

$$A(P, \theta, f) = A(20\%, \theta, f)\frac{\ln\left(\frac{80}{P}\right)}{\ln(4)} \tag{12-8}$$

Step 4: For path elevation angles in the range $20° > \theta \geq 7°$, the fade distribution is assumed to have the same value as at $q = 20°$. That is,

$$A(P,q,f) = A(P,20°,f) \tag{12-9}$$

In Figure 12-1 is a family of cumulative fade distributions at 1.5 GHz for elevation angles ranging from 20° to 60° calculated using the above formulation.

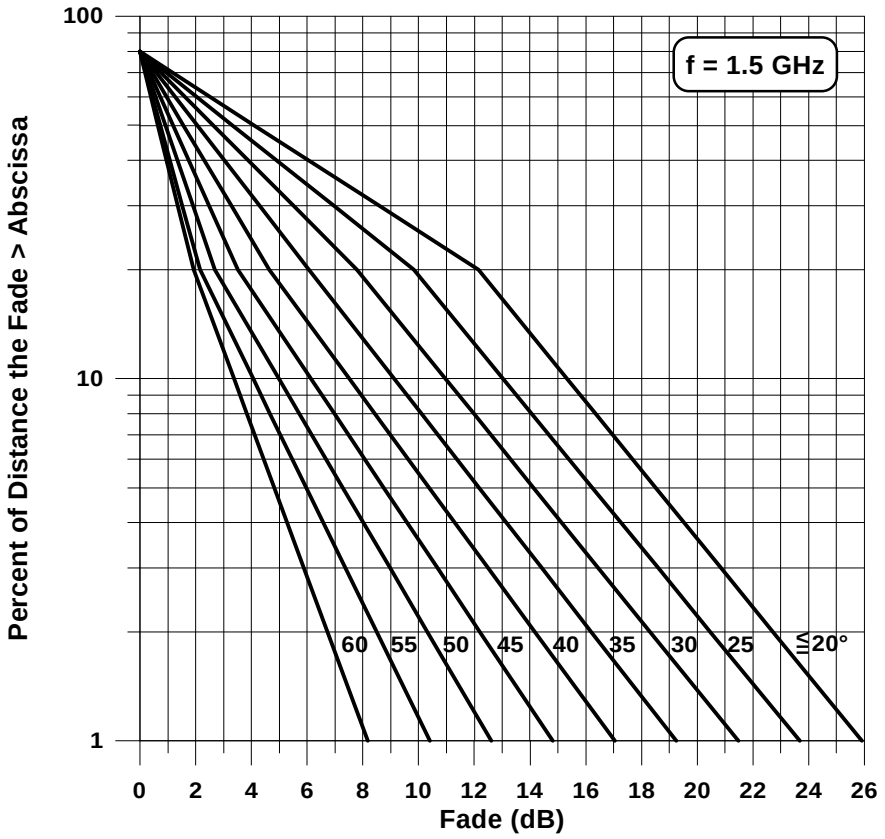

Figure 12-1: Family of cumulative fade distribution curves derived from application of the EERS model at 1.5 GHz.

12.3.2 Effects of Foliage

Systematic measurements of the effects of foliage have been made for mobile-satellite scenarios at UHF (870 MHz) and K-Band (20 GHz). The empirical relations are:

At $f = 870\ MHz, 1\% \le P \le 80\%$

$$A(\ foliage) = 1.24 \cdot A(no\ \ foliage) \tag{12-10}$$

At $f = 20\ GHz, 1 \le A(no\ \ foliage) \le 15\ dB\ \ (1\% \le P \le 50\%)$

$$A(\ foliage) = 0.351 + 6.825 \cdot [A(no\ \ foliage)]^{0.578} \tag{12-11}$$

where $A(\ foliage)$, $A(no\ \ foliage)$ are the equal probability values of the foliage and non-foliage attenuations expressed in dB, respectively. The expression (12-11) is identical to

that of the static run except that the range of validity is different in percentage and attenuation ranges.

12.3.3 Suggestions for Future Efforts

The EERS formulation has been validated at 870 MHz, 1.5 GHz, 3 GHz and 20 GHz. It is recommended that further validation be applied at 5, 10, and 15 GHz. This formulation should be further extended to frequencies in excess of 20 GHz for systems where appropriate fade margins are available.

12.4 Signal Degradation for Line-of-Sight Communications (Chapter 4)

Cumulative fade distributions are presented for land-mobile satellite scenarios where multipath is the dominant cause of signal degradation. The multipath environment may be due to roadside trees, utility poles, terrain, or a nearby body of water and is generally dependent on the antenna beamwidth characteristics.

12.4.1 Empirical Multipath Model

The following empirical multipath model is valid at frequencies between 870 MHz and 20 GHz and elevation angles between 8° and 60°.

For $1\% \le P \le 50\%$ or $0.6 \le A \le 4.6\ dB$

$$P = 94.37 \cdot \exp(-9.863 \cdot A), \tag{12-12}$$

where P is the percentage of the distance driven over which the attenuation A (dB) is exceeded, assuming only multipath conditions. The model distribution uncertainty is approximately within ± 1.5 dB of 12 measured distributions at equal percentages greater than 2%. Between 1% and 2%, it is within ± 3 dB.

The model (12-12) includes scenarios that correspond to: (1) canyons at 870 MHz and 1.5 GHz for 30° and 45° elevations, (2) rolling hills and mountains at 1.5 GHz for elevation angles of 10° to 14°, (3) roadside tree measurements at 870 MHz and 1.5 GHz for elevation angles from 10° to 60°, (4) roadside tree measurements at 20 GHz for an elevation angle of 38°, (5) open fields and near-water at 20 GHz for elevation of 8° for which the vehicle shielded reflections from the water. The formulation (12-12) does not apply to scenarios where multipath reflections from nearby bodies of water may exist and are not filtered out by the antenna gain characteristics. Such measurements gave fades as high as 14 dB at the 1% level. Maritime multipath models described in Section 12.9 (and Chapter 9) should be used when receiving multipath reflections from a nearby body of water.

Multiple type antennas were used for the above-described measurements. These included the following: (1) UHF and L-Band measurements at elevations between 30° and 60° for canyons and tree-lined road scenarios were executed using an antenna beamwidth of 60° (15° to 75° in elevation and azimuthally omni-directional). (2) Low elevation L-Band

measurements were obtained using a tracking helix antenna with beamwidths in the principal planes of approximately 36°. (3) Low and high elevation angle measurements at 20 GHz were made using a tracking horn antenna with a beamwidth of 27°.

12.4.2 Suggestions for Future Work

The multipath formulation (12-12) was validated at frequencies of 870 MHz, 1.5 GHz and 20 GHz for three specific antenna types. It is suggested this formulation be further validated at intermediate frequencies and with other antennas having wider beamwidths.

12.5 Fade and Non-Fade Durations and Phase Spreads (Chapter 5)

Fade and non-fade duration models are given for tree-lined roads at L-Band. These were derived from measurements made in Central Maryland and Southeastern Australia and are presently ITU-R Recommendations. Also given are cumulative distributions of phase spreads for roadside tree scenarios exhibiting moderate and extreme shadowing.

12.5.1 Fade Duration Model for L-Band

The conditional cumulative distribution of fade duration for tree-lined roads exhibiting moderate to extreme shadowing (presently an ITU-R Recommendation) was found to follow the following lognormal distribution given by

For $dd \geq 0.02\ m$

$$P(FD > dd | A > A_q) = \frac{1}{2}\left\{1 - erf\left[\frac{(\ln dd - \ln a}{\sqrt{2}s}\right]\right\}, \tag{12-13}$$

where $P(FD > dd | A > A_q)$ represents the probability that the fade duration FD exceeds the duration distance dd under the condition that the attenuation A exceeds A_q. Also, erf is the error function, s is the standard deviation of $\ln dd$, and $\ln a$ represents the mean value of $\ln dd$. The left-hand expression of (12-13) was estimated by computing the percentage number of "duration events" which exceed dd relative to the total number of events for which $A > A_q$. An event of duration distance dd occurs whenever the fade crosses a threshold level A_q and persists "above that level" for the driving distance dd. For the case in which the threshold $A_q = 5\ dB$,

$$a = 0.22\ m, \quad s = 1.215\ m \quad . \tag{12-14}$$

The RMS deviations of actual measured fade duration distributions, when compared to the above model, was smaller or equal to 18%. The formulation (12-13) was derived from Australian measurements (elevation angle of 51°) and validated in central Maryland, USA, at elevation angles of 30°, 45°, and 60°.

12.5.2 Cumulative Distributions of Non-Fade Durations

A "non-fade duration" event of distance duration dd is the distance over which the fade levels are persistently smaller than a prescribed fade threshold. The measured data resulted in the following non-fade duration cumulative distribution

$$P(NFD > dd | A < A_q) = b\ (dd)^{-g}\ , \tag{12-15}$$

where $P(NFD > dd | A < A_q)$ is the percentage probability that a continuous non-fade distance NFD exceeds the duration distance dd (in m) given the condition that the fade is smaller than the threshold A_q. The values of the parameters b, g in the formulation (12-15) are listed in Table 12-1 for road types exhibiting "moderate" and "extreme" shadowing assuming a 5 dB fade threshold. A single best-fit power curve has been derived for the two "moderate" runs.

Table 12-1: Non-fade duration regression values of b, g satisfying the power expression (12-15) at a 5 dB threshold for road types exhibiting "moderate" and "extreme" shadowing at a path elevation angle of 51° (f = 1.5 GHz).

Shadowing Level	b	g	%RMS Deviation	Distance (km)
Moderate	20.54	0.58	33.3	33.0
Extreme	11.71	0.8371	9.3	2.4

12.5.3 Cumulative Distributions of Phase Fluctuations

For conditions in which L-Band fades were in excess of 2 to 8 dB for tree-lined road scenarios, the "best fit" phase fluctuation distributions were found with good accuracy to follow a fifth-order polynomial over a percentage exceedance range of 1% to 90% having the form

$$P(f > f_u | A > A_q) = \sum_{i=1}^{6} a_{i-1} f^{\,i-1}\ , \tag{12-16}$$

where (12-16) may be read as the probability that the phase f (degrees) exceeds the threshold level f_u given a fade A (dB) exceeds the threshold level A_q. In Table 12-2 is given a listing of the values of the polynomial coefficients a_i at the threshold fade level of 5 dB for the "extreme" and "moderate" road types.

Table 12-2: Listing of polynomial coefficients characterizing phase fluctuation distributions of the form (12-16) for road types exhibiting "moderate" and "extreme" shadowing and a 5 dB fade threshold.

Road Type	Polynomial Coefficients					
	a_o	a_1	a_2	a_3	a_4	a_5
Moderate	56.51	-6.516	7.325×10^{-2}	2.380×10^{-2}	2.059×10^{-4}	-3.985×10^{-5}
Extreme	54.23	-4.242	-1.0897×10^{-2}	6.425×10^{-3}	2.082×10^{-5}	-4.258×10^{-6}

The above results demonstrate that the influence of phase excursion on demodulation techniques are small over the range of probabilities from 5% to 95%, since the phases are within $\pm 15°$ relative to the median.

12.5.4 Suggestions for Further Work

It is suggested that the above results be extended to other frequencies such as UHF, S-Band, and K-Band as well as to elevation angles smaller than 20° where existing databases are available. Extension of the formulations to hilly and mountainous terrain is also suggested.

12.6 Polarization, Antenna Gain and Diversity Considerations (Chapter 6)

Fading effects are examined at UHF and/or L-Band using antennas with multiple polarizations and different antenna gains. Fade reduction experienced by changing lanes is described. Diversity gains are characterized as a function of antenna spacing and satellite pointing

12.6.1 Frequency Re-Use

Co- and cross-polarization measurements at 1.5 GHz have demonstrated that insufficient isolation exists for mobile-satellite scenarios. For example, when a fade of 5 dB was experienced, isolation of only 11 dB existed in the cross polarized channel. Hence, frequency re-use through the transmission of multiple polarizations is not a viable solution.

12.6.2 Multipath Effects for Variable Antenna Gains

Where multipath reflections from the ground do not arise, small fade differences occur when using antennas of different gains. On the other hand, for earth-satellite geometries in which ground multipath may arise, the use of higher gain antennas may substantially reduce fading by as much as 10 dB. The former and latter conclusions are based on measurements at 1.5 GHz and 20 GHz, respectively.

12.6.3 Effect of Switching Lanes

Where the satellite path is orthogonal to the driving direction, switching lanes is likely to increase or reduce the fading depending on the elevation angle and the satellite location relative to the vehicle direction (e.g., right or left of the vehicle). An equal probability fade of 10 dB at UHF or L-Band, for example, was found to reduce to 5 dB at both frequencies by switching lanes. The amount of fade reduction is elevation angle dependent, i.e., the higher elevation angle scenarios (e.g., 60°) give greater fade reduction than a smaller ones (e.g., 30°).

12.6.4 Diversity Gain by Spaced Antennas

Figure 12-2 depicts the diversity gain variation versus antenna separation distance for a family of single terminal fade margins. These curves correspond to L-Band (1.5 GHz) for tree-lined road scenarios. We note that two antennas pointing at the same satellite but separated by 5 m will result in L-Band diversity gains of 3 dB and 5 dB at single terminal fades of 5 dB and 10 dB, respectively. Increasing the separation to 10 m results in further diversity gain improvements of only an additional 0.5 dB (at most) for these single terminal fades.

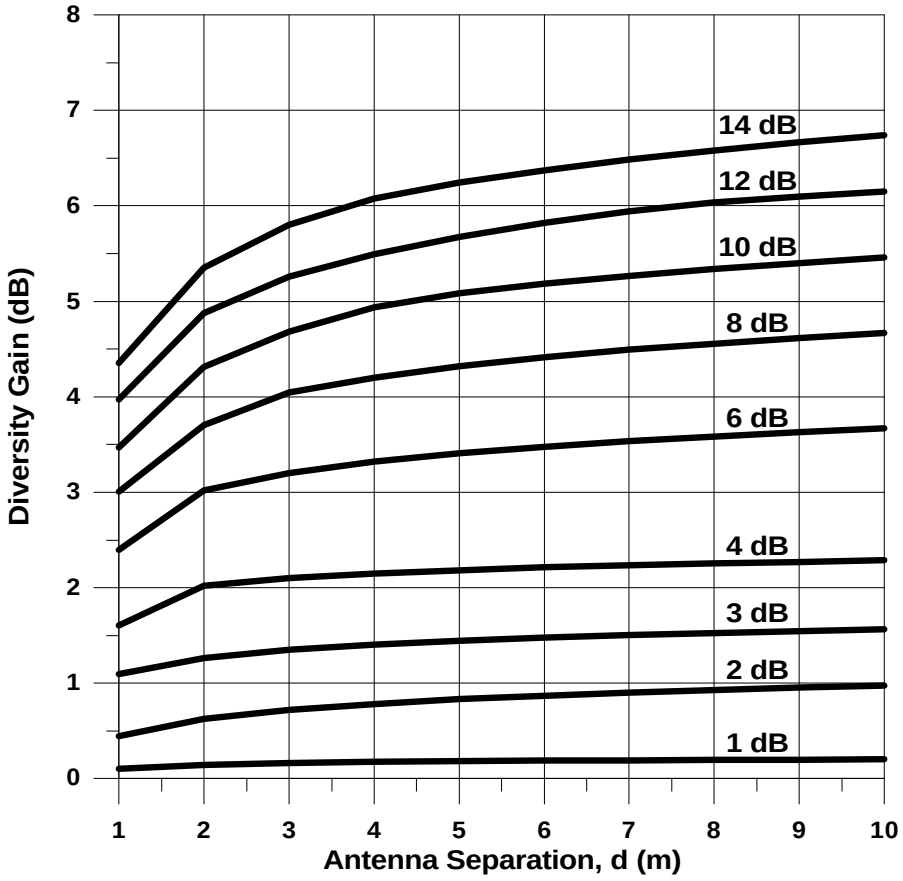

Figure 12-2: Diversity gain versus antenna separation distance at 1.6 GHz for a family of single terminal fade margins for tree-lined road scenarios.

12.6.5 Satellite Diversity

Figure 12-3 and Figure 12-4 have been derived from optical measurements and simulations employing the Globalstar constellation of orbiting satellites for urban Japan. The methods used to calculate these figures are summarized in Section 12-10. At the 20% level, the highest satellite fade at L-Band is noted to be 17 dB (Figure 12-3). A diversity gain of 12 dB may be gained by sequential switching to the satellite giving the smallest fading (highest signal level). Although percentages smaller than 20% give improved diversity gains, the joint probability fade level may nevertheless be too great for practical communications (e.g., at 1%, the joint fade level exceeds 20 dB). Figure 12-4 shows that, in general, one dB difference exists between the "hand-off" and "combining" diversity modes of operation.

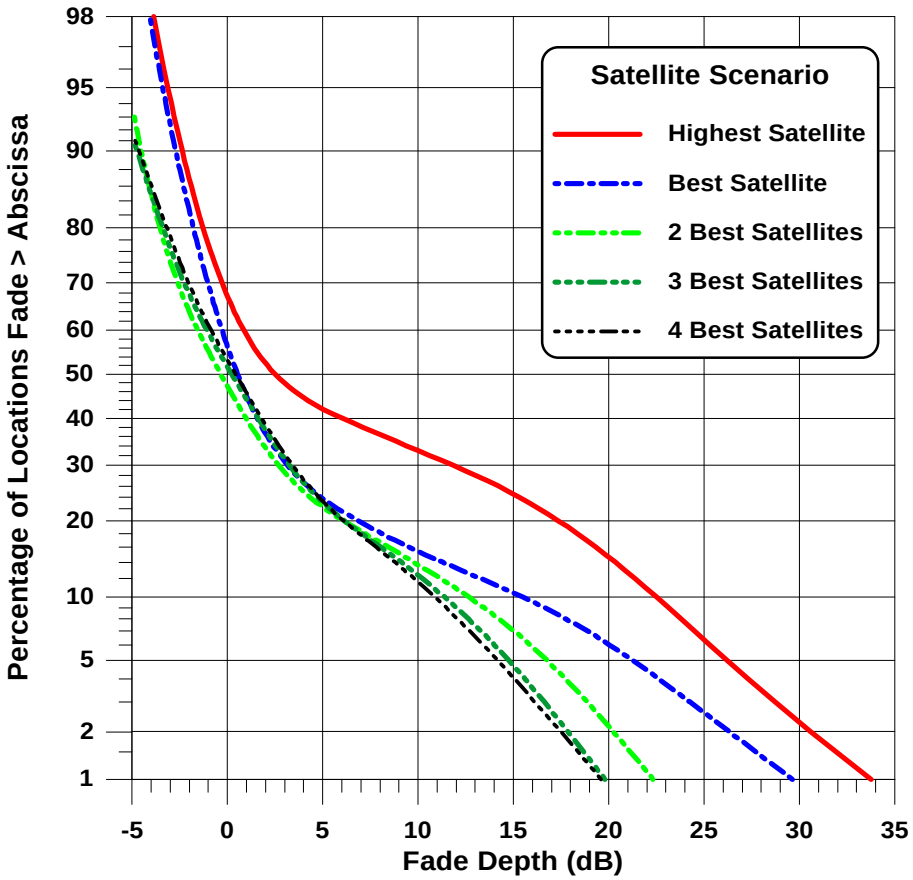

Figure 12-3: Cumulative fade distributions at 1.6 GHz for the simulated Globalstar constellation of satellites assuming combining diversity for urban Japan.

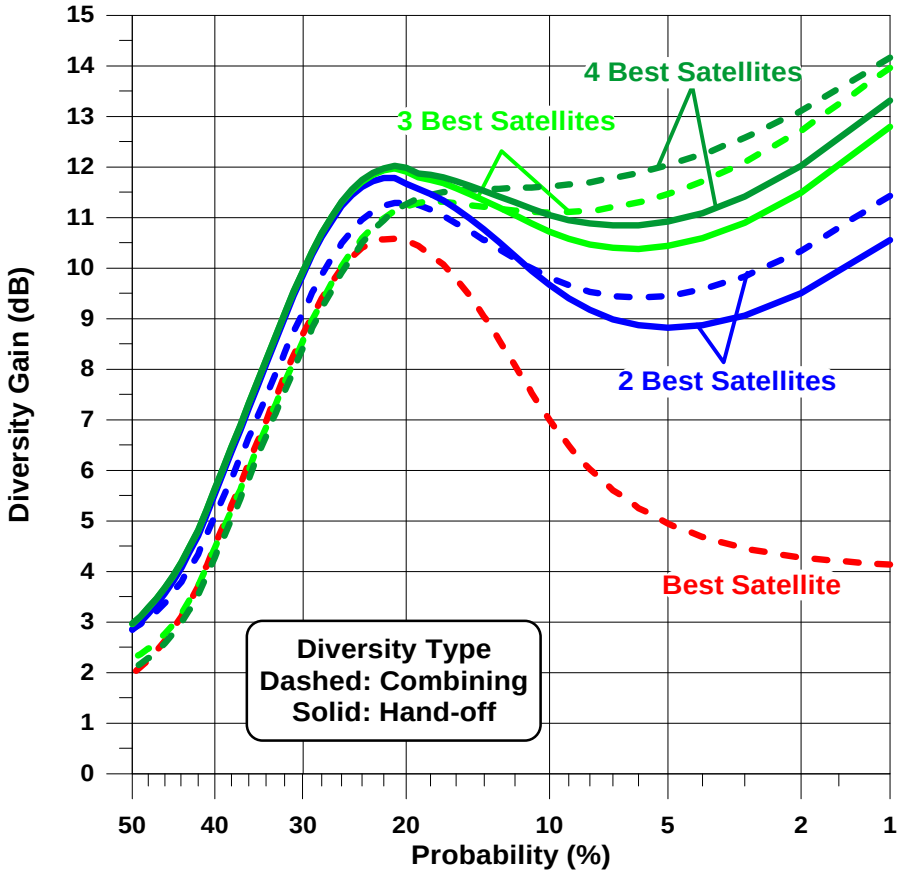

Figure 12-4: Diversity gains achieved through satellite pointing methods as a function of the fade exceedance probability. These curves were derived by simulating the Globalstar constellation of satellites for urban Japan at 1.6 GHz.

12.6.6 Suggestions for Further Work

Where databases exist at UHF and K-Band, diversity gain simulations based on spaced antennas should be executed and the results compared with those for L-Band described above. Satellite diversity simulations should be performed for other frequencies and for tree-lined roads and mountainous regions.

12.7 Investigations from Different Countries (Chapter 7)

A compendium of cumulative fade distributions associated with land-mobile-satellite scenarios is given for significant experiments throughout the world. Comparisons are made between measured distributions and those calculated using the EERS model.

12.7.1 Compendium of Measurements

In Table 12-3 are listed entries of fade levels at the 1% and 10% probabilities for 54 measured distributions. The large range in the fades are caused by such factors as variable density of foliage cutting the earth-satellite path, bearing to the satellite,

blockage effects due to roadside obstacles and the presence of underpasses. The last column of this table represents the number of experiments examined in arriving at the indicated fade ranges. The numbers in parentheses represent the EERS values. Where angle and/or frequency ranges are given, the EERS value is calculated at the lower elevation angle and larger frequency (highest fade case). The system designer interested in selecting a design fade margin may use the worst case fade or the mid-value depending upon the individual system constraints. Alternate suggested fade margin levels may be obtained using the indicated EERS values that are representative of roadside tree shadowing where the tree density exceeds 55%.

Table 12-3: Fade level ranges at the 1% and 10% probabilities derived from measured distributions which were culled in terms of frequency and elevation angle.

f (GHz)	El (°)	Fade		Number
		P = 1%	P = 10%	
0.87	5	>30 (18)	21.5 (10.5)	1
0.87	15-20	13-18 (18)	5.5-8 (10.5)	2
0.87	30	14-20 (15)	6-10 (7.5)	1
0.87-0.893	45	7-15 (10.5)	2-7.5 (4)	2
0.87	60	3-12 (5.5)	2-5 (2.5)	1
1.5	19-26	11-21 (26)	3.5-16 (15.5)	5
1.5-1.55	30	17.5-25 (22)	8-13 (11)	2
1.5-1.6	40-50	2.5-32 (18)	1-20 (8)	7
1.3-1.6	50-60	5-18.5 (13)	2-7.5 (5)	7
1.3-1.6	80	8-12	2-3	3
2.05-2.09	18-21	>30 (31)	>15 (18.5)	2
2.09-2.66	40-45	12-17.7 (22.5)	7-11.5 (10)	3
2.5-2.6	60	12-22.5 (11)	5-9 (10)	3
2.5-2.6	80	10.5-16	4.5-6	2
10.4	60	27.5-28 (17.5)	13-18.5 (7)	2
10.4	80	24-26	10.5-13	2
20	8	>25 (63)	>25 (37)	1
18.7-20	30-38	21-40 (52)	9-33 (27)	4
20	46	8 to >30 (35)	2-30 (14.5)	3
20	54.5	28 (26)	15 (10)	1

12.7.2 Suggestions for Further Work

Measurements at elevation angles smaller than 60° appear to be unavailable in the frequency interval between 3 to 20 GHz and at frequencies greater than 20 GHz. Future measurement programs should fill this gap.

12.8 Earth-Satellite Propagation Effects Inside Buildings (Chapter 8)

This chapter deals with propagation effects inside buildings for scenarios in which the transmitter is located on a satellite or a platform simulating a satellite. Relative signal losses are characterized in terms of spatial, temporal and frequency effects for different structure types over a frequency interval of 500 to 3000 MHz.

12.8.1 Required Fade Margins Inside Buildings

Figure 12-5 gives the median, 95% and 5% fading inside six buildings at L and S-Bands. It is clear that a fade margin of 30 dB is required to achieve reliable communications.

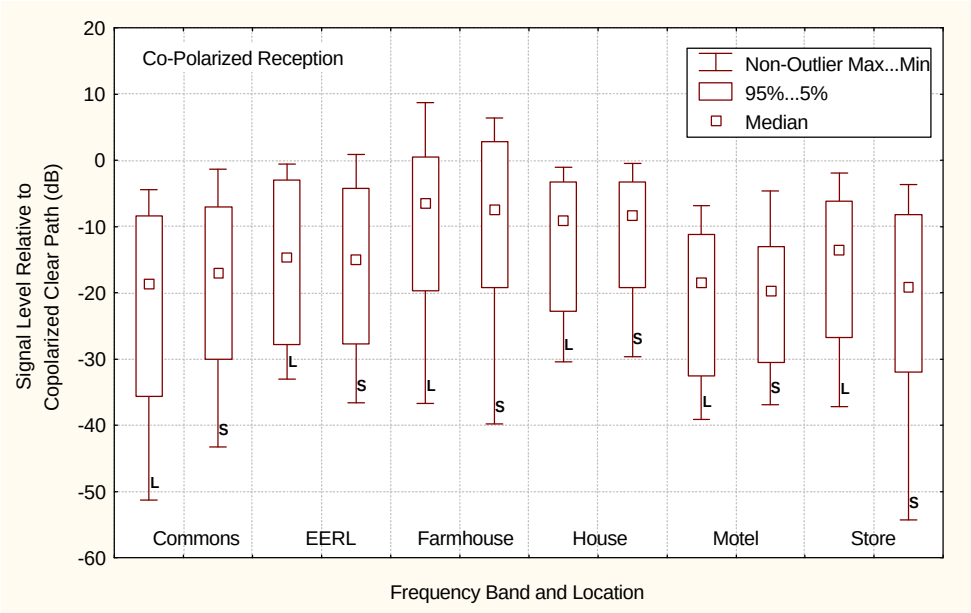

Figure 12-5: Median, 95%, and 5% fade levels of the relative power losses inside six buildings at L- and S-Bands.

12.8.2 Fading Dependence on Frequency

Fade differences over 100 MHz frequency intervals may exhibit variations with frequency as large as 25 dB. When these fade differences are averaged and examined over a multi-GHz frequency interval, a fading trend of $\leq +3$ dB/GHz ensues with increasing frequency (to 3 GHz).

12.8.3 Distortion Due to Bandwidth

In Figure 12-6 is plotted the standard deviation of signal fading (inside building structures) versus the bandwidth for frequencies ranging from 700 MHz to 1800 MHz and bandwidths between 2 MHz and 90 MHz. These results imply that relatively small distortions should be expected for bandwidths between 1 to 10 MHz (standard deviations smaller than 1.7 dB in signal fading).

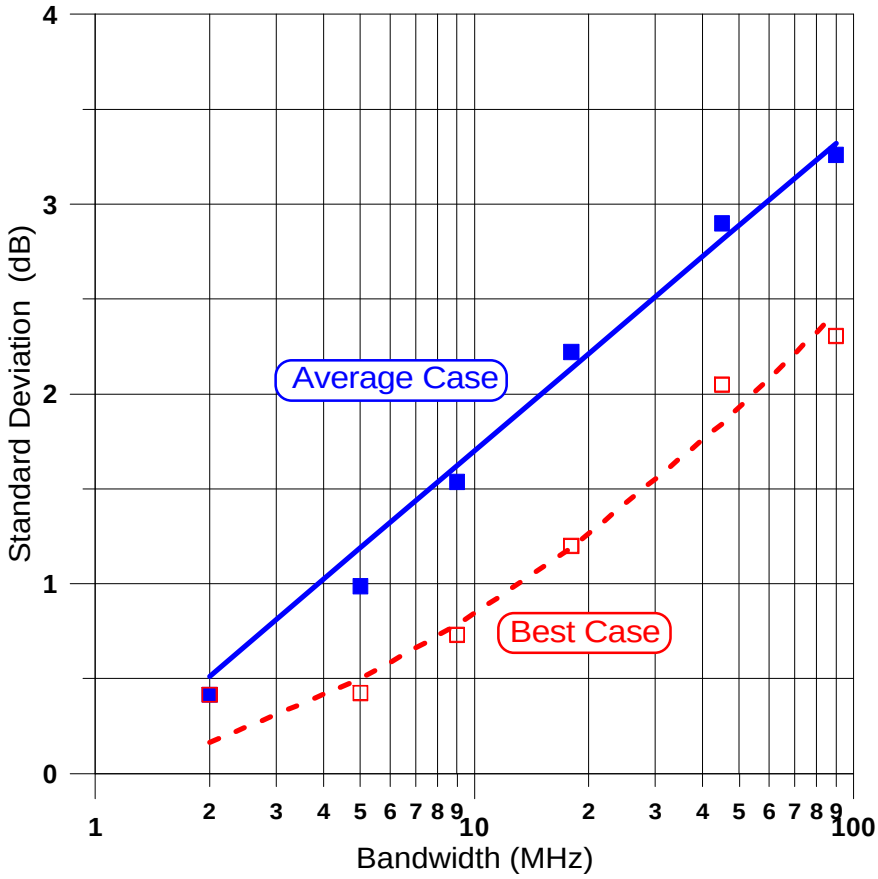

Figure 12-6: Standard deviation of signal fading versus-Bandwidth for UHF to L-Band frequencies for inside building measurements

12.8.4 Fading Effects Due to Antenna Positioning

The median antenna displacement giving minimum and maximum signal levels was found to be between 35 and 45 cm independent of frequency between 0.7 and 1.8 GHz. Differences in signal levels between the values at maximum and minimum locations have been noted to be as high as 30 dB. These distances are suggested antenna spacing values for diversity gain operation.

12.8.5 Effects Caused by the Human Body

A person blocking the transmission may cause fades between 6 to 10 dB in the frequency interval of 700 to 1800 MHz. People moving near the receiving antenna but outside the antenna Fresnel region typically produce variations of less than 0.5 dB. A hand-held terminal at 900 MHz may result in a signal decrease of 4 to 7 dB when held at the waist and 1 to 2 dB when held against the head.

12.8.6 Suggestions for Further Work

Analysis of the type described in the chapter should be carried out at frequencies above 3 GHz.

12.9 Maritime-Mobile Satellite Propagation Effects (Chapter 9)

This chapter deals with multipath fading from the ocean when low gain antennas are employed at low elevation angles for ship-satellite scenarios. The results apply predominantly at L-Band.

12.9.1 Fading Depth Due to Sea Surface Reflections

Below is a summary of steps adopted by the ITU-R for evaluating the fading depth due to sea surface reflections:

Step 1: Confirm the applicable parameters for which the method is valid. These are:

Frequency range from 1 to 2 GHz (nominal frequency is 1.5 GHz).

Polarization circular or horizontal. Vertical polarization may be used for elevation angles above 8°. Below 8°, noticeable errors may exist for vertical polarization due to Brewster angle complications.

Elevation angle q_o is within the interval

$$3^o \le q_o \le \frac{BW}{4}. \tag{12-17}$$

The sea condition is such that the roughness parameter u is defined as

$$u = \frac{4p}{l} h_o Sin(q_o), \tag{12-18}$$

where u has the range

$$2 \le u \le 10 \tag{12-19}$$

and where l is the wavelength in m, q_o is the elevation angle to the satellite, h_o is the RMS wave height in m related to the significant wave height H by

$$H = 4h_o. \tag{12-20}$$

Equation (12-20) implies

$$1.5 \le H \le 7.3, \quad 0.4 \le h_o \le 1.8 \quad (m). \tag{12-21}$$

Step 2: Find the relative antenna gain D_r (in dB) in the direction of the specular reflection point of the sea. The relative antenna gain is approximately given by

$$D_r = -4 \times 10^{-4} (10^{G_o/10} - 1) q_r^{\,2}, \tag{12-22}$$

where G_o is the antenna gain in dB (dB above isotropic), and

$$q_r = 1.5\, q_o \tag{12-23}$$

and where the beam center is in the direction of the satellite. The factor of 1.5 (as opposed to 2) is used since a significant portion of the multipath energy comes from the region between the true specular reflection point and the horizon.

Step 3: Obtain the Fresnel reflection coefficient R_{ij} (in dB) where i represents the polarization of the incident wave and j is the polarization of the reflected wave. These reflection coefficients are tabulated for the sea at 1.5 GHz in Table 12-4 for horizontal polarization R_{HH}, vertical polarization R_{VV}, and circular polarization R_{CC}.

Table 12-4: Fresnel reflection coefficient values of the sea at 1.5 GHz for various polarizations.

Elevation, q (deg)	Polarization		
	Horiz., R_{HH} (dB)	Vertical, R_{VV} (dB)	Circular R_{CC} (dB)
1	-0.03	-2.86	-1.34
2	-0.06	-5.83	-2.52
3	-0.09	-9.05	-3.57
4	-0.12	-12.58	-4.52
5	-0.15	-16.01	-5.39
6	-0.18	-17.41	-6.19
7	-0.21	-16.01	-6.94
8	-0.24	-13.95	-7.64
9	-0.27	-12.19	-8.3
10	-0.30	-10.81	-8.92
11	-0.33	-9.7	-9.52
12	-0.36	-8.81	-10.09
13	-0.39	-8.07	-10.64
14	-0.42	-7.46	-11.16
15	-0.45	-6.93	-11.67
16	-0.48	-6.48	-12.17
17	-0.51	-6.09	-12.65
18	-0.54	-5.74	-13.12
19	-0.57	-5.44	-13.58
20	-0.60	-5.16	-14.03

Step 4: Calculate the correction factor C_q in dB given by

$$C_q = 0 \quad for \quad q_o \geq 7^\circ \qquad (dB) \tag{12-24}$$

and

$$C_q = (q_o - 7)/2 \quad for\ q_o < 7^\circ \quad (dB). \tag{12-25}$$

Step 5: Find the mean power of sea reflected waves P_r (in dB) relative to the direct power. This is given by

$$P_r = D_r + R_{ij} + C_q \qquad (dB). \tag{12-26}$$

Step 6: Find the fading depth A (relative to the direct power) by substituting P_r into

$$A = a \exp\left(-\frac{P_r}{b}\right) \qquad (dB), \tag{12-27}$$

where the parameters a, b in (12-27) are tabulated in Table 12-5 for different fade exceedance percentages. The expression (12-27) and the tabulated values in Table 12-5 represent "best-fit" formulations of those given by the Nakagami-Rice distributions. The fading depth A is the dB difference between the signal of the direct incident wave and a threshold level that the resultant signal level exceeds with a probability of P percent of the time.

As an example, consider a receiver system with circular polarization, at a frequency of 1.5 GHz, elevation angle of 6°, and an antenna gain of 10 dB. The fading depth at the 99% exceedance level may be shown to be –9 dB.

Table 12-5: Parameters a, b at the given probabilities that fit (12-27) representing the Nakagami-Ricean Distribution.

Probability (%)	a	b
1	9.5414	-10.3467
10	6.7844	-9.0977
50	2.9286	-3.5705
90	-8.1119	-8.6521
99	-24.8271	-6.9088

12.9.2 Fading Depth Dependence on Frequency and Significant Wave Height

Examples of fading depth dependence on significant wave height and frequency are given in Figure 12-7 for the 99% probability. The curves assume the elevation angle is 5°, circular polarization, the antenna gain is 15 dB, and wind-wave sea conditions are dominant. A significant wave height of 2 m results in approximate fading depths of 3.5, 4.5, and 5.5 dB at frequencies of 10, 5, and 3 GHz, respectively.

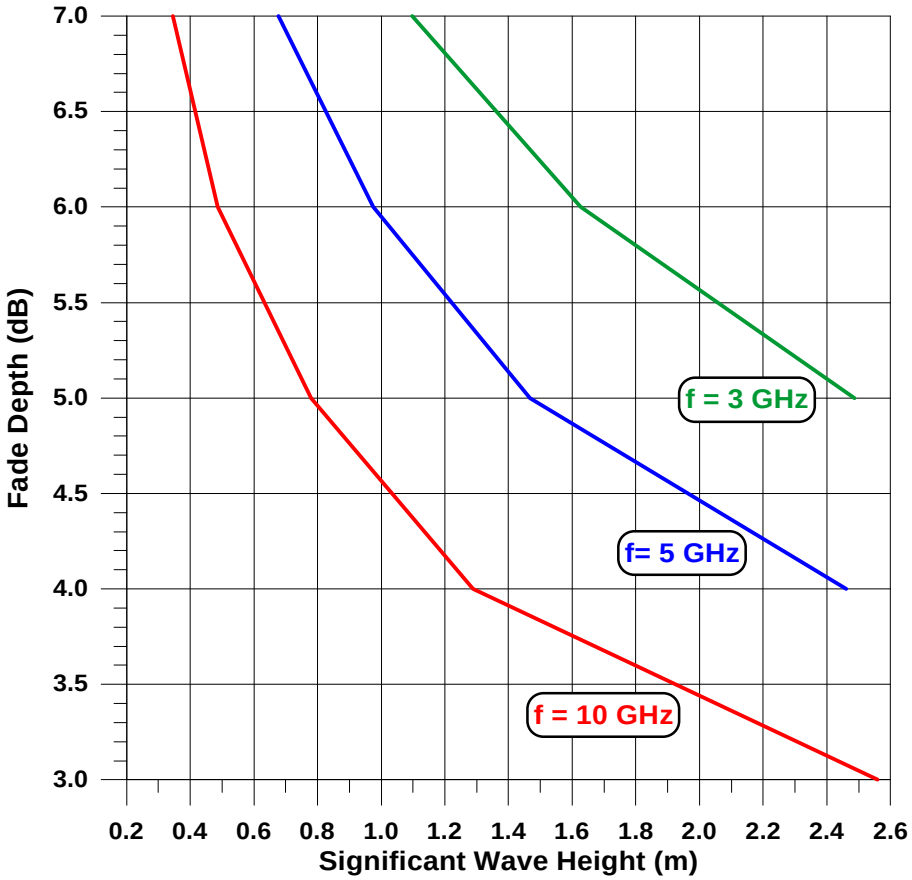

Figure 12-7: Fading depth versus significant wave height at 3, 5, and 10 GHz in the region where incoherent multipath dominates.

12.9.3 Suggestions for Further Work

Measurements and models should be extended to vertical polarization and to higher frequencies (above L-Band).

12.10 Optical Methods for Assessing Fade Margins for Shadowing, Blockage, and Clear Line-of-Sight Conditions (Chapter 10)

The assessment of fade margins for land-mobile scenarios have traditionally required transmitter platforms, vehicle tracking systems and complex receiver-data acquisition systems. More recently, innovative methods have been developed requiring photographing roadside images of the ambient environment, image reduction and analysis and application of existing models assuming known constellations of satellites. Employment of this methodology, referred to as photogrammetry, has led to estimates of a number of single and joint fade distributions and diversity results for urban areas at L-Band for earth-satellite scenarios.

12.10.1 Urban Three-State Fade Model

The photogrammetric method employs the Urban Three-State Model (UTSFM), where the probability density function f_n (PDF) for the signal envelope has the following form

$$f_n(n,a) = C(a)\ f_{Rice}(n) + S(a)\ f_{Loo}(n) + B(a)\ f_{Loo}(n), \tag{12-28}$$

where $C(a), S(a), B(a)$ are probabilities of clear, shadowed, and blocked states and are dependent on the elevation angle a. The Ricean density distribution is given by

$$f_{Rice}(v) = 2Kv\exp\left[-K(v^2+1)\right]I_o(2Kv). \tag{12-29}$$

Loo's density function is given by

$$f_{Loo}(v) = 8.686\sqrt{\frac{2}{p}}\frac{Kv}{s}\int_0^\infty \frac{1}{v}\exp\left[-\frac{(20\log(v)-m)^2}{2s^2} - K(v^2+z^2)\right], \times I_0(2Kvz)dz \tag{12-30}$$

where v is the received voltage relative to the clear path voltage, K is the ratio of the direct power received to the multipath power, $I_o(v)$ is the modified Bessel function with argument v, m is the mean of $\log v$, and s is the standard deviation of $\log v$. The parameters K, m, s are tabulated in Table 12-6 for urban Japan at 1.5 GHz and $C(a), S(a), B(a)$ are listed in Table 12-7 as a function of elevation angle (averaged over a 360° azimuth).

Table 12-6: Fade parameters of the Urban Three-State Fade Model.

Fade State	PDF Type	Parameter	Urban 3-State
C	Rice	K	5.9
S	Loo	K m s	20 10 2
B	Loo	K m s	501 100 5.4

Table 12-7: Tabulation of azimuth averaged values of $C, S,$ and B in (12-28) for different elevation angle intervals for urban Japan.

Elevation Angle Interval (°)	C	S	B
0-4	0.02	0.03	0.95
5-9	0.07	0.06	0.86
10-14	0.17	0.08	0.75
15-19	0.28	0.08	0.64
20-24	0.37	0.08	0.56
25-29	0.44	0.07	0.48
30-34	0.51	0.07	0.42
35-39	0.58	0.06	0.36
40-44	0.63	0.06	0.31
45-49	0.67	0.05	0.27
50-54	0.72	0.05	0.23
55-59	0.76	0.04	0.20
60-64	0.80	0.03	0.17
65-69	0.83	0.03	0.14
70-74	0.86	0.03	0.11
75-79	0.89	0.02	0.09
80-84	0.92	0.02	0.06
85-89	0.93	0.02	0.06

12.10.2 Probability Distributions and Diversity Gains

Probability distributions and diversity gains derived employing the above-described methodology have been described in Section 12.6.5 (Figure 12-3 and Figure 12-4).

12.10.3 Suggestions for Future Work

Although the above method has been validated using measurements for Japan, it is suggested that it be validated against existing measurements, such as in Central Maryland for tree-lined roads and in mountainous terrain. Extension of the methodology to frequencies other than L-Band is also suggested.

12.11 Theoretical Modeling Considerations (Chapter 11)

A variety of LMSS models are available to the systems designer, with three main classes of models being (1) empirical regression models, (2) probability distribution models and (3) geometric-analytic models. Empirical regression models provide simple functions for probability distributions of fades based on experimental measurements. Statistical

probability distributions models are the composite of Rayleigh, Ricean, and lognormal probability density functions with more or less physical reasoning. Geometrical analytical models attempt to predict the combined effects of scatterers by applying electromagnetic theory.

12.11.1 Choosing a Model

The choice as to which model is most appropriate depends very much on the intended application and what propagation phenomenon one wants to predict. Of the different types, empirical models do not provide insight into the physics of propagation processes, but they characterize the sensitivity of the results to important parameters. Statistical models build upon an understanding of the processes that cause signal variations, but with simplifying assumptions. Analytical models attempt to describe a particular propagation scenario deterministically, but then have to use statistics to extend the results to realistic situations.

12.11.1.1 Empirical Regression Models

The EERS model has already been summarized in this chapter under Section 12.3.1. As it is based on a large amount of data, it gives reasonably realistic estimates of fading distributions by roadside trees.

12.11.1.2 Statistical Models

Propagation effects on mobile satellite links are caused when transmissions are reflected diffusely or specularly, when they penetrate through trees or diffract around buildings. All these different propagation states can be associated with specific statistical distributions. Models need to allow for a number of states appropriate to the environment under consideration. The Loo and Lutz models work well in environments with two states, the three-state model (Chapter 10), however, covers more outdoor scenarios. The more states are incorporated into a model, the more specific site and parameter data are required.

12.11.1.3 Analytical Models

Analytical models are mainly useful for describing canonical propagation phenomena, as such they can be very useful in studying the effect of varying particular parameters, such as the bandwidth, or antenna pattern.

12.11.2 Suggestions for Future Work

A deficiency of the models presented in Chapter 11 is that they were derived for vehicular mobile applications, whereas today's emphasis of satellite services has shifted towards hand-held personal user terminals. The environment selections have therefore also broadened from highways to essentially anywhere, including but not limited to outdoors, inside buildings, inside cars, aboard trains and airplanes, etc. Although data characterizing some of these scenarios have been presented in earlier chapters, e.g., fade measurements into buildings, there has been no concurrent systematic model

development. Models pertaining to the wide range of operating environments and conditions contemplated for personal satellite communications systems need to be made available to their designers.

Index

Index

E

F

G

H

I

J

K

L

M

N

O

P

R

S

T

U

V

W

Y